Development of spheroids and organoids on the microfluidic chip

by Guocheng Fang

Thesis submitted in fulfilment of the requirements for the degree of

Doctor of Philosophy

under the supervision of Prof. Dayong Jin, Dr. Hongxu Lu, Dr. Gungun Lin, A/Prof. David Gallego-Ortega

University of Technology Sydney
Faculty of Science

09/2021

Certificate of Original Authorship

I, Guocheng FANG, declare that this thesis is submitted in fulfilment of the requirements for the award of Doctor of Philosophy, in the School of Mathematical and Physical Sciences, Faculty of Science, at the University of Technology Sydney.

This thesis is wholly my own work unless otherwise reference or acknowledged. In addition, I certify that all information sources and literature used are indicated in the thesis. This document has not been submitted for qualifications at any other academic institution.

This research is supported by an Australian Government Research Training Program and the China Scholarship Council Scholarship.

Signature: Production Note:
Signature removed prior to publication.

Date: 31-Aug-2021

Acknowledgements

First and foremost, I would like to express my deep and sincere gratitude to my supervisors. I am particularly grateful to Prof. Jin for offering the opportunity to pursue my PhD in such a great research platform, to Dr Lu for the patient advice and guidance in the experiment designs and knowledge of biological engineering, to Dr Gungun Lin for the mentoring of microfluidic chip design and equipment, to A/Prof David Gallego-Ortega for the support of mammary tumour organoids, and Prof. Majid Ebrahimi Warkini for mentoring the knowledge in microfluidics. I would like to thank each of them for their constructive criticisms and helpful discussions on my PhD thesis. Their research attitudes always inspire me to work happily and professionally.

I would like to address a special thanks to Dr. Yuan Liu for the help of droplet techniques, Dr Joris Goudsmits for the help of lithography techniques, Mr Dejiang Wang and Mrs Xaingjun Di for the help of cell culture, Mr Sajad Razavi Bazaz for the help of 3D printing moulds, Mr Hamidreza Aboulkheyr Es for the help of tumour-associated fibroblasts analysis, Mrs Laura Rodriguez de la Fuente and Dr Andrew Law for the mouse samples and related analysis.

I would like to mention all the member of the IBMD (past and present), who has provided technical supports or experiments suggestions and assistance. I enjoy working with these lovely people and appreciate their help whenever I get any experimental difficulties. I would like to thank Prof Peng Xi who supports my research in lens-free imaging. I would like to thank all of the friends I have who exist outside the realm of research during the three years in Sydney. Thanks for being so understanding and always keeping my feet on the ground.

I would like to thank my supportive family for their continuous supports and love throughout my whole life.

Finally, I would like to acknowledge the Australian Government Research Training Program and the China Scholarship Council Scholarship for providing the scholarship and research opportunities.

Format of Thesis

The thesis consists of six chapters. Chapter 1 introduces the biological fundamentals of multicellular spheroids and organoids and reviews the state-of-art microfluidic technology of spheroid and organoid culture. Chapters 2~5 cover the research in my PhD course that utilize microfluidic chips to culture spheroids and organoids and the sequential application of these models. Chapter 6 summarizes all the work and gives a brief perspective for potential future work. The thesis flow chat is illustrated below.

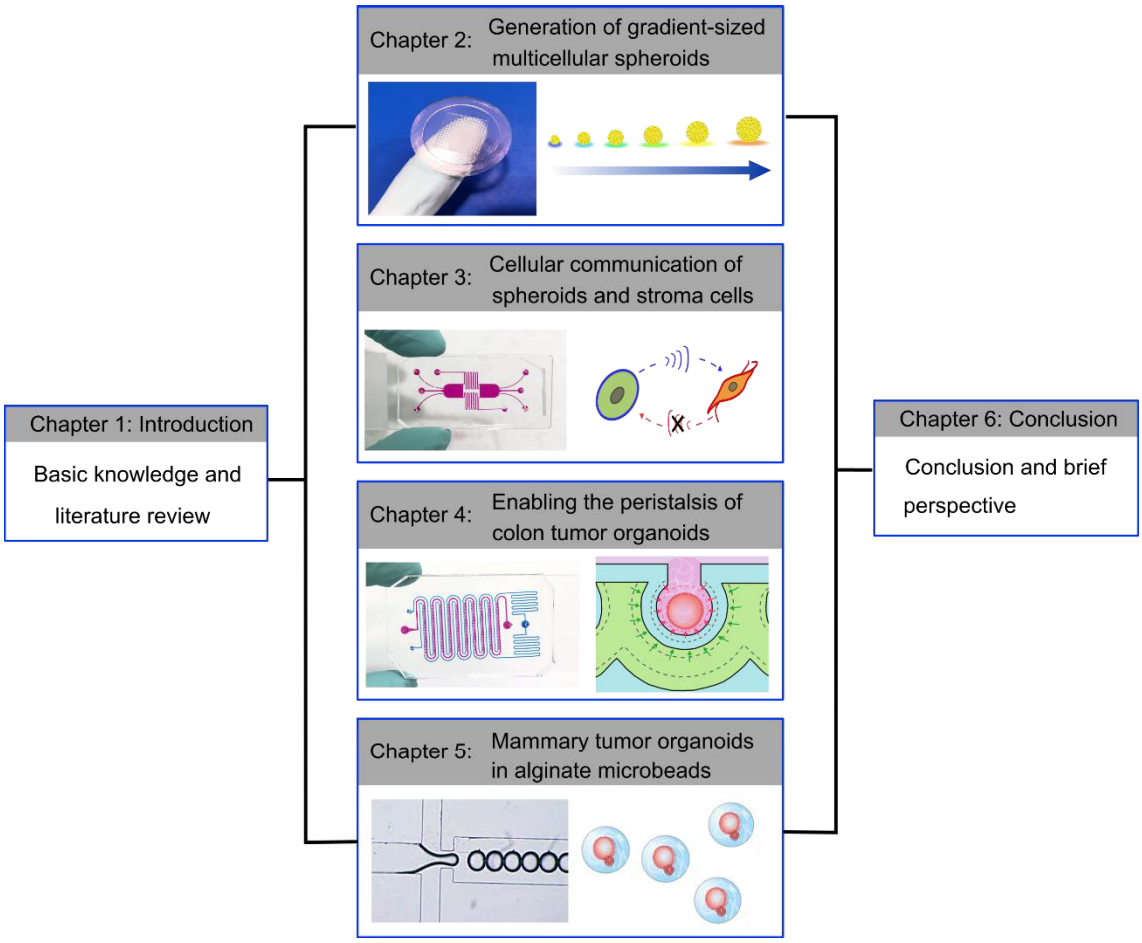

My PhD work aims to develop novel multicellular spheroids and organoids culture methods utilizing the microfluidic and microfabrication technology, also named on-chip technology. Chapter 2~3 focus on the spheroids and chapter 4~5 focus on the organoids. Chapter 2 describes a method to generate multicellular spheroids with gradient sizes on a single chip. Chapter 3 designed cell co-culture chip, which allows unidirectional signal communication, to investigate interactions between tumour spheroids and stromal cells.

In chapter 4, peristalsis is mimicked on microfluidic chips for the mechano-stimulated culture of human colon tumour organoids. In chapter 5, alginate is found to be a good candidate material for establishing the culture of mouse mammary tumour organoids. Taking the advantages of the droplet technique, we achieved high-throughput generation of mammary tumour organoids. Moreover, this model can be used to measure the luminal pressure during culture. In the last chapter, I conclude my PhD research work and briefly describe the potential future work.

List of Publications

➢ Articles

1. **G. Fang**, H. Lu*, R. Al-Nakashli, R. Chapman, G. Lin, D. Jin*. Enabling peristalsis of human colon tumour organoids on microfluidic chips. (Under revision in *Biofabrication*)
2. **G. Fang**, H. Lu*, L. Fuente, A. Law, G. Lin, D. Jin, D. Gallego-Ortega*. Mammary tumour organoids culture in non-adhesive alginate for luminal mechanics and drug screening. *Advanced Science (2021)* (DOI: 10.1002/advs.202102418).
3. **G. Fang**, H. Lu*, D. Jin*. Advances in spheroids and organoids on a chip. (In preparation).
4. **G. Fang**, H. Lu*, HA. Es, D. Wang, Y. Liu, ME. Warkiani, G. Lin, D. Jin*, Unidirectional intercellular communication on a microfluidic chip. *Biosensors and Bioelectronics (2020)* 175, 112833.
5. **G. Fang**, H. Lu*, A. Law, D. Gallego-Ortega, D. Jin, G. Lin, Gradient-sized control of tumour spheroids on a single chip. *Lab on a chip (2019)* 19 (24), 4093-4103.
6. A. Law, J. Chen, Y. Colino-Sanguino, S. Grimes, H. Lu, **G. Fang**, …, H. Ji and D. Gallego-Ortega*, ALTEN: a high-fidelity primary tissue-engineering platform to assess cellular responses in situ, submitted to *Advanced Science*, 2021
7. Y. Liu, F. Wang, H. Lu, **G. Fang**, S. Wen, …, L. Zhang, M. Stenzel, D. Jin*. Super-Resolution Mapping of Single Nanoparticles inside Tumour Spheroids. *Small (2020)* 16 (6), 2070030.
8. S. Jiang, M. Guan, J. Wu, **G. Fang**, X. Xu, …, S.Wang, P. Xi*. Frequency-domain diagonal extension imaging. *Advanced Photonics (2020)* 2 (3), 036005.
9. P. Jia†, **G. Fang**†, Z. Li, H. Liang, Y. Hong, T. Liang, J. Xiong*. Bellows spring-shaped ultrasensitive fiber-optic Fabry-Perot interferometric strain sensor. *Sensors and Actuators A: Physical* (2018) 277, 85-91.

([1-5] are closely related to my PhD program)

Abbreviations

2D	two-dimensional
3D	three-dimensional
aSCs	adult stem cells
BME	based membrane extract
BMP4	bone morphogenetic protein 4
BSA	bovine serum albumin
CAF	cancer-associated fibroblast
CAGR	compound annual growth rate
CE	counter electrode
CPA	chlorpromazine
DMD	digital micromirror device
DOX	doxorubicin
ECM	extracellular matrix
EGF	epithelial growth factor
ESCs	embryonic stem cells
FACS	fluorescence-activated cell sorting
FBS	fetal bovine serum
FoV	field of view
HR	hormone receptor
HUVECs	human umbilical vein endothelial cells
ICCP	interactive co-culture plates
IDTs	interdigital transducers
iPSCs	induced pluripotent stem cells
MSCs	mesenchyme stem cells

NA	numerical aperture
NK	natural killer
PAAm	prepolymer polyamide
PBS	phosphate buffer saline
PDMS	polydimethylsiloxane
PEG	polyethylene glycol
PHPMA	poly (N-(2-hydroxypropyl)methacrylamid)
PSCs	pluripotent stem cells
RE	reference electrode
RGD	arginylglycylaspartic acid
SIM	structured illumination microscopy
SPR	surface plasma resonance
SSAW	Surface acoustic wave
STORM	stochastic optical reconstruction microscopy
TGF-β1	transforming growth factor beta 1
TWPV	thick-wall pressure vessel
UV	ultraviolet
WE	working electrode
WNT	proto-oncogene protein
α-SMA	α-smooth muscle actin

Table of Contents

List of Figures

Abstract

Multicellular spheroids and organoids are typical *in vitro* models widely used in developmental biology, drug screening, precision medicine etc. Regulation and optimisation of these models and their residential microenvironments are crucial to maintaining their functions and behaviours. With the advances in microfabrication technology, microfluidic devices gradually become a useful tool for biomedical engineering of cultured spheroids and organoids. Building the complex multicellular systems on the microfluidic chips offers apparent advantages on these models (showcases in Chapter 1). The aim of this thesis is to implement a series of new designs of microfluidics devices and materials to improve the state-of-art cell co-culture and engineering of spheroids and organoids.

Multicellular spheroids are commonly used *in vitro* tumour models as they replicate the *in vivo* tumour. The size of spheroids plays a crucial role in cell responses during drug screening. Chapter 2 reports a method that can generate gradient-sized spheroids on a single chip with microwell arrays. As a liquid dome of cell suspension was formed on the chip, the size of spheroids can be regulated by the position of the microwells under the liquid dome.

Though tumour cells in the native microenvironment can be influenced by neighbouring stromal cells, the conventional co-culture cannot reveal the directional communications due to the random signal diffusion. In Chapter 3, a novel type of microfluidic chip was developed for the unidirectional communication between breast tumour spheroids and stromal cells.

The conventional culture of *in vitro* models lacks the mechanical cues, especially for the gastrointestinal organoids. In Chapter 4, a microfluidic chip that can mimic intestinal peristalsis was developed for human colon tumour organoids. The chip allows organoids' high-throughput dynamic culture individually and parallelly in a microwell array.

The matrix that supports 3D cell growth poses another challenge that currently hinders the developments of organoid culture, due to the high cost and batch-to-batch variations. Chapter 5 found that the naturally-derived polymer, alginate, can be used for the mouse mammary tumour organoids, especially for the luminal organoids.

In summary, this thesis has developed a series of microfluidic designs and techniques for spheroids/organoids culture towards their applications in drug screening, cell biology and nanomedicine. This thesis advances the potential of on-chip technology, materials and devices for biomedical engineering.

Chapter 1 Introduction

1.1 Multicellular spheroids and organoids

Three-dimensional (3D) cell culture has now been well-accepted and broad-used since Mina Bissell, and her team highlighted the significance of extracellular matrix (ECM) in adjusting the cell behavior while establishing the *in-vitro* cell models in 1980's[1]. Compared to the two-dimensional (2D) monolayer culture where cells adhere to the surface of a plate, 3D cell culture allows the 3D growth and interactions with surroundings, which mimics the specificity and homeostasis *in vivo*[2]. Accordingly, the 3D cell models remain high fidelity in proliferation, differentiation, drug resistance and metabolism, and stimulus response. Global market size of 3D cell culture is valued at USD 1.5 billion in 2020 and is projected to reach USD 3.2 billion, at a CAGR of 11.3%[3].

Multicellular spheroids and organoids are the main representative models in 3D cell culture. Multicellular spheroids refer to the well-rounded and compacted cell aggregation that usually consists of a single type of cells (epithelial, mesenchymal, endothelial, etc.)[4]. They could derive from the cell lines, single cells or crypts from the tissue sample via biopsy (**Figure 1-1**). Different types of cells could also be mixed to form the randomly distributed or cell type-based hierarchic spheroids. Spheroid formation can be divided into two stages: 1) formation of loose cell aggregates via integrin-ECM binding by constraining the cells in a confined space (e.g. round-bottom wells); 2) formation of compact spheroids via cadherin expression, accumulation and interaction [5]. Many reviews summarized the formation technics of spheroids[6-8].

The multicellular spheroids have similar growth kinetics to the *in-vivo* solid tumours. From a microscopic, when the solid tumour gets larger, the increased distance to the blood vessel decreases the metabolism of the tumour cells. According to the proliferation rate, a solid tumour has the proliferative zone, quiescent zone and hypoxic zone. Thus, there are also chemical gradients (PH, oxygen, glucose, ATP distribution, lactate accumulation, etc.). The cells in various zones respond to drug differently, which is the main reason for drug resistance[9, 10]. The hierarchic layout and chemical gradient could be formed in multicellular spheroids. This is caused by the proliferative cells on the rim and necrotic

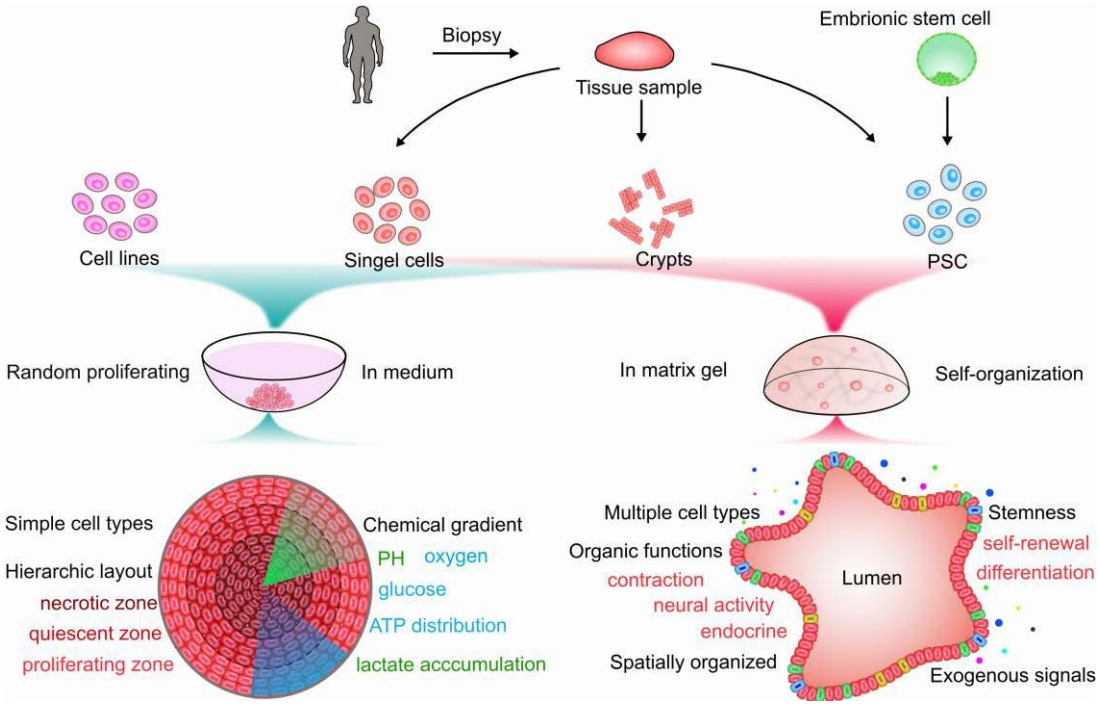

Figure 1–1 | Schematic establishment of spheroid and organoid, and their characteristics. Spheroids are developed (usually in medium) from simple cells, with random proliferation, solid and hierarchic layout, and chemical gradient. Organoids are usually derived from the stem cells (PSCs and aSCs) embedded in the matrix gel and supported by the exogenous signals. They contain multiple cell types with high polarization and certain organotypic functions.

cells in the core. Moreover, the spheroids can secret similar ECM molecules[11, 12]. These promise the multicellular spheroids of well mimicking the solid tumour.

The current definition of organoid is a 3D structure grown from stem cells and consisting of organ-specific cell types that self-organizes through cell sorting and spatially restricted linage commitment[13]. Before 2005, the word organoid was an extension of 3D culture[14]. The stem cells can originate from the adult stem cells (aSCs) derived from the dissociated tissue samples (single cells or crypts). Another type of the stem cells is the pluripotent stem cells (PSCs) and pluripotent embryonic stem cells (ESCs). The cells are usually embedded in the matrix gel to maintain self-organization. Some research mistakes the multicellular spheroids as organoids. The most intuitive difference is that the multicellular spheroids mimic the chaotic proliferation of solid tumour, while the organoids are highly-ordered and polarized 3D structures, and some have the typical lumens (gastrointestinal organoids, lung organoids, etc.). The organoids contain multiple cell types and have self-renewal and differentiation supported by exogenous signals[15].

They have organic functions, for instance, periodic contraction (cardiac organoids), neural activity (brain organoids), endocrine secretion (mammary gland organoids).

Until now, more than 15 kinds of organoids have been successfully established via the aSCs or PSCs, such as the brain organoid, retina organoid, stoma organoid, liver organoid, kidney organoid, intestine organoid, pancreas organoid, prostate organoid, endometrium organoid, etc. It should be noticed that the various relevant tumour organoids are also established. Compared to the tumour spheroids, the tumour organoids preserve the high heterogeneity from the original organ. The organoids are now widely used in organogenesis, pathogenesis, drug discovery, personalized medicine, disease models, etc.

1.2 Advances in spheroids and organoids on a chip

Reproducing and optimizing the microenvironment is the tenet to establishing the *in-vitro* multicellular spheroids and organoids. In the conventional culture, the formation of spheroids and organoids rely on the random self-assembly or self-organization in the

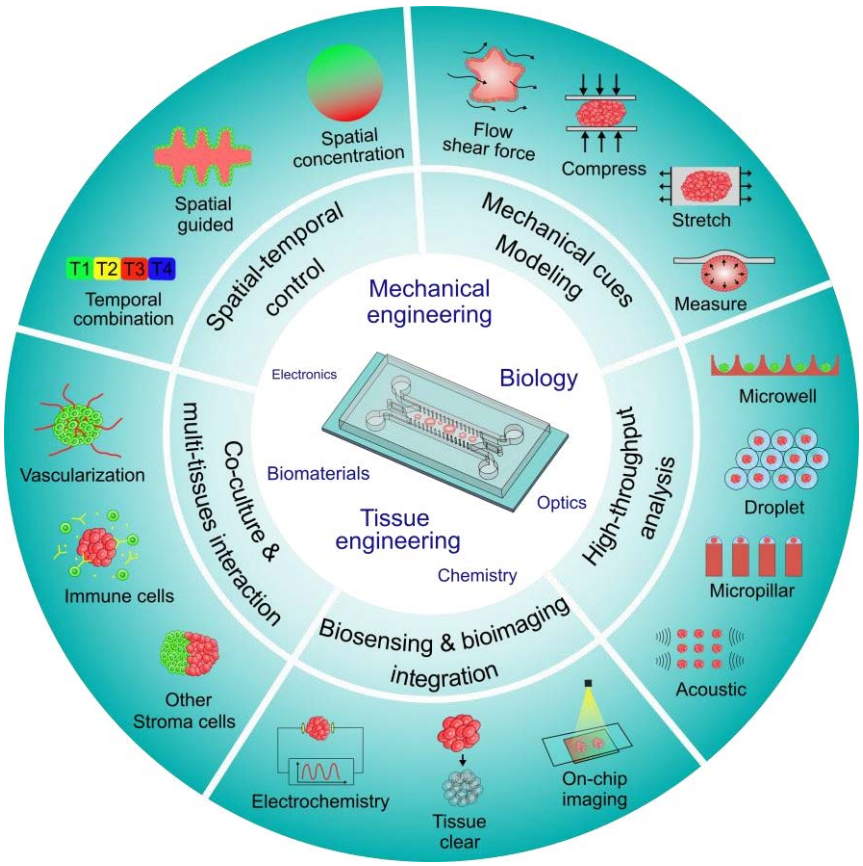

Figure 1–2 | Overall advances of spheroids and organoids on a chip. Microfluidic chip enables the spatial-temporal control, mechanical cues modelling, high-throughput analysis, multi-tissues or -organs interaction, and biosensing and bioimaging integration.

medium, lack of the stimulus such as chemical gradient and mechanics, which are common *in vivo*. Therefore, more engineering is required further to promote the culture of spheroids and organoids *in vitro*.

With the development of microfabrication, microfluidic technology becomes a valuable tool to address the problems in the conventional culture of the spheroids and organoids. The microfluidic device can manipulate the fluids on a small scale, similar to the size of spheroids and organoids. Small volume control enables microfluidics with low sample consumption, microdomain effects, facilitating observation and analysis. The integration of micropumps and microvalves could also accelerate automation and industrialization. In this review, we summarize the recent advances of spheroids and organoids on the chip. As shown in **Figure 1-2**, in general, the microfluidic technology could facilitate the establishment of spheroids and organoids in the following aspects: 1) spatial-temporal control; 2) mechanical cues modelling; 3) high-throughput analysis; 4) multi-tissues or organs interaction; and 5) integration of biosensing and bioimaging.

1.2.1 **Spatial and temporal control**

Organogenesis from stem cells to organoids requires the biochemical stimulus of exogenous signals, also called the morphogens, such as the bone morphogenetic protein 4 (BMP4), proto-oncogene protein (WNT3), Noggin. One target in developmental biology is to understand the exact functions of each morphogen. In conventional culture of organoids, the stem cells or pre-formed organoids expose to a uniform concentration gradient of these morphogens, leading to the radially symmetric spatial organization. This on the one hand deviates from some asymmetric development *in vivo*, on the other hand may obscure the functions of morphogens.

Spheroids- and organoids-on-a-chip technology could control the spatial distribution of the morphogens, magnifying the response and reveal their functions[16, 17]. As shown in **Figure 1-3a**, a microfluidic device for exposing the human PSCs to a localized morphogen source is fabricated. The cell chambers were separated from external perfusion channels by barriers formed from inner polyethylene glycol (PEG) hydrogel. A concentration gradient can be generated in the cell chamber, following the source-sink model of Fickian diffusion. The nonuniformed exposure leads to the asymmetric expression of pluripotency markers (MIXL1, SOX2, etc.) in human ESCs. This

engineered signalling helps to investigate the self-organization of stem cells. A similar device was also used to study the heterogeneous response of the colorectal tumour to a concentration of drug nanoparticles[18], the neural tube development in a WNT gradient by the gradient generator[19].

For the spheroid investigation, more work is focused on the spatial control of drug or nutrition concentration[20-22]. The most common setup is the combination of gradient concentration generator with microwell array or microdroplet array, as shown in **Figure**

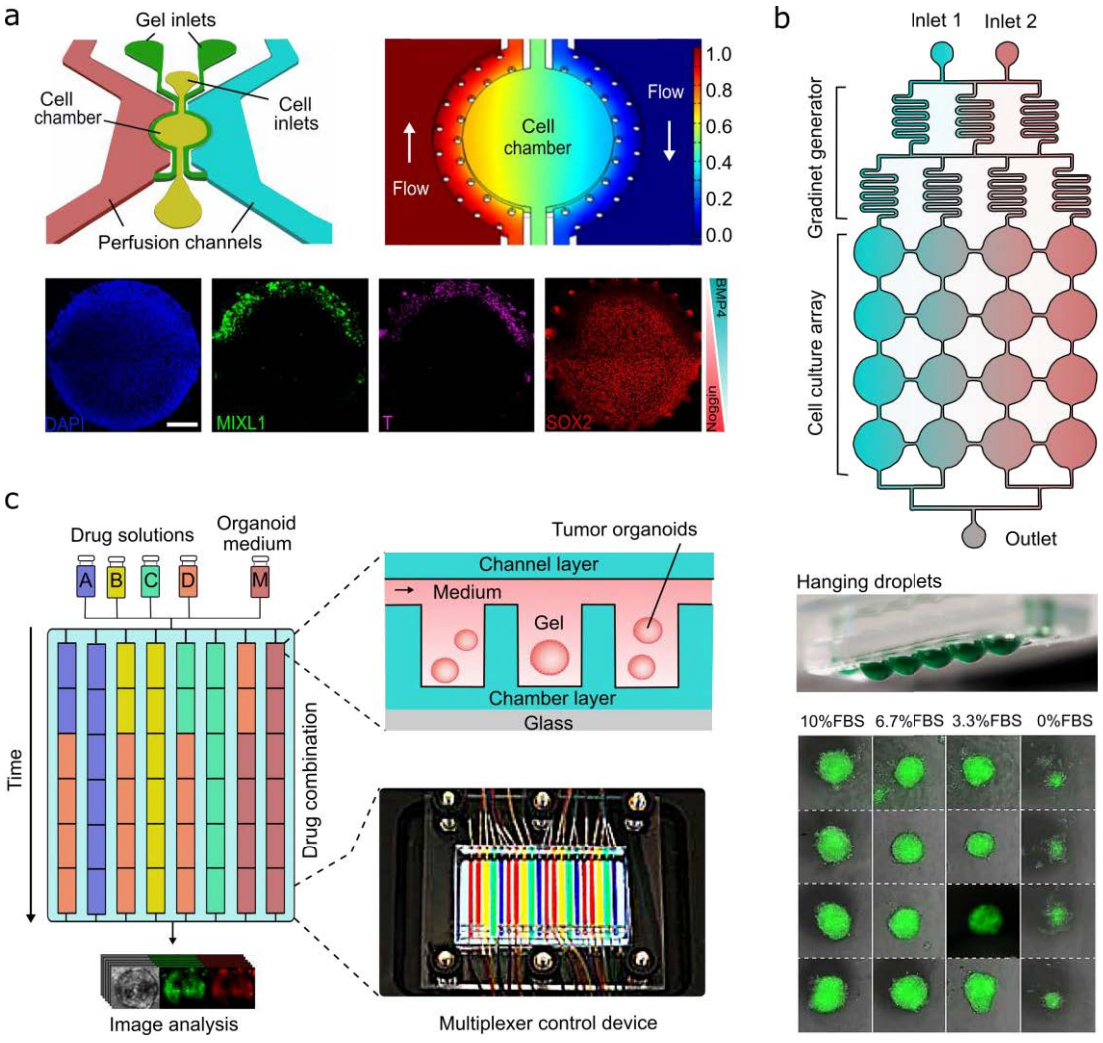

Figure 1–3 | Concentration control and temporal control of spheroids and organoids on a chip. (a) Differentiation of the stem cells exposed to the morphogens with a gradient concentration following the source-sink model. The human ESCs could form asymmetric pluripotent expression. Scale bar:200 μm. Copyright 2019, Nature Publishing Group. (b) Droplet array combined with the concentration gradient generator to investigate the growth under different dosage of nutrition or drug. Copyright 2014, Nature Publishing Group. (c) Temporally-modified drug treatment of organoids on a chip. Copyright 2020, Nature Publishing Group.

1-3b. By increasing the inlets and extend the spheroid culture array, multiplexed drug combination could be achieved on the chip[23].

Except for the spatial combination of the drug, spheroids- and organoids-on-a-chip technology enables the time-sequential drug combination[24], as shown in **Figure 1-3c**. The organoids are cultured in the microwell layer and supported by the above medium layer. The microvalves configurated on the chip automatically provides the temporally-modified drug treatments, which is more effective than constant-dose monotherapy or combination therapy.

Spheroids- and organoids-on-a-chip technology could reproduce and optimize the intrinsic morphology shown *in vivo*[25]. For instance, the epithelial organoids formed in the matrix gel usually leads to closed and cystic structures. Although bud sprouting occurs on the mature organoids, these developed organoids maintain a massive gap with the real organs in size, lifespan and morphology. As shown in **Figure 1-4a**, the on-chip technology formed the millimetre-scaled and tube-shaped intestinal organoids with the crypt- and villus-like domains, guided by the scaffold shape[26]. Matrigel channel ablated by laser assists the self-organization of the organoid cells, which could also be connected with the external pumping system for continuous perfusion. Similar spatial expansion of intestinal organoids can also be achieved by 3D bioprinting technology[27].

The produced topography on the chip can conversely create the source-sink biochemical gradient, which induces the homogeneous differentiation of the organoids[28]. For instance, in **Figure 1-4b**, the engineered crypt-villus-shaped collagen scaffold results in a vertical concentration gradient of the gamma-secretase inhibitor DAPT and WNT during the culture of intestinal epithelium cells. Notably, the gradient maintained a stem cell-progenitor cell zone and promoted cell migration along the crypt-villus axis, which replicates an *in-vivo* phenomenon[29, 30]. High-resolution 3D stereolithography was also used to replicate the topography of the crypt and villus using the Caco-2 cells in another study[31].

Similarly, spatial-induced differentiation was used to study the early development of cardiac organoids on the gel-based micropatterns[32, 33]. As shown in **Figure 1-4c**, the geometric- confined cells showed spatial patternings, such as the higher $OCT4^{+}$ and SM22 expressed at the perimeter and higher cardiac troponin T and sarcomeric α-actin

expressed at the central. This could serve as the embryotoxicity assay. The on-chip micropattern strategy was also designed for the investigation of tubulogenesis in epithelial organs[34], cell migration[35] and differentiation of mesenchymal stem cells[36].

Spatial control to guide the morphology was also applied for spheroids. Generally, the intrinsic-achieved spheroids are solid, hardly used to model some luminal tissues. As shown in **Figure 1-4d**, a gelatin sacrificial method was proposed to form the spherical topography for the hollow spheroids[37]. The gelatin microbeads with the cells mixed inside were embedded in another hydrogel. After melting the gelatin at 37ºC, the cells sedimented at the bottom of the hollow chamber and then grew along the spherical inner surface to form a hollow spheroid. Except for the architecture, the size of the spheroids

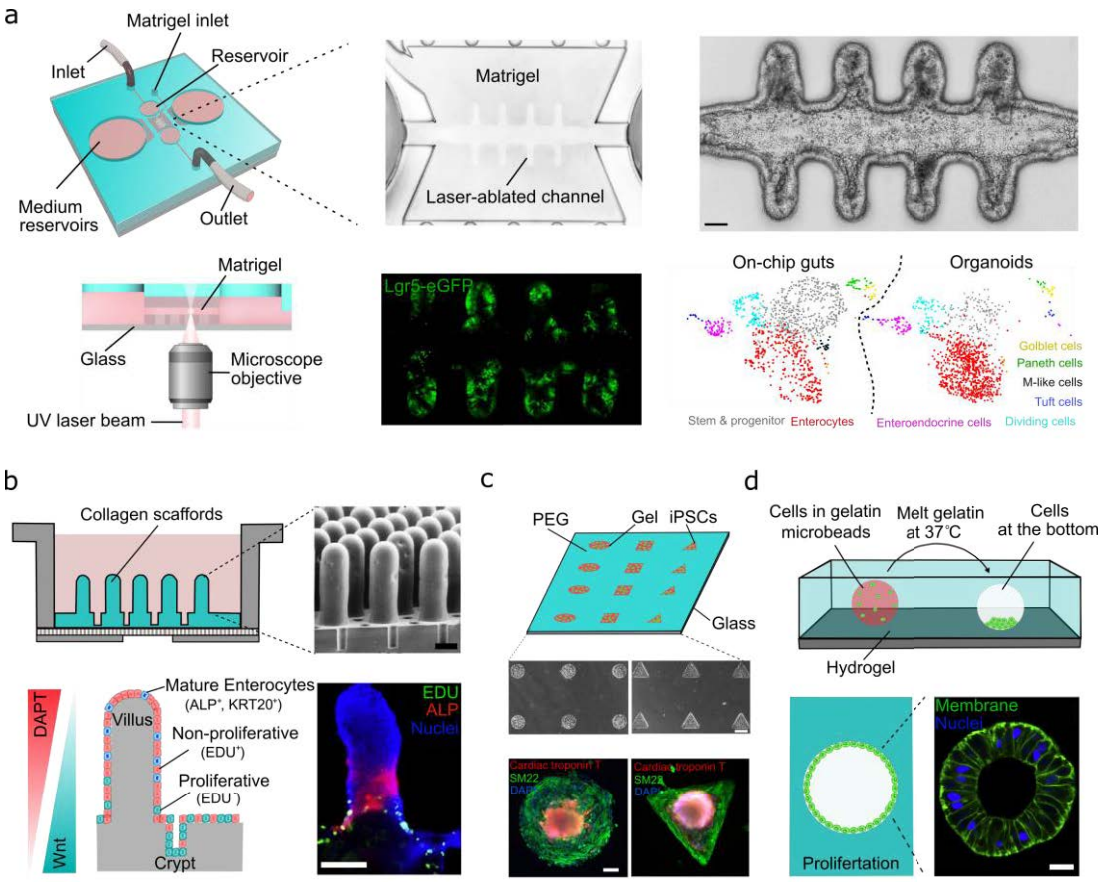

Figure 1–4 | Spatial control of the spheroids- and organoids-on-a-chip technology. (a) Scaffold-guided spatial control of the morphology of intestinal organoids. The Matrigel channel was ablated by laser on the chip. Scale bar:50 μm. (b) Polarized differentiation of the intestinal epithelium induced by the crypt-villus scaffold. Scale bar:100 μm. Copyright 2017, Elsevier. (c) Micropattern-based investigation for early cardiac organoids. The pattern is usually fabricated by the light-activated hydrogel via the photomask. Scale bar: 100 μm. Copyright 2018, 2015, Nature Publishing Group. (d) Hollow spheroid formation by the gelatin sacrificial method. Scale bar: 20 μm. Copyright 2017,

could also be controlled via the on-chip spatial control[38, 39]. Moreover, the shape of the spheroids could also be controlled, for instance, geometric-guided by hydrogel templates via digital micromirror device(DMD)-patterning[40]. Investigation of the spheroid architecture facilitates the research on tissue engineering and drug delivery.

1.2.2 **Mechanical cue modelling**

Cells and tissues *in vivo* live in a 3D microenvironment composed of various biochemicals and dynamic mechanics. It is impossible to ignore the function of the physical mechanics that regulate cell behaviour and fate, especially in the developmental process[12, 41-43]. These mechanics include the shear force of haemal or humoral perfusion, expansion stress of pulmonary alveoli, contraction stress of heart beating or myokinesis, etc. A number of diseases are proved to be related to the disorder of the mechanics, such as coronary calcification and pseudo-obstruction. Unfortunately, in the conventional culture of spheroids and organoids, the microenvironment lacks mechanical cues, which may deviate from the real tissues *in vivo*.

Spheroids- and organoids-on-a-chip technology could well incorporate the shear force of the fluidic perfusion into the development of these models due to the intrinsic advantages of microfluidic. Detailly, the on-chip technology can well control the parameters of flow speed, flow direction, renewal frequency and flow pattern (laminar, vortex or turbulence). Significant improvement of the shear force was seen during the culture of spheroids and organoids[44, 45]. For instance, as shown in **Figure 1-5a**, the vascularized kidney organoids under the flow stimulus showed more podocyte and tubular compartments with increased polarity, compared with those under static culture[46]. The shear force induced more endothelial progenitors and perusable lumens, which is the fundamental architecture for the filtering function of the kidney.

Another work showed that the flow-stimulated islets spheroids in the microwells expressed more hair-like microvilli, tighter cell-cell junctions and higher insulin secretion compared to those under static culture[47], as shown in **Figure 1-5b**. It should be noticed that when the flow rate exceeded a certain value (25 µl/h), the improvement was reduced. Compared to the optimal flow rate (4.27 ml/min=256.2 ml/h) in the culture of the vascularized kidney, the difference illustrates the optimal flow rate varies when culturing

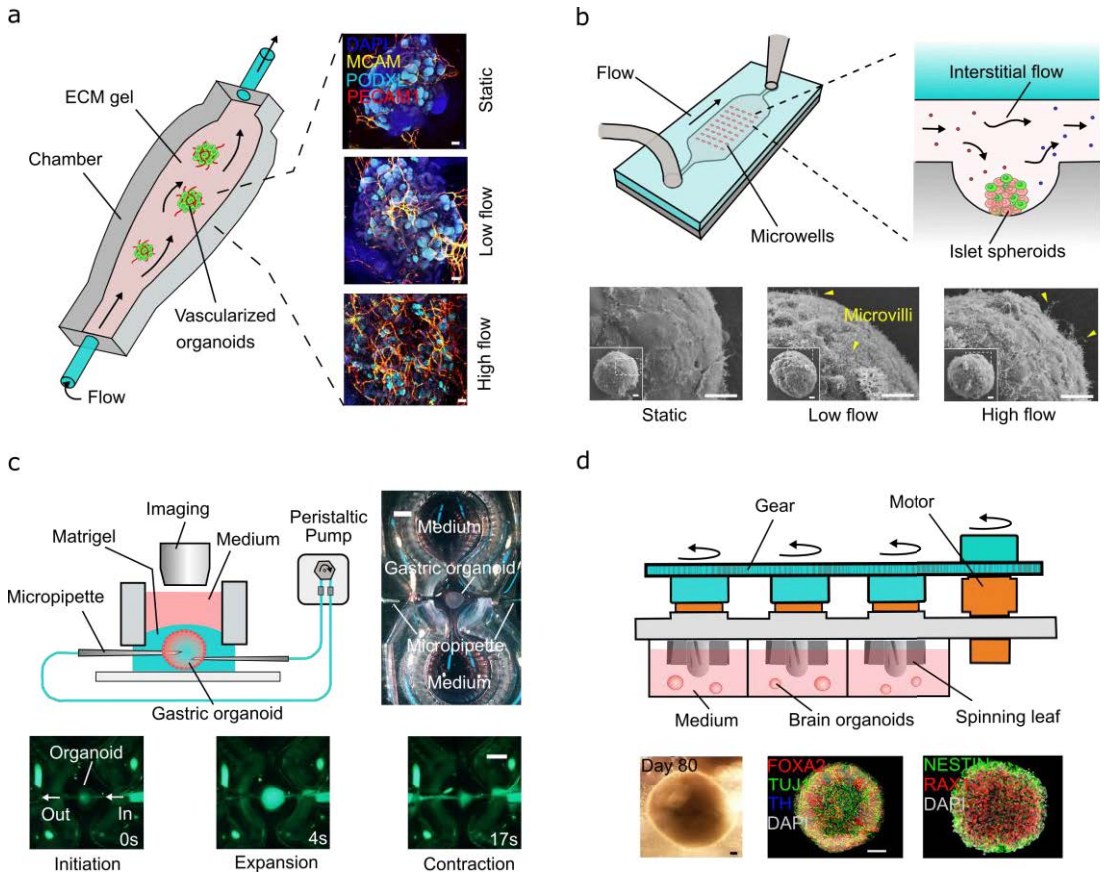

Figure 1–5 | Flow force control of the spheroids- and organoids-on-a-chip. (a) Flow-enhanced vascularization and maturation of the kidney organoids. Scale bar:100 μm. Copyright 2019, Nature Publishing Group. (b) Flow-enhanced culture of human islet spheroids on the microwell-array chip. Scale bar: 10 μm. Copyright 2019, Science Publishing Group. (c) Luminal flow in the gastric organoid controlled by the peristaltic pump. Scale bar: 2mm. Copyright 2018, Royal Society of Chemistry. (d) Brain organoids cultured on the mini-stirrer system driven by the 3D-printed gear and motor. Scale bar: 200 μm (left) and 100 μm (right). Copyright 2016, CellPress.

different types of spheroids and organoids. Significantly, in this work, a simple osmotic micropump replaced the traditional syringe pump to fulfil the mild flow.

Archenteric organs, such as the esophagus, stomach and intestine, suffer from the mechanical stimulus induced by the movement of the chyme. However, the conventional-established gastric or intestinal organoids form the closed lumens, which hinders the mimicking of intraluminal mechanics. As shown in **Figure 1-5c**, Kang et al. established the stomach-on-a-chip technology with a micropipette inserted inside, achieving the luminal flow. The flow system was controlled by a peristaltic pump, allowing for the organoid's stretch and contraction [48].

Research indicates that the brain organoids (e.g. forebrain or midbrain organoids) also show a positive response to flow stimulus due to the improved nutrition and oxygen

supply[49]. As shown in **Figure 1-5d**, a cascaded mini-stirrer driven by the gear-motor system was integrated with the culture of brain organoids. The brain organoids without external control usually lack specificity and contain diverse cell types in the forebrain, hindbrain and retina. This platform could not only increase the specificity of the achieved brain organoid but also avoid the waste of medium, recapitulate the key features of human brain development[50].

Cells and organs *in-vivo* suffer from the surrounded strain and stress which regulate their fate, attracting much engineering-related research[51-53]. Spheroids- and organoids-on-a-chip technology could well apply the strain and stress for the flexible substrate (Polydimethylsiloxane, PDMS) and open-operability. Typical research is the $Lgr5^{+}$ intestinal stem cell significantly affected by the compressive stress. As shown in **Figure 1-6a**, $Lgr5^{+}$ cells self-renew along the crypt-villi axis, resulting in the physical heterogeneity via cell expansion. Yiwei et al. established the intestinal organoids in the compressed Matrigel by adding weight. Under the squeezing conditions, organoids showed upregulated growth. It is also proved this phenomenon resulted from the enhancement of WNT/β-Catenin signalling via the PEG-induced osmotic compression[54]. A stretchable array for spheroids is developed utilizing the flexibility of PDMS/PAAm (prepolymer polyamide), as shown in **Figure 1-6b**. The cell alignment and spreading behaviours were significantly influenced by the dynamic mechanical stimuli[55]. It is also illustrated the spheroids in a confined condition would not impair cell rounding but negatively affect the mitotic progression by altering spindle polarity[56].

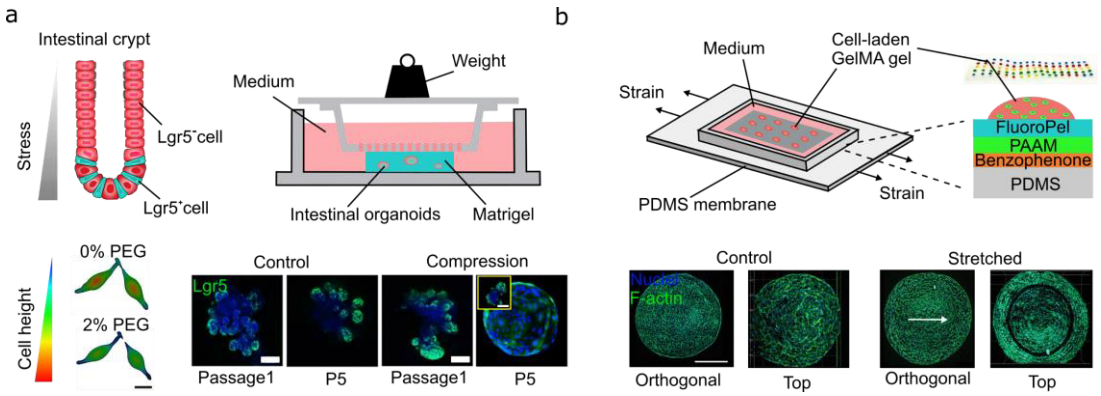

Figure 1–6 | Compression and stretch control of the spheroids- and organoids-on-a-chip technology. (a) Compression induced by weight or osmotic upregulated the growth of intestinal organoids. Scale bar: 80 μm. Copyright 2020, CellPress. (b) Multicellular spheroids cultured on the PDMS membrane applied periodical stretch. Scale bar: 200 μm. Copyright 2020, Wiley-VCH.

The mechanical cues developed by the spheroids and organoids can be, in turn, measured on the chip. Luminal pressure and tension of the epithelial organoids and tissues are essential with developmental defects, inflammatory conditions and cancer. As shown in **Figure 1-7a**, Ernest et al. developed an epithelial lumen-on-a-chip method to measure the luminal pressure and tension according to the deformation of the flexible PDMS substrate. The surface of the PDMS was covered with fibronectin, where epithelial cells could attach, except for the uncovered patterns. With the proliferation of the cells, the lumen will be formed on the patterns. Surprisingly, the luminal sheet was found to be active super-elastic materials with cellular areal strain up to 1,000%[57].

Mechanical features of the solid tumour spheroids play essential roles during tumour development and metastasis, especially the expanding force towards the surroundings. Kevin et al. utilized a microfluidic chip to encapsulate the tumour cells inside the alginate capsules, as shown in **Figure 1-7b**. The cells in the permeable capsules formed spheroids and generated pressure on the alginate shell. The alginate could be treated as elastic materials. By analysing the decreased thickness of the shell, the compressive force in the

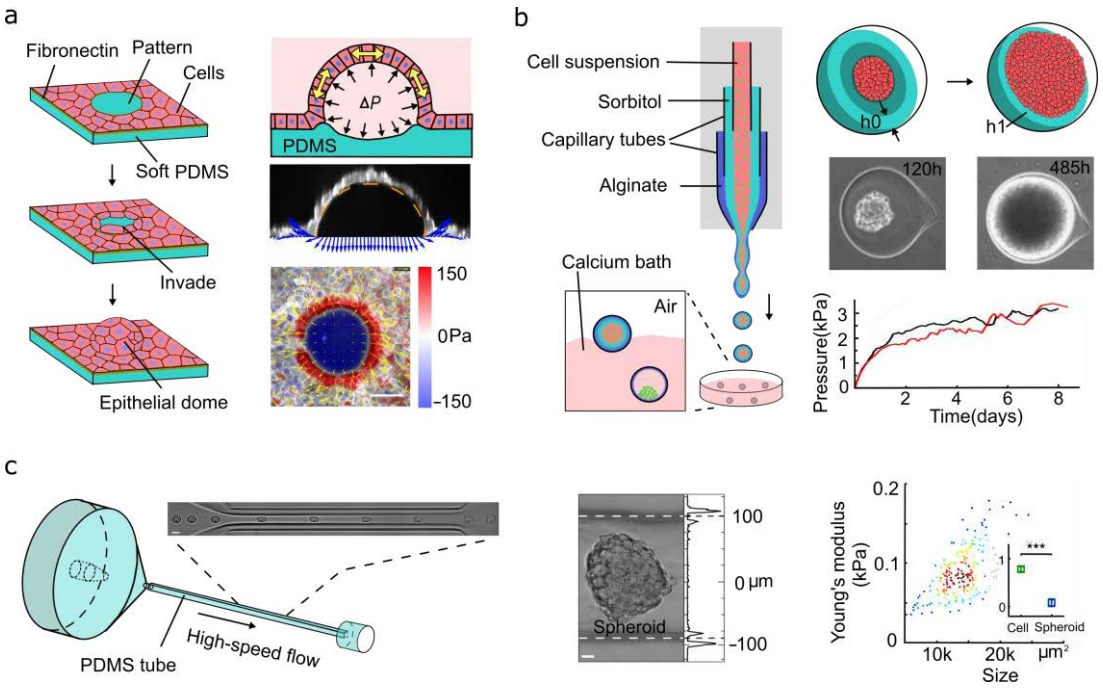

Figure 1–7 | Mechanical sensing of the spheroids- and organoids-on-a-chip technology. (a) Measurement of luminal pressure and tension via epithelial lumen on the PDMS chip. Scale bar: 50 μm. Copyright 2018, Nature Publishing Group. (b) Alginate capsules as a tool to investigate the compressive force generated by the spheroids. The pressure could be up to more than 3 kPa. Copyright 2013, PNAS. (c) Spheroids-on-chip cytometer for the Young's modules investigation under hydrodynamic stress. Scale bar: 20 μm. Copyright 2020, Nature Publishing Group.

spheroids could be measured. They found that the pressure could be up to 3 kPa[58]. The hydrodynamic force has been widely used to investigate the mechanics of single cells[59, 60]. As illustrated in **Figure 1-5c**, the spheroids were introduced into a flow cytometry to study their Young's modules under the hydrodynamic stress. This allows the high-throughput analysis, which showed the averaged Young's modules of the HEK293T spheroids was a factor of ten smaller than single cells[61].

1.2.3 **High-throughput analysis**

Reliable conclusions require a mass of experimental samples and data. High-throughput generation and analysing capability of spheroids and organoids help to reduce the contingency and variability. This is important for biological and medical experiments where many parameters and processing steps are involved. The spheroids- and organoids-on-a-chip technology has considerable advantages in this aspect.

Most-widely used tools are microwells, especially for the spheroid culture. The microwell array is usually generated by the hydrogels (agarose, gelatin, methacryloyl, etc.) with the pillar stamps, the polyester plastics with micro-drilling, or the 3D printing, which could increase the yield and control the size[38, 47, 62-65]. As for the organoids, most types of organoids (e.g. intestinal organoids, gastric organoids) require the matrix gel, which hinders their culture in microwells due to the complex manipulation of matrix gels. One method is the lateral microwells combined with the medium channels[66]. The matrix gel in the channel was removed finally. Another method is the bottom microwell combined with the above perfusion layer[24]. It should be mentioned that, as shown in **Figure 1-8 a**, a PEG hydrogel microwell array was designed for the large-scale suspension development of gastrointestinal organoids[67]. The researchers replaced the solid Matrigel with the ENR-CV expansion medium containing 2% v/w soluble Matrigel during the beginning 60 hrs and the differentiation medium during the later culture. The absence of the solid matrix simplifies the microwell-array culture of organoids and reduces the organoid heterogeneity. Additionally, the development of islets organoids derived from the iPSCs does not need the matrix and has successfully been combined with microwell culture[68].

Droplet technique, one of the most representative in microfluidic technology, can generate droplets or microbeads in a high-throughput way[69], suitable for the scalable

establishment of spheroids and organoids. Spheroids have been successfully formed in the mono-dispersed alginate or agarose beads[70, 71], which, however, could only form many tight organizations[71-73]. Therefore, the droplet culturing method[74, 75] and the core-shell method[76, 77], such as (liquid core, collagen core etc.) were widely investigated. As for organoids, the challenge is the manipulation of the matrix, which need mild and tens of minutes for gelation. As shown in **Figure 1-8b**, pure Matrigel droplets were generated by the flow-focusing chip under 4 ºC, which was followed by moving the droplets to 37 °C for gelation. The Matrigel microbeads can be stored in medium for few weeks, which fulfils the development of acinar organoids[78, 79]. To speed the gelation and enhance strength, microbeads with alginate shell and Matrigel core were generated using the electrostatic co-spraying technique. Due to the enhanced mass transfer in droplets, gastrointestinal organoids had higher expression of CD44, Lgr5 and Ki67, compared with the bulk culture[80]. Some organoids that do not need the support of matrix (islet organoids, etc.) were scaled up in the microbeads with liquid core and alginate shell[81]. Moreover, hydrogel fibre can be generated on the chip easily, allowing for another kind of high-throughput analysis of spheroids and organoids[82-85].

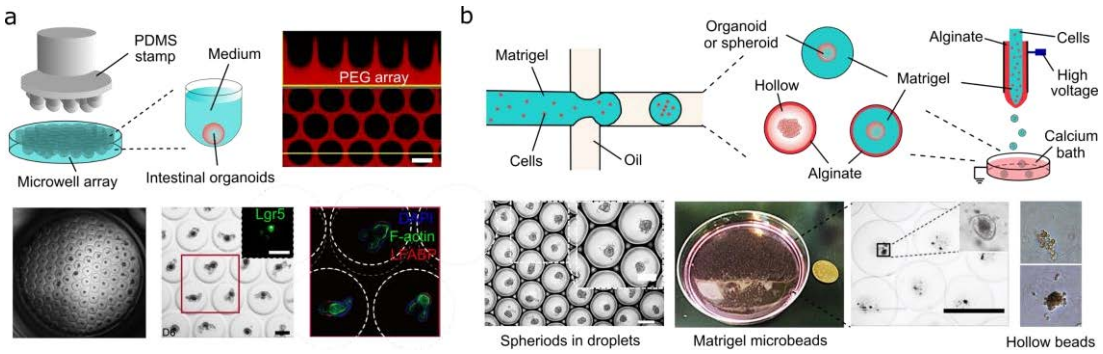

Figure 1–8 | Microwell and droplet strategy for high-throughput culture. (a) Microwell-based development of gastrointestinal organoids with suspension culture. Scale bar: 200 μm. Copyright 2020, Nature Publishing Group. (b) Droplet technique for the massive culture of spheroids and organoids. Pure hydrogel microbeads, hollow microbeads and microbeads with Matrigel core and alginate shell were generated for different kinds of spheroids and organoids. Scale bar: 500 and 200 μm (left), 2 mm (right). Copyright 2018, Elsevier; 2017 and 2020, Wiley-VCH.

Micropillars on the chip can further be used for the high-throughput development of spheroids and organoids. One function of these micropillars is the spatial separation and constrain of the cells in a small group[86]. As shown in **Figure 1-9a**, iPSCs seeded among the micropillars were aggregated together and then differentiated into the liver organoids under perfusion of differentiation medium[87]. Combined with microwell array, the

micropillar array can achieve a high-throughput screen of dosage, duration dynamics and combinations of cellular factors. As shown in **Figure 1-9b**, gel-encapsulated cells were seeded on each of the micropillars, which were then inserted into microwells for independent culture. Microengineering vastly enhanced the capacity of culture throughput compared to 96-well or 386-well plates[88]. As shown in **Figure 1-9c**, micropillars in the microfluidic chamber were used to capture the cells. The captured cells can grow into spheroids *in situ*[89]. Parameters such as the size, shape, density of micropillars were essential for this design.

Surface acoustic wave (SSAW) technique has been widely used in microfluidics[90-92]. The SSAW technique could help for the high-throughput generation of spheroids. As shown in **Figure 1-9d**, interdigital transducers (IDTs) are usually integrated with the microfluidic chambers on a single chip, generating an acrostic field in the cell-suspended

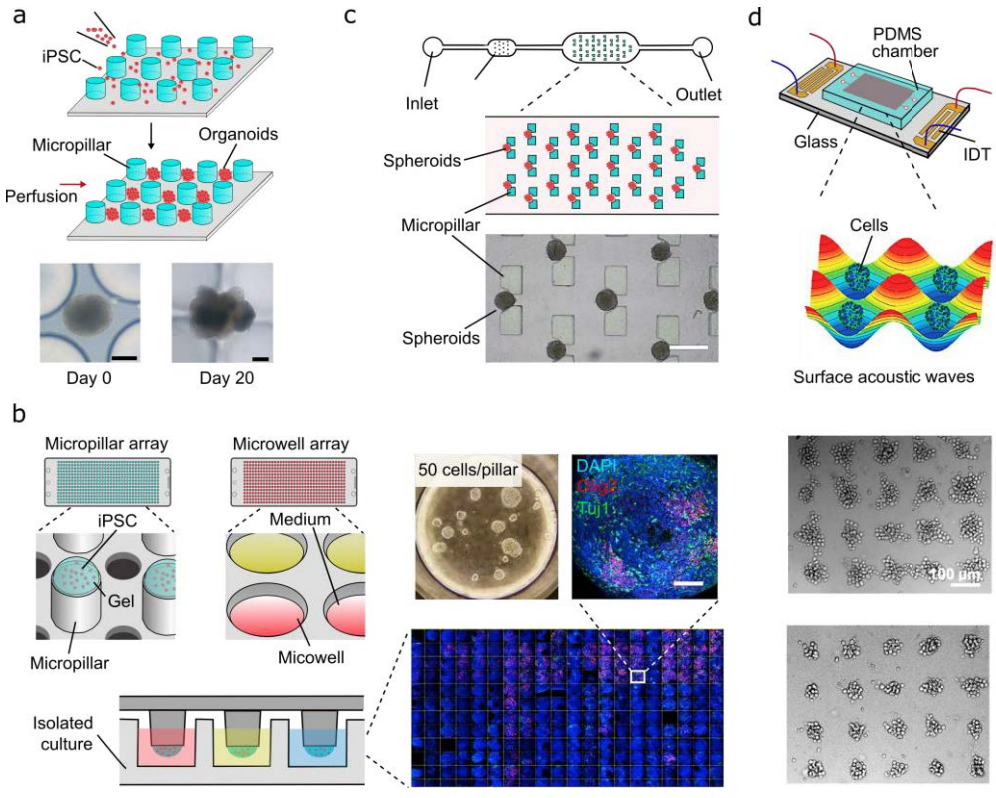

Figure 1–9 | Micropillar and acrostic strategy for high-throughput culture. (a) Liver organoids developed among the micropillars. Scale bar: 50 μm. Copyright 2018, Royal Society of Chemistry. (b) High-throughput micropillar-microwell array for independent culture of PSCs. Scale bar: 1 mm. Copyright 2020, Science Publishing Group. (c) Cells captured by micropillars grow into spheroids *in situ*. Copyright 2014, AIP Publishing Group. (d) High-throughput generation of spheroids via surface acrostic wave techniques. Scale bar: 100 μm. Copyright 2016 and 2019, Royal Society of Chemistry.

chamber. The cells would move to the pressure node and form the small clusters, which then grow into spheroids[93, 94].

1.2.4 **Co-culture and multi-tissue interactions**

Microenvironment of cells *in vivo* includes interactions with other kinds of neighboring cells (stromal cells, immune cells etc.) and other tissues/organs. The complexity works together to maintain the balance and functions. Spheroids- and organoids-on-a-chip technology facilitates the investigation of co-culture and multi-tissue interactions due to the easy control, integration and analysis on the chip.

One issue of *in vitro* spheroids and organoids is the limitation of nutrition supply with the size increasing due to lack of vascular network[95]. Therefore, the establishment of a vascular network in these models has great significance. Although the microfluidic channel can play the role of blood vessels in a certain, this is not the immediate solution. Epithelial blood vessels have been successfully produced on the chip in vasculogenesis or angiogenesis[96, 97]. The strategy for spheroid vascularization is to co-culture the spheroids with the established blood vessel network. As shown in **Figure 1-10a**, human umbilical vein endothelial cells (HUVECs) were seed in the lateral channels. The middle channel was filled with hydrogel (usually the fibrinogen), which is suitable for blood vessel formation. Tumour spheroids were loaded inside the middle channel. After several days' co-culture, the vascular network could merge with the spheroids, as shown in the side view. Fluorescent experiments showed the vascular network could facilitate transportation, allowing for higher proliferation activities and lower cell death. It should be noticed that the fibroblasts introduced into the co-culture system could accelerate vascularization[98-101].

There are two strategies for the vascularization of organoids (HUVECs mixture and networks coalescence). Here we detailly discuss the coalescence strategy similar to the above vascularization of spheroids. Taking colon organoids as an example, the challenge is the optimized ECM and culturing medium for both blood vessels and colon organoids, as shown in **Figure 1-10b**. In the conventional culture, the ECM for blood vessels and colon organoids are fibrinogen and Matrigel, respectively. The medium for the former and the latter is the endothelial growth medium (ECGM2) and colon organoids medium, respectively. Shravanthi et al. investigated various conditions and finally confirmed the

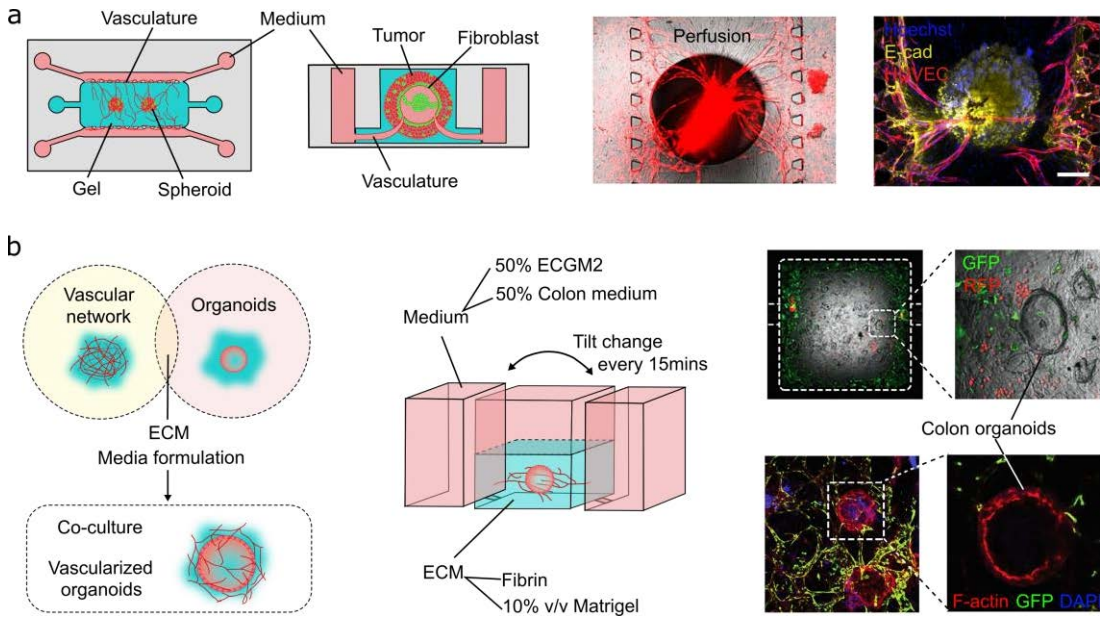

Figure 1–10 | Vascularization by co-culturing spheroids and organoids with HUVECs. (a) Vascularization of tumour spheroids on the chip with the vascular network. Scale bar: 50 μm. Copyright 2020, Elsevier. (B) Vascularization of colon organoids with the vascular network. Copyright 2020, Wiley-VCH.

optimal parameters are 50% ECGM2 and 50% colon medium for final medium, 90% fibrin and 10% v/v Matrigel for the ECM. The plate changed the tilt every 15 mins. Under these conditions, colon organoids could well coalesce with the vascular network[102]. Another strategy is the co-culture of mixed organoid cells and HUVECs, such as the development of vascularized kidney organoids[46] and liver organoids[103]. In this strategy, the flow mechanical cues established on the chip are essential to the development of vascular tubes. Vascularization of organoids is the precondition of the application in transplant *in vivo*[104, 105] and drug delivery[106, 107]. The on-chip technology offers a suitable tool for the research.

Tumour-immune interactions in the microenvironment govern the tumour progression and drug response. Spheroids- and organoids-on-a-chip technology becomes an excellent tool to investigate these interactions due to the convenient observation, cell manipulation and sample analysis[108, 109]. Immune checkpoint blockade has been demonstrated as an effective clinical therapy for tumour. However, inevitably, monoclonal antibodies (e.g., PD-1 and CTLA4) targeting therapy gives rise to significant toxicity for some patients. Precision immune-tumour *in vitro* trials are essentially needed, which requires the immune-tumour interactions. As shown in **Figure 1-11a**, tumour spheroids derived from murine and patients were seed on the chip, which contained the autologous lymphoid and

myeloid cells. After 6-day culture, the spheroids can flourish while maintaining the immune cells. Cytokine can also be profiled by sampling on the chip. Control experiments of αPD-1 and IgG illustrated the sensitivity of tumour response to the immune checkpoint blockade therapy [110, 111]. A similar microfluidic model was established for the hepatitis B virus -related hepatocellular carcinoma[112].

In immunotherapy, immune cells need to extravasate through the blood vessel and target the tumour via migrating through the cell's density. This dynamic progress is hard to be investigated by conventional *in vitro* models. As shown in **Figure 1-11b**, a microfluidic

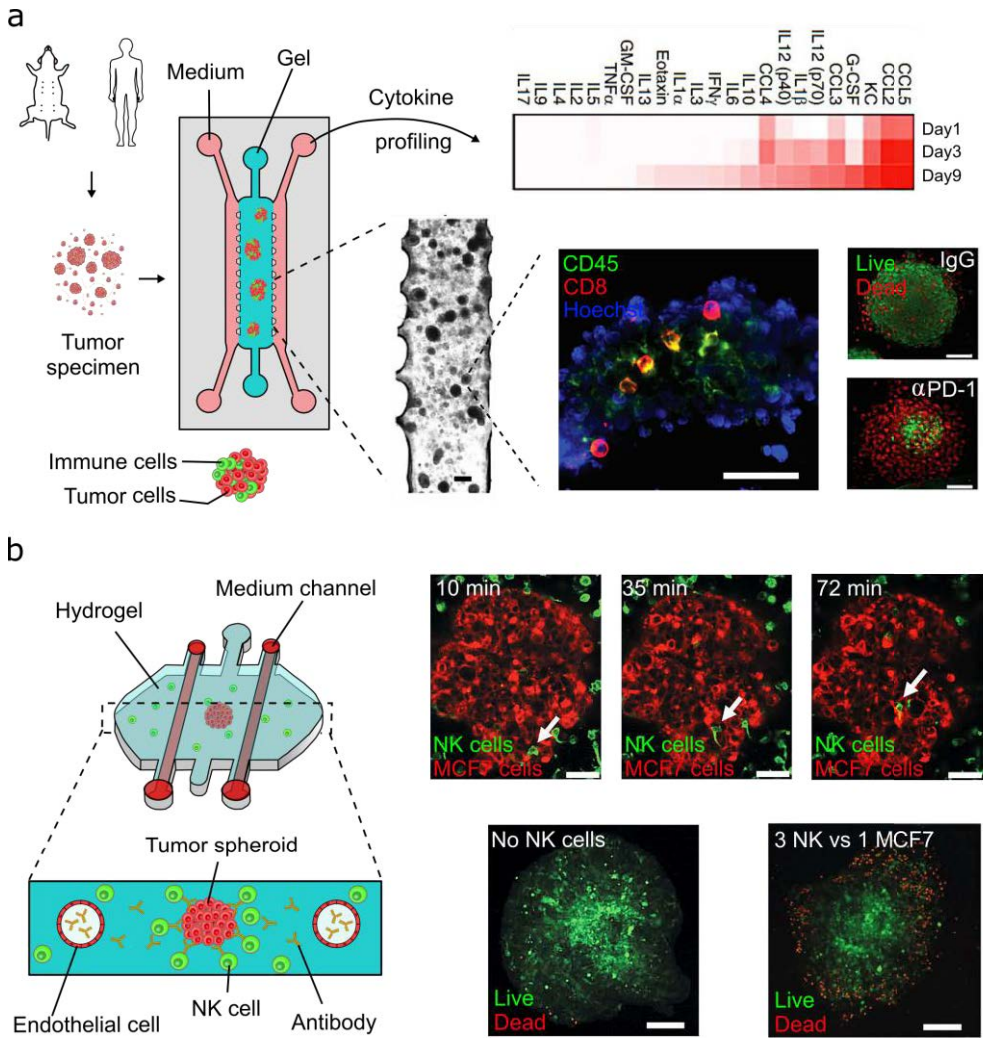

Figure 1–11 | Co-culture spheroids and organoids with immune cells. (a) Immune checkpoint blockade therapy demonstrated on the tumour spheroid chip, which can achieve the tumour microenvironment maintaining, histological analysis, cytokine profiling, live/dead imaging and drug screening. Scale bar: 0.5 mm (left), 50 μm (middle and right). Copyright 2018, AACR publications. (b) Dynamic targeting tumour spheroids by NK cells migrating through blood vessels and dense cells on the chip. Scale bar: 50 μm (top) and 200 μm (bottom). Copyright 2018, Taylor & Francis Group.

chip was designed to study the natural killer (NK) cells targeting the breast tumour spheroids. Artificial blood vessels were established, and NK cells' activity could be monitored on the chip in real-time. Results indicate that NK cells can sense the presence of tumour spheroid several hundred micrometers away and kill tumour cells from both periphery and innermost layers[113].

Co-culture of spheroids/organoids with other stromal cells are widely investigated on the chip, such as the fibroblast, cancer-associated fibroblast (CAF), stellate cells and adipocytes[83, 106, 114-120]. Strategies such as the on-chip spatial arranging and multicompartment microbeads and fibers are chosen for the investigation. Recently, some versatile and innovative methods are developed. As shown in **Figure 1-12a**, a strategy for spheroid sequential merging was proposed by using the droplet-capillary anchors. The step-like anchors allowed the capture of droplets sequentially where spheroids were developed. By triggering the droplet merger, different kinds of spheroids could grow together in a single droplet. This cascaded culturing method allows the dynamic control of cell-cell interactions and the heterogeneity of 3D culture[121]. As shown in **Figure 1-12b**, a stamp-based microfluidic chip was used to investigate the interactions of breast tumour spheroids (in well) and adipocytes (on the surface). It indicates the differentiation to adipocytes was decreased significantly by the tumour cells[122].

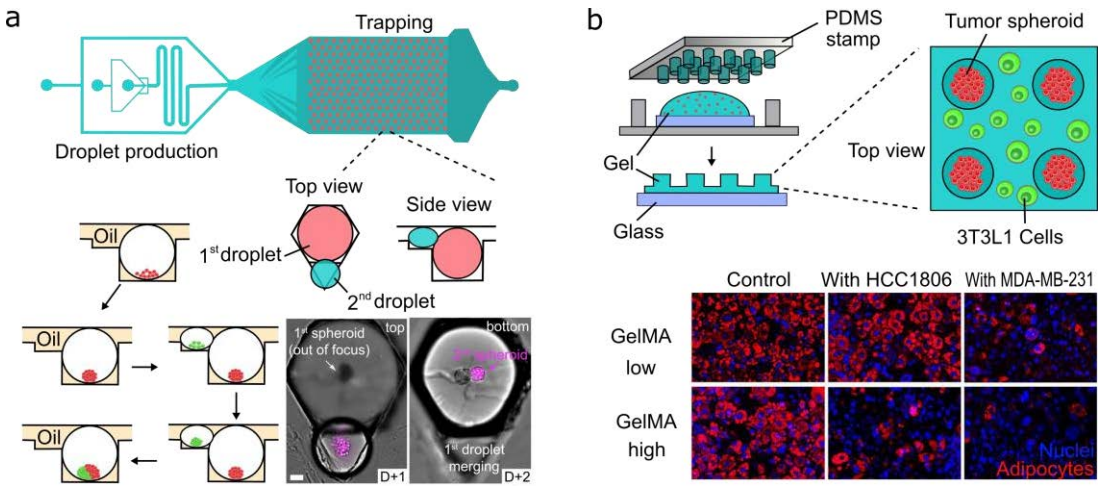

Figure 1–12 | Co-culture spheroids and organoids with stromal cells. (a) Spheroid sequential merging on the anchors chip for various type co-culture. Scale bar: 50 μm. Copyright 2020, CellPress. (b) Stamp-based microfluidic chip for co-culture of tumour spheroids and adipocytes. Copyright 2018, Elsevier.

1.2.5 **Integration of biosensing and bioimaging**

To date, most of the applications of spheroids and organoids are still stuck in the laboratory, limited by the generalized and standardized analysing method and evaluation criterion. Manual manipulation and judgement involve huge errors. Spheroids- and organoids-on-a-chip technology enables the integration of biosensing and bioimaging, which allows the automatic analysis and decreased error.

Electrochemical sensor is widely used for the monitor of biochemical parameters, such as PH[123-125], oxygen[126-128], glucose[129-131]. As shown in **Figure 1-13a**, a typical setup is designed to continuously monitor the lactate and glucose level of the on-chip spheroids by using the electrochemical sensor. The electrode chip could be plugged in the hanging-drop chip, which contains four platinum working electrode (WE), a platinum counter electrode (CE) and an Ag/AgCl reference electrode (RE). To monitor the lactate and glucose, the electrode was functionalized with the oxidase enzymes[132]. Except for these general parameters, specific biomarkers need to be monitored. The standard methods, such as immunosorbent assays (ELISA) and surface plasma resonance

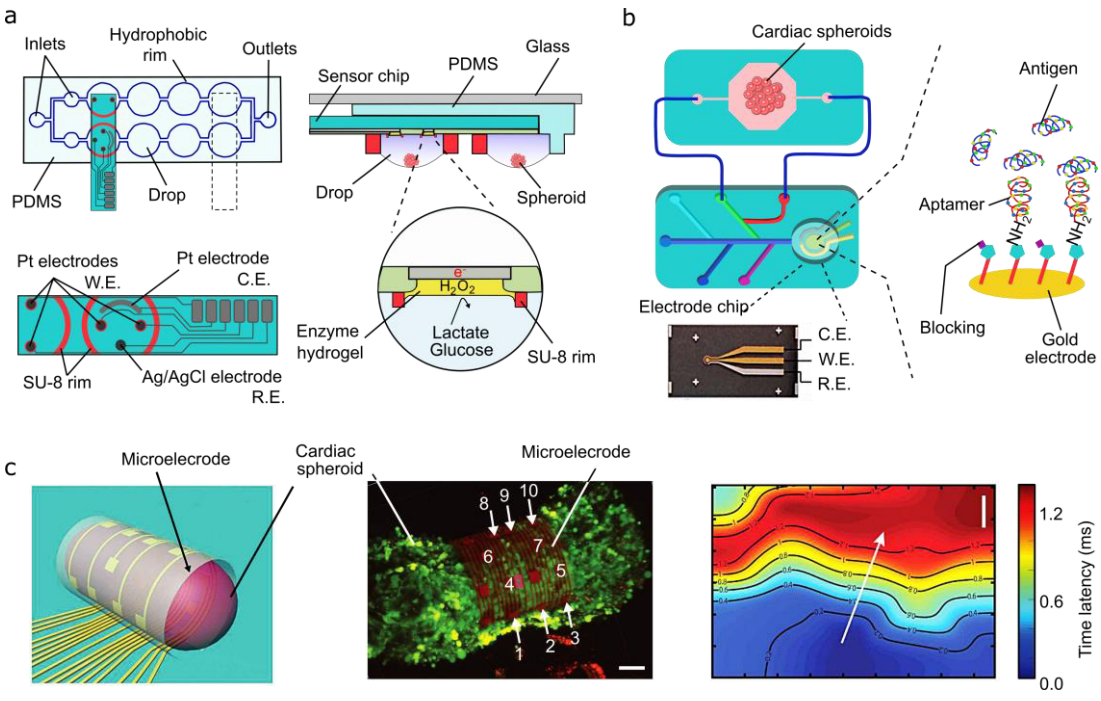

Figure 1–13 | Integration with biosensing device. (a) Continuous monitor of lactate and glucose by electrochemical sensor integrated with the spheroids on-a chip. Copyright 2016, Nature Publishing Group. (b) Aptamer-functionalized electrode for detecting creatine kinase-MB with the cardiac organoids on a chip. Copyright 2016, ACS publications. (c) Self-rolled biosensor array for recording of potential field of cardiac spheroids. Scale bar: 50 μm. Copyright 2019, Science Publishing Group.

(SPR), sometimes suffer the limited sensitivity and nonspecific binding[133, 134]. To increase the sensitivity and selectivity, the aptamer-functionalized electrode was designed to capture the creatine kinase-MB (biomarkers secreted by the damaged cardiac organoids), as shown in **Figure 1-13b** [135].

Cardiac spheroids and organoids are the heart 3D models that usually require the measurement of dynamic electrical signals, beat rating and contraction force. Various methods are developed, such as the flexible electrode[136], nanoelectronics mesh[137] and electronical nanopillars[138]. As shown in **Figure 1-13c**, a self-rolled biosensor array was used to multiplexed record the field potentials on the surface of cardiac spheroids, even the calcium imaging. This strategy allows both high sensitivity and spatiotemporal resolution[139]. Except for the measurement of the electrical signal, the electric field influence on the spheroids was also investigated on the chip[140].

Another advance of the spheroids- and organoids-on-a-chip technology is the easy integration of bioimaging. Good-quality imaging requires high resolution, large field of view (FoV), strong penetration and high speed. Spheroids and organoids on the chip usually limit the light penetration and significantly light scattering due to their high cell density and large size. As shown in **Figure 1-14a**, an on-chip clearing technique for 3D tissues was described. Different processing agents can be sequentially introduced into the channels. The scattering lipid molecules that hinder the imaging can be removed fast by 567-folds, allowing 20X more quickly than the current passive clearing approaches[141].

FoV of conventional imaging, such as the commonly-used confocal microscopy, is limited by the numerical aperture (NA) of the objective lens, which impedes the advances of spheroids- and organoids-on-a-chip technology. Lens-free imaging promises large FoV and high resolutions[142-145], especially combined with microfluidic chips[146]. **Figure 1-14b** shows that a lens-free imaging system was integrated with the spheroids on a chip. The setup generally contains multi-angle or multi-color light sources and the imaging sensors (CMOS or CCD) with the above sample chip. Light propagates through the samples and arrives on the image sensors with the changed phase information. Results illustrated the achieved image could be as good as that via confocal microscopy. The FoV could reach 3.4 mm x 2.3 mm x 0.3 mm[147]. Another potential imaging method for the spheroids- and organoids-on-a-chip technology is the chip-based nanoscopy, which ensures the FoV and higher resolution. This mainly relies on the high-integrated and high-

refractive-index waveguide chip, combined with the structured illumination microscopy (SIM)[147] or stochastic optical reconstruction microscopy (STORM)[148]. As shown in **Figure 1-14c**, the high-refractive-index waveguide chip could provide strong evanescent light for fluorescent molecules switching. The STORM on-chip microscopy ensures an FoV of 0.5 mm x 0.5 mm and a resolution of around 340 nm. It is also believed the lattice light-sheet microscopy could have good applications for the on-chip high-throughput analysis of spheroids and organoids[149]. Imaging for the deep penetration of spheroids and organoids was also investigated[150-153].

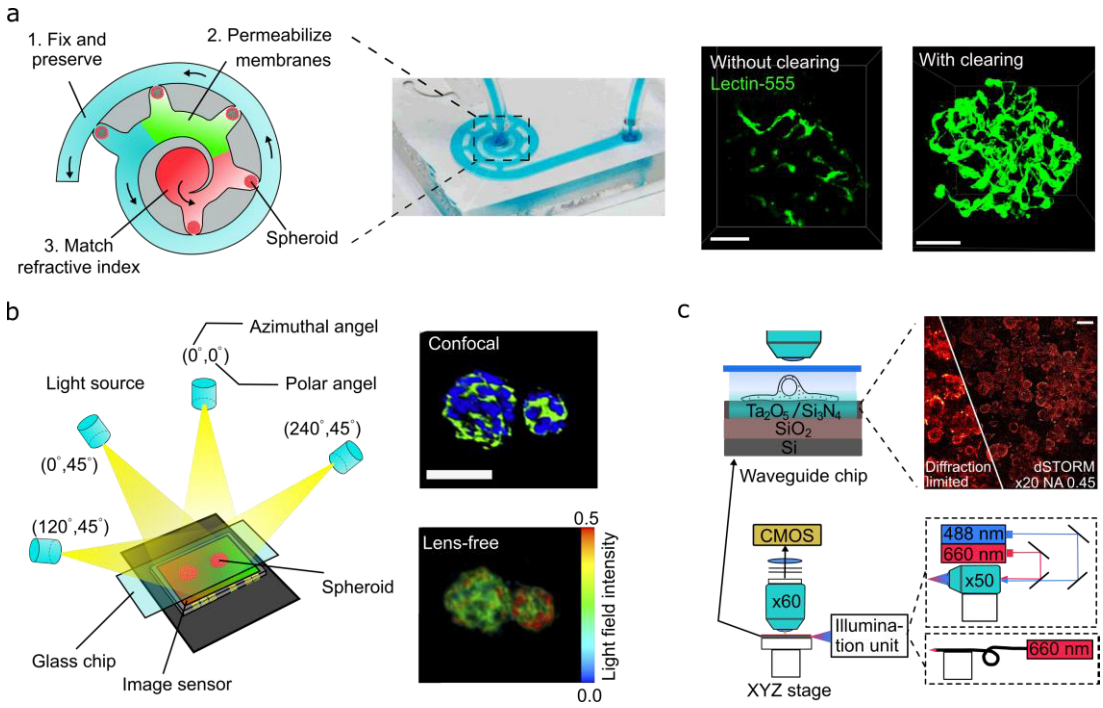

Figure 1–14 | Integration with imaging device. (a) On-chip clearing of spheroids which is 20X faster than conventional clearing approach. Scale bar: 50 µm. Copyright 2016, PNAS. (b) Lens-free imaging for the spheroids on a chip. Scale bar: 50 µm. Copyright 2020, OSA publishing. (c) On-chip STORM-based wide FoV nanoscopy. Scale bar: 50 µm. Copyright 2017, Nature Publishing Group.

1.3 Aims and outline

During my PhD research, I aim to combine microfluidics, microfabrication, and 3D cell culture to (1) create new tools and devices to investigate spheroids and organoids; (2). replicate and optimize the microenvironment of spheroids and organoids *in vitro*; (3). increase the yield of spheroids and organoids for downstream high-throughput analysis.

Chapter 2 developed a strategy to generate gradient-sized multicellular spheroids on a single chip in a high-throughput way. Although many methods have been developed to generate the spheroids, it is still challenging to manage multi-sized spheroids. This facile

method helps to study the size-mediated behaviour of spheroids, such as drug penetration and response.

In chapter 3, we studied the cellular communication between tumour spheroids and stromal cells. Conventional methods to investigate cellular communication cannot avoid the crosstalk effect or offer continuous effect due to the random diffusion. Here we proposed a unidirectional communication by controlling flow directions on the chip. We studied the communication of tumour spheroids and stromal cells (fibroblasts and mesenchyme stem cells (MSCs)) to investigate the CAFs which plays important roles in tumour microenvironment.

In chapter 4, we proposed a novel method to apply mechanical stimulus on human colon tumour organoids in a high-throughput way. Many methods have been proposed to apply mechanics on spheroids. However, it is challenging to apply mechanical stimulus on organoids due to their growth in Matrigel. Using human colon tumour organoids as a model, we achieved the peristalsis to replicate the *in-vivo* environment.

In chapter 5, we found mammary tumour organoids can be successfully established in alginate. Using the fast crosslinking of this material, we achieved the high-throughput generation of mammary tumour organoids in alginate microbeads by droplet chip. This will significantly reduce the cost of mammary tumour organoids and increase the reliability of the downstream high-throughput analysis.

Chapter 2 Gradient-sized multicellular spheroids on a single chip

Multicellular tumour spheroids are attracting more attention as a physiologically relevant *in vitro* tumour model for biomedical research. The size of spheroids is one of the critical parameters related to drug penetration and cellular responses. It remains challenging to generate a large number of gradient-sized spheroids in one culture vessel. Here, a liquid-dome method was used to simultaneously produce more than 200 gradient-sized spheroids on an agarose chip. Surface tension effect was used to modulate the liquid spatial distribution and achieve a range of spheroid sizes. MCF-7 cells formed multiple spheroids on the chips for concept validation. It showed that different configurations of the liquid domes exhibited different levels of size control. Relative to the smallest spheroids in the configuration, hemispheric and square domes produced spheroids up to 3.4 and 12.8-folds larger in area, respectively. In addition, the co-culture of MCF-7 and fibroblasts helped to elucidate the tendency of fibroblasts towards the spheroid centre. Other size-dependent behaviours were profiled; larger spheroids behaved differently from smaller spheroids in terms of spheroid growth, drug penetration and cellular responses. This method breaks the boundary between the preparation of gradient-sized spheroids and significant time/labour demand. It can be useful for drug screening and *in vitro* tumour modelling.

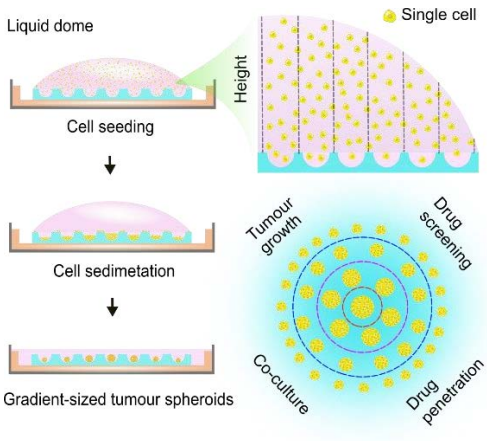

The contents of this chapter have been published in:

G. Fang *et al.*, Gradient-sized control of tumour spheroids on a single chip, *Lab on a chip*, 2019, 19, 4093-4103

Chapter 2

2.1 Introduction

Size of multicellular spheroids, which is in a range of tens to hundreds of microns in diameter, is critical for cell functions and model applications. In avascular spheroids, gradient distribution of oxygen, nutrition, pH, and metabolic wastes results in the division of three typical zones (proliferation, quiescent and necrotic zones). In principle, throughout modelling chemotherapeutic penetration in a spheroid, the size of spheroids depends on the mass transfer properties of the drug. John P. Ward studied the relation between cell survival and spheroid size when exposed to drugs, indicating that small spheroids (diameter 50 μm) gave high surviving fraction and a slight difference in drug actions[154]. Glicklis et al. modelled the drug mass transfer using different-sized hepatocyte spheroids and indicated that the spheroid size affected albumin secretion due to a size-induced oxygen difference[155]. Tumour stem cells are a particular cell type found in the tumour, which has the potential to generate new tumours and contribute to tumour metastasis. It has also been reported that the spheroid size can affect the cancer stem cell number due to the different zones in tumour spheroids[156].

Various methods[8] have been developed for spheroid formation *in vitro*, including non-adhesive surface, spinner flasks, scaffold support[157], acoustic tweezer[93, 94], hanging drop[22, 158], microwells[68, 159, 160], and microfluidic carriers[70, 161]. The methods of non-adhesive surface, spinner flasks, and scaffold support can only form spheroids with random and uncontrolled sizes. The hanging drop and microwell methods combined with precision fabrication techniques (e.g. lithography, 3D-printing, computerized numerical control mill) can achieve plenty of spheroids with uniform size. It is worth mentioning that Frey et al. developed a method to generate uniform spheroids that continuously irrigates the hanging drops in an open network, which solves the common deficiency of limited medium volume in drops[22]. The droplet carriers produced by microfluidic technology can encapsulate the cells in a high-throughput way, which could form a host of uniform spheroids. However, the microfluidic encapsulation setup needs either high-voltage spinning[77], complicated channel structure or oil–water collaboration[70]. Furthermore, the formation of spheroids in the droplet systems requires complicated channels to form double emulsions with liquid cores for cell residence and solid shell for physical support[162, 163].

Gradient-sized spheroids cannot be easily achieved through the above methods directly. Different-sized spheroids formed on a single chip remains challenging. To achieve a variety of multi-sized spheroids, different densities or volumes of cells are essential, which requires burdensome dilution and counting, suffering from low throughput. As for the microfluidic droplet method, size modulation could be achieved by adjusting the size of droplets, which requires skilful and precise flow control. Marimuthu et al. presented a microfluidic chip that automatically formed multi-sized spheroids using a constant cell concentration[38]. By designing conical holes with different taper angles above the flow channels, the capillary force ensures various medium volumes in the holes, leading to altered cell seeding numbers. This method requires four layers of PDMS bonding, and the hanging drop requires precise control of flow speed. Different-sized microwells or micropatterns can also be used to control the size of spheroids[159, 164, 165]. These methods can effectively control the size and influence spheroid growth induced by the difference of patterns. Other active methods, such as acoustic tweezers, can precisely control the size of spheroids, which, however, can only achieve one size at once[93].

2.2 Aims and approaches

We aim to generate the gradient-sized spheroids on a single chip. The agarose chip (**Figure 2-1a**) consists of a surrounding agarose channel and a plate with arrayed microwells. Gradient-sized spheroids could be simultaneously formed on the single-chip following a position-dependent rule. **Figure 2-1b** shows the formation mechanism of the

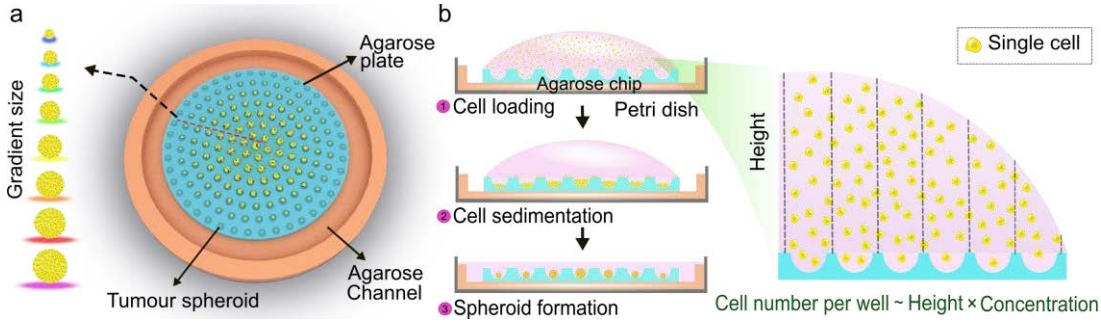

Figure 2–1 | Schematics showing the liquid dome-assisted formation of gradient-sized spheroids on an agarose chip. (a) Structure of the agarose chip and position-dependent distribution of the spheroids. Large spheroids are distributed at the centre, and small spheroids are at the edge. (b)Mechanism of the formation of gradient-sized spheroids on the agarose chip: 1) cell suspension is loaded on the chip. Due to the constraint by liquid surface tension effect, a liquid dome forms above the chip. 2) Cells deposit in the microwells. Due to the difference in height affected by the dome shape, cell number per well alters. 3) Cells aggregate and form spheroids with the position-dependent sizes.

gradient-sized spheroids. First, the cell suspension is loaded on the plate area of the agarose chip. Due to the agarose–air interface, the cell medium is confined to the plate area. The liquid generates a hemispheric dome because of the surface tension effect, where the cells in the medium deposit into the microwells by gravity after several minutes. The hemispheric liquid dome leads to different liquid heights: higher in the centre and lower at the edge, resulting in more cells sedimenting in the central microwells and fewer cells at the border. Cells spontaneously aggregate and form the spheroids facilitated by the non-adhesive property of agarose and the conical shape of the microwells during the incubation. The size of spheroids depends on the cell seeding number, which is proportional to the arithmetic product of liquid height and concentration. It can be predicted following the position-dependent rule where larger spheroids are formed at the centre and smaller spheroids at the edge. It is worth noting that after the cell sedimentation, the dome can be pricked using a pipette, and the spare cells will flow into the channel from where they can be collected.

The chip can be integrated with a commercial culture dish and a peristaltic pump for the dynamic irrigation and long-time culture (**Figure 2-2**).

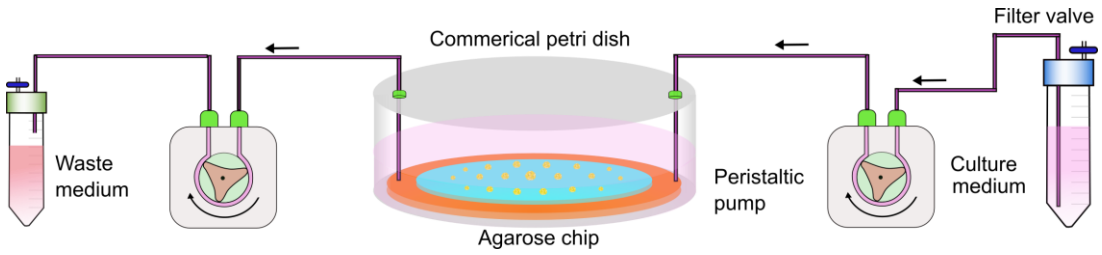

Figure 2–2| Schematic of the dynamic irrigation culture system integrated with the peristaltic pump and commercial cell culture plate.

2.3 Materials and methods

2.3.1 Chip fabrication and characterization

The plastic mould for the agarose chip was designed using Solidworks 2016 and fabricated by the Form 2 printer (Formlabs Inc. USA). The printing material is the commercial 3D printing ink-Grey Resin. A mould can be finished within 45 min using this printer. To demonstrate the modulation ability, we designed the arrays aligned into a round and a square shape, respectively (**Figure 2-3 a&b**). The micropillars' height is 300 μm, the diameter is 400 μm and the conical top is 100 μm in height. The distance between

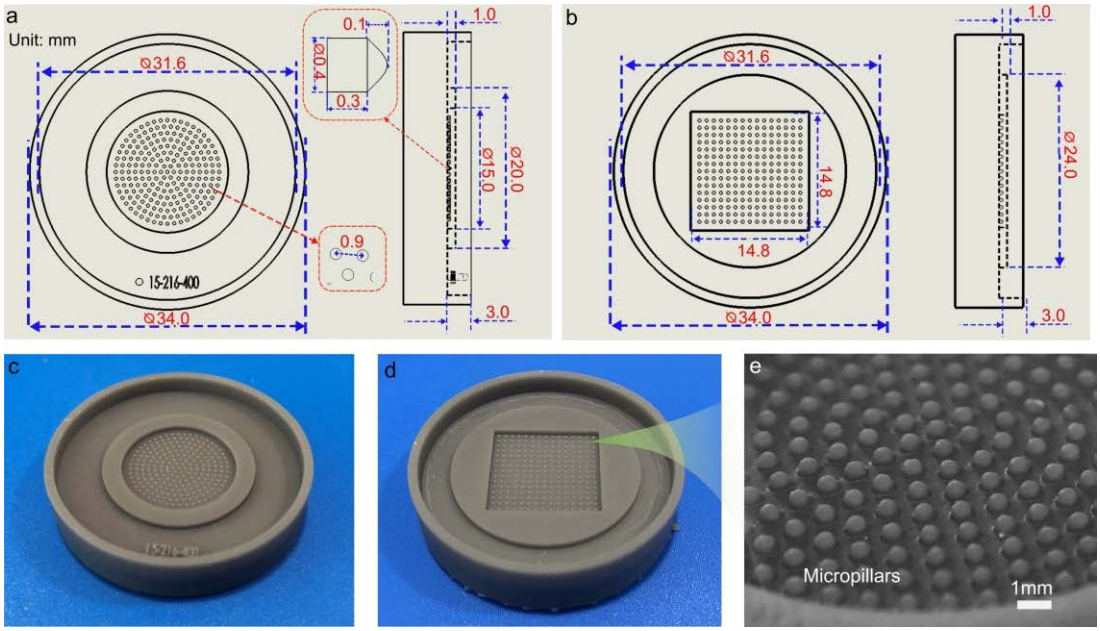

Figure 2–3 | 3D-printed mould. (a)&(b) Parameters of the round-array mould and the square-array mould. (c)&(d) Moulds with the round array and with the square array. (e) Enlarged views of the micropillars. Scale bar: 1mm.

each micropillars is 0.9 mm. There are 217 and 225 microwells on the round-array chip and the square-array chip, respectively (**Figure 2-3 c-e**). The thickness of the agarose chip is designed to be less than 3 mm.

Before using, the 3D printed mould was cleaned up in isopropanol using ultrasound, immersed in 80% ethanol for 20 min, and then air-dried in a biosafety cabinet. The mould was designed to fit 35 mm Petri dishes and six-well cell culture plates.

A microwave oven was used to melt the agarose gel into a solution. The agarose will clot once the temperature drops down. Then the agarose solution was dropped on the mould using a micropipette and put in a 4℃ fridge for 5 min, allowing for the gelation. Next, the agarose chip was peeled off from the mould using a small blade and put into the six-well cell culture plate (**Figure 2-4 a&b**).

The chips can be immersed in the cell medium for up to several weeks without significant shape change. The microwells showed good sphericity and a conical shape with a relatively flat bottom (**Figure 2-4 c&d**). The diameter of the top opening is ~530 μm, although the diameter of the mould pillar is designed as 400 μm. The height is about ~360 μm. In the middle height, the diameter is ~400 μm. With this dimension design, the microwell can allow the spheroids up to 400 μm (**Figure 2-4e**).

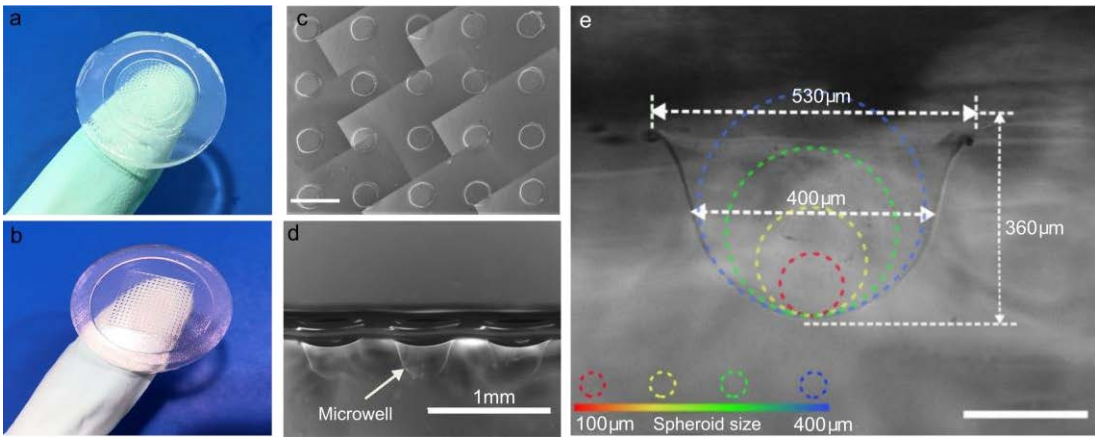

Figure 2–4 | Agarose chip and characterization. (a) Agarose chip peeled from the round-array mould. (b) Agarose chip peeled from the square-array mould. (c)&(d) Top-view and side-view images of the microwell array. Scale bar: 1mm. (e) Enlarged views of the microwell. Scale bar: 1 mm.

2.3.2 **Cell seeding**

The cell seeding (**Figure 2-5**) procedure consisted of four steps: 1) The medium for agarose immersion was removed by a pipette (**Figure 2-5 a-i**). The agarose chip was air-dried for 10 min. 2) 200~300 μL cell suspension was loaded on the agarose plate using a pipette (**Figure 2-5 a-ii**). The liquid generated a hemispheric dome and a square dome due to the surface tension effect. It can be observed that the dome on the chip had much different position-dependent liquid level distribution. Due to the constraint of the agarose-air interface, the dome was stable. The cells in the dome deposited into the microwells by gravity within 5 mins. 3) The dome was gently pricked using a pipette. The spare medium flowed into the side channels (**Figure 2-5 a-iii**). 4) The spare medium in the channel was collected using a pipette and 2 mL fresh medium were added to ensure the chip was submerged in the medium (**Figure 2-5 a-iv**). Finally, the cell culture plate was removed to the incubator very gently, avoiding leaking of cells from the microwells.

To further prove the mechanism of the liquid dome, a chip without the microwells was fabricated via a mould without the micropillars (**Figure 2-5 b-insert**). After cell suspension loading and sedimentation, the cells were distributed on the whole surface. It could be seen that the distribution of the cells indeed followed the central-edge rule. More cells at the central and less cell on the edge. (**Figure 2-5b**) Images in the coloured circles show the enlarged views of the cells in four different places (**Figure 2-5c**). By analysing the cell area in the circles, an obvious increase was seen from the edge to the central (**Figure 2-5d**). The cell area at the central is around twice as larger as that on the edge.

This indicates that after cell sedimentation, the chip with microwell array had the same phenomenon. The images were captured before pricking the liquid dome.

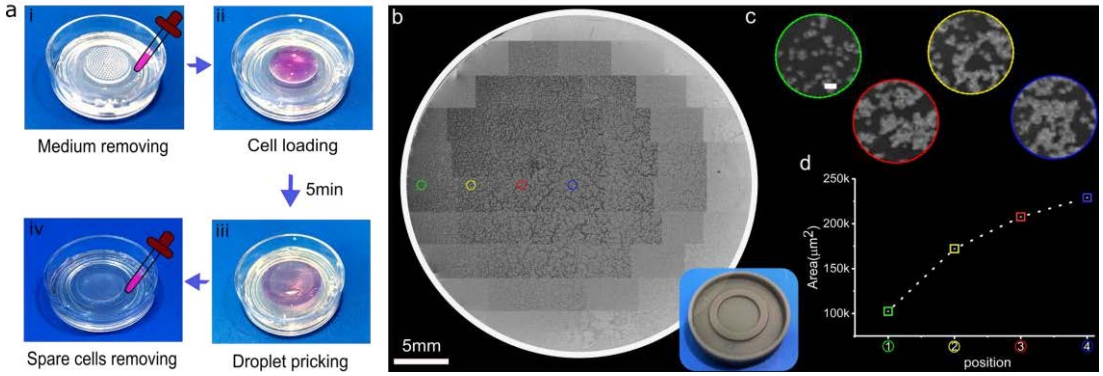

Figure 2–5 | Cell seeding and characterization on the chip. (a) Cell seeding process on the agarose chip: i) Medium for agarose equilibration is removed. ii) The cell suspension is loaded on the array area and forms the liquid dome. iii) After cell deposition, the liquid dome is pricked gently using a pipette. iv) The spare medium flowing into the channel is removed, and the fresh medium is gently added to immerse the whole chip. (b) Image of the cell distribution after the sedimentation. Inset is the mould without micropillars. Scale bar: 5 mm. (c) Enlarged view of the four selected spots along the diameter (Scale bar:100 μm). (d) Relationship of the cell area and position of the coloured circles.

2.3.3 **Dome shape simulation and analysis**

Here, we assumed that the medium volume loaded on the chip could change the contact angle and used the hemisphere-shaped models to analyse the contact angle effect (**Figure 2-6a**). According to **Figure 2-6b** and **Table 2-1**, it indicates that when the contact angle changed from 15º to 60º, the height difference ratio (central height/edge height) changes slightly, which remains ~3 folds. Here, we define the size modulation ability is proportional to the height difference ratio. Accordingly, we could conclude that the medium volume and the contact angle had an ignorable influence on the modulation ability of the liquid dome in this study. Mathematical models were established to simulate the shape effect. The round dome was reconstructed in Matlab following the sphere model (**Figure 2-6 c-i**). It was illustrated that the liquid height at the central could reach almost 3-folds higher than that at the edge. The square dome is calculated following the shape differential calculus [166](**Figure 2-6 c-ii**). Compared with the hemispheric dome, the square dome had larger liquid height ratio of more than 10 folds, allowing a higher size modulation ability over the round chip. The size of spheroids is nonlinearly positive correlated with the initial number of seeding cells[159]. This simulation elucidated the

Table 2-1 | Theoretical simulation of the liquid height at different positions under different contact angle. (Value in blanket is the ratio of central height to middle height or edge height.)

	15º	*30º*	*45º*	*60º*
central	*0.132*	*0.268*	*0.414*	*0.577*
Middle(50%)	*0.099(1.33)*	*0.204(1.31)*	*0.323(1.28)*	*0.464(1.24)*
Edge(85%)	*0.037(3.75)*	*0.078(3.44)*	*0.130(3.18)*	*0.204(2.83)*

size modulation ability of the proposed liquid dome method. Round liquid dome and square liquid dome on the chip is shown **Figure 2-6d.**

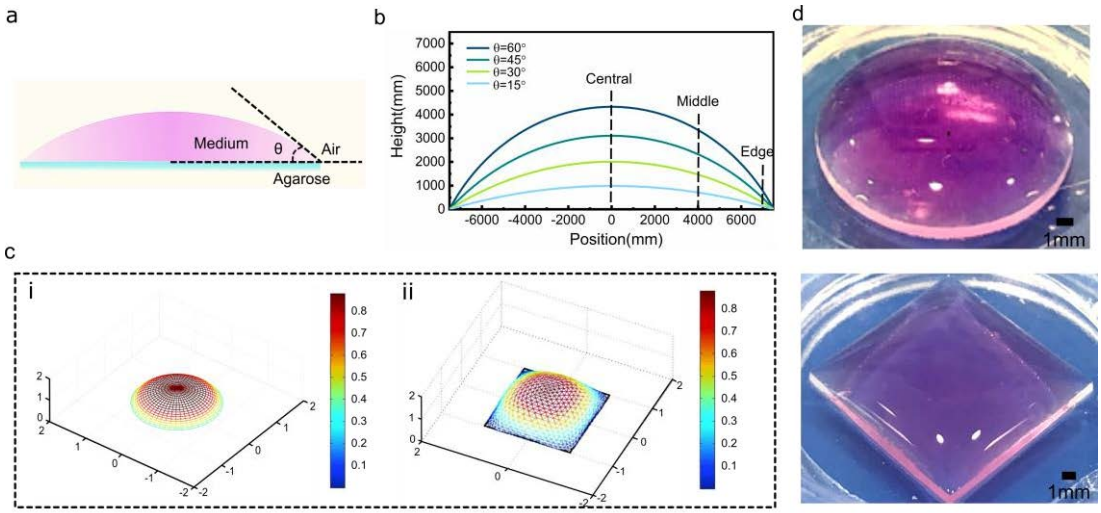

Figure 2–6 | Liquid dome shape analysis and simulation. (a) Schematic of the contact angle (loaded medium volume) at the air-medium-agarose barrier area. (b) The relationship of liquid height and position under different contact angle situation based on the hemisphere-shaped dome model. (c) Mathematical simulation: i) hemispheric dome based on the sphere mould theory. ii) square-shaped dome based on the theoretical calculation [166]. (d) Images of the hemispheric liquid dome and the square liquid dome.

2.3.4 **Cell culture**

MCF-7 cells from Australia Cell Bank were cultured with RPMI1640 medium (in vitro technologies, Australia) in six-well cell culture plates. The medium was supplemented with 10% fetal bovine serum (FBS) and 100 U mL^{-1} penicillin/ streptomycin. Cells were incubated in a standard incubator with 5% CO_2 at 37 °C. When the cells reached 70–80% confluence, a cell passage was performed. The cells could be used after 3–4 passages. Before cell seeding, the cells were treated with Trypsin–EDTA solution for 3 min followed by the centrifugation for 5 min at 500 × g. After removing the supernatant, the cells were re-suspended in 1 mL fresh medium and mixed well using a micropipette. The

cell concentration was 1×10^6 ~1×10^7 mL^{-1}. Lower concentration would lead to smaller spheroids.

For the double co-culture, normal human dermal fibroblasts (Sigma-Aldrich, Australia) were cultured with RPMI1640 medium in a six-well cell culture plate. Before the co-culture, fibroblasts were first stained by CellTracker Orange CMRA Dye (Thermo Fisher Australia) in the six-well cell culture plate for 15 min. After the staining, the fibroblasts were washed with phosphate buffer saline (PBS), detached, centrifuged and re-suspended in 1 mL fresh medium. MCF-7 cells were collected in the same way except for the staining. Then 1×10^6 fibroblasts and 3×10^6 MCF-7 cells were mixed together in a 15 mL centrifuge tube. After the centrifuging, the supernatant was discarded, and 1 mL fresh medium was added, achieving a solution with a total cell density of 4×10^6 mL^{-1} at a fibroblast and MCF-7 mixed ratio of 1 : 3. The cell suspension was seeded on the chip with the above-described seeding protocol. The mixed solution was also seeded in sixwell cell culture plates for the 2D monolayer culture. After 2-day growth, the formed spheroids were stained with Hoechst 33342 for 1 h to label the cell nuclei. The 2D cultured cells were stained with Hoechst 33342 for 20 min. Then the cocultured spheroids were observed under the laser scanning confocal microscope (FV1200, Olympus, Japan). The CellTracker has fluorescence with an excitation at ~548 nm and emission at ~576 nm. Hoechst 33342 has fluorescence with an excitation at ~350 nm and emission at ~461 nm.

For the triple co-culture, HUVECs (Sigma-Aldrich, Australia) were cultured with endothelial cell growth medium (SigmaAldrich, Australia) in a six-well cell culture plate. Before the seeding process, the HUVECs were stained by Tubulin Tracker™ Deep Red (Thermo Fisher, Australia) for 30 min. At the same time, the fibroblasts were stained by Orange CMRA Dye for 30 min. After 3 times wash by PBS, the MCF-7, fibroblasts and HUVEC were mixed at the ratio of 5 : 1 : 1 and seeded on the chip. When the spheroids were formed, the spheroids were stained by Hoechst 33342 before the observation. The culture medium was the mixture of RPMI1640 medium and endothelial cell growth medium at a ratio of 1 : 1.

For the spheroid culture on the chip, the medium in the cell culture plate was changed every 2 days, with 2 mL medium being enough in each well and ensuring the spheroids immersed in the medium. The spheroids were visually inspected under an optical microscope every day.

2.3.5 **Drug penetration experiment**

DOX has the fluorescence with excitation at ~559 nm and emission at ~630 nm. 3-day-old spheroids were used for this experiment. The medium was firstly removed, and then 2 mL fresh medium with 30 μg mL^{-1} DOX was added, followed by the incubation at 37 °C for 1 h, 2 h, 3 h and 4 h. At each time point, the distribution of DOX in spheroids was observed by the confocal microscope. The spheroids need to be washed by PBS twice before the observation, followed by the drug medium reloading after the observation.

2.3.6 **Cell viability after drug treatment**

The 3-day-old spheroids were used in this experiment. The medium was firstly removed, and then 2 mL fresh medium with latrunculin A at a concentration of 5 μM or nocodazole at a concentration of 3.5 μM was added, separately. These concentrations were selected according to the recommended dosages[167]. In the control group, 2 mL fresh medium with the same volume of PBS was added. After three days' culture, the viability was measured by the Live/Dead Cell Assay kit (Sigma-Aldrich, Australia) with staining for 1 h at 37 °C. Then the spheroids were imaged under the confocal microscope. Due to the limited penetration of the dyes in spheroids, images with different depth were captured in a 15 μm step. Then the images were merged in ImageJ by Max Projection. The live and dead area were measured with ImageJ by the threshold function. Although the measurement based on fluorescence have unavoidable fluctuation, this method for cell viability has been applied and verified by several published studies[168].

2.3.7 **Spheroids with cells from mouse tumour**

The animal experiments were performed at the Garvan Institute of Medical Research under the approval of the St. Vincent's Campus Animal Ethics Committee (AEC #19/02). BALB/c mice was inoculated with 50 000 4T1.2 cells in the fourth inguinal mammary gland to generate tumour tissues. The mouse 4T1.2 tumour tissue was collected 4 weeks post inoculation and chopped into small chunks. The chunks were treated with TrypLE™ Express (Thermo Fisher, Australia) for 10 min to dissociate into single cells, which was followed by filtering through a 300 μm cell strainer to remove the undissociated chunks. The cells were mixed with fibroblasts at a ratio of 3 : 1 and seeded on the agarose chip. The culture medium was DMEM containing 10% FBS, 1% Lglutamine, 5 μg mL^{-1} insulin, 10 ng mL^{-1} epithelial growth factor (EGF) and 10 ng mL^{-1} cholera toxin. As for the drug

resistance, the 2-day-old spheroids were treated by doxorubicin at a concentration of 30 μg mL^{-1} for 3 days. Then the live/dead staining was performed before the observation with confocal microscopy.

2.4 Results and discussion

2.4.1 Size distribution of the spheroids on the chip

For proof of concept, MCF-7 cells at a density of ~5 × 10^6 cells per mL were seeded for spheroid formation. After cell seeding, the MCF-7 cells formed spheroids within 12 h. **Figure 2-7** shows the whole bright-field image of the spheroids on the round-array chip after incubation for one day. The images in the right panel show the enlarged view of three representative spheroids on the edge, middle and central area, with the diameters of 140 μm, 200 μm, and 264 μm, respectively. The images were processed using ImageJ, whose ROI function can extract the spheroid images and colour them based on their area size. As shown in **Figure 2-7a**, the area size of each spheroid on round-array chip ranges from 16k-54k $μm^2$ (diameter: 140-264 μm). This modulation ability correlates well with

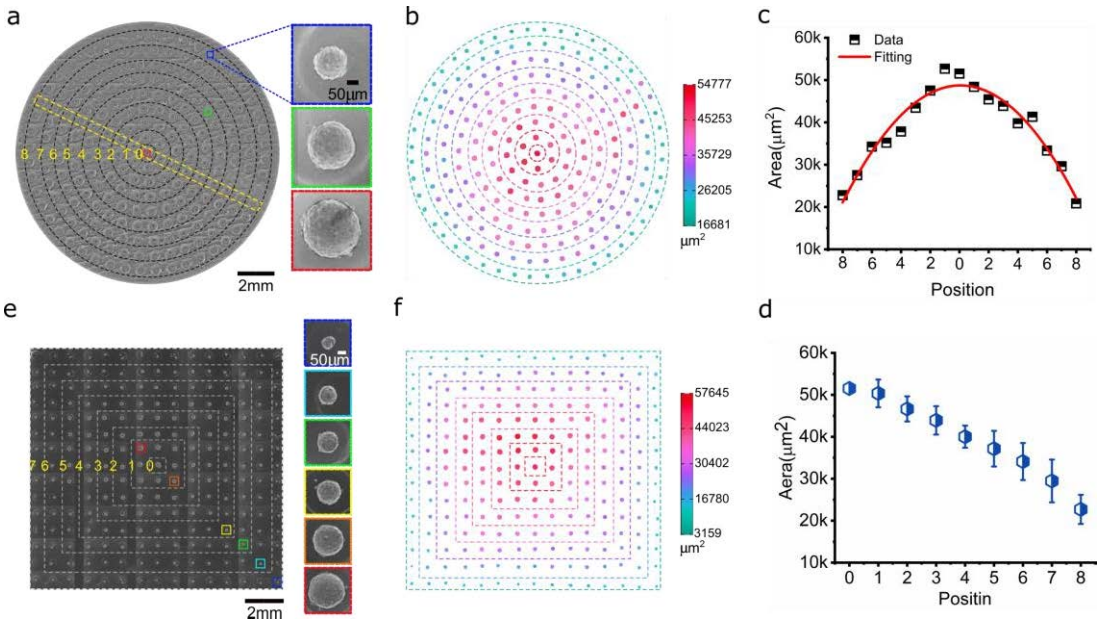

Figure 2–7 | Size distribution of the MCF-7 spheroids on agarose chips. (a) Bright-field image of the spheroids on the round-array chip. Scale bar: 2mm. The right shows the enlarged views of the spheroids at the edge, middle and central area. Scale bar: 50 μm (b) Size distribution of the spheroids on the round-array chip. (c) The size distribution of the spheroids along a diameter of the chip. (d) The average size of the spheroids in each circle from the centre to the edge on the round-array chip. (e) Bright-field image of the spheroids on the square-array chip. Scale bar: 2 mm. The right is the enlarged views of the spheroids from the centre to the edge. Scale bar: 50 μm. (f) The size distribution of the spheroids on the square-array chip.

the mathematical simulation: the smaller ones distributed at the edge and the larger ones located at the central. Area sizes of the spheroids along one diameter of the chip are shown in **Figure 2-7c**. The distribution curve is similar to the hemisphere shape, which also demonstrates the surface tension effect. The average area of spheroids on each circle indicates the position-dependent size modulation (**Figure 2-7d**). Due to the lower liquid height at the edge induced by the shape, the square dome showed greater size variability. The size distribution in the square dome follows the same rule as that of the hemispheric dome (**Figure 2-7 e&f**). The diameter of the spheroids shown on the right in **Figure 2-7e** is 76 μm, 108 μm, 125 μm, 143 μm, 186 μm and 228 μm, respectively. The spheroid areas on the square-array chip range from 4k–58k μm^2 (diameter: 76–264 μm). In summary, the hemispheric dome demonstrated a ~3.4-fold variability in spheroid area, and the square-shaped dome could have a 12.8-fold variability in spheroid area. The difference results from the radial position-dependent liquid height caused by the dome shape. This method only needs one-step cell seeding and is facile and effective for biologists and pharmacists, who need a high-throughput approach for gradient-sized spheroids.

The spheroids on the chip had high roundness as shown in **Figure 2-8**, most of which were around 0.9. The roundness was automatically calculated by the ImageJ. This indicates that the roundness of the spheroid was independent with the size at the initial growing stage. Size in this Chapter refers to projected area.

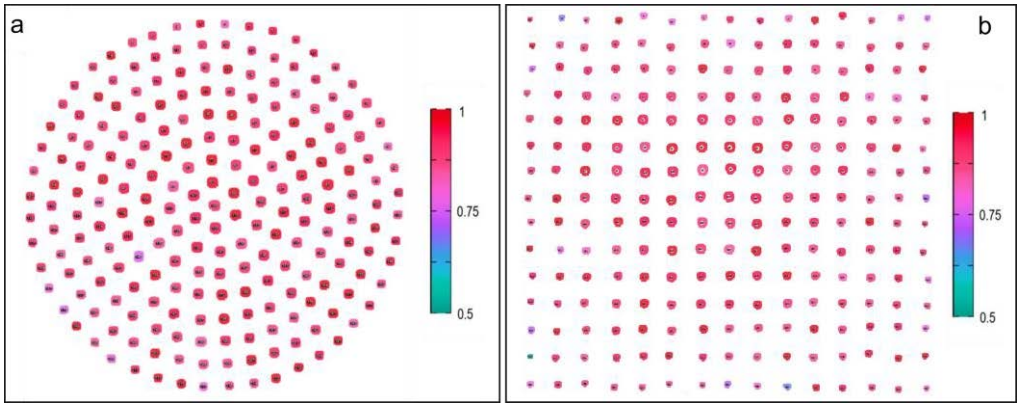

Figure 2–8 | Roundness of each spheroid (1-day-old) (a) on the round chip and (b) on the square chip.

2.4.2 Size-dependent growth rate of the spheroids

To characterize the growth of the MCF-7 spheroids with different initial sizes, we recorded the sizes of the spheroids for five days. The initial area sizes of the #1–#7

spheroids were 13.9k, 19.5k, 28.9k, 30.4k, 40k, 48k, and 49.4k μm^2 , respectively (**Figure 2-9a**). The optical micrographs showed that the opaque and chaotic area occurred earlier in larger spheroids compared to the smaller spheroids. The spheroids larger than 48k μm2 could occupy the whole microwell on the fourth day. The time-dependent size increase indicated that the smaller spheroids showed a more substantial change in size; while the size increase of the larger spheroids was gradually reduced (**Figure 2-9b**). The plateauing of growth in larger spheroids may be caused by the accumulation of metabolic waste and the constraint of the microwells. However, the overall growth ratio (μm^2 per day) of the larger spheroids was higher than that of the small spheroids (**Figure 2-9c**). The largest spheroids could reach ~21k μm^2 per day growth rate, which was almost 1.5-fold faster than that of the smaller ones. Furthermore, the spheroid area growth rate was linearly proportional to the initial area ($r^2 = 0.95$), which could predict the MCF-7 spheroid size based on the initial size and culture time.

The roundness change of the spheroids on the round chip was tracked for 5 days. According to **Figure 2-10**, it was seen that the overall sphericity was around 0.92. On the second day, the overall roundness slightly increased, which was followed by a drop on

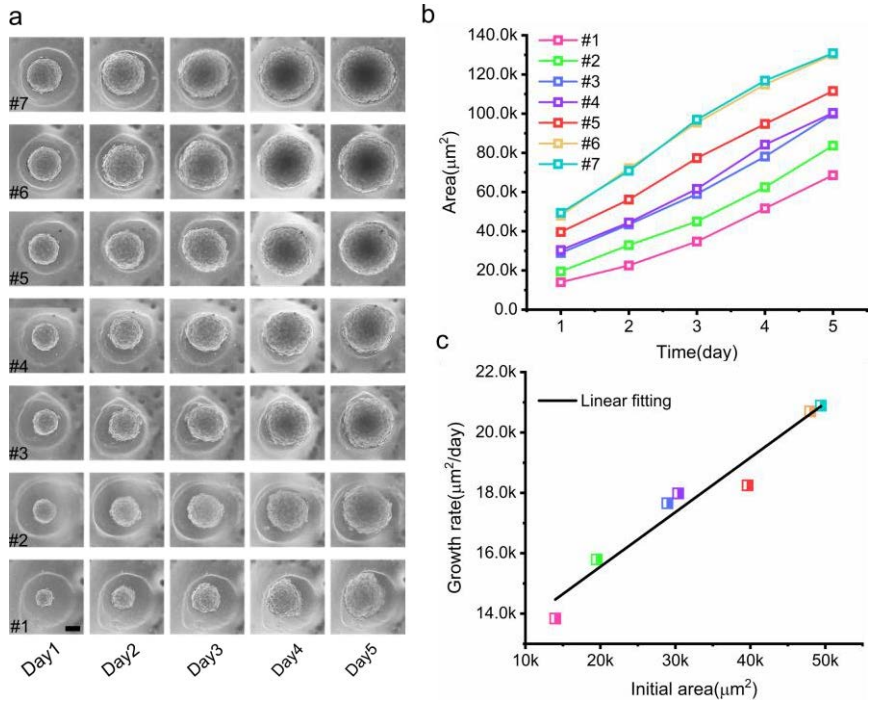

Figure 2–9 | Growth profile of the MCF-7 spheroids with different initial sizes. (a) Bright-field image of the MCF-7 spheroids (scale bar: 100 μm) after 5day culture. (b) Time-dependent increase of the area sizes from different initial sizes. (c) Size growth rate versus initial area size.

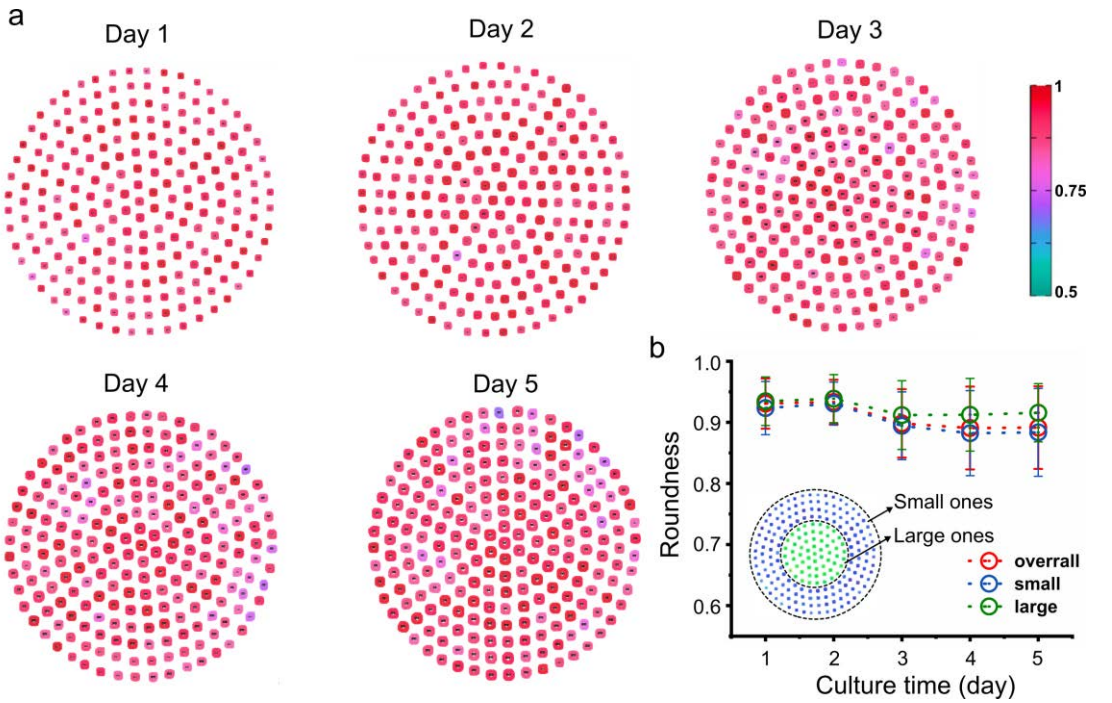

Figure 2–10 | Roundness of the MCF-7 spheroids on the chip. (a) Roundness profile of the MCF-7 spheroids on the chip for 5 days. (B). Roundness change versus culture time.

the third day. Then the roundness stayed at 0.90 on day 4 and 5. After 5-day's culture, although the roundness of some spheroids became worse to around 0.75, most spheroids had high sphericity (remaining at around 0.9).

To characterize the difference of perfusion (dynamic) culture and the static culture, we added the microfluidic perfusion unit. The microfluidic perfusion setup, as shown in **Figure 2-11** consisted of a peristaltic pump, a tube containing fresh medium, a tubing containing waste medium, the chip in the 6-well cultural plate and the silicon tube. The flow rate was set as 50 uL/h, which could offer 1 mL fresh medium for 1 day. The medium of the control group was changed with 2 mL every 2 days. Interestingly, we found that the spheroids with dynamic perfusion had a smoother surface, as shown in **Figure 2-11 b&c**. Distribution of the smooth and coarse spheroids under static culture is shown in **Figure 2-11d**. Without the perfusion, the spheroids at the central area tended to have a coarse surface, and those at the edge prefer a smooth surface. We supposed that the central area had fast nutrition consume and metabolic waste accumulation under the static culture. When the perfusion was applied, the nutrition had a homogeneous distribution and the metabolic waste could be cleaned up in time. We also compared the difference in growth rate. **Figure 2-11e** shows the growth of two spheroids with the same position on the chip.

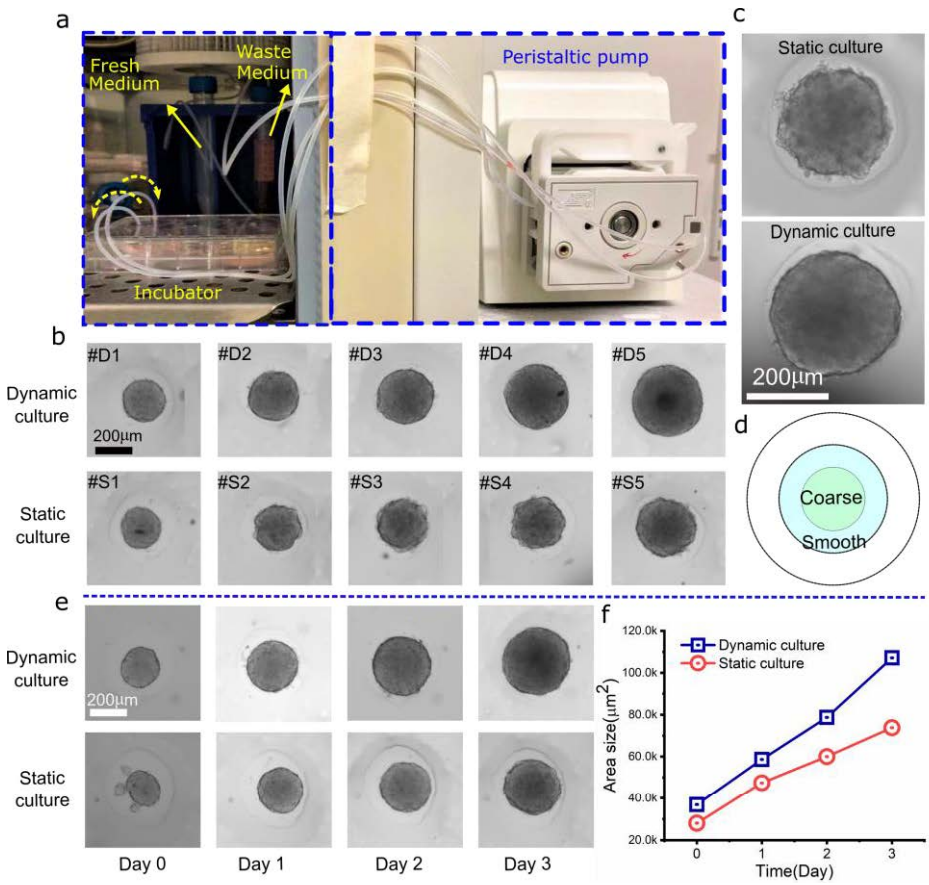

Figure 2–11 | Dynamic culture of the MCF-7 spheroids on the agarose chip. (a) Experimental setup of the microfluidic dynamic culture. (b) Comparison of the spheroids with dynamic culture and static culture observed with a 4X objective lens. (c) Surface of the spheroids with dynamic culture and static culture. (d) On-chip distribution of the spheroids with coarse and smooth surface under static culture. (e) Growth of the spheroids with dynamic culture and static culture. (f) Growth curve of the spheroids with dynamic culture and static culture.

According to Fig. **Figure 2-11f**, the spheroids with perfusion had an increasing growth rate. However, the spheroid without perfusion showed a decreasing growth rate. This indicates that the microfluidic unit could offer a better living environment for the spheroids.

2.4.3 Size-dependent co-culture of different cells

Except for tumour cells, tumour *in vivo* also contains plenty of other cells, such as the stromal cells (fibroblast, cancer-associated fibroblasts, stellate cells, etc.), immune cells (macrophage cells, monocyte, T-cells, B-cells, etc.), and epithelial cells. These synergistical communication and behaviours determine the fate of the tumour. Moreover, their different secretion constitutes the various ECM components. These together formed

the complicated tumour microenvironment, mediating the tumour growth, invasion and metastasis[169].

Multicellular spheroids, used as the common *in vitro* models, should also contain different types of cells, to mimic the complexity of the tumour microenvironment. The complexity leads to a number of factors, determining the downstream drug response during the drug screening and clinical treatment, such as the spheroid structure (hypoxia and acidosis), complex interaction between the tumour cells and other cell types, the ECM (collagen, laminin, fibronectin), etc.[170] For instance, it is reported that the Caco-2 spheroids co-cultured with the fibroblasts can decrease the resistance to 5-FU/oxaliplatin by 38% but no impact to 5-FU/irinotecan.[171] Spheroids that only contained the single type of cells may lose some physiological functions and features, probably leading to deficient drug response.

Co-culture the tumour cells with stromal cells provides a better way to mimic the complexity of the tumour tissues[172-174]. Here, we co-cultured the MCF-7 cells with fibroblasts using the agarose chips. To the best of our knowledge, this is the first work to form gradient-sized co-culture spheroids on a single chip. The fibroblasts were firstly pre-stained with the CellTracker™ Orange CMRA Dye (Thermo Fisher Australia) and then mixed with MCF-7 cells at a ratio of 1 : 3. The mixed cells were cultured on the hemispherical liquid-dome platform (**Figure 2-12a**). After 2-day culture, the formed spheroids on the chip were stained with Hoechst 33342. The mixed cells were also cultured in cell culture dishes as a monolayer culture control. This two-colour staining helped us to distinguish the distribution of the two kinds of cells and furthermore reduce the dye influence on the spheroid formation. In the monolayer culture, the fibroblasts formed a network around the MCF-7 cells uniformly (**Figure 2-12b**). Once the cell mixture reached almost 100% confluent, the growth of the cells was severely inhibited. The co-cultured spheroids also followed the size distribution rule on the chip. **Figure 2-12c** showed the area of coculture spheroids ranged from 7.9k μm^2 to 65.2k μm^2, respectively. Interestingly, we found that the fibroblasts aggregated together and formed a core in the centre of the spheroids. This phenomenon was more evident in the larger spheroids than in the smaller ones. Furthermore, based on the bright-field images, it could easily distinguish the fibroblast core and tumour cell shell in the large spheroids.

We hypothesized that this central tendency of fibroblasts was induced by the different cohesion of the two cells[175]. Besides, it has been reported that hypoxia could attract the migration of fibroblasts in the tumour microenvironment, which could be another reason for the core–shell structure[176].

To better mimic the tumour microenvironment, we introduced the HUVECs into the spheroids and co-cultured these three types of cells, as shown in **Figure 2-13a**. HUVECs are commonly used for the modelling angiogenesis in 3D models. The co-culture of HUVECs with tumour cells and fibroblasts could help to research the crosstalk between tumour cells and endothelial cells, which is critical for the new blood formation, known as the angiogenesis. Here, the fibroblasts were stained red with CellTracker CMRA, HUVECs were stained greed with Tubulin Tracker Deep red, as shown in **Figure 2-13a**. Then the MCF-7, fibroblast and HUVEC were mixed at a ratio of 5:1:1 and seeded on the

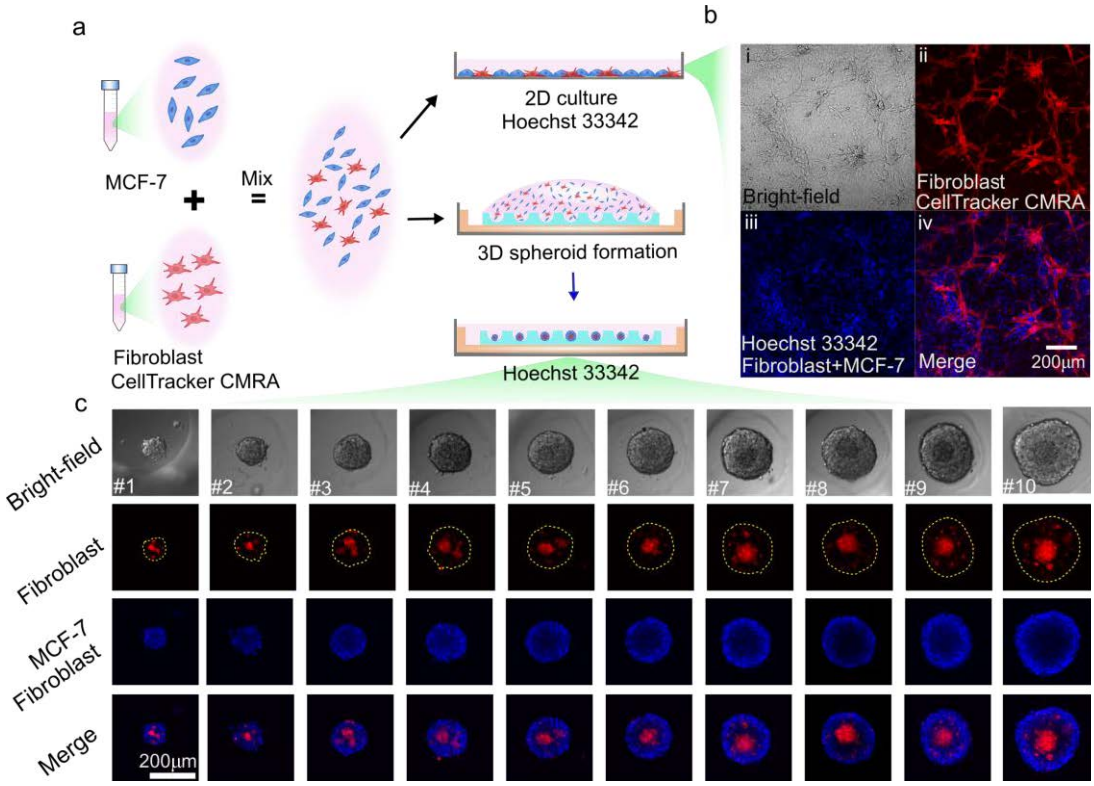

Figure 2–12 | Coculture MCF-7 and fibroblasts in the spheroids. (a) Schematic co-culture of MCF-7 cells and fibroblasts. MCF-7 and pre-stained fibroblasts were firstly mixed and then seeded in a tissue culture dish as a monolayer control or in the agarose chip for gradient-sized spheroids. After that, the monolayer cells and the spheroids were stained by Hoechst 33342 to visualize the distribution of the two cell types. (b) Images of the monolayer co-culture: i) bright-field image, ii) image of fibroblasts stained by CellTracker CMRA, iii) image of cell nuclei stained by Hoechst 33342, iv) merged image of ii and iii. (c) Gradient-sized spheroids co-cultured with MCF-7 cells and fibroblasts. Scale bar = 200 μm.

chip followed the process in the manuscript. After 1 day's culture, the gradient-sized triple-cell spheroids were formed on this chip, as shown in **Figure 2-13b**. It could be seen that the roundness of the spheroids had a slight decrease when the HUVEC were added, especially for the small spheroids. The central tendency of the fibroblasts changed a little bit. More fibroblast cores occurred in the spheroids; however, the central tendency could also be seen in some large spheroids. Another interesting thing is that the green fluorescence seemed to overlap well with the red fluorescence, indicating that the HUVECs preferred to stay together with the fibroblasts.

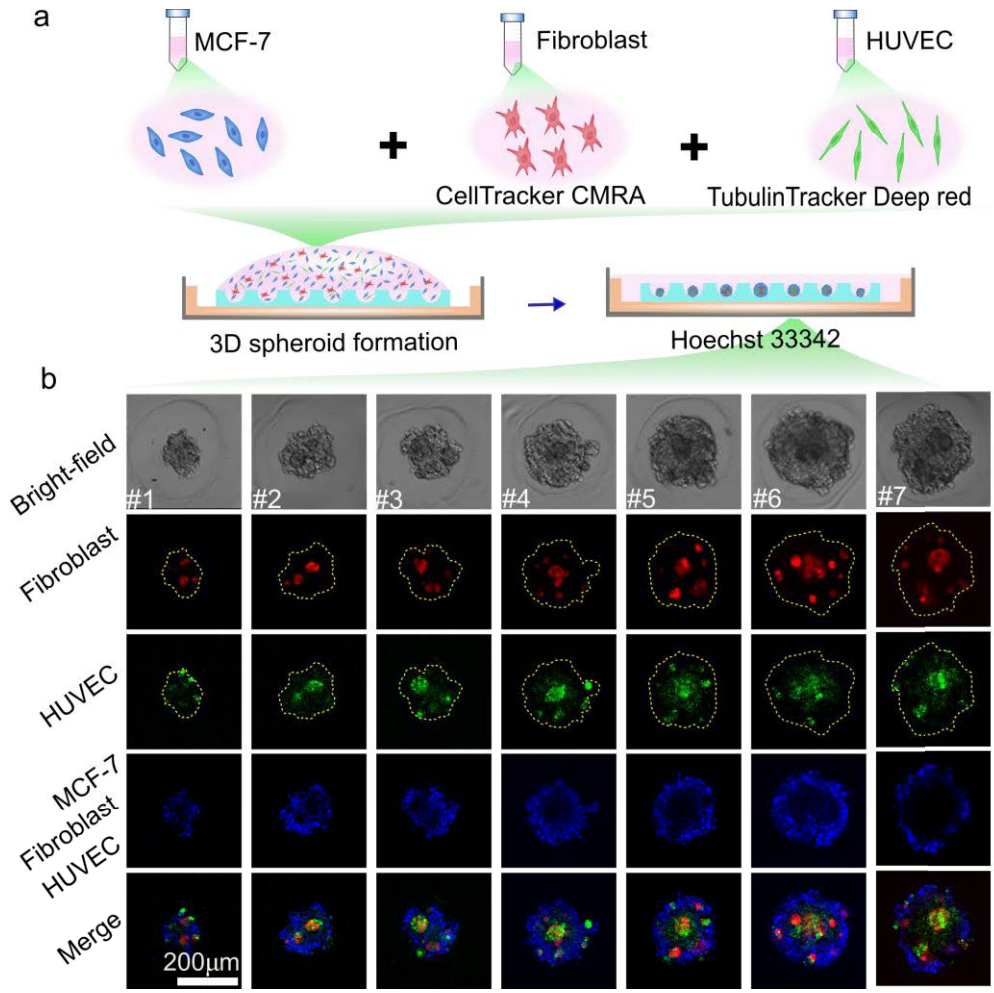

Figure 2–13 | Coculture MCF-7, fibroblast and HUVEC in the spheroids. (a) Schematic of the triple coculture of MCF-7, fibroblasts and HUVEC. (b) Gradient-sized spheroid formed by MCF-7, fibroblast (red fluorescence) and HUVEC (green fluorescence). Scale bar:200 μm.

To better illustrate the capacity of this method, we used the mouse 4T1.2 tissue as a model of the patient tumour sample to fabricate the gradient-sized spheroids on this chip. As shown in **Figure 2-14a**, at first, the mouse 4T1.2 tumour was removed and chopped into

small chunks. Then 14 the chunks were treated with TrypLE™ Express (Thermo Fisher, Australia) for 10 mins to dissociate into single cells. Next, the small chunks were removed by a cell strainer with 200 μm pore size. Then the single cells were mixed with fibroblasts at a ratio of 3:1, which followed the seeding process in the Materials and Methods. As shown in Fig. **Figure 2-14b**, the gradient-sized spheroids could be formed on this chip. Compared to the MCF-7 (cell line), some cells scattered around the spheroids. To investigate the distribution of the 4T1.2 tumour and fibroblasts in spheroids, we stained the fibroblasts cells red with CellTracker CMRA and the whole spheroids blue with Hoechst 33342. As shown in **Figure 2-14c**, the fibroblasts could well integrate with the tumour tissues. We believe that this spheroid model formed on this chip could offer a better choice for drug screening.

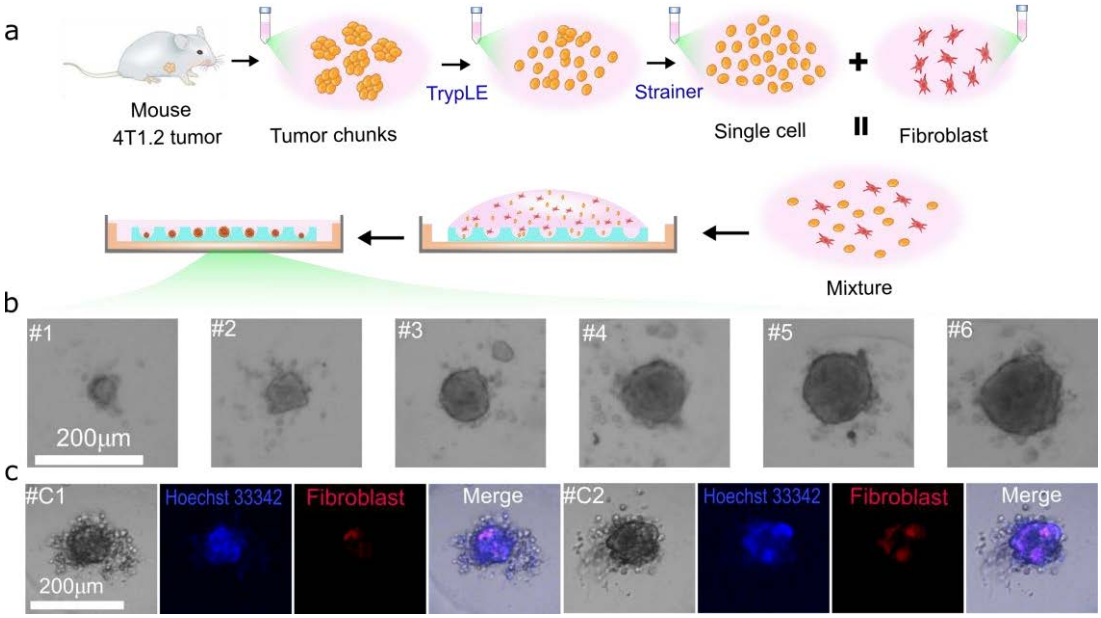

Figure 2–14 | Spheroid formation derived from the 4T1.2 tissues. (a) Schematic of the spheroids formation process on this chip with mouse 4T1 tumour cells and fibroblasts. (b) Mouse 4T1.2-fibroblast spheroids with gradient size formed on the chip. (c) Distribution of the mouse 4T1.2 cells and fibroblast in the spheroids. Fibroblasts were stained red with CellTracker CMRA Orange, and the whole spheroids were stained blue with Hoechst 33342.

2.4.4 Size-dependent drug penetration

The difference in drug penetration in the solid tumour is mainly caused by interstitial transport, which in turn affects the anti-cancer drug efficacy. Compared to the monolayer cell culture, 3D spheroids mimic the cell–cell and cell–matrix microenvironment and show more accurate responses to drug tests. However, the size of spheroids affects cell viability, matrix distribution, and spheroid compactness, which leads to a significant

difference in drug penetration. In this study, the doxorubicin (DOX) penetration in MCF-7 spheroids of different sizes was investigated. DOX has been clinically applied for breast cancer and other solid tumours[177]. **Figure 2-15a** shows the cross-section images of each spheroid under laser scanning confocal microscopy. The area size of the spheroids was 7.7k, 15.5k, 22.7k, 27.4k, 31.9k, 36.7k, 38.9k and 56.7k μm^2, respectively. Schematic of the cross-section image is shown in **Figure 2-15b**. No noticeable change of penetration depth could be seen in small spheroids (e.g. #1,#2 and #3, area <20k μm^2). But the fluorescence intensity was increasing during incubation, indicating the accumulation of DOX in the spheroids (**Figure 2-15c**). The change of penetration depth was more evident in the large spheroids (e.g. #7, #8, area >35k μm^2) than in the smaller spheroids. A strong fluorescence spread from the edge towards the core. The DOX penetration rate was about

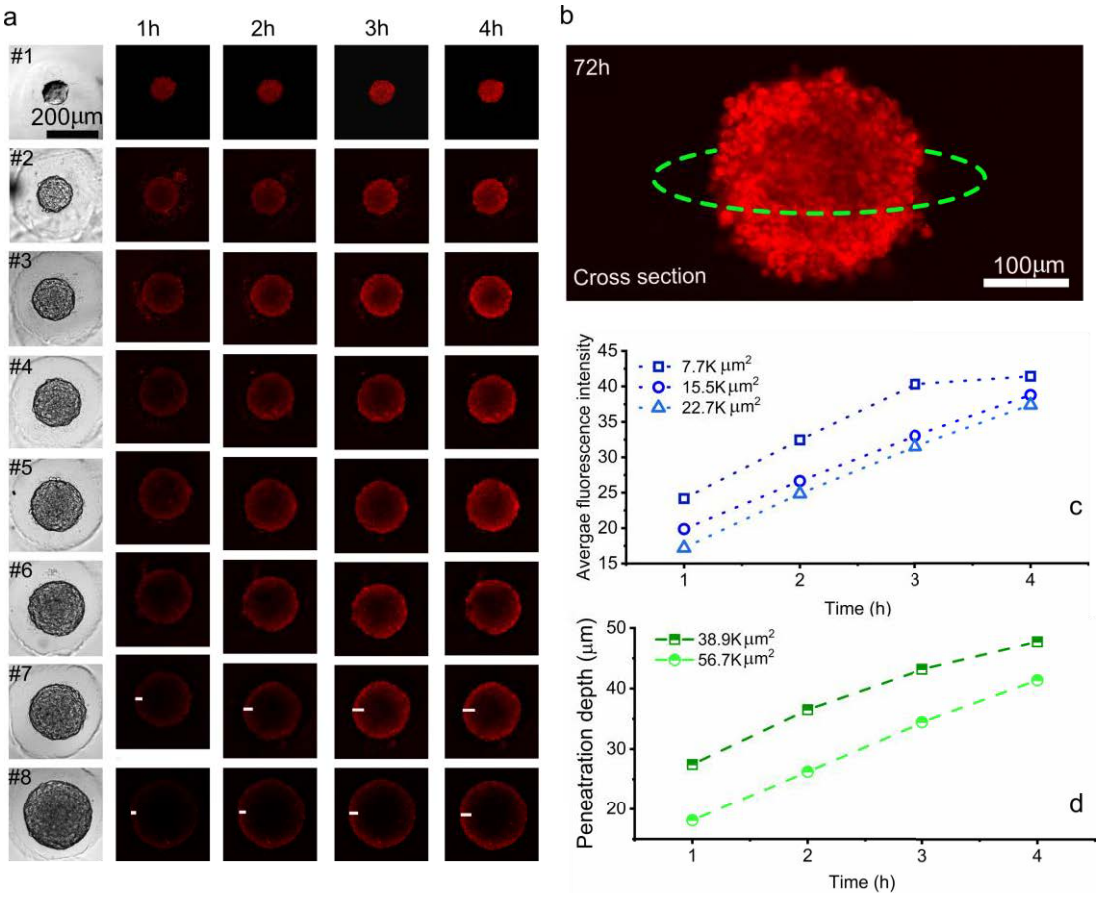

Figure 2–15 | DOX penetration in gradient-sized MCF-7 spheroids. (a) Fluorescence cross-section image of the spheroids under the confocal microscopy at 1 h, 2 h, 3 h and 4 h (scale bar = 200 μm). The white lines illustrate a 90% intensity decrease of the fluorescence compared to the edge fluorescence (b) schematic of the cross-section in a spheroid after 72 h DOX treatment (scale bar = 100 μm). (c) Time-dependent average fluorescence intensity in #1, #2 and #3 spheroids. (d) Time-dependent DOX penetration depth in #7 and #8 spheroids.

10 μm h^{-1} (**Figure 2-15d**). The DOX fully penetrated the entire spheroid after 72 h incubation no matter the spheroid size. A cross-section image of a spheroid treated for 72 h is shown in **Figure 2-15b**. The experiment indicates that the spheroid size influences drug penetration. Therefore, it indicates that the size of the spheroid models should be considered in drug screening.

2.4.5 Size-dependent response to anti-cancer drugs

The cellular responses to the anti-cancer drugs in spheroids relates to the drug penetration, cell status and ECM distribution, which are associated with the size of the spheroids. Here, we used a Live/Dead Cell Assay kit for the test of cell viability in spheroids after anti-cancer drug treatment. As the dye for dead cells (propidium iodide) had the same

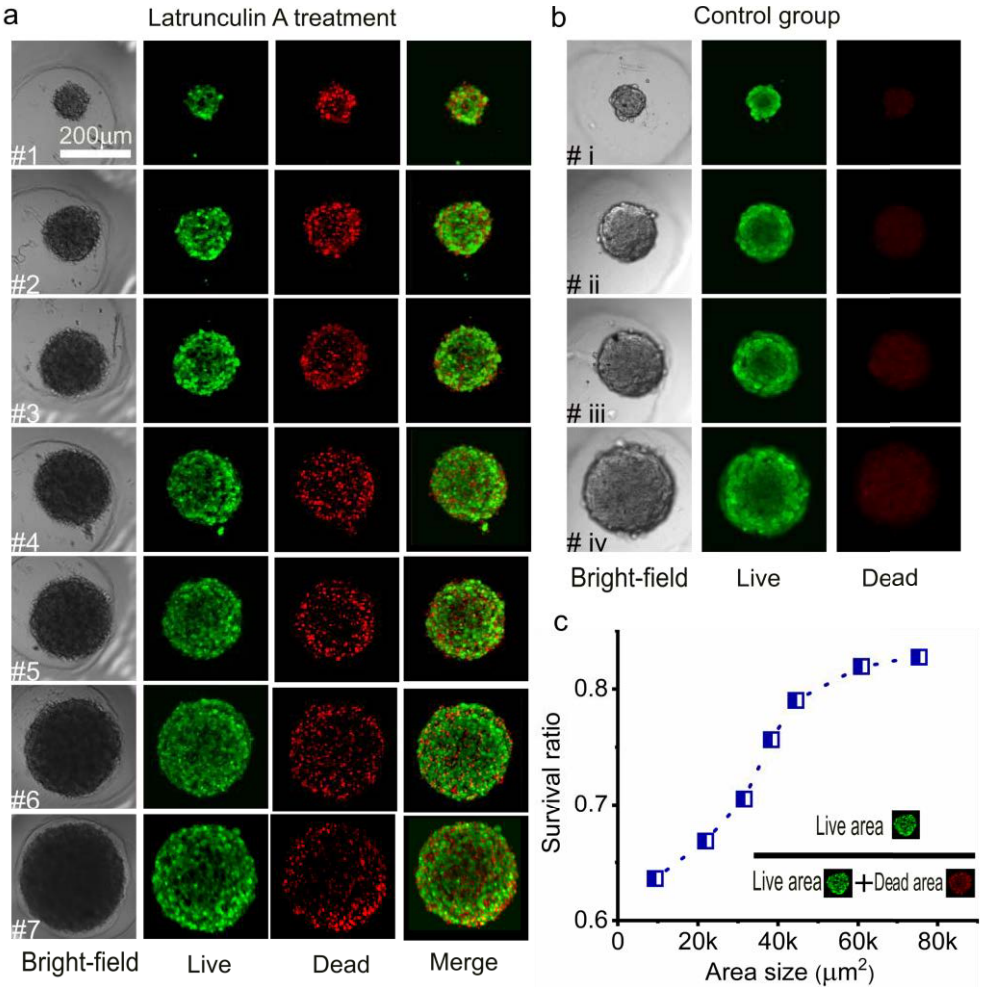

Figure 2–16 | Size-dependent cellular responses to latrunculin A in MCF-7 spheroids. (a) Cell viability in gradient-sized spheroids after the latrunculin A treatment for 72 h. (b) Cell viability in the control group. (c) Size-dependent survival ratios in spheroids. Survival ratio = live area / (live area + dead area) (scale bar = 200 μm).

excitation and emission as DOX, latrunculin A was used in this section. Latrunculin A blocks actin polymerisation by sequestering G-actin and preventing F-actin assembly. The 3-day-old spheroids were treated with 5μM concentration on the chip. After 3-day incubation, the viability of the spheroids on the chip was measured with confocal microscopy. It shows that the spheroids became turbid in the bright-field images (**Figure 2-16a**), compared with the control group (**Figure 2-16b**). The sizes of spheroids from #1–#7 ranged from 9.4k μm^2 to 75.4k μm^2, respectively. With the size increase, the area of red fluorescence decreased, indicating the higher cell viability in larger spheroids. We define the survival ratio as the ratio of the live area (green area) to live area + dead area (red area). It indicates that the survival ratio was around 60% in small spheroids after the latrunculin A treatment. With the size increase, the survival ratio increased, indicating that the larger spheroids had higher chemo-resistance than the smaller spheroids (**Figure 2-16b)**. Meanwhile, in the untreated control group, the spheroids remained high viability. The pale red fluorescence in the control group is the background of propidium iodide, which is difficult to be cleaned when they are used to stain the 3D tissues. It is confirmed that the anti-cancer drugs cannot effectively exert toxicity against slow-proliferating or quiescent cells which are more in larger spheroids. To our knowledge, this was the first to show the drug response in gradient-sized spheroids on a single chip.

2.5 Conclusions

In this study, a facile method was developed for gradient-sized tumour spheroid formation on a single chip. The liquid dome of cell suspension on the microwell array aligned on the chip, formed by the surface tension effect, could effectively control the liquid height, allowing a different number of cells to be deposited in the microwells. The distribution of the spheroid size on the chip followed the shape of the liquid dome and fit the simulation models of the domes. We show that the square liquid dome had more than 3-folds higher modulation ability than the round liquid dome. Using about 250 μL cell suspension (~1.2×10^6 cell) and one-step cell seeding, we can generate more than 200 gradient-sized spheroids on a single chip at once. The spheroids could be cultured on the chip for up to 7 days with less than 1% vacancy rate in the microwells. A microfluidic unit was introduced to dynamic irrigation and long-time culture. We further found the difference in growth rate in gradient-sized spheroids with or without dynamic irrigation. Co-culture was conducted on the microwell array, and the central tendency of fibroblasts

was first observed in the gradient-sized spheroids. Other cell types such as HUVECs can also be introduced into the spheroid co-culture. The size-dependent drug penetration and cellular responses in gradient-sized spheroids further indicated the effects of the spheroid size on drug treatment. In addition to cell lines, cells isolated from mouse tumour tissues have been used to form spheroids of gradient sizes. We believe that this facile and cost-effect method can provide a new approach for the size control of tumour spheroids, which will benefit the 3D *in vitro* tumour model development and the potential application in biomedical fields and translational personalised medicine.

Chapter 3 Unidirectional cellular communication on a microfluidic chip

Tumour microenvironment is supported by the communications with their neighbouring cells. Investigating the interactions between tumour spheroids and other cells helps to understand the mechanism of tumour development. Cell co-culture serves as a standard method to study intercellular communication. However, random diffusion of signal molecules during co-culture may arouse crosstalk among different types of cells and hide directive signal-target responses. Here, a microfluidic chip is proposed to study unidirectional intercellular communication by spatially controlling the flow of the signal molecules. The chip contains two separated chambers connected by two channels where the culture media flows oppositely. A zigzag signal-blocking channel is designed to study the function of a specific signal. The chip is applied to study the unidirectional communication between tumour spheroids and stromal cells. It shows that the expression of α-smooth muscle actin (a marker of CAF) of both MRC-5 fibroblasts and mesenchymal stem cells can be up-regulated only by the secreta from invasive MDA-MB-231 spheroids, but not from non-invasive MCF-7 spheroids. The proliferation of the tumour cells can be improved by the stromal cells. Moreover, transforming growth factor beta 1 is found as one of the main factors for CAF transformation via the signal-blocking function. The chip achieves unidirectional cell communication along X-axis, signal concentration gradient along Y-axis and 3D cell culture along Z-axis, which provides a useful tool for cell communication studies.

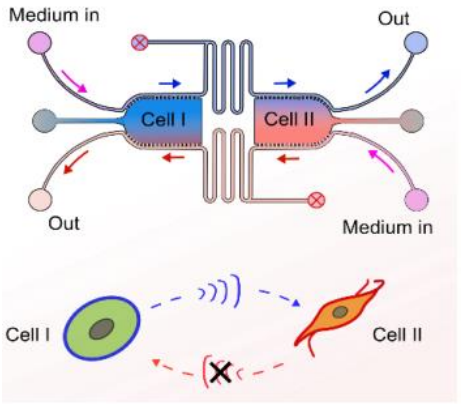

The contents of this chapter have been published in:

G. Fang *et al.*, Unidirectional intercellular communication on a microfluidic chip, *Biosensors and Bioelectronics*, 2020,175, 112833.

3.1 Background

Intercellular communication is crucial to coordinate cell behaviours and maintain cell functions in multicellular organisms[178]. Cells communicate by means of signal molecules through Signal-Target-Response activities[179]. These signals may include proteins, small peptides, amino acids, nucleotides, fatty acid derivatives, and even dissolved gases such as nitric oxide and carbon monoxide. Most of these signal molecules are secreted from the signalling cell and interact with the receptors in the target cell to trigger a response that alters the behaviour of the target cell[180].

There are two types of communications between cells: the direct communication between physically connected cells via gap junctions and the indirect communication between noncontacted cells via paracrine and hormonal secretion[179]. To study cell communications, cells are isolated from organisms and cultured *in vitro* so that specific signals can be tested and cellular responses can be measured [181]. Cell co-culture has been developed as a standard approach to study the communication between different types of cells. The current methods of cell co-culture can be divided into three major categories, as shown in **Figure 3-1**. The contact co-culture mixes different types of cells and cultures in the same culture vessel (**Figure 3-1a**). It offers physical contact between the cells. With this method, the population morphology of the cell may be lost, and it is difficult to identify whether the target cell receives signals via gap junctions or other receptors in the cell.

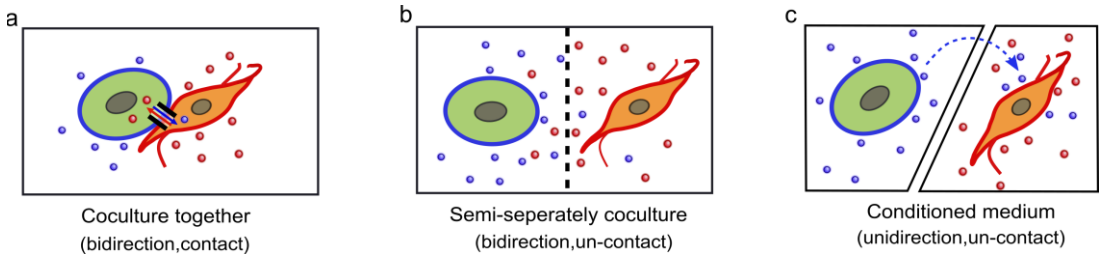

Figure 3–1 | Co-culture approaches to study the cellular communications. (a) Cell co-culture in the same vessel offers the bidirectional and contact communication. (b) Semi-separated co-culture offers bidirectional and noncontact communication. (c)Transferring the conditioned medium offers unidirectional and noncontact communication.

The semi-separate co-culture restricts cells in a separated space while enables commutation of signals in the culture media (**Figure 3-1b**). The most frequently used device is the cell culture inserts hanging in multi-well plates. Cells grow on the permeable

membrane of the inserts, separating from another type of cells grow in multi-well plates. At the same time, the signals from both cell types can be exchanged during culture. As the cells in the inserts cannot be visualized in a real-time fashion, interactive co-culture plates (ICCP) have also been developed with two horizontally arranged chambers that are separated by a permeable membrane[182, 183]. Microfluidic technology has been rapidly developed in the past decades and become a promising approach in biomedical research[114, 184]. The miniaturize microfluidic chips offers precise control of fluid, low consumption of reagents, high efficiency of analysis, and high throughput capacity[185-187]. Various chip-based methods have been applied to study cell communications [173, 188-190]. Generally, two or more chambers are fabricated on a chip; the chambers are semi-separated using physical barriers, such as flow channels, permeable membrane and hydrogels, which only allow the exchange of signal molecules but not cells [184, 186, 188, 191, 192]. For example, Zervantonakis et al. fabricated a microfluidic chip with three channels separated by physical barriers to study the communication of tumour cells and endothelial cells [190]. The tumour cells were mixed in 3D ECM hydrogel in the middle channel, and endothelial cells were monolayer cultured in one of the side channels. Jeong et al. co-cultured tumour spheroids and fibro-blasts in a collagen matrix-incorporated microfluidic chip to study the interaction between different cell types [173]. Recently, Yu et al. designed a kind of culturing modules that can be reconfigured together, holding potentials to be applied to study the communication of unlimited types of cells[189]. However, in the above methods, the exchange of signal molecules relies on passive diffusion, which cannot avoid the crosstalk of signals from both different cell types; the influenced and radically changed cells may, in turn, affect the secretor cells[193] . It may conceal the truth underlying mechanisms in intracellular communications.

Transferring of conditioned medium from one cell type to another provides a solution to avoid the crosstalk and interference of communication signals (**Figure 3-1c**). The advantages of conditioned 4 media include its simplicity in allowing for the detection of any soluble factor-related effects, along with the potential for subsequent identification of these factors in the co-culture media [194]. However, as the conditioned media are collected and then transferred, the signals may suffer a loss of bioactivities and compromised nutrient supply.

In this study, we report a microfluidic-chip-based cell co-culture method to study unidirectional intercellular communication. The chip consists of two separated chambers and two surrounded medium channels. Two types of cells mixed in Matrigel can be loaded into different chambers, respectively. The flow directions of the medium in the two channels were set as the opposite. The signal molecules secreted from each chamber can enter the channel and flow to the opposite chamber. Thus, we can monitor the unidirectional communication between the cells due to the flow control. Besides, due to the matter of diffusion, there will be a concentration gradient of the signal molecules vertically. Moreover, another advantage of the unidirectional chip is the real-time analysis of the functional signals with the signal-blocking inlet. For instance, when one wants to know the function of Signal I, the related blocking agents could be introduced in the channels. The agents will interact with the Signal I in the zigzag mixing channel, then block their functions before reaching another cell culture chamber. Amongst various cell types within the tumour microenvironment, CAFs are in abundance, serving to modulate the behaviours of cancer cells in progression [195-199]. Little is yet known about how cancer cells transform normal stromal cells into CAFs[200]. It is not clear whether direct contact with cancer cells is necessary for the transformation of CAFs. Several growth factors and cytokines have been reported to transform 5 normal stromal cells into CAFs [197, 198]. At the same time, CAFs also secret various signal molecules to regulate cancer cells. With the previously reported methods, it is challenging to reveal the unidirectional influence from one cell type to another. Thus, a reductionist approach is desired to study the unidirectional interaction between stromal cells and tumour cells. In this work, we used the microfluidic chip to study the unidirectional communication of breast cancer cells (invasive MDA-MB-231 and non-invasive MCF-7 cells) and stromal cells (MRC-5 fibroblasts and MSCs). We observed the growth and spheroid formation of cancer cells and the transformation of MRC-5 and MSCs into myofibroblasts-like cells. We also used an antibody against transforming growth factor beta 1 (TGF-β1) to demonstrate the function of the signal blocking inlet as TGF-β1 secreted from cancer cells have been reported to induce the formation of CAFs.

3.2 Aims and approaches

We aim to achieve the unidirectional cellular communication with the advantages of microfluidic chip, to avoid the cellular crosstalk effect. The proposed microfluidic chip

consists of two separated half-ellipse shaped chambers, as shown in **Figure 3-2a**. Each chamber has an inlet, which is used for cell loading. The thickness of the chamber is designed as 125 μm, and the width of the inlet channel is about 350 μm. The chambers are surrounded by two channels of 250 μm width for medium flow. The chambers and channels are semi-separated by physical barriers. The channels also connect the two chambers by a zigzag-shaped part. As shown in **Figure 3-2b**, two types of cells are mixed in Matrigel separately and then injected into the left and right chambers, respectively. Due to the barriers between the chambers and the channels, the Matrigel will be restrained within the chamber area. Cell culture medium flows in the channels, and the flow directions are opposite, as shown by the black arrows. Due to the Matrigel and the physical barriers, the medium could only flow along the channels. The nutrition and oxygen in the medium can diffuse into the Matrigel through the gap between the barriers. The blocking agent inlets are closed unless we evaluate the function of signal molecules and their targets.

The working mechanism of the unidirectional chip is shown in **Figure 3-2c**. The Signal I secreted by Cells I from the left chamber can diffuse into the medium channel and flow with the medium. When they arrive the channel around the right chamber, the Signal I molecules will diffuse into the matrix through the gaps between the barriers, and then target Cells II. We could imagine that the closer to the top channel, the larger the concentration of the signal molecules is. It will form a vertical concentration gradient of the Signal I in the right chamber. At the bottom of the right chamber, there is an area containing almost no Signal I molecules. Similarly, Signal II molecules secreted by the Cells II in the right chamber will flow into the left chamber, form a concentration gradient and then work on the Cells I. The flow direction enables the unidirectional communication that the Cells I could only be influenced by the original type of the cells II and thus avoids the interference from the affected Cells II.

Moreover, compared to the conditioned medium, the continuous flow can supply the signalling factors in a steady and homogeneous way. The conditioned medium would degrade after adding to the cells, leading to a decreased concentration of the signalling factors. Additionally, the conditioned medium is usually used with the normal medium, which may cause different concentrations of nutrition. The on-chip continuous flow in our design can completely avoid this issue and ensure the same nutrition concentration.

This design also avoids the waste of factors during the collection of conditioned medium (centrifugation, filtration), especially the physical destruction.

The chip can achieve the unidirectional communication of cells along X-axis, the concentration gradient along Y-axis and 3D cell culture along Z-axis. Owning to the nature of the microfluidic device, it can significantly reduce the consumption of cells, medium and reagents as well as facilitate the observation of cell responses. Also, another advantage of our unidirectional chip is the real-time analysis of the functional signals with the signal-blocking inlet, as shown in **Figure 3-2d**. For instance, if we want to know the function of Signal I, the related blocking agents could be introduced in the channels. The agents will interact with the Signal I in the zigzag mixing channel, then block their functions when they reach another cell culture chamber.

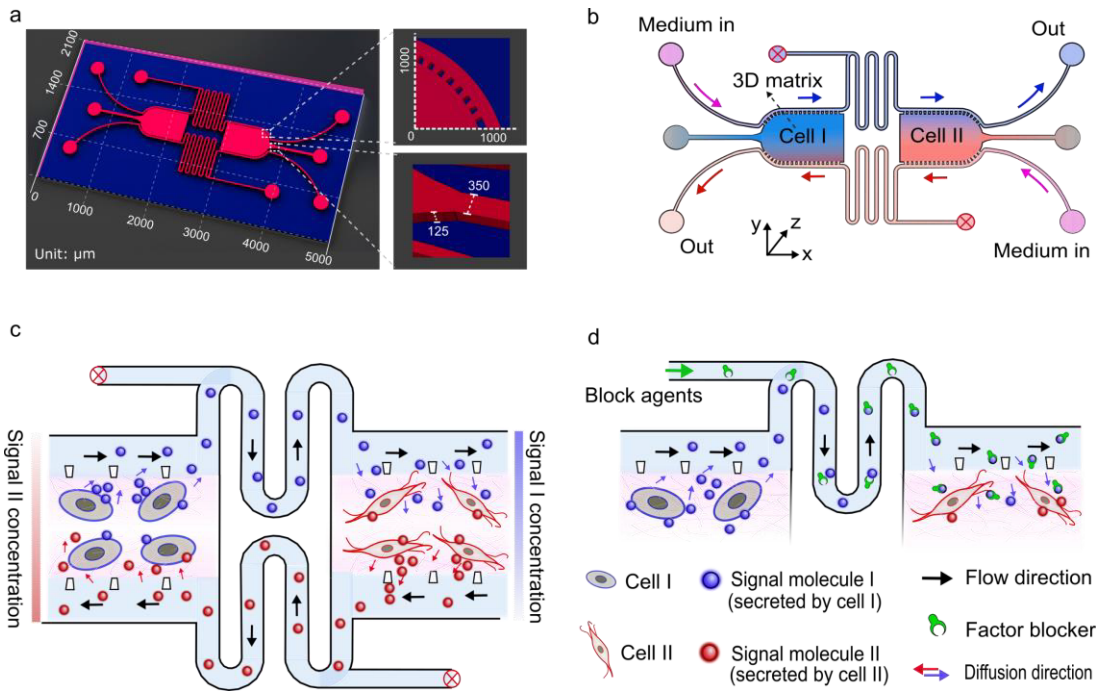

Figure 3–2 | Mechanism of the unidirectional cellular communication on the microfluidic chip. (a) Design of the unidirectional microfluidic chip. (b) Schematic is showing how the chip works during co-culture. Different types of cells are cultured in the left and right chambers with Matrigel, respectively. The black arrows show the flow directions of the cell culture media in the channels. The signal-blocking inlets are close unless a specific signal is being neutralized. (c) Detailed working mechanisms of the unidirectional communication chip. Due to the matter of diffusion, there is a concentration gradient of signal molecules along Y-axis. (d) Detailed working mechanisms for signal-blocking studies.

3.3 Materials and methods

3.3.1 Chip fabrication

The design of the microfluidic device was shown in **Figure 3-2a** and **Figure 3-3a**. The device was fabricated with PDMS (Sylgard® 184, Sigma Aldrich) by replicate mould on a SU8-2075 silicon master. Firstly, a 4-inch silicon wafer was cleaned using isopropanol and then heated in an oven at 150ºC for 20 min. The SU8-2075 was spin-coated on the wafer at 1,250 rpm for 30 s, which was followed by soft bake at 65 ºC for 5 min and 95 ºC for 25 min. The thickness of the SU8-2075 layer was around 125 µm. Then the SU8-2075 wafer was exposed under a laser scanning lithographer (µPG 101, Heidelberg Instruments, Germany) to generate patterns designed with CAD software. After the exposure, the wafer was incubated at 65 ºC for 5 min and 95 ºC for 30 min followed by a

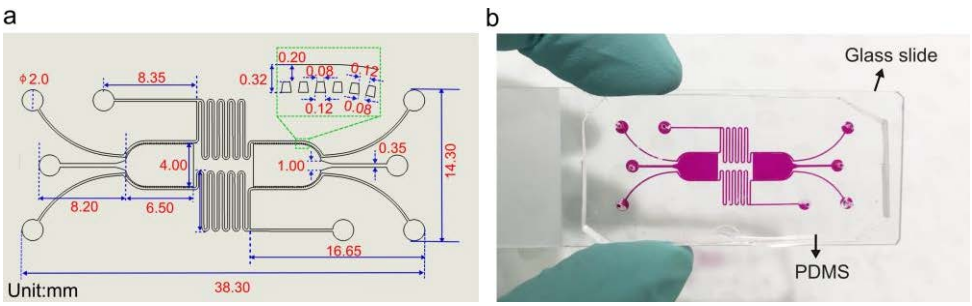

Figure 3–3 | Chip design and its image. (a) Parameters of the designed chip. (b) Image of the fabricated PDMS chip.

development process for 30 min at room temperature. Finally, the SU8-2075 master was treated with a process called hard bake at 150 ºC for 30 min. Once the master was prepared, PDMS was mixed thoroughly with the curing agent at a weight ratio of 10:1. Then the PDMS was poured on the master mould and heated in the oven at 80 ºC for 2 hr. After the solidification, the PDMS was gently peeled off from the mould and trimmed with a scalpel. Then the inlets and outlets on the PDMS were punched with an Ø1mm puncher. The thickness of the PDMS was 5 mm. Finally, the PDMS piece was firmly bound to 1.2-mm thick glass slides after plasma treatment for 1min, which was followed by heating at 80 ºC for 2 hr. Before cell seeding, the chips were laid aside for 24 hr to reduce the hydrophilicity induced by the plasma treatment.

The whole chip is 38.30 × 14.30 mm (length × width) in dimension. There are two cell chambers with a length of 6.50 mm and a width of 4.00 mm. The chamber is surrounded

by two channels with a width of 200 μm. There are trapezoidal barriers between the chambers and the channels, with the top line of 80 μm, the baseline of 120 μm and the gap of around 100 μm. The distance can trap the Matrigel inside the chambers without leaking into the channel during the Matrigel loading process. In front of each chamber is the loading channels with a width of 350 μm. The width of the junction around the channel and the chamber is increased to 1.00 mm, one-fourth of the chamber width. This design can guide the flow of Matrigel and avoid the generation of air bubbles during gel loading. Between the two chambers is the mixing channels with a width of 200 μm. The total length of the mixing channel is designed as 66 mm, which can offer about 22 min for the reaction between target molecules and blocking agents at a flow speed of 50 $\mu m \cdot s^{-1}$. If we slow the flow speed, the reaction time could reach a few hours, which is depended on the research targets. The PDMS chip bonded on the glass slide is shown in **Figure 3-3b**.

3.3.2 **Cell Signal molecule diffusion in the chamber**

We used several fluorophores with different sizes to verify the diffusion of signal molecules and the formation of concentration gradients. The experiment was observed under a laser-scanning confocal microscope, as shown in **Figure 3-4a**. The fluorophores dissolved in PBS was introduced into one channel of the Matrigel-loaded chip, and blank PBS was introduced into the opposite channel. The flow directions were set as opposite, and the flowing rate was set about 50 $\mu m\ s^{-1}$. First, we used the Cy5-labelled anti-rabbit antibody, which has a molecule weight of around 150 kDa, as a model of protein diffusion. The diffusion was profiled at 20 min, 6 hr and 24 hr, respectively, as shown in **Figure 3-4b**. The fluorescence intensity was quantified by ImageJ. We could see that the proteins were mainly distributed in the channel at the beginning of injection. After 6 hr, the proteins diffused into the Matrigel towards the opposite channel, and the fluorescence intensity in the middle area reached 20%. The fluorescent curvy showed a slightly concave shape. After 24 hr, the fluorescent distribution curve became straight. The fluorescence intensity in the middle area reached around 40%. The fluorescence illustrated the formation of concentration gradient of proteins. The fluorescence distribution in the whole chamber was profiled after 24 hr, as shown in **Figure 3-4c**. A 3D illustration of the intensity for the concentration gradient was shown in **Figure 3-4d**.

The diffusion of doxorubicin (molar mass: 543.52 g mol^{-1}) was also investigated with the same method described above. As shown in **Figure 3-4e**, at 20 min, doxorubicin diffused over about 500 μm in the Matrigel. After 6 hr, weak fluorescence reached the opposite side of the Matrigel. Differently, the fluorescence intensity near the physical barrier was stronger than that in the flow channel, which means that the doxorubicin accumulated in the edge of the Matrigel. After 24 hr, the red fluorescence fulfilled the whole chamber with a concentration gradient. The fluorescence intensity of the middle area reached around 60% of that at the edge.

Poly (N-(2-hydroxypropyl)methacrylamid) (PHPMA) -based micelles have been used as nanocarriers to deliver anticancer agents . Here, the PHPMA micelles labelled with fluorescence are used to model the diffusion efficiency of nanosized vesicles. The structure of the PHPMA micelle is shown in **Figure 3-4g**. The average size of the micelles

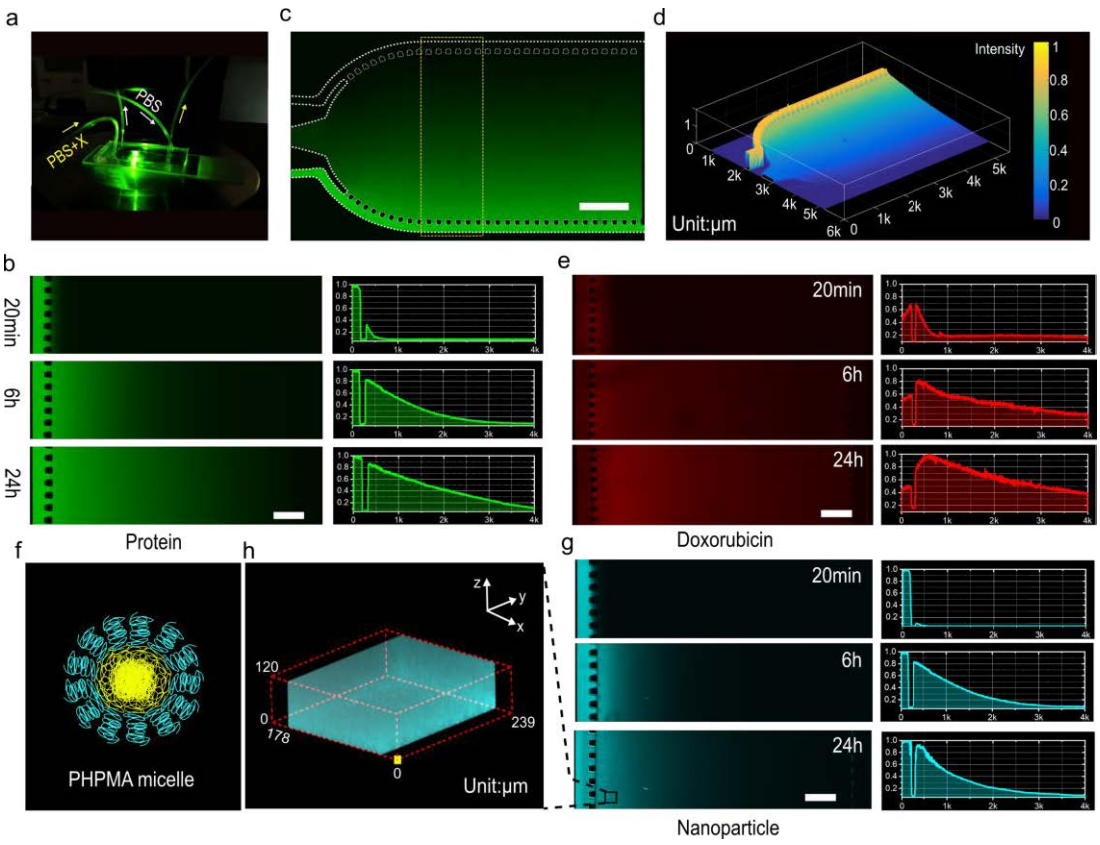

Figure 3–4 | Molecule diffusion on the chip. (a) Experimental setup under the confocal microscope. (b) Diffusion of antibody (immunoglobulin, large molecule) in the Matrigel on the chip. (c) Protein distribution in one chamber after 24h. (d) 3D illustration of the protein concentration in the chamber after 24h. (e) Doxorubicin (small molecule) distribution in the Matrigel on the chip. (f) Structure of the PHPMA micelle. (g) PHPMA micelles distribution in the Matrigel on the chip. (h) Enlarged 3D view of the distribution of PHPMA micelles in the Matrigel.

was 15 nm measured by dynamic light scattering. As shown in **Figure 3-4h**, the nanoparticles diffused little into the Matrigel after 20 min. After 6 hr, the nanoparticles gradually diffused into the Matrigel. The fluorescence intensity of the middle area reached only around 18% with the intensity curvy being a little concave. After 24 hrs, the fluorescence near the flow channel was enhanced. However, the fluorescence far away from the flow channel only changed slightly. The intensity curvy became more concave than the beginning. The results show that the distribution of the nanoparticle concentration was also gradient. To test the cross talk among signal 1 and signal 2, we introduced the IgG and Doxorubicin in the opposite channels simultaneously, the IgG and Doxorubicin gradients can be formed on the chip at the same time. This indicated that Signal 1 and Signal 2 on the chip do not cross on the chip. Compared to the three molecules, the result shows a size-dependent diffusion pattern in the Matrigel, indicating that the chip allows intercellular communication via the molecule diffusion through Matrigel, and can effectively avoid the crosstalk among the opposite cells.

3.3.3 **Cell culture and cell seeding**

Human breast carcinoma cell, MDA-MB-231 and MCF-7, and lung fibroblasts MRC-5

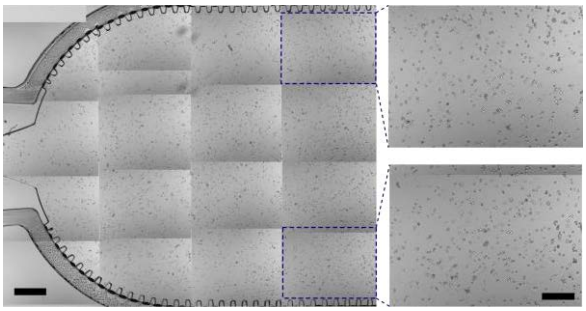

Figure 3–5 | Cell distribution after cell seeding. (left image, scale bar: 1 mm) and enlarged views (right two images, scale bar: 200 μm).

from Australia Cell Bank were cultured with DMEM medium with 10% FBS and 100 U/mL penicillin/streptomycin (Life Technologies, Australia) in 25 mm2 flasks. Human bone marrow MSCs were purchased from Merck Australia and cultured with Stemline® mesenchymal stem cell expansion medium (Sigma Aldrich, Australia) in 25mm_2 flasks. The cells were incubated in an incubator with 5% CO_2 at 37 °C and passaged once they reached 70~80% confluence.

To collect cell suspension, the cells were treated with Trypsin-EDTA solution for 3 min, followed by centrifugation for 5 min at 500 ×g. After removing the supernatant, the cells

were re-suspended in 75 μL Matrigel (Corning, USA) by pipetting at a density of 1×10^6 cells mL^{-1}. The 75 μL Matrigel allowed loading of three chambers, which means that a chip with two chambers only needs 50 μL Matrigel. The whole process was operated on the ice, avoiding the gelation of the Matrigel. The chips were sterilized under UV for 30 min before the cell seeding. Then the Matrigel containing cells were loaded gently into the culture chambers in the middle of the chip with 1 mL syringes.

Due to the surface tension effect around the barriers, the Matrigel could only fulfil the chambers but without any leakage into the medium flow channels. To ensure the uniform distribution of cells in the chamber, we should mix the cells with Matrigel well. The cell distribution was mapped and shown in **Figure 3-5**. After the cell seeding, the chips were put in the incubator for 30 min to allow gelation of the Matrigel. The chip was then connected to 3 mL medium containing syringes through polyethylene tubing (outer Ø of 1 mm and inner Ø of 0.8 mm). A syringe pump (11 Elite, Harvard Apparatus) was used to control the injection volume at $1\mu L\cdot min^{-1}$, which resulted in a flow speed in the channels at 50 $\mu m\cdot s^{-1}$. The flow directions were set opposite to allow unidirectional communication of signal molecules and nutrition supply.

3.3.4 **Characterization of cell response**

To quantify the MDA-MB-231 and MCF-7 cells on the chip, we used the Hoechst 33342 and Orange CMRA Cell Tracker (Life technologies) to stain cell nuclei and membrane, respectively. Firstly, the cells were fixed with 100 μL 4% phosphate-buffered paraformaldehyde for 1 hr on the chip. Then the staining solution of Hoechst 33342 (10 ng mL^{-1}) and Orange CMRA CellTracker (1:1000 dilution) in PBS was perfused for 3 hrs. PBS was used to wash the chip to remove unbound dyes. The cells were then observed under the confocal microscopy.

To evaluate the induction of CAFs, we measured the expression of α-smooth muscle actin (α-SMA) by immunofluorescence staining. The cells were first fixed with 4% paraformaldehyde on the chip for 1hr. To accelerate the staining and washing process, we then used a scalpel to separate the PDMS piece from the glass slide. The Matrigel and cells were kept in the PDMS chamber, and we directly stained the cells on the PDMS. The cells in the Matrigel were treated with 1% Triton X-100 for 1 hr, followed by washing with PBS three times. Then cells were blocked with 5% bovine serum albumin

(BSA)/PBS solution at 37°C for 1 hr before the anti α-SMA antibody (Sigma Aldrich) (1:100 dilution in 0.1% BSA/PBS) was applied to the cells for 1 hr. After washing with PBS thrice, the cells were immersed in the Cy5-labelled second antibody solution (1:100 dilution in 0.1% BSA/PBS) at 37 °C for 1 hr. The antibody was dissolved in the 0.1% BAS PBS solution. The cells were then observed under microscopy.

3.4 Results and discussion

3.4.1 MDA-MB-231 and MCF-7 spheroids are different to influence stromal cell

The tumour tissue consists of tumour cells and stromal cells, such as the normal fibroblasts, CAFs, vascular cells, and some resident immune cells. The communication between the tumour cells and the stromal cells are critical to regulating tumour cell responses to the treatment. CAF is a heterogeneous population of dynamically varied from mesenchymal cells with functions that are likely different from those of resident fibroblasts[197, 198]. They are abundant in the tumour, which could help to stimulate the angiogenesis, support the formation, proliferation, and metastasis of the tumour. The origin of CAFs is debated; however, it is commonly believed that they are the communication product of tumour and more than one precursor cells[201]. The normal fibroblasts are an attractive candidate. In this study, we studied the unidirectional communication between breast tumour cells and normal fibroblast. The cells were loaded into the chambers separately and cultured on the chip.

Here we co-cultured MRC-5 fibroblasts with invasive MDA-MB-231 or non-invasive MCF-7 breast tumour cells. After three days' co-culture, we measured the growth of tumour cells as well as the morphology and the expression of α -SMA of fibroblasts. As shown in **Figure 3-6 a&b**, during the culture, the influenced MDA-MB-231 formed more spheroids with a larger size, compared to the uninfluenced MDA-MB-231. This indicates that the secrets from the MRC-5 fibroblasts could increase the growth of the MDA-MB-231 cells even without direct contact. As shown in **Figure 3-6 c&d**, the MRC-5 fibroblasts also enhanced the growth of MCF-7 cells under unidirectional communication. The 3D profile of MDA-MB-231 and MCF-7 cells in the left chamber demonstrated that the MRC-5 fibroblasts enhanced the tumour growth (**Figure 3-7**). We measured the size distribution of the spheroids (**Figure 3-6e**), which shows that for the growth stimulation effects on MDA-MB-231 and MCF-7 by the fibroblasts was evident in most groups.

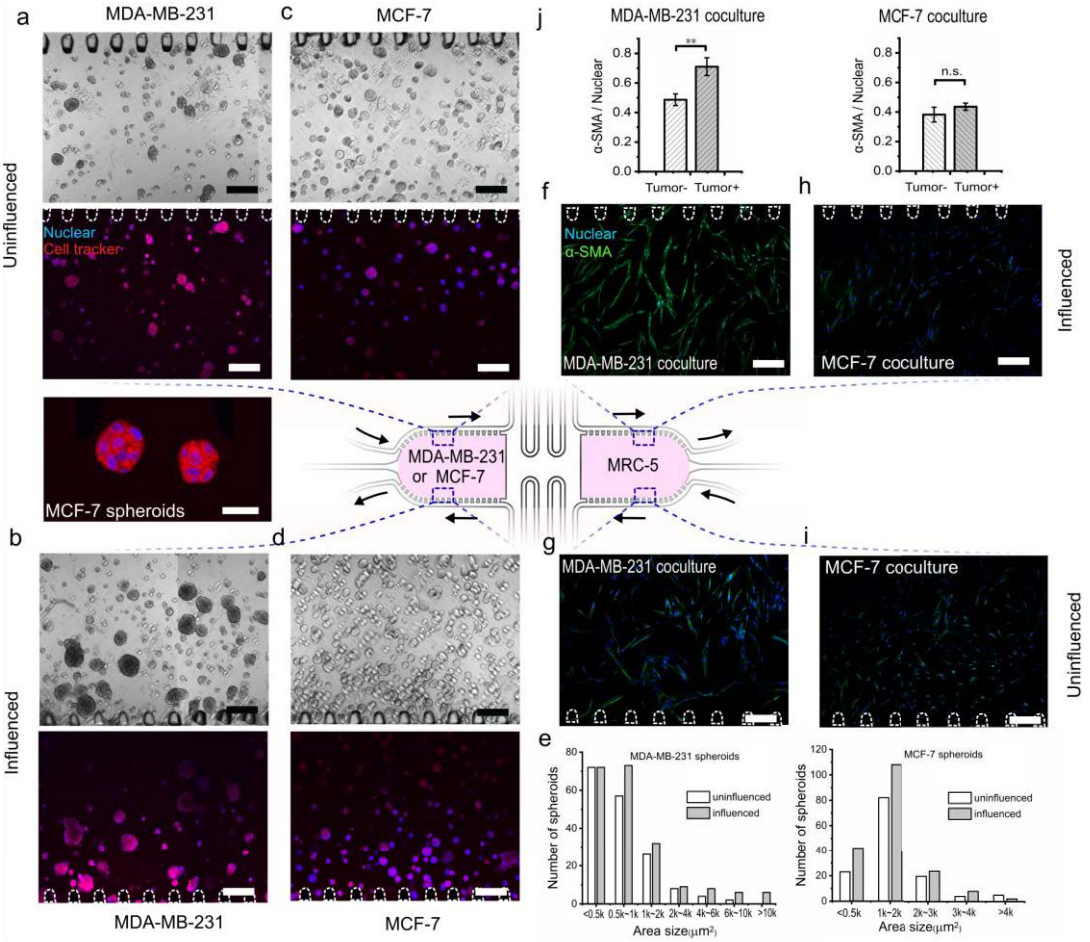

Figure 3–6 | Unidirectional communication between MRC-5 fibroblasts and MDA-MB-231 or MCF-7 cells. (a) MDA-MB-231 cells without the influence from MRC-5 fibroblasts. Upper and lower are the bright-field and fluorescent images, respectively. (b) MDA-MB-231 cells with the influence from MRC-5 fibroblasts. Upper and lower are the fluorescent and bright-field images, respectively (c) MCF-7 cells without the influence from MRC-5 fibroblasts. Upper and lower are the bright-field and fluorescent images. Scale bar: 200μm. The insert is the MCF-7 spheroids under a 60× objective lens. (d) MCF-7 cells with the influence from MRC-5 fibroblasts. (e) The number of MDA-MB-231 and MCF-7 spheroids with or without the influence from MRC-5 fibroblasts. (f) & (g) α-SMA expression of the MRC-5 fibroblasts influenced or uninfluenced by MDA-MB-231 cells, respectively. (h)&(i) α-SMA expression of the MRC-5 fibroblasts influenced or uninfluenced by MCF-7 cells, respectively. (j) The ratio of fluorescence of α-SMA to cell nuclei in MRC-5. Data present as means ± SD. **, statistical difference, $p < 0.01$. n.s., no statistical difference, $p > 0.05$. Scale bar = 50 μm (the insert) or 200μm (the others).

Differently, the MDA-MB-231 cells formed fewer and smaller spheroids compared with MCF-7 cells. Size of the spheroids refers to their projected area.

On the other hand, we observed high expression of α-SMA of MRC-5 fibroblast induced by the secrets of MDA-MB-231 cells (**Figure 3-6 f&g**). We quantified the expression of α-SMA by using the fluorescence ratio of α-SMA to cell nuclei (**Figure 3-6j**) [173]. The ratio of the influenced fibroblasts was around 1.4-folds compared to the uninfluenced

fibroblasts when cocultured with the MDA-MB-231 (statistically different, $p < 0.01$). When co-cultured with the MCF7, the MCR-5 fibroblasts showed no obvious difference in the expression of α-SMA, as shown in **Figure 3-6 h&i**. The ratios of α-SMA/cell nuclei on both sides were almost the same in the coculture with the MCF-7 cells ($p > 0.05$). It indicates that the secreta of MDA-MB-231 cells could effectively turn the MRC-5 fibroblasts into CAFs, compared to the MCF-7 cells. Thus, it can be concluded that the transformation of normal fibroblasts into CAFs-like cells can be induced by tumour cells via unidirectional communication.

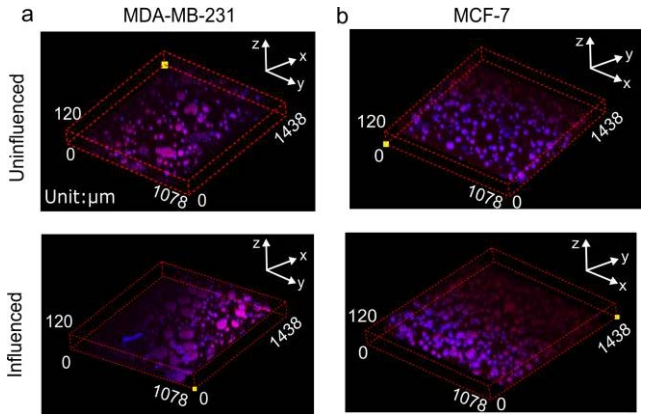

Figure 3–7 | 3D profile of MDA-MB-231 and MCF-7 spheroids that were either influenced or uninfluenced by MRC-5 fibroblasts. (a) MDA-MB-231 spheroids; (b) MCF-7 spheroids.

3.4.2 Unidirectional communication of MDA-MB-231 and MSCs

MSCs have been widely used as an important cell source for regenerative medicine due to the pluripotent differentiation, diverse sources, easy separation and amplification [173, 202]. Moreover, MSCs display tropism to inflammation and malignant tumours and tend to migrate towards areas of wound healing or tumour growth[203-206]. So far, many studies have utilized MSCs to delivery drugs or nanomedicines into tumours, synergistic with chemotherapy, photothermal therapy, and photodynamic therapy for tumour theranostics[203, 205]. As an essential type of tumour stromal cells, MSCs are also a top candidate of the CAFs [207].

As shown in **Figure 3-8**, we characterized both the tumour cells and MSCs after three days' unidirectional communication on the chip. The fluorescence and bright-field images of the MDA-MB-231 cells on the uninfluenced & influenced side were shown in **Figure 3-8 a&b**, respectively. It was found that the MDA-MB-231 proliferated faster and formed larger spheroid on the influenced side than did on the uninfluenced side; while

the density of the spheroids was opposite. The tumour spheroids under a 60 × objective lens were also shown in the insert of **Figure 3-8**. To better illustrate the difference, the 3D morphologies of the tumour spheroids on the two sides were analysed, as illustrated in **Figure 3-8c**. Although there were also many spheroids around the barriers on the uninfluenced side, the whole density of the spheroids was lower than that on the influenced side (**Figure 3-8c**). The area size of the spheroids was analysed by ImageJ and shown in **Figure 3-8d**. The number of spheroids on the influenced side was higher than that on the uninfluenced side. The project area of some spheroids was even larger than 5k μm^2 affected by the secreta from MSCs. In addition, we co-cultured MSCs and MDA-

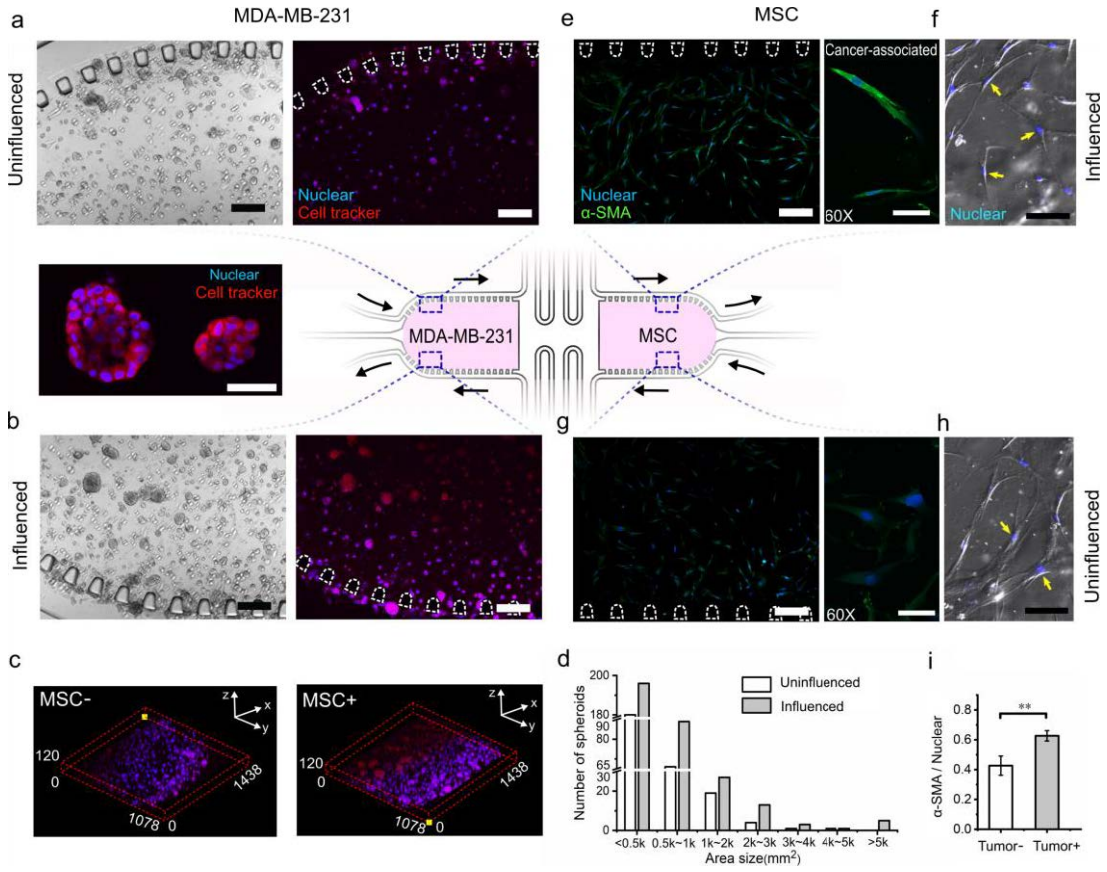

Figure 3–8 | Unidirectional communication between MSCs and MDA-MB-231 cells. (a) MDA-MB-231 cells without the influence from MSCs. Left and right are the bright-field and fluorescent images, respectively. Scale bar: 200μm. Inset is the MDA-MB-231 breast tumour spheroids under a 60× objective lens. Scale bar: 50μm (b) MDA-MB-231 cells with the influence from MSCs. Scale bar: 200μm. (c) 3D profile of the MDA-MB-231 cells without & with the influence from MSCs. (d) The number of spheroids without & with the influence from MSCs. (e) α-SMA expression of the influenced MSCs (scale bar: 200μm) and the typical α-SMA expression under a 60× objective lens (scale bar: 50μm). (g) α-SMA expression of the influenced MSCs. Scale bar: 200 μm and the typical α-SMA expression under a 60× objective lens. Scale bar: 50μm. (f) & (h) Morphology of the typical MSC on the influenced side & on the uninfluenced side in the Matrigel. Scale bar: 50μm. (i) Fluorescence ratio of α-SMA to cell nuclei. Data present as means ± SD. **, significant difference, $p < 0.01$.

MB-231 cells with the same flow direction (**Figure 3-9a**). The results show that the two sides of MDA-MB-231 cells influenced by MSCs showed no obvious difference, indicating that even normal MSCs have evident impacts on tumour cells.

Then we measured the expression of α-SMA in MSCs with immunofluorescent staining, as shown in **Figure 3-8 e&g**. Compared to the uninfluenced side, the influenced MSCs showed a brighter fluorescence, indicating a higher α-SMA expression. We also observed the changes in cell morphology. The MSCs with high α-SMA expression tend to show an elongated spindle shape, which is also observed in the bright-field images (**Figure 3-8 f&h**). To quantify the fluorescence of α-SMA, we used the average fluorescence ratio of α-SMA to Hoechst 33342 stained cell nuclei (**Figure 3-8i**). We found that the ratio of MSCs on the influenced side is around 1.5-fold higher than that on the uninfluenced side (statistically different, $p < 0.01$). We mono-cultured the MSCs on the chip as the control group (**Figure 3-9b**). It showed that the α-SMA fluorescence of monocultured MSCs was similar to that of uninfluenced MSCs. They did not present an apparent elongated shape. Thus, the secreted signal molecules of MDA-MB-231 cells up-regulated the expression of α-SMA, which indicates the induction of MSC to CAF-like cells even without direct contact. Both MSCs and MRC-5 fibroblasts are potential sources of CAFs in solid tumours.

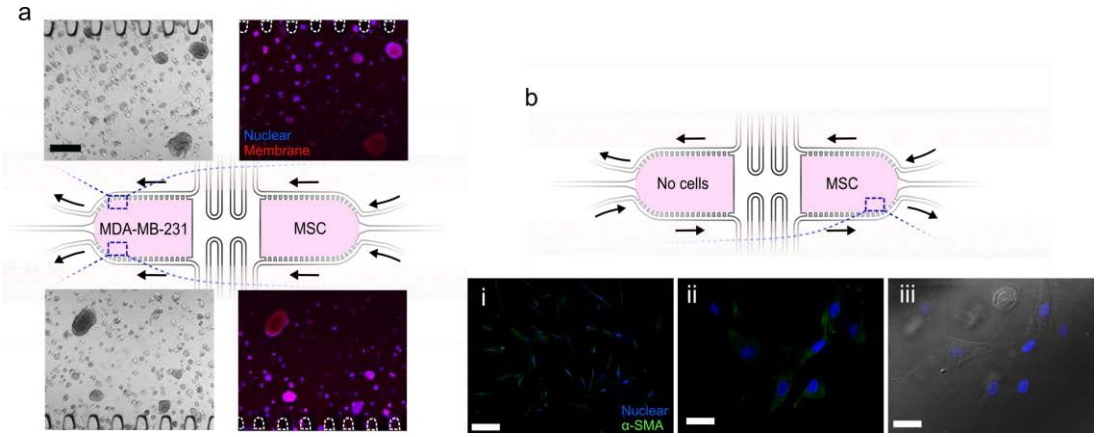

Figure 3–9 | Control experiments. (a) Co-culture MDA-MB-231 spheroids and MSCs with the same flow direction. (b) Mono-culture MSCs on the chip.

3.4.3 TGF-β1 secreted from MAD-MB-231 cells induced MRC-5 fibroblasts into CAFs

It has been reported that the TGF-β1 secreted by the tumour cells could induce fibroblasts transferring into CAFs[208]. Here, we used the blocking channel to verify the role of TGF-β1 on this proposed chip. As shown in **Figure 3-10a**, MDA-MB-231 cells and MRC-5 fibroblasts were seeded on the left and right chambers, respectively. The flow speed was set as 0.5 μL min^{-1} at each inlet. The antibody of TGF-β1 at a concentration of 10 ng mL^{-1} was introduced into the top blocking channel with the cell culture medium. The flow speed was set as 0.5 μL min^{-1}, which ensures around 20 min for the neutralization of TFG-β1 with the antibody before it reached the fibroblast culture chamber. Medium with the antibody was introduced into the bottom blocking channel as a control. As shown in **Figure 3-10b**, we hypothesized that if the TGF-β1 was blocked by the antibody, it could not transfer MCR-5 into CAF-like cells. After three days' culture, we found that the expression of α-SMA of the influenced MRC-5 was not statistically different from the uninfluenced MRC-5 (bottom area) **Figure 3-10 c&d**. The ratio of α-

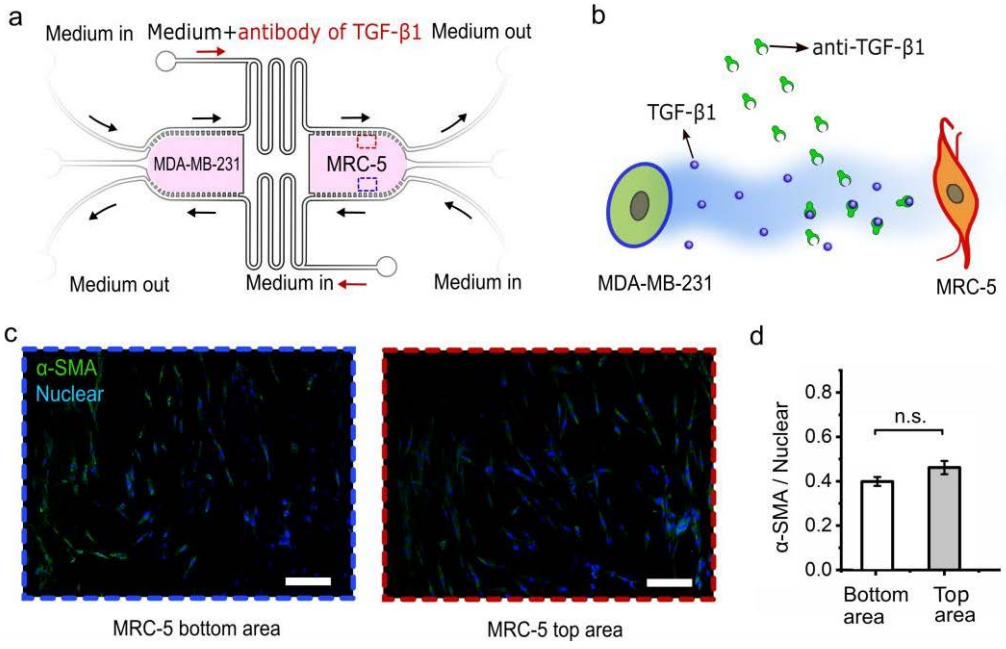

Figure 3–10 | Injection of TGF-β1 antibodies through the blocking channel ceased the transformation of MCR-5 fibroblasts into CAFs-like cells. (a) The setup of using signal blocking inlet on the chip to study the effects of TGF-β1. (b) The schematic of using the antibody of TGF-β1 to block its function to MRC-5. (c) α-SMA expression of the MRC-5 on the bottom area (Left, without the influence from MDA-MB-231 cells) and on the top area (Right, with the influence from MDA-MB-231 cell with the TGF-β1 antibody). (d) Fluorescence ratio of α-SMA to nuclei of MRC-5 cells in the right chamber. Data present as means ± SD. n.s., no statistical difference, $p > 0.05$.

SMA/Nuclei was 0.42 ± 0.02 was also much lower than the ratio of unblocked MRC-5 cells at 0.71 ± 0.06 in Fig. 3E. These results indicate that the TGF-β1 secreted by the tumour cells is one of the driven forces to turn the normal fibroblasts into CAFs. The blocking channels on the chip functioned adequately, which could simplify the biological experiments and reduce the system errors.

3.4.4 **Discussion**

Microfluidic devices have been attracting more attention from biomedical researchers[199, 209, 210]. The microfluidic chips enable real-time monitoring, provide excellent visualization, reduce sample and reagent usage, control the chemical concentration gradients, and enhance cell responses through restrained culture space, which could reduce the consumption of cells, medium and some expensive agents. Many microfluidic devices have been used to study intercellular communications [211, 212], especially between tumour cells and stromal cells [213]. For example, Rahman et al. evaluated intercellular communication between breast cancer cells and adipose-derived stem cells via passive diffusion in a two-layer microfluidic device [214]. A similar design was utilized to study the interactions between A549 lung cancer cells and vascular endothelial cells during treatment with exosome encapsulating microRNA[191]. Under 3D microenvironment, the cells in 3D can better reflect the reality of cells in the body [47]. Seok et al. fabricated three on-chip channels which were connected by collagen scaffolds[215]. One cell type was seeded in the middle channel, and the medium or the other types of cells were introduced into the side channels. Fang et al. investigated the communication of tumour cells with fibroblasts and vascular endothelial cells in gradient-sized 3D spheroids on agarose chips[62]. Truong et al. developed a 3D organotypic microfluidic platform, integrated with hydrogel-based biomaterials, to mimic the vascular niche of glioma stem cells and study the influence of endothelial cells on patient-derived glioma stem cells and identify signalling cues that mediate their invasion and phenotype [209]. Furthermore, other methods were proposed using the microfluidic such as the droplet co-culture[121, 216-218], micro-Boden chamber[219], and communication in single-cell level[219]. However, the above reported methods co-culture the cells without considering the direction of signal transfer. In this work we provide a new approach of cell co-culture with unidirectional transfer of signal molecules to clear the details of the

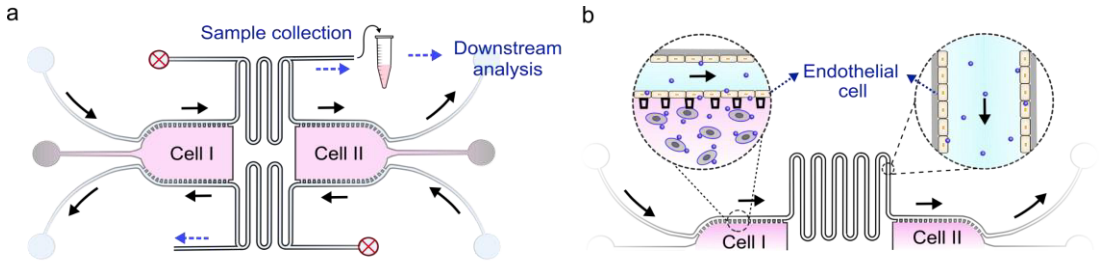

Figure 3–11 | Potential extension of the unidirectional microfluidic chip. (a) An outlet in the middle channel may provide connections to further analysis of signals, such as exosomes. (b) The unidirectional microfluidic chips may be tailored to mimic the endocrine communication.

intercellular communication. The special design could control the signal direction and provide a 3D microenvironment for cells to study the Signal-Target-Response pathway.

The tumour microenvironment composed of stromal cells and ECM has crucial roles in tumourigenesis, tumour progression, metastasis, and therapy resistance[206]. Moreover, tumour cells can influence the stromal cells and modify the ECM generating a favorable niche that facilitates tumour progression [207, 208]. Both MDA-MB-231 and MCF-7 cells are breast cancer cell lines. They displayed distinct capacities to turn normal fibroblasts into myofibroblast-like cells. The MRC-5 fibroblasts demonstrated up-regulated α-SMA expression induced by MDA-MB-231 cells other than MCF-7 cells. In breast cancer, TGF-β1 is highly expressed, especially at the advancing edges of primary tumours and in metastatic foci of lymph nodes [220]. It has been reported that the more invasive MDA-MB-231 cells produced five times more TGF-β1 than the less invasive MCF-7 line when cultured *in vitro* with 10% serum plus DMEM/F12 [221]. It indicates that TGF-β1 plays an important role to influence the neighbouring stromal cells. The fibroblasts influence the behaviours of tumour cells via a range of growth factors and cytokines including HGF, EFG, BMPs, interleukins, and even lactate products[197, 207, 222]. It is difficult to identify a specific inhibitor that can block the function of the complicated secret from fibroblasts. On the other hand, TGF-β1 has been proven as one of the major factors to transfer fibroblasts into CAFs[208, 223]. Our results in **Figure 3-10** show the blocking of TGF-β1 can stop the transformation of CAFs as well as demonstrated the blocking function of the unidirectional chip.

Previous studies have demonstrated that mesenchymal stem/stromal cells contribute to direct interaction with tumour cells and promote mutual exchange/induction of cellular markers[207, 224] (Karnoub et al., 2007; Shi et al., 2017). Alternatively, MSC interaction

can be mediated indirectly by the release of soluble biological factors and/or vesicles such as exosomes whereby MSC can affect cellular functionality of distant cell populations in a paracrine manner. The signal molecules secreted by the tumour cells can also influence the targeting, migration and functions of MSCs. These effects can be mediated both, by signal proteins such as CXCL12-CXCR4 and CCL19-CCR7[205], and RNAs including mRNAs and miRNA[191, 225]. It has been reported that the proliferation and migration of cancer cells increased following direct co-culture with MSCs. These results suggest that MSCs induce epithelial mesenchymal transition in cancer cells via direct cell-to-cell contact and may play an essential role in cancer metastasis [226]. In this work, we found that unidirectional indirect contact can trigger the response of cancer cells and CAFs, which may be due to the high bioactivities of signal molecules in the chip without a decrease in conditioned medium storage and transferring.

The unidirectional microfluidic chips have high extensibility that is applicable for different research, such as exosome or endocrine studies **Figure 3-11**. Exosomes are known for intercellular communication in both normal and diseased tissue. They are involved in the regulation of programmed cell death, modulation of the immune response, inflammation, angiogenesis, and coagulation [225, 227, 228] The exosomes secreted by stromal cells, such as MSCs, have been demonstrated to alter tumour cellular functionalities with the capacity to reconstruct tumour microenvironment[229]. It has been reported that cancer cells induce CAFs through TGF-β1 encapsulated exosomes [223]. Cancer exosomes trigger MSC differentiation into pro-angiogenic and pro-invasive myofibroblasts [230]. Injection of antibodies to block the exosomes may be used to study the functions of a specific type of exosomes. Opening an outlet in the middle channel can provide an exosome harvesting path or a connection path to other microfluidic devices for monitoring of exosomes. Microfluidics-based separation and detection of exosomes have attracted more attentions for research and clinical applications [101, 231]. It is expected that the proposed unidirectional microfluidic chip can be extend with the chips for separation and detection of exosomes, which may provide an efficient approach for exosome studies. Our unidirectional microfluidic device may also be used in endocrine studies. By optimizing the middle channel length and introducing endothelial cell culture in the channels and physical barriers, the unidirectional chip may be a simple model that mimics the *in vivo* endocrine transfer pathway.

3.5 Conclusions

In this work, a microfluidic chip was fabricated for cell co-culture to study the unidirectional intercellular communication. The chip achieved unidirectional communication of 3D cultured cells. Moreover, the unidirectional chip enables the analysis of a specific signal via the signal blocking inlet. Our results showed that MRC-5 and MSCs could enhance the growth of tumour cells. The invasive MDA-MB-231 could more effectively induce the MRC-5 and MSCs into CAF-like cells via unidirectional stimulation. By using the signal-blocking function, we also proved that TGF-β1 secreted by cells was one of the major factors to up-regulate the expression of α-SMA of the stromal cells. The device offers a unique, facial and effective tool for the study of intercellular communication.

Chapter 4 Enabling peristalsis of human colon tumour organoids on microfluidic chips

The organ *in vivo* suffers from mechanical cues (stretch, contraction, etc.), which helps to maintain the organ's functions. Establishment of spheroids and organoids requires the replication of the mechanical stimulus. Many methods have been developed to apply the mechanical effect on tumour spheroids, such as stretching spheroids by culturing them on the stretchable membrane or pressing spheroids by fixing them between two plates. However, it is still challenging to apply the mechanical cues on organoids due to the requirements of Matrigel. Furthermore, it is challenging to apply the mechanical stimuli to them in a high-throughput manner.

Human colon tumour organoids have been successfully established and been widely used in drug screening and developmental biology. However, these models lack the peristalsis stimulus, which is the primary mechanics for the intestinal microenvironment. Peristalsis in the digestive tract helps to maintain physiological functions. It remains challenging to mimic the peristaltic microenvironment during the development of organoids, especially for the gastrointestinal and pulmonary organoids. Here, we demonstrated a mechano-stimulated culture of human colon tumour organoids on the microfluidic chip to mimic the peristalsis. The chip contains hundreds of lateral microwells and a surrounding pressure channel. Human colon tumour organoids growing in the microwell can be periodically contracted by the pressure channel, mimicking the *in vivo* mechano-stimulus applied by the intestinal muscles. This strategy allows the easy control of the amplitude and rhythm of contraction, and the high-throughput, simultaneously. By applying around 8% contraction amplitude with 8~10 times/min, we observed enhanced Lgr5 and Ki67 expression compared to those cultured in the Matrigel dome. Moreover, ellipticine-loaded micelle nanoparticle testing illustrated a decreased uptake in the organoids under peristalsis. The organoids developed under the peristalsis also showed a reduced efficiency of the anti-cancer nanoparticles. We believe the proposed strategy enables the attainment of more reliable and representative organoids.

Chapter 4

4.1 Background

Organoids, stem cell-derived and self-organized miniature organs, have attracted more attention in developmental biology, cancer biology and cancer treatments [232-234]. Conventional gastrointestinal organoids utilise BME hydrogel as a static scaffold to support the growth and development of mini-organs, which lacks the dynamic microenvironment [235].

However, cells *in vivo* face various stimuli, especially mechanical forces, that regulate their behaviours, such as metabolism, differentiation, migration and self-assembly. Insight into an organ level, mechanical stimuli are also critical to maintaining the normal functions of organs. Peristalsis is the most common wave-like movement in the digestive tract, achieved by the constriction of the muscle layer, controlled by the vagus nerves, and developed since the foetal stage [236]. Under the peristaltic stimulus, the gastrointestine has balanced nutrition absorption and bacterial growth, avoiding the disease of dyspepsia, constipation, and achalasia[237]. Furthermore, the mechanical signals (a complex of strain, shear, tension, etc.) caused by peristalsis have an essential effect on physiology and pathology. For instance, peristalsis could stimulate the cellular proliferation and differentiation in intestinal epithelial cells, increase the cell-matrix interactions and the cell migration that works in inflammation and wound healing. In gastrointestinal malignancy, the mechanics are related to tumour cell adhesion, proliferation, and dissemination[238].

Studying the role of mechanics in gastrointestinal models is essential. Using fly midgut, Li et al. found mechanical stress could regulate stem cell differentiation[239]. Organoids tend to be used for mechanics-related research, especially combined with on-chip technology[240]. Yiwei et al. found the volumetric compression regulates the growth of the intestinal organoids by statically adding the weight on the Matrigel[54]. Furthermore, Holly et al. demonstrated the uniaxial strain, by using a nitinol spring, in human intestinal organoids transplanted in mice induces the growth and maturation of organoids[51]. Kang et al. achieve the stretch and contraction of the human gastric organoids by using a micropipette[48]. Lots of organ-on-chip models also investigated the strain mechanics effect on gastrointestinal models[241, 242].

It is still challenging to apply the peristalsis-like stimulus on the gastrointestinal organoids individually in a high-throughput way. Potential difficulties result from their tiny size and hydrogel-based microenvironment. However, high-throughput analysis is the key advantage of the organoid models in drug screening compared to the organ on chip and animal trials [67, 243, 244].

Here, we developed a dynamically mechano-stimulated high-throughput culture of human colon tumour organoids on microfluidic chips mimicking peristalsis. The microfluidic chip was composed of a microwell array interconnected by a channel for medium flow, and a parallel pressure channel wraps all the microwells providing rhythmic contraction and relaxation. Human colon tumour organoids were cultured in the microwells individually and regulated by the pressure channel's mechanical stimuli mimicking the colon's peristalsis. The microwells are semi-open, allowing the supply of nutrition/oxygen, removing waste, and the Matrigel reserve. The amplitude and rhythm were adjusted by the pressure and contraction rate of the channel. By applying ~ 8% amplitude contraction at 8~10 times/min, we found the up-regulated Lgr5 and Ki67 expression in organoids under peristalsis, compared to those cultured in Matrigel domes and on the chip without peristalsis. Moreover, we also found that the mechano-stimulated culture of colon organoid resulted in decreased uptake and compromised anti-tumour efficiency of ellipticine-loaded polymeric micelles. This platform can be used for not only the gastrointestinal organoids but also oesophagus, lung, and even cardio organoids under periodic mechanic stimuli. The dynamic culture method of organoids can offer more reliable models for biomedical research by providing a mechanical responsive microenvironment.

4.2 Aims and approaches

Despite the colon organoids derived from induced pluripotent stem cells (iPSC), the human colon tumour organoids can be established by embedding the colon tumour cells from patients via the biopsy (**Figure 4-1a**). Conventionally, they are cultured in the Matrigel dome immersed in culture medium, as shown in **Figure 4-1a**. Human colon tumour organoids could grow into spherical shape around 100~200 μm in diameter and small or large lumens. Physiologically, the human colon epithelium layer *in vivo* suffers the peristalsis microenvironment from the surrounding muscles that have periodical

contraction and relaxation, as shown in **Figure 4-1b**. Thus, the organoids generated from the current way lack the peristalsis stimulus.

The proposed microfluidic chip, assembling of a glass slide and a polydimethylsiloxane (PDMS) layer, contains 10×20 microwells that are connected by the medium channel and surrounded by the pressure channel, as shown in **Figure 4-1 c&d**. The semi-opened microwell can hold the Matrigel, allowing the organoids to grow in the microwell individually and parallelly, as shown in **Figure 4-1e**. The organoid growth medium was

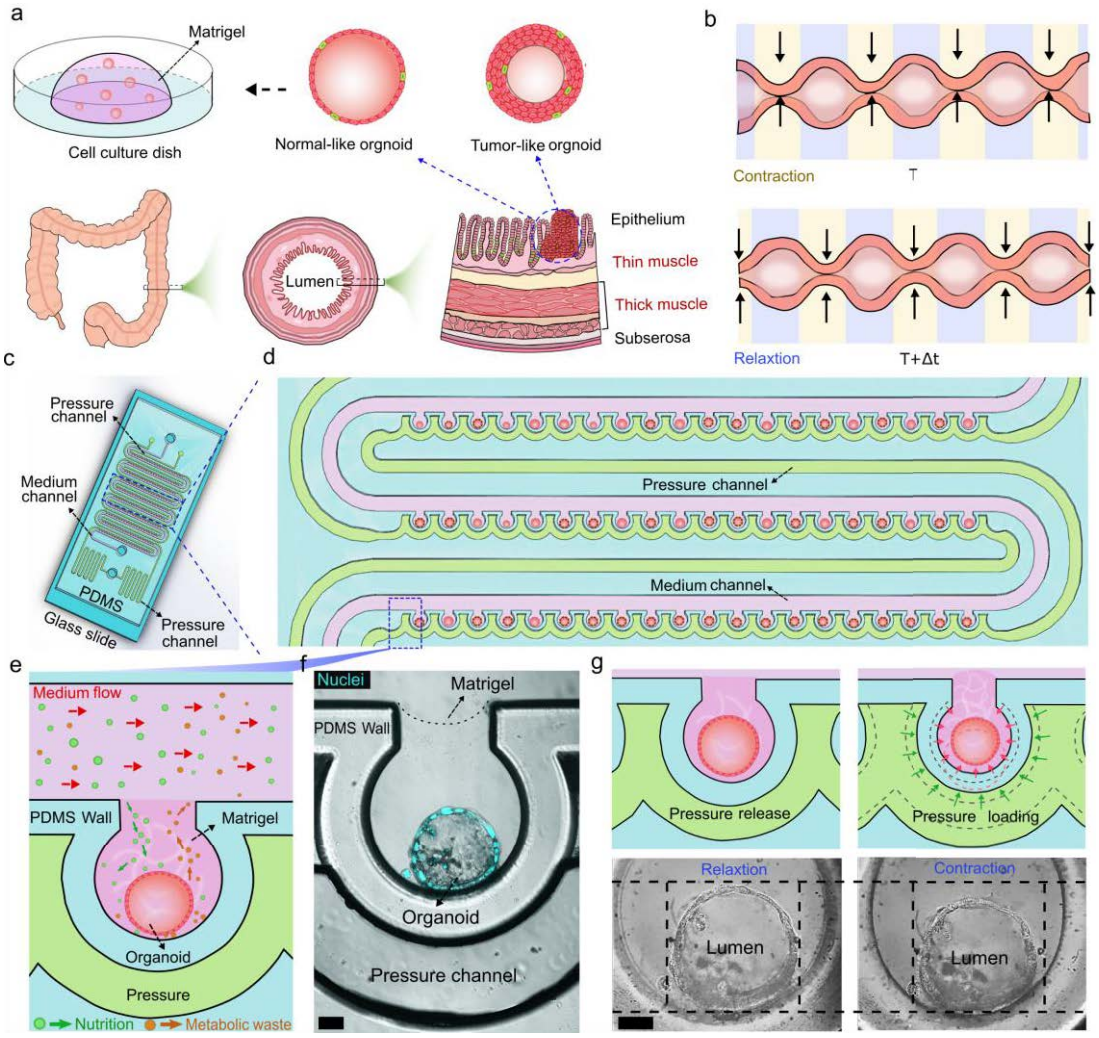

Figure 4–1| Concept design to contract the human colon tumour organoids mimicking the peristalsis. (a) Conventional culture of the human colon tumour organoids and its physiological environment. (b) Peristalsis movement of the colon that contains the periodical contraction and relaxation. (c) Proposed microfluidic chip. (d) Enlarged view of the layout that contains the semi-opened microwell array with medium channel and its surrounded pressure channel. (e) Enlarged view of the microwell. Matrigel can be kept in the microwell and the organoids grow at the bottom which was surrounded by the pressure channel. (f) Confocal image of the organoid that grew in the microwell. (g) Demonstration of the mechano-stimulus that mimic the peristalsis, and the organoid with pressure released and loaded. Scale bar:50μm.

introduced into the medium channel at a rate of 10 μL/min. To ensure sufficient space and nutrition supply for organoid growth, we set the microwell with a diameter of 300 μm and a 180 μm opening. A mature organoid with a 150 μm lumen diameter is illustrated in **Figure 4-1f**. To mimic the peristalsis, the pressure in the channel could be adjusted, which leads to the deformation of the PDMS wall. Thus, the deformed wall gives rise to the contraction of the organoids and the Matrigel, as shown in **Figure 4-1g.** The round microwell design allows the uniform squeezing of the organoids. **Figure 4-1g** shows an organoid at the released sate and its contracted state with an 8.7% deformation in diameter.

4.3 Materials and methods

4.3.1 Chip fabrication and characterization

The design of the microfluidic chip was shown in **Figure 4-2a&b**. The diameter and opening width of the microwell were set as 300 μm and 180 μm, respectively. The width of the PDMS wall and pressure channel was set as 100 μm and 160 μm, respectively. Standard soft lithography was used to fabricate the SU-8 mould and the PDMS layer. See the details in Chapter 3. It should be noticed that the leakproofness of the PDMS and glass

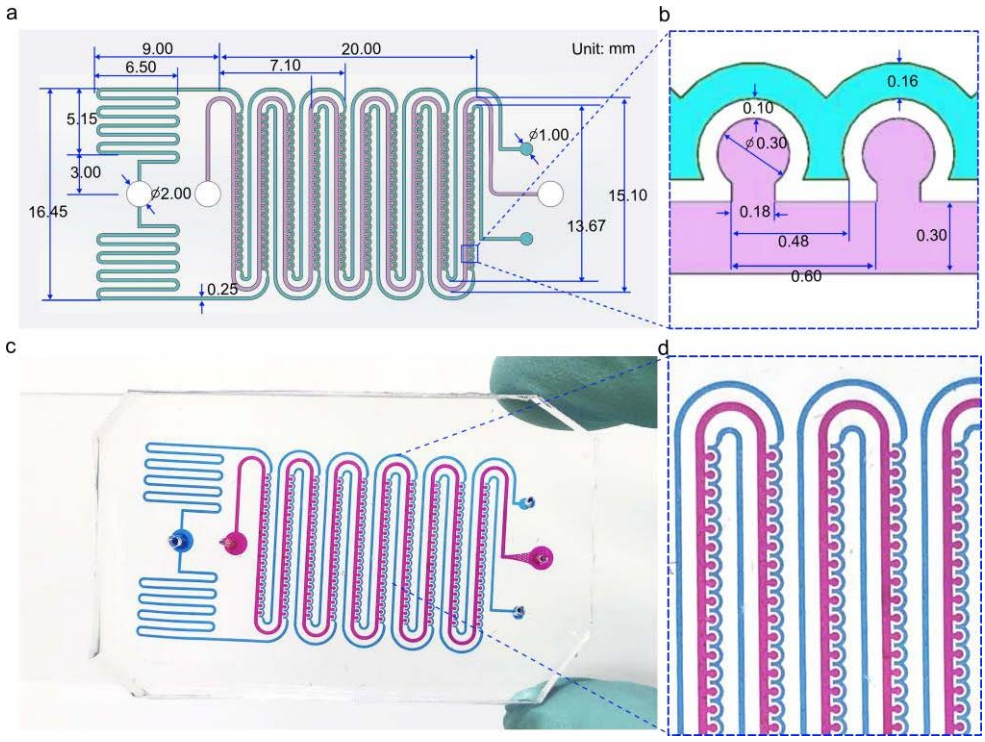

Figure 4–2| Chip design. (a) Schedule drawing of the microfluidic chip. (b) Main parameters of the semi-open microwells and the pressure channel. (c) Image of the assembled microfluidic chip. (d) Enlarged view of the microwell array.

slide is essential. Here, the glass slide was treated with the plasma for 120 s in the machine (Diener, Plasma Surface Technology). Then the PDMS was processed with the plasmonic for 5s together with the glass slide. Next, the PDMS was covered on the glass slide and pressed with fingers for around 10s. The thickness of the PDMS layer should exceed 4 mm to avoid the deformation induced by the pressing and enhance the capability of gas absorption in the following steps. Then the fabricated chips were put inside the vacuum desiccator for degassing. Before that, the chips should be sterilized under the ultraviolet for 20 mins and checked for the leakproofness with the syringe. The fabricated chip and its enlarged view could be seen in **Figure 4-2 c&d**.

4.3.2 **Organoid culture and cell loading**

The human colon tumour organoids (HCM-CSHL-0142-C18, ATCC, American) was cultured in the Matrigel (FAL356230 Corning, In Vitro Technologies, Australia) dome in a six-well plate. The complete growth medium was the Advanced DMED:F12 (Sigma) which was added by 10 mM HEPES (83264, Sigma), 2 nM L-Glutamine (59202C, Sigma), 1X B-27 (17504044, Thermo Fisher Scientific-AU) 100 $ng \cdot mL^{-1}$ Noggin (ab73756, Abcam), 50 $ng \cdot mL^{-1}$ Epidermal growth factor (EGF, E5036, Sigma), 10 nM Gastrin (G9020, Sigma), 10 μM SB202190 (S7067, Sigma), 500 nM A83-01 (SML0788, Sigma), 10 mM Nicotinamide (N0636, Sigma), 1.25 mM N-Acetyl Cysteine (A7250, Sigma) and 100 $U \cdot mL^{-1}$ penicillin/streptomycin (P4333, Sigma). The organoids were passaged via mechanical dissociation and TrypLE Express (12605-010, Thermo Fisher Scientific) 12 mins treatment to single cells.

Before the cell loading, the single cells were mixed with the Matrigel with a final concentration of $1.5\sim2\times10^6$. The Matrigel solution was introduced into the medium channel via a 1 mL syringe pump. One challenge is how to encase the cells in the microwell array uniformly and simultaneously ensure continuous perfusion for nutrition supply. Direct cell loading will lead to the air bubble in the microwell, which prevents the cells from flowing into the microwells. Inspired by the slight gas permeability of PDMS[245], we adopted a degassing strategy. As shown in **Figure 4-3a**, the pre-fabricated PDMS-glass chip was firstly kept in the vacuum desiccator for more than 2 hrs for degassing (**Figure 4-3 a-I**). Then the Matrigel mixed with the enzyme-digested colon single cells was injected into the medium channel via a 1mL syringe. During the

operation, the chip should be placed on a cold plate or ice (**Figure 4-3 a-II**). The Matrigel cannot flow into the microwell due to the intrinsically hydrophobic surface of the PDMS and glass. Next, the whole chip was inserted into the ice vertically. (The openings of the microwells were designed with the direction.) Due to PDMS permeability, the air bubble can be gradually absorbed, which allowed the Matrigel filling (**Figure 4-3b**). The cells would also fall to the microwell bottom (**Figure 4-3 a-III**, **Figure 4-3c**) due to gravity. It took around 10~15 mins. Then the chip was kept in the incubator vertically for about 30 mins to ensure the gelation of the Matrigel (**Figure 4-3 a-IV**). Next, the Matrigel in the medium channel was removed by pumping air into the channel (**Figure 4-3 a-V**, **Figure 4-3d**). Finally, the chip was connected with the tubes that supply the medium and periodic

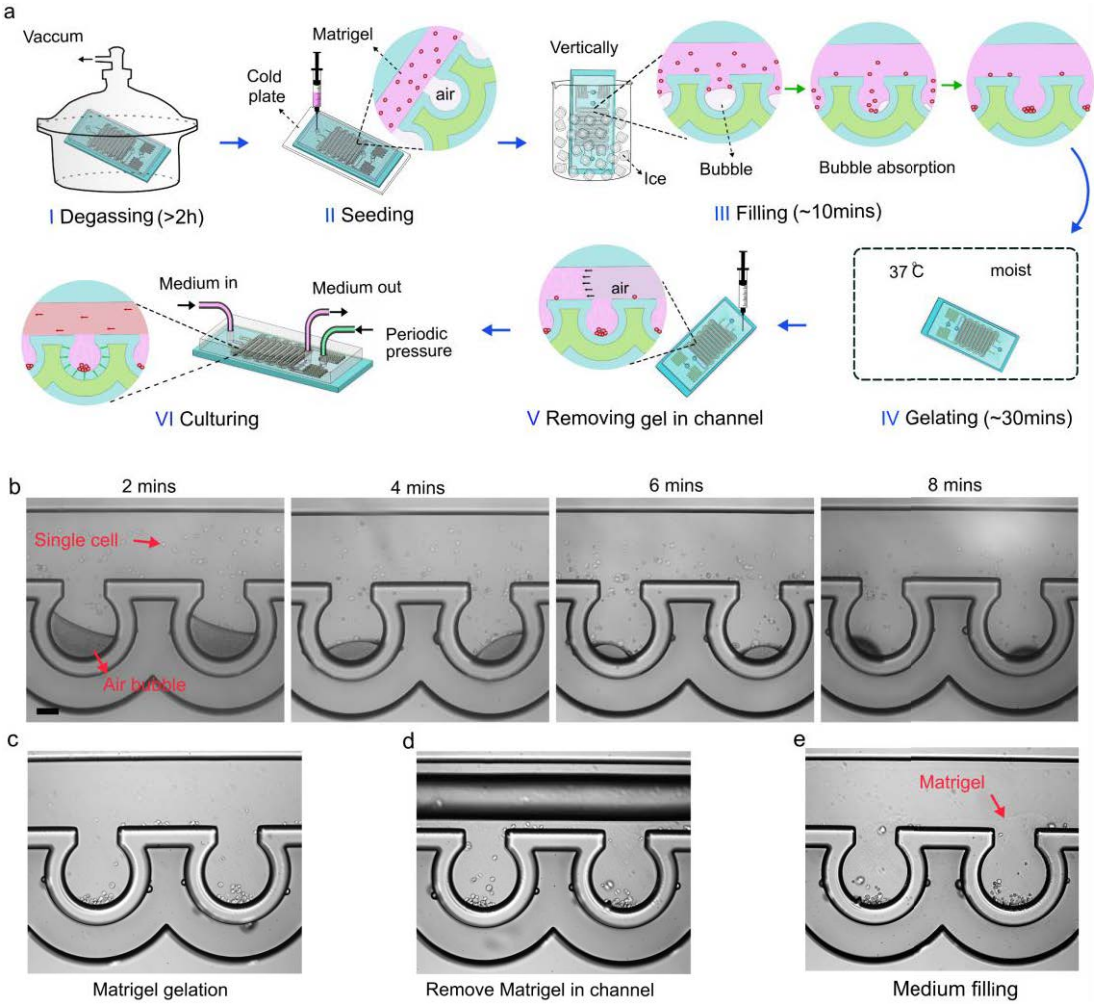

Figure 4–3 | Cell seeding. (a) Encasing the Matrigel and cells in the microwells. (b) Degassed chip gradually absorbed the air bubble in the microwell when the Matrigel was introduced into the channel. Simultaneously, the cells gradually fell into the microwell. (c) The gelated Matrigel was removed by pumping the air into the medium channel. (d) Refilling the medium channel with culture medium. The Matrigel could be well held in the microwell. The red arrow illustrated the Matrigel edge. 100 μm.

pressure (**Figure 4-3 a-VI**, **Figure 4-3e**). It should be noticed that the pressure channel should also be filled with medium to avoid the air penetrating into the medium channel via the PDMS wall.

4.3.3 System setup

The setup of the pressure control could be seen in **Figure 4-4**, which contains a compressor, Fluigent controller (ELUPPU1000, Flugient, France) with a safety valve and a filter, a syringe pump for medium supply and a laptop. To avoid the air bubble induced by the pressure channel, the pressure channel was filled with the medium. The controller system could adjust the amplitude and frequency of the pressure quickly. Here, we selected the 150kPa amplitude pressure and 1/6 Hz frequency. We used the simple commercial microscopy and the smartphone to quantify and record the contraction of the organoids.

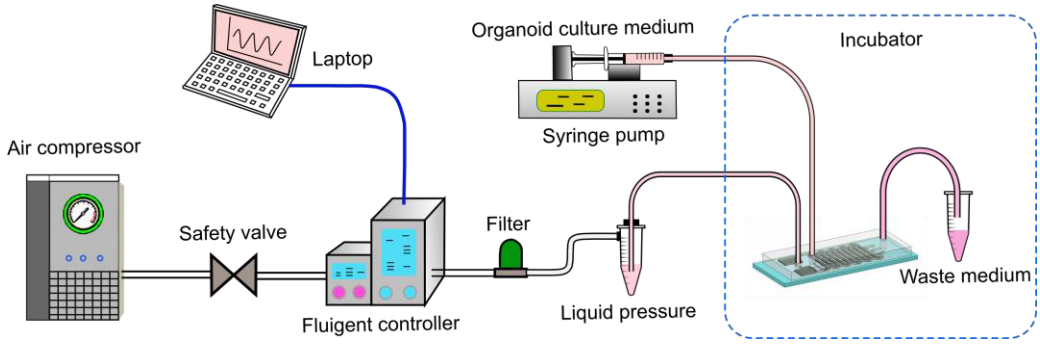

Figure 4–4 | Setup of the pressure control and the medium perfusion.

4.3.4 Penetration and deformation simulation

To quantify the efficiency of the nutrition supplying, the PHPMA-based block copolymeric micelles were introduced into the medium channel, which was dissolved in PBS with a concentration of 100 $\mu g \cdot mL^{-1}$. The flow rate of the syringe pump was set as 3.5 $\mu L \cdot min^{-1}$. The penetration process was monitored under confocal microscopy. It indicated that the fluorescent intensity in the microwell could reach the intensity in the perfusion channel after 18 mins penetration (**Figure 4-5 a&b**). Due to the molecules of the most nutrition smaller than the PHPMA micelles, we could conclude that the nutrition supply should be sufficient to grow of organoids in microwells.

Using Comsol software, we simulated the deformation of the PDMS wall when pressure was loaded. **Figure 4-5c** shows the deformation of a PDMS wall with 80 μm thickness

and 200 μm height under 150 kPa. The maximum deformation occurs at the middle height of the wall, which could reach around 35 μm deformation in radius. Thus, it can easily achieve 20% deformation considering the 300 μm microwell in diameter. It can be imagined that the deformed wall would like a hand to squeeze the Matrigel and the embedded organoids in the microwells. Deformation of various-thickness PDMS wall was also simulated. Thinner PDMS will give rise to more considerable deformation, but it will challenge the manufacturing and increase the risk of air leakage. To balance the fabrication, deformation, encapsulation, and gas penetration, around 80~100 μm thickness was finally adopted.

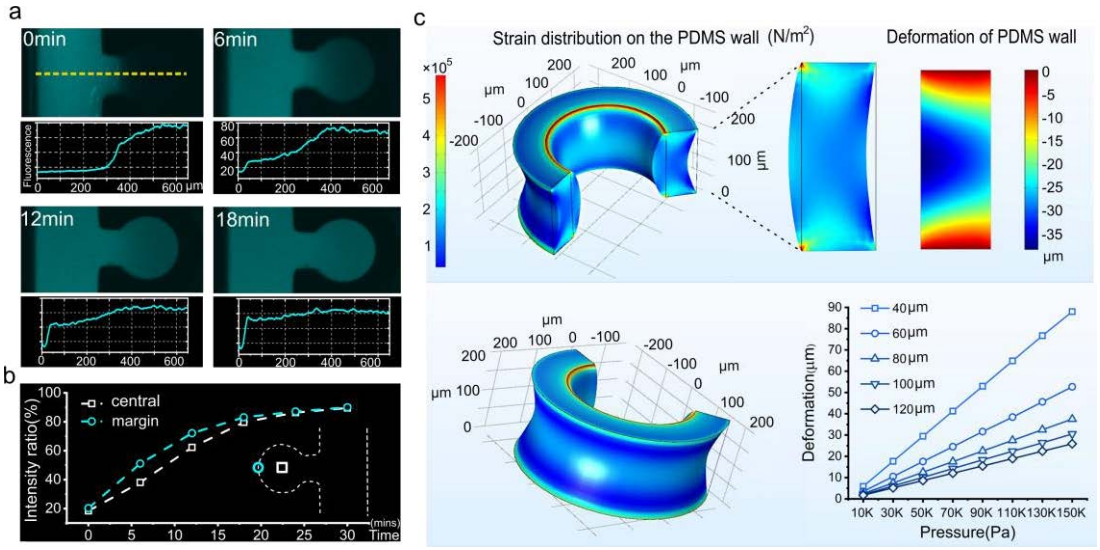

Figure 4–5 | Penetration and deformation simulation. (a) Fluorescent nanoparticles penetration from the side channel to the Matrigel in microwell (b) Fluorescence VS. time. (c) Simulation of the deformation of the microwell under pressure. The data in the image are all from the simulation.

4.3.5 Immunostaining and quantification of the organoids

The organoids cultured in the gel dome were collected by stirring the Matrigel 20 times via a 1 mL pipette. As for the organoids cultured on the chip, we separated the PDMS layer and glass with a scalpel. The organoids would be remained on the PDMS layer and were directly stained on the PDMS. Firstly, the organoids were fixed with the 4% paraformaldehyde for 30 mins. Then, they were treated with the 0.5% Triton X-100 for 1h, which was followed by 3 times washing of PBS. Next, the organoids were immersed in 5% BSA/PBS solution at 37ºC for 1 hr. Next, the anti Lgr5 antibody (Sigma)(1:50 dilution in 0.1% BSA/PBS) and Ki67 antibody (Sigma)(1:100 dilution in 0.1% BSA/PBS) were applied on the organoids for 1 hr at 37ºC, respectively. After 3-time

washing of PBS, the Cy3-labelled second antibody (1:200 dilution in 0.1% BSA/PBS) were applied to the organoids for 1 hr at 37ºC. Finally, the Hoechst 33342 (1:1000 dilution) were used for 15 mins. The stained organoids in the gel dome or on the chip were placed in a glass-bottom petri dish or covered on a glass slide for observation under the confocal microscopy (Olympus FV1200) with a 60X objective.

The brightness of the fluorescent images was reduced by the same value in Image J to eliminate the background noise. False colour was added with the *LUT* function in Image J (Cyan hot: nuclei, Orange hot: Lgr5, Yellow hot: Ki67). For the fluorescent quantification, the images were first transferred into 16-bit, then the same threshold value was selected to find the region of interest (ROI). Then function '*Measurement*' was used to quantify the averaged fluorescence intensity of the ROI.

4.3.6 **Synthesizing ellipticine-loaded micelles**

The block copolymer P(HPMA-co-MAA)-b-PMMA were synthesised via reversible addition−fragmentation chain-transfer (RAFT) polymerisation according to the reported method. For micelle preparation, 25 mg of P(HPMA-co-MAA)-b-PMMA and 5 mg of ellipticine were dissolved in 2 mL dimethylformamide. Subsequently, 2 mL of MilliQ water was added dropwise to the polymer using a syringe pump (0.2 mL/hr) under stirring. The samples were dialysed against MilliQ water for 24 hr using a dialysis membrane (MWCO 6000–8000). To remove the solvent, water was changed at regular time intervals. The micelles were characterised using transmission electron microscopy (TEM).

4.3.7 **Blocking endocytosis**

8-day-old organoids were treated with the 25 $\mu g \cdot mL^{-1}$ chlorpromazine (CPA) for 1h by adding the CPA in the culture medium. Then, the ellipticine-loaded micelle nanoparticles were added into the experimental group (CPA-treated) and control group (untreated). After 2 hrs co-culture, the organoids were washed with PBS 3 times and fixed before the observation under confocal microscopy.

4.4 Results and discussion

4.4.1 Organoid array on chip and its viability

We also characterized the organoid viability on the chip by the calcine-AM and PI staining. A one-week-old organoid array was shown in **Figure 4-6a**. It indicated that the organoids kept good viability in each microwell and formed the lumen successfully. Thus, one chip could establish 20×10 organoids individually and parallelly at a time. **Figure 4-6b** illustrates the bright-field image of an organoid with a large lumen. The middle layer and bottom layer were presented here. Most of the organoids were developed at the bottom of the microwells.

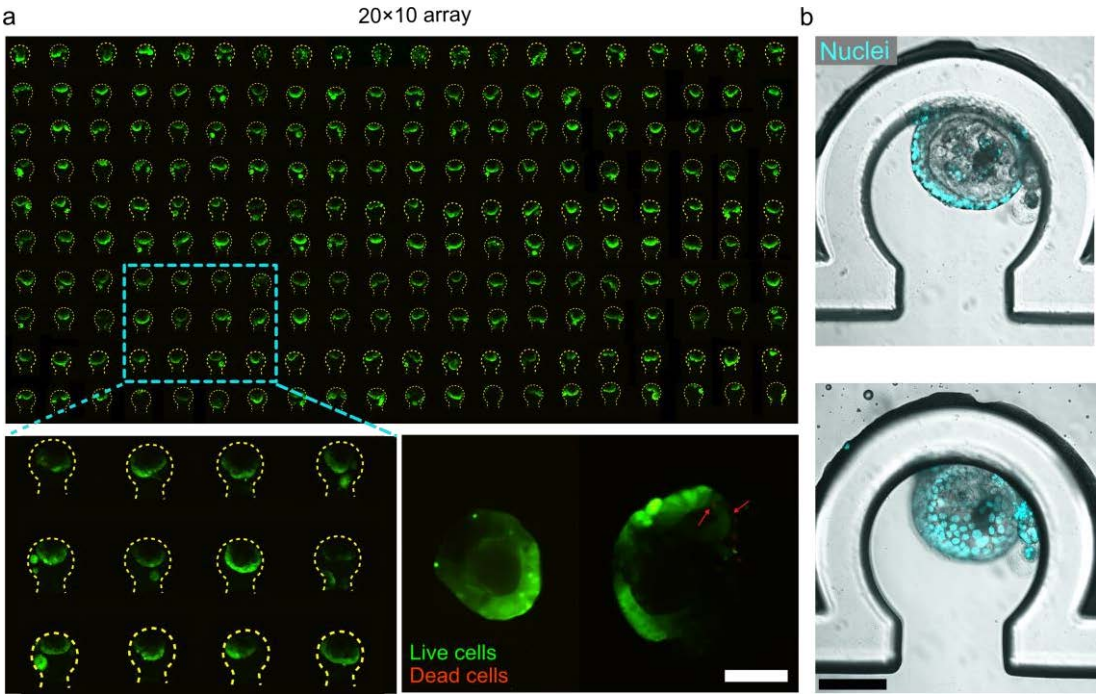

Figure 4–6 | Organoid developed on the chip. (a) Organoid array achieved on the proposed chip after 7-day culture and their viability. (b) Bright-field image of the organoids in the microwell (middle layer and bottom layer). Scale bar: 100 μm.

4.4.2 Characterization of organoid peristalsis

The organoids were contracted by the deformation of the PDMS wall, which could be adjusted by pressure. **Video 1**(appendix I) shows the deformation of the PDMS wall under periodical pressure. According to the simulation, the deformation of the PDMS wall can fulfil our requirement. We first tested the contraction of the organoids with large lumen under various pressure. As shown in **Figure 4-7a**, an around 130um organoid with a large lumen was demonstrated. With the increase of pressure, the organoid was gradually

contracted. **Video 2** shows the peristalsis-like movement of the organoids under 50, 150 and 250 kPa separately. The contraction frequency was set as 1/6 Hz according to the natural rhythm *in vivo*[241]. The initial contour was marked with the blue and green lines. We further characterized the contraction of a 150 μm organoid with a small lumen, as shown in **Figure 4-7b**. Similarly, the organoid can be efficiently contracted. See **video 3**. We quantified the deformation of the microwell and two types of organoids. As shown in **Figure 4-7c**, the diameter deformation of the microwell linearly increased with the pressure. From 0 to 150 kPa, the coupling efficiency of the large-lumen organoid deformation following the microwell in the y-axis was almost 100%. After 150 kPa, the

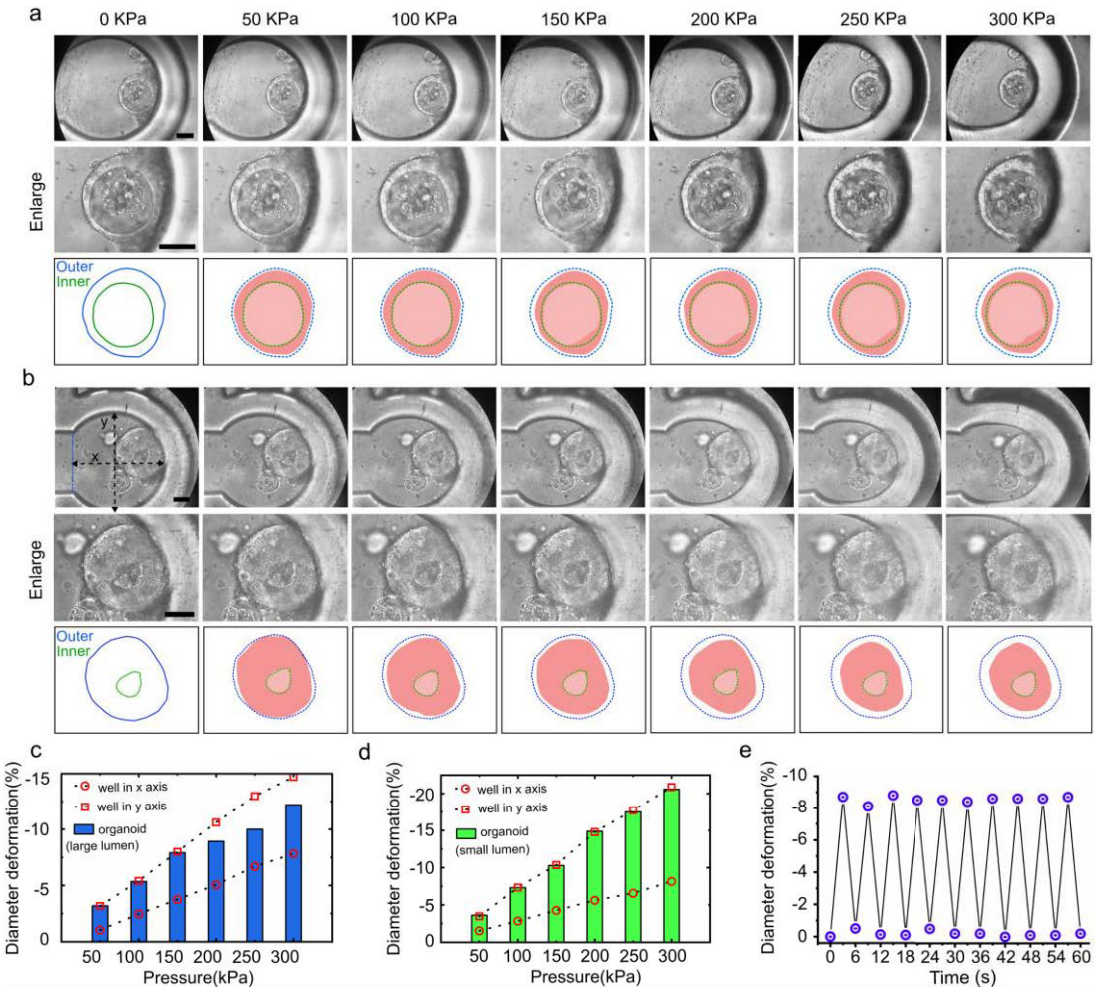

Figure 4–7 | Characterization of the deformation of organoids. (a) Contraction the organoids with large lumen in the microwell under various pressure. Blue line refers to the initial outer edge of the organoids. Green line refers to the initial inner edge of the lumen. Red area refers to the compressed organoids. (b) Contraction the organoids with small lumen in the microwell under various pressure. (c) Diameter deformation of large-lumen organoid and microwell. Point plot: microwell; bar plot: organoid. (d) Diameter deformation of large-lumen organoid and microwell. Point plot: microwell; bar plot: organoid. (e) Diameter deformation of an organoid under continuous contraction cycles. Scale bar: 50 μm

coupling efficiency gradually decreased. The deformation of the large-lumen organoid could reach 12% under 300 kPa. Differently, according to **Figure 4-7d**, the coupling efficiency of the small-lumen organoid deformation following the microwell y-axis deformation was almost 100% from 0 to 300 kPa. The small-lumen organoid could reach around 21% under 300 kPa. Definition of x and y axes of the microwell and the averaged diameter of organoid could be seen in the first image in **Figure 4-7b**. The deformation of the microwell in the x axis was around half of that in the y axis, resulting from the microwell's opening. According to the gut-on-chip investigation, we set the contraction of around 8% with a 1/6 Hz frequency[241]. We also recorded the deformation within continuous 10 cycles, and the organoid demonstrated stable capability for the contraction, as shown in **Figure 4-7e**. After 10-days culture, the chip still showed good capacity for the contraction. Furthermore, the Matrigel still remained in the microwell during the culture under peristalsis. The video information could be seen in Appendix I.

4.4.3 Characterization the growth and development of organoids

To profile the physiological difference among the organoids cultured in gel dome and on chips with/without the mechano-stimulus, we tested the expression of Lgr5 and Ki67, which are the primary markers of adult colon stem cell and cell proliferation, respectively. $Lgr5^{+}$ cells control the renewal and differentiation of the colon organoids. 8-day-old organoids were used for the immunostaining. As shown in **Figure 4-8a**, the organoids

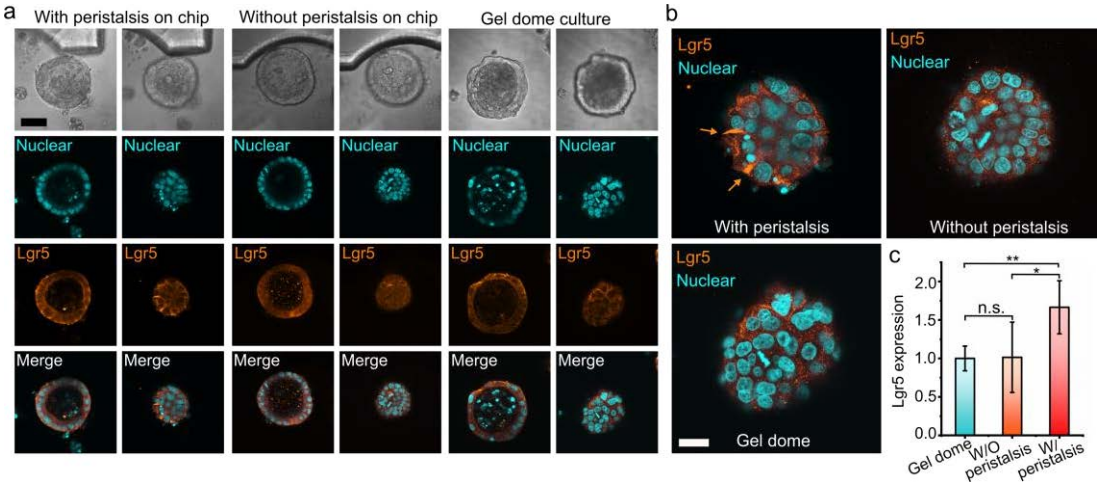

Figure 4–8| Lgr5 expression in large-lumen organoids. (a) Lgr5 immunostaining results of the colon organoids cultured on the chip with peristalsis, without peristalsis, and in the Matrigel dome. Scale bar: 100 μm. (b) Enlarged view of the Lgr5 immunostaining results. Scale bar: 20 μm. (c) Quantification of the Lgr5 expression.

with peristalsis showed higher and more intensive fluorescence compared to those without the peristalsis and cultured in the gel dome. The bottom and middle layers showed the same trend. Enlarged views could be seen in **Figure 4-8b**. We further quantified the Lgr5 expression by the fluorescence intensity, as shown in **Figure 4-8c**. Lgr5 expression of organoids cultured in the gel dome was set as 1.0. Results indicated the organoids with mechano-stimulus showed a 1.6-folds up-regulated expression. The organoids without the mechano-stimulus showed similar lgr5 expression with that cultured in the gel dome. Lgr5 expression of organoids with small lumens also showed the same trend, as shown in **Figure 4-10a**. These results indicate that the peristalsis-like mechano-stimulus promote the expression of Lgr5.

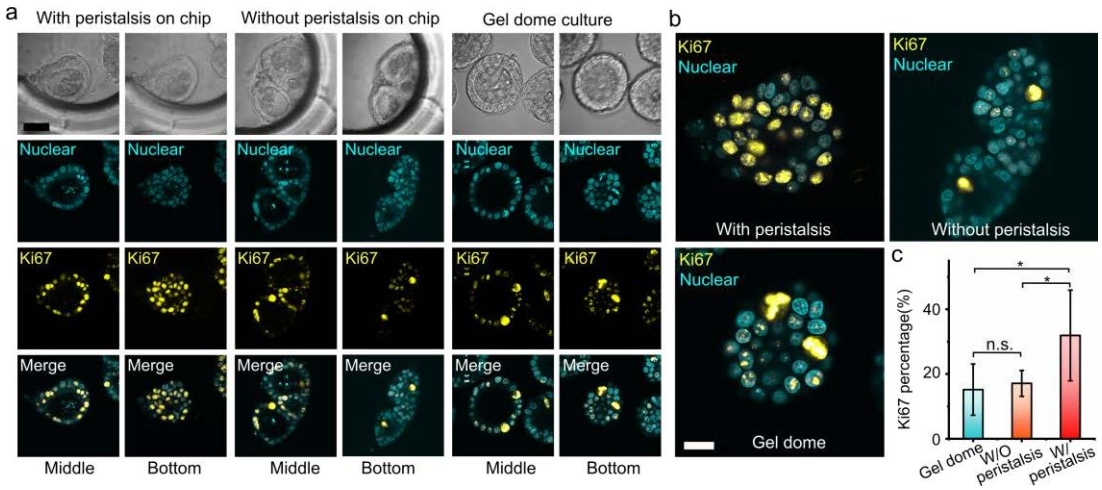

Figure 4–9| Ki67 expression in large-lumen organoids. (a) Ki67 immunostaining results of the colon organoids cultured on the chip with peristalsis, without peristalsis, and in the Matrigel dome. Scale bar: 100 μm. (b) Enlarged view of the Ki67 immunostaining results. Scale bar: 20 μm. (c) Quantification of the Ki67 expression.

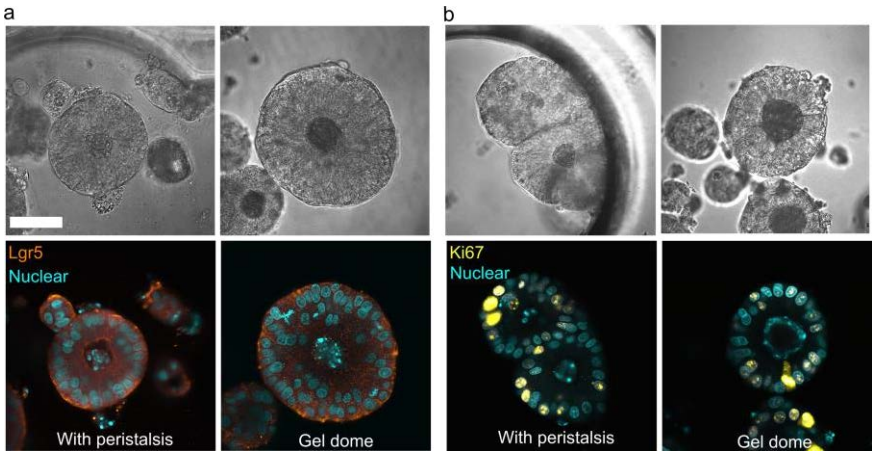

Figure 4–10 | Lgr5 and Ki67 expression in small-lumen organoids.

As for the Ki67, the results showed that organoids with peristalsis illustrated 4-folds up-regulated expression than that cultured in the gel dome. The on-chip culture without the peristalsis also could enhance around 1.8-folds expression, as shown in **Figure 4-9**. Similar results could also be seen in the organoids with small lumens, as shown in **Figure 4-10b**. Thus, it can be concluded that the peristalsis-like mechano-stimulus could enhance the proliferation of cells in human colon tumour organoids.

4.4.4 **Anticancer-drug screening on the chip**

To investigate the difference in drug response of these organoids, ellipticine-loaded micelles were synthesized, which was the common carrier for nanomedicine [246, 247]. As shown in **Figure 4-11a**, the PHPMA micelles had hydrophilic ends outside and hydrophobic ends inside. Ellipticine (hydrophobic) could be constrained inside. The SEM image of the synthesized micelles shown in **Figure 4-11b** illustrates the average size was 30 nm. After 2h treatment by the micelles, we found that the organoids showed obviously uptake and accumulation of the micelles, as shown in **Figure 4-11c**. Organoids under peristalsis exhibited the lowest fluorescent intensity. The organoids cultured in the gel dome showed the strongest fluorescence. As shown in **Figure 4-11d**, the accumulation of micelles in the organoids under peristalsis was around a fifth of that cultured in the gel dome, one third of that without stimulus. Thus, it is concluded that organoids under the peristalsis decrease the uptake of nanomedicine, which should be seriously considered during drug screening.

We treated the organoids with the nano drugs for two days and observed different morphology of the organoids, as shown in **Figure 4-11e**. The organoids cultured in the gel dome exhibited significant disaggregation. We measured the live and dead cells (**Figure 4-11f**) and found around 80% of cells dead. The organoids developed on the chip without mechano-stimulus showed slightly disaggregation and about 45% dead cells. The organoids developed under the peristalsis still maintained the original morphology, and only approximately 20% cells dead. This indicates that the human colon tumour organoids developed with the peristalsis strategy may lead to dull drug response during the drug screen.

It has been demonstrated that mechanical stimuli and membrane surface tension can influence the endocytosis of cells. We hypothesized that the peristalsis disturbs the

endocytosis of the organoids and thus hindered the cellular uptake of micelles. We treated the organoids with chlorpromazine (CPA), the inhibitor for clathrin-dependent endocytosis. As shown in **Figure 4-11 g&h**, the CPA-treated organoids showed significantly decreased uptake of the micelles, demonstrating the micellar uptake into organoids was clathrin-dependent endocytosis. Thus, the peristalsis inhibits the accumulation of nanoparticles in the organoids; it may shed light on the nanomedicine development for tumours under peristalsis.

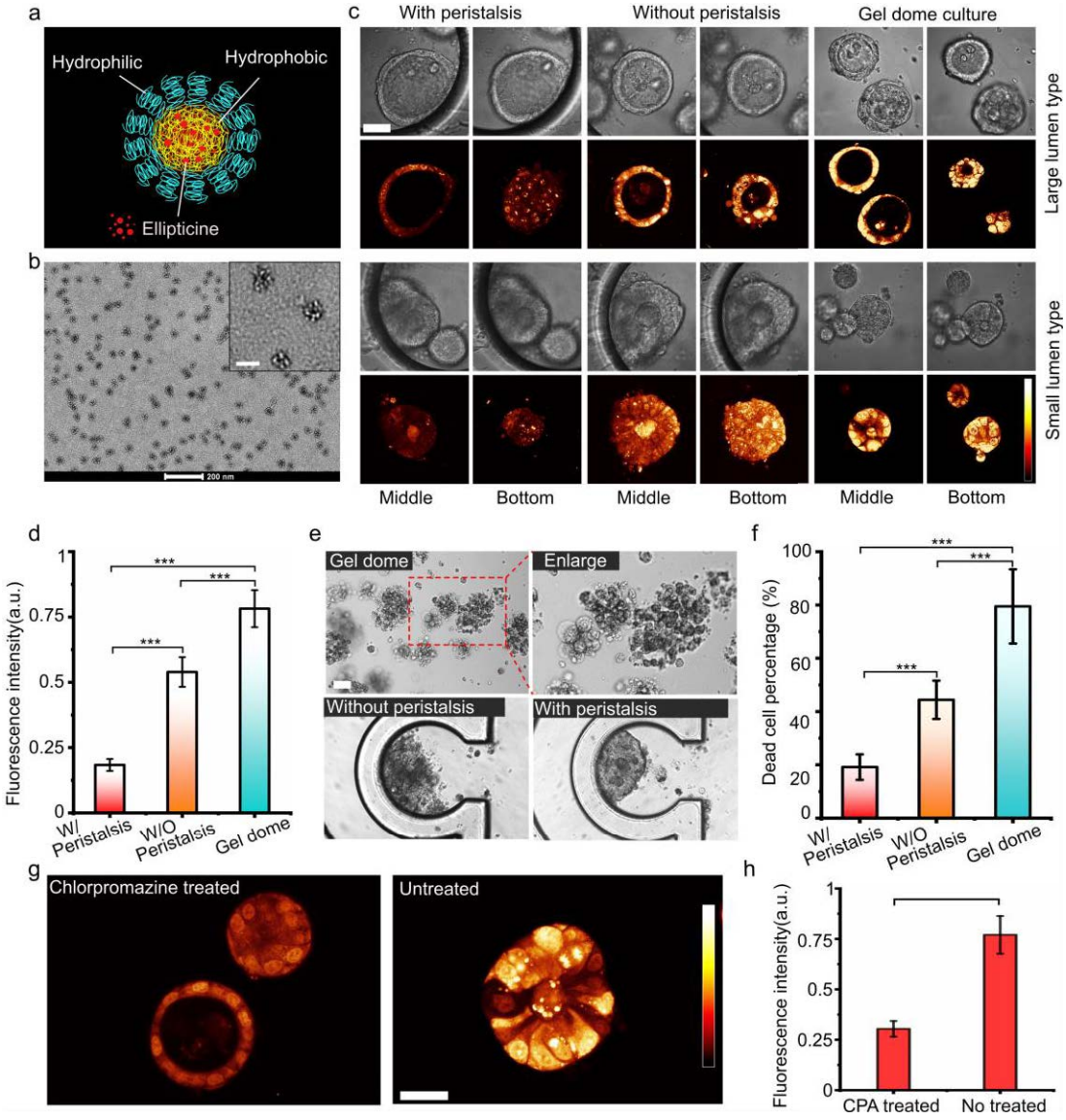

Figure 4–9| Organoid response to drug-loaded nanoparticles (a) Schematic of the structure of the ellipticine-loaded PHPMA micelles. (b) SEM image of the micelles. Scale bar: 50 nm. (c) Micelle uptake in the organoids cultured in different ways. (d) Quantification of the micelle nanoparticle uptake. (e) Morphology of the organoids after 2-day nanodrug treatment. Scale bar: 50 μm. (f) Dead cells in organoids after 2-day treatment. (g) Micelle uptake in the organoids with/without CPA treatment. Scale bar: 50 μm. (h) Quantification of the micelle nanoparticle uptake in the drug treated/untreated organoids. *** $p<0.001$.

Thus, in conventional drug screening based on the organoids cultured in the static gel dome, the results may be exaggerated, leading to the deviation of the downstream analysis. The peristalsis chip offers an efficient dynamic development for organoids under the peristalsis microenvironment.

4.5 Conclusions

Conventional culture of colon tumour organoids lacks the mechano-stimulus that could not mimic the peristalsis *in vivo*. To address this issue, we designed a microfluidic chip that could enable the peristalsis of human colon tumour organoids separately and parallelly. The round microwell design allows efficient mass transmission and contraction simultaneously. Compared to the organoids without peristalsis, the mechano-stimulated organoids showed upregulated Lgr5 and Ki67 expression. Moreover, these organoids illustrated decreased nanomedicine uptake and different drug response. We believe this platform could help to establish the gastrointestinal organoids, or other organoids underneath the mechano-cues, allowing the high-reliable drug screening.

Chapter 5 Mammary tumour organoids in alginate microbeads for luminal mechanics and drug screening

Tumour spheroids and organoids play an important role in drug screening. It is highly desired for the high-throughput generation of spheroids and organoids. Mammary tumour organoids have been recognized as a promising *in vitro* model for drug screening and personalized medicine. However, the dependency on the basement membrane extract (BME) as the growth matrices limits their comprehensive application. In this work, mouse mammary tumour organoids were established by encapsulating tumour pieces in non-adhesive alginate. High-throughput generation of organoids in alginate microbeads was achieved utilizing microfluidic droplet technology. The tumour pieces developed luminal- and solid-like organoids in the alginate microbeads. These organoids demonstrated a high similarity to the original fresh tumour in cell phenotypes and cellular compartment. The mechanical forces given by the alginate capsules to the organoids were analyzed with the theory of the thick-wall pressure vessel (TWPV) model. The pressure to the organoid luminal structure increased with the growth of organoids and could reach 2kPa after two weeks' culture. Finally, the organoids were treated with model drugs to evaluate the potential applicability for drug screening. It was found that the drug response is related to the luminal size and pressures of organoids. This high-throughput culture for mammary tumour organoids may present a promising tool for preclinical drug target validation and personalized medicine.

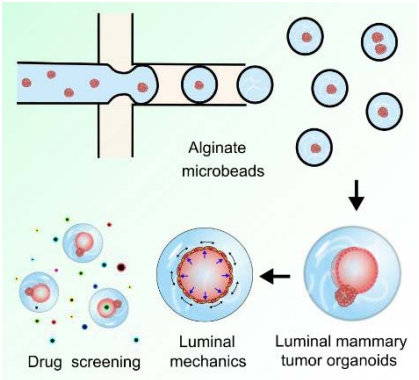

G. Fang *et al.*, Mammary tumour organoid culture in non-adhesive alginate for luminal mechanics and high-throughput drug screening, *Advanced Science*, 2021.

Chapter 5

5.1 Background

Mammary tumour organoids are now more attractive as they show the promising potential in biology development, drug screening and personalized medicine[248-251]. Among them, luminal-type organoids are unique as they substitute the hormone receptor-positive (HR^+) mammary tumour that constitutes 70% of the diagnosed cases[252-254]. To date, the extensive application of organoids is hindered by the high cost from hydrogel materials and throughput.

The scaffolds mimic the *in vivo* microenvironment by offering mechanical cues, binding sites, etc., allowing the formation of highly-ordered organoids with hierarchical or luminal structures. The most widely used material for organoid development is the tumour-derived based membrane extract (BME), usually offered as the commercial products Matrigel or CultreBME2. These hydrogels contain a cocktail of extracellular matrix proteins, proteoglycans, and some growth factors secreted by Engelbreth–Holm–Swarm murine sarcomas[255]. The low yield and complicated components give rise to the high price and batch-to-batch variation, limiting the high-throughput generation and accurate analysis. To simplify the components, defined materials (mainly including fibrin and laminin-111) were extracted for most human epithelial organoids[256]. Some synthesized hydrogels were also designed for the intestinal organoids, such as the PEG-based matrix[235, 257, 258].

Another barrier that hinders the development of organoids is their yield, hazarding the reliability in downstream analysis. Microfabrication technology, such as the microfluidic device, is now widely investigated to increase the throughput of organoids. For instance, the microwell arrays are used for the high-throughput culture of gastrointestinal organoids [67]. Matrigel microbeads on the microfluidic droplet devices enabled the high-throughput culture of clonal organoids. [78-80]. However, the rigorous storage and gelation of Matrigel are still challenging the design and operation of microfluidics.

Alginate, derived from the brown algae, is extensively investigated in microfluidic droplets due to its mild and fast gelation with divalent cation (e.g. Ca^{2+}, Ba^{2+}), good biocompatibility, and low cost[259]. Alginate microbeads can be fast generated, allowing the promising potential for the high-throughput culture[260, 261]. However, as alginate is naturally non-adhesive to cells, the cells inside can keep alive but hard to differentiate into ordered structures, let alone the luminal organoids[73, 162, 262]. To overcome this

drawback, the alginate is usually used as the capsule's shell, and the core is usually filled with Matrigel, collagen, and even medium for organoid culture[80, 81, 263-265]. Previous work found that the non-adhesive alginate can support the growth of intestinal organoids by encapsulating the intestinal spheroids inside[266].

Here, we found that mammary tumour organoids can be established in the non-adhesive alginate by embedding the mouse tumour chunks inside. Combined with the droplet technics, the tumour chunks could be encapsulated inside the pure alginate microbeads, allowing the high-throughput culture. Interestingly, the chunks inside the alginate microbeads can form the luminal-type organoids. One luminal organoid in one microbead could be achieved. The growth and key proteins of the lumen were profiled. Fluorescence-activated cell sorting (FACS) results indicated that the established organoid showed similar cell compartments to the fresh tumour. Moreover, utilizing the thick-wall pressure vessel (TWPV) model, we established the analysis of luminal mechanics of the organoids based on the microbeads. Finally, we demonstrated the drug screening capability of the tumour organoids on the microwell array. Size-dependent drug uptake among the organoids was observed. The chip could be achieved with the homemade soft lithography system or low-cost 3D printer due to the simple requirement for the device. We believe this strategy could help the development and extensive application of mammary tumour organoids.

5.2 Aims and approaches

Concept design is illustrated in **Figure 5-1**. Firstly, the mammary tumour in the mouse was extracted by using the scalpel. Most of the mammary is the fatty tissues that surround the acinus and the ducts. The mammary tumour usually comes from the out-control growth of cells lining the acinus and ducts, as shown in **Figure 5-1a**. Then the large tumour tissue was minced with the chopper. After that, the size of the tumour chunks ranges from 10~1000μm with lots of single cells inside. Next, the tumour chunks were filtered by the strainer with the pore size of 100 and 300μm, respectively, as shown in **Figure 5-1b**. We then mixed the tumour chunks (100~300μm) with the alginate/Ca-EDTA evenly. With the help of the microfluidic chip, the tumour chunks could be well encapsulated inside the alginate droplets. The Ca^{2+} chelated in the EDTA can be released in the acidic environment and then induces the gelation of the alginate droplets. The alginate microbeads could be extracted from the oil and then cultured in the cell dish, as

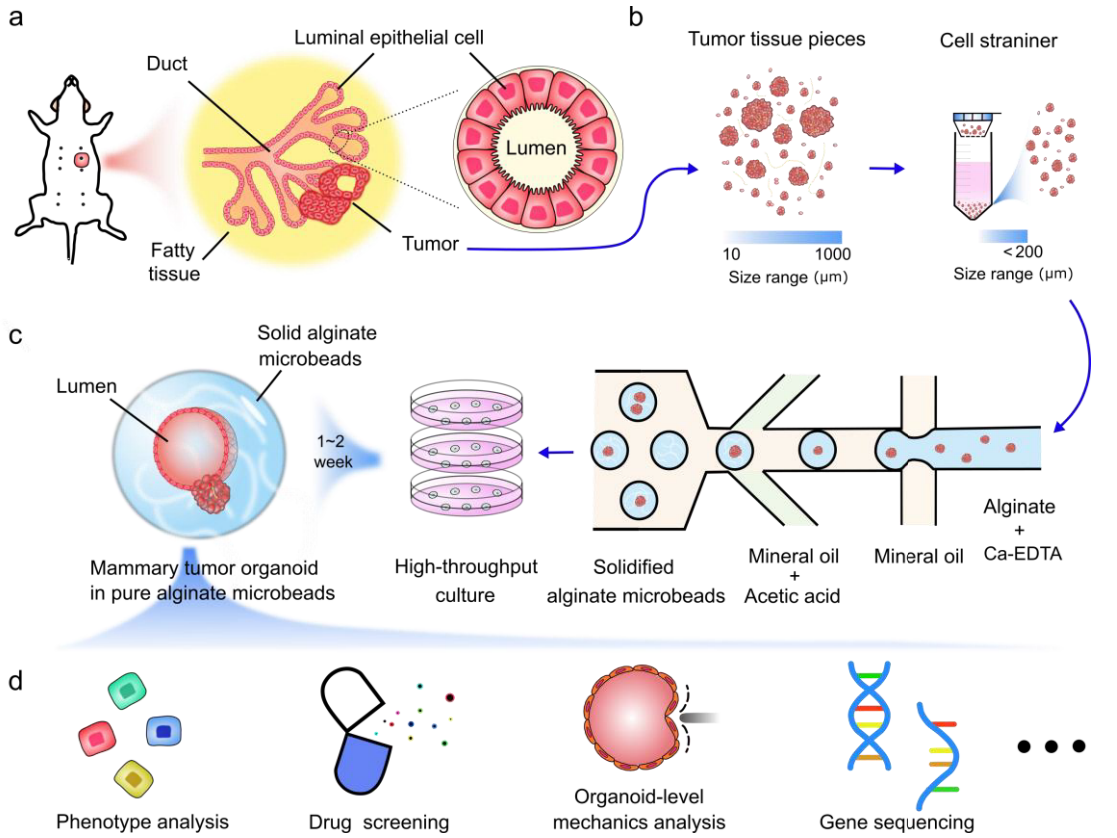

Figure 5–1 | Concept design of the mammary tumour organoids in alginate microbeads. (a) Schematic of mouse mammary tumour in vivo. (b) Cutting the tumour into chunks and get uniform-sized chunks using cell strainer. (c) High-throughput generation of solid alginate microbeads with tumour chunks encapsulated by the microfluidic droplet technics. After 1~2 weeks culture, the mammary cancer organoids with lumens formed in the solid alginate microbeads. (d) Potential application of the mammary cancer organoids in alginate microbeads.

shown in **Figure 5-1c**. Interestingly, the tumour chunks in the solid alginate could continue to grow, and some even form luminal-type organoids after several days' culture. These luminal structures are the primary and representative morphology of the epithelium organoids, usually formed in the Matrigel. Thus, by using this simple method, the high throughput of mammary cancer organoids can be achieved in a low-cost way. The organoids in the alginate microbeads could be used for high throughput drug screening, organoid-level mechanic analysis, and disease mechanism by gene sequencing, as shown in **Figure 5-1d**.

5.3 Materials and methods

5.3.1 Chip fabrication and characterization

As the size of the tumour chunks ranged from 100~300 μm, the width of the co-flow channel was designed as 700 μm. The chip mould could be fabricated with a commercial

3D printer or homemade soft lithography device due to the large scale. Here we show the latter method. Firstly, the mask was fabricated by a commercial printer (iRADV 4551i Canon) and a transparent plastic sheet (**Figure 5-1a**). The pattern was drawn in the Adobe Illustrator CS6. The mask was used with two overlapped layers which could reduce the roughness of the edge and the transmission, as shown in **Figure 5-2 b&c**. The SU-8 2150 photoresist was then spin-coated on the 4-inch silica wafer with a thickness of around 550 µm. Next, the photoresist was exposed under a UV LED for 2 mins with the mask covered

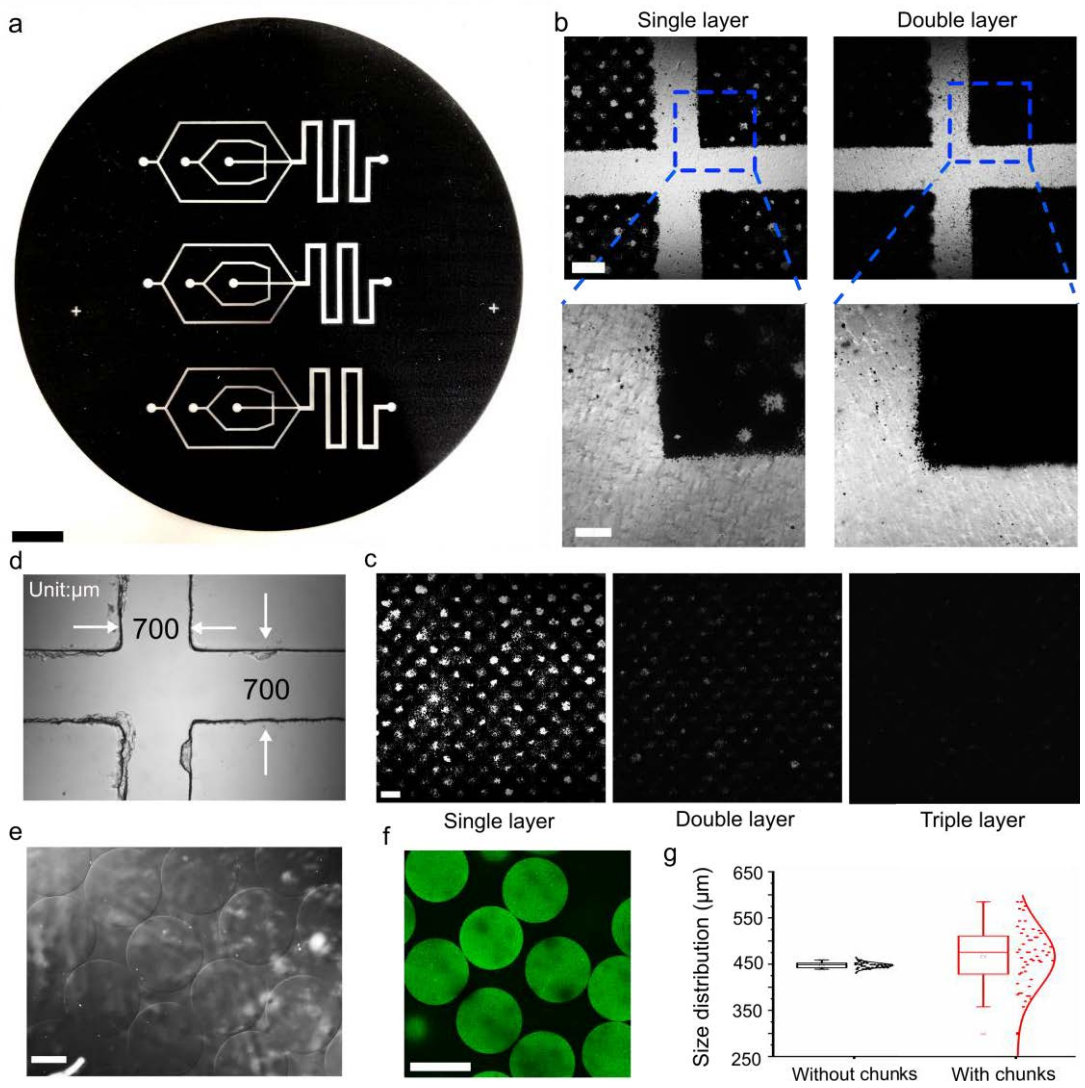

Figure 5–2 | Plastic mask fabricated by commercial printer (a) Double-layer plastic mask fabricated by the commercial ink-jet printer. Scale bar: 1cm. (b) Bright-field image of the mask under the confocal microscopy with single and double layer, respectively. Scale bar: 500µm. Scale bar of the enlarged view: 200µm. (c) Details of the mask with single, double and triple layer. Scale bar: 500µm. (d) Microfluidic chip channel under the 4X objective lens. (e) Bright-field image of the uniform-size alginate microbeads. Scale bar: 200µm. (f) Fluorescent image of the alginate microbeads. Scale bar: 400 µm . (g) Size distribution of the alginate beads without/with chunks inside.

on it, followed by the standard post bake, develop and hard bake process. After the fabrication of the SU-8 mould, the PDMS was mixed with the curing agent in a ratio of 10:1 and then poured on the mould. Finally, the peeled-off PDMS was bonded with the glass slide by using the plasma machine. The chip image was shown in **Figure 5-2d**. Although the edge of the structures was a little rough, the chip can completely meet the requirement of the droplets with several hundred micrometers. The alginate microbeads could have a uniform size, shown in **Figure 5-2 e&f**. However, when the alginate mixed with the chunks, the generated microbeads had a relatively large size range due to the flow disturbance induced by the large-sized chunks, as shown in **Figure 5-2g**.

5.3.2 **Mouse tumour tissue process**

The mouse experiments were performed at the Garvan Institute of Medical Research under the approval of the St. Vincent's Campus Animal Ethics Committee (AEC #19/02). BALB/c mice were inoculated with 50 000 PyMT cells in the fourth inguinal mammary gland to generate tumour tissues. The mouse PyMT tumour tissue was collected 4 weeks post inoculation and chopped into small chunks.

5.3.3 **Alginate microbeads generation and collection**

Sodium alginate (Sigma-Aldrich) was dissolved in PBS with a concentration of 2wt% under the ultrasound. The calcium-EDTA was generated by mixing the disodium-EDTA solution (100×10^{-3}M) and the calcium solution (100×10^{-3}M) with the ratio of 1:1. PH of the calcium-EDTA was finally adjusted to around 7.4 by adding the sodium hydroxide. Then the sodium alginate was mixed with the calcium-EDTA solution with an equal ratio. The final concentration of the alginate is 1wt%. Under this condition, the calcium irons were chelated inside the EDTA and would not gelate with the alginate chains. Span 80 (Sigma-Aldrich) was added inside the mineral oil (Sigma-Aldrich) with a concentration of 3.5 vol% for the second inlet. Mineral oil mixed with 3.5 vol% span80 and 0.08 vol% acetic acid is prepared for the third inlet. The channel surface is treated as hydrophobic by 1wt% 1H,1H,2H,2H-Perfluorododecyltrichloro in isopropanol.

The filtered and centrifuged tissue chunks were mixed with the alginate-calcium-EDTA solution uniformly. Due to some medium remained at the bottom, the final concentration of the alginate should be lower than 1wt%. The alginate, mineral oil, and mineral oil with acetic acid were introduced into the chip respectively by syringe pump. The droplets

generated at the junction would gelate when meeting the acidic mineral oil. Because the calcium irons would be released from the EDTA when the environment becomes acidic. The alginate microbeads were collected in the tube where some culture medium was at the bottom, and some mineral oil with acetic acid was at the top. The alginate microbeads would naturally settle from the mineral oil to medium. Finally, the microbeads were transferred to the cell culture dish for further culture.

5.3.4 **Mammary tumour organoid culture**

The alginate microbeads were cultured in the medium in six-well cell culture plates. The medium is the DMEM medium with 10% FBS, 5 μg/mL insulin, 1% HEPES, 1% glutamine, 10 ng/mL human epithelial growth factor (hEGF) and 10 ng/mL cholera toxin. The medium was replaced every two days.

5.3.5 **Immunostaining**

The 2-week-old organoids were used for the immunostaining. The medium was removed from the well of the six-well plate. Then around 2mL Tris Acetate-EDTA buffer (Sigma-Aldrich) was added to degrade the alginate gradually. After 10 mins, the released tumour organoids were collected to the well of a 96-well plate. The tumour organoids were fixed with 4% paraformaldehyde for 20mins. After washing by PBS three times, 100 μL 0.5% Triton X-100 was added to each well and incubates at room temperature for 1 hr. After washing by PBS three times, the tumour organoids were then blocked with 5% BSA/PBS solution at 37°C for 1 hr. Next, the anti ki67, CD133 and fibronectin antibody (Sigma-Aldrich) (1:200, 1:50, 1:200, dilution in 0.1% BSA/PBS) were added to the well, respectively, and incubated at 37°C for 1 hr. After washing with PBS thrice, the cells were immersed in the Cy3-labelled second antibody solution (1:500 dilution in 0.1% BSA/PBS) at 37 °C for 1 hr. Finally, after washing with PBS thrice, the Hoechst 33342 (Sigma-Aldrich, 1:1000) and deep red tubulin dye (Sigma-Aldrich, 1:1000) were applied and incubated for 10min, before the observation under the confocal microscopy.

5.3.6 **Flow cytometry analysis**

Fresh tumour tissues were chopped into small chunks and then enzymatically dissociated in DMEM/F12 (1:1) supplemented with 2 mg/ml collagenase and 200 U/ml hyaluronidase. After dissociation, red blood cells were lysed in ammonium chloride and

processed to a single cell suspension by sequential digestion with 0.25% Trypsin, 5 mg/ml dispase and 1 mg/ml DNase and filtered through a cell strainer. Organoids in the microbeads were collected and treated with Tris Acetate-EDTA buffer to remove the alginate and then dissociated into single cells with TrypLE. Single cell suspensions were then incubated with primary antibodies, incubated with 4',6-diamidino-2-phenylindole (DAPI) and analysed by flow cytometry using a FACSAria II.

5.3.7 **Synthesis of fluorescent alginate**

The synthesis of the fluorescent alginate followed the work[267]. Firstly, alginates were dissolved in PBS (PH 7.2-7.4, Sigma) to give approximately 90 mM carboxylic groups. Then, EDC (1-Ethyl-3-(3-dimethylaminopropyl) carbodiimide hydrochloride, Sigma) and sulfo-NHS (N-hydroxysulfosuccinimide sodium salt, Sigma) were added to 9 mM of each. The solution was kept at room temperature with stirring for 2 h. Next, 0.45 mM fluorescein amine (Sigma) was added. The reaction was stirred at room temperature for 18 h in place. Then, the solution was transferred to dialysis membranes (12,000-14,000) and dialyzed against ion-free water overnight at 4°C. Then the solution was dialyzed in 1 M NaCl for 24 h until the water lost yellow color (5 shifts). Finally, the solution was freeze-dried protected from light.

5.3.8 **Cell viability and drug treatment**

For the drug screening, the 2-week-old tumour organoids were used. The microwell agarose array was generated following chapter 2 or the commercial microwell mould. Before using the microwell plate, the agarose plate should be immersed in the medium for at least 2 hrs. The microbeads were then added to the microwell via the pipette. Next, the medium was firstly removed, and then 2 mL fresh medium with Doxorubicin at a concentration of 3.5 μM or Latrunculin A at a concentration of 1 μM was added, separately. In the control group, 2 mL fresh medium with the same volume of PBS was added. During the culture, the medium was changed every 2 days. The viability was measured by the Live/Dead Cell Assay Kit (Sigma-Aldrich, Australia) with staining for 1h at 37ºC. Then the microbeads were imaged under the confocal microscope.

5.4 Result and discussion

5.4.1 Growth of mammary tumour organoids in alginate microbeads

Tumour chunks in the alginate microbeads were cultured in the medium in the 6-well plates. After one-day culture, small lumens would be observed under microscopy. Then lumen appears more and more. But they were not formed at the same time. Some lumens

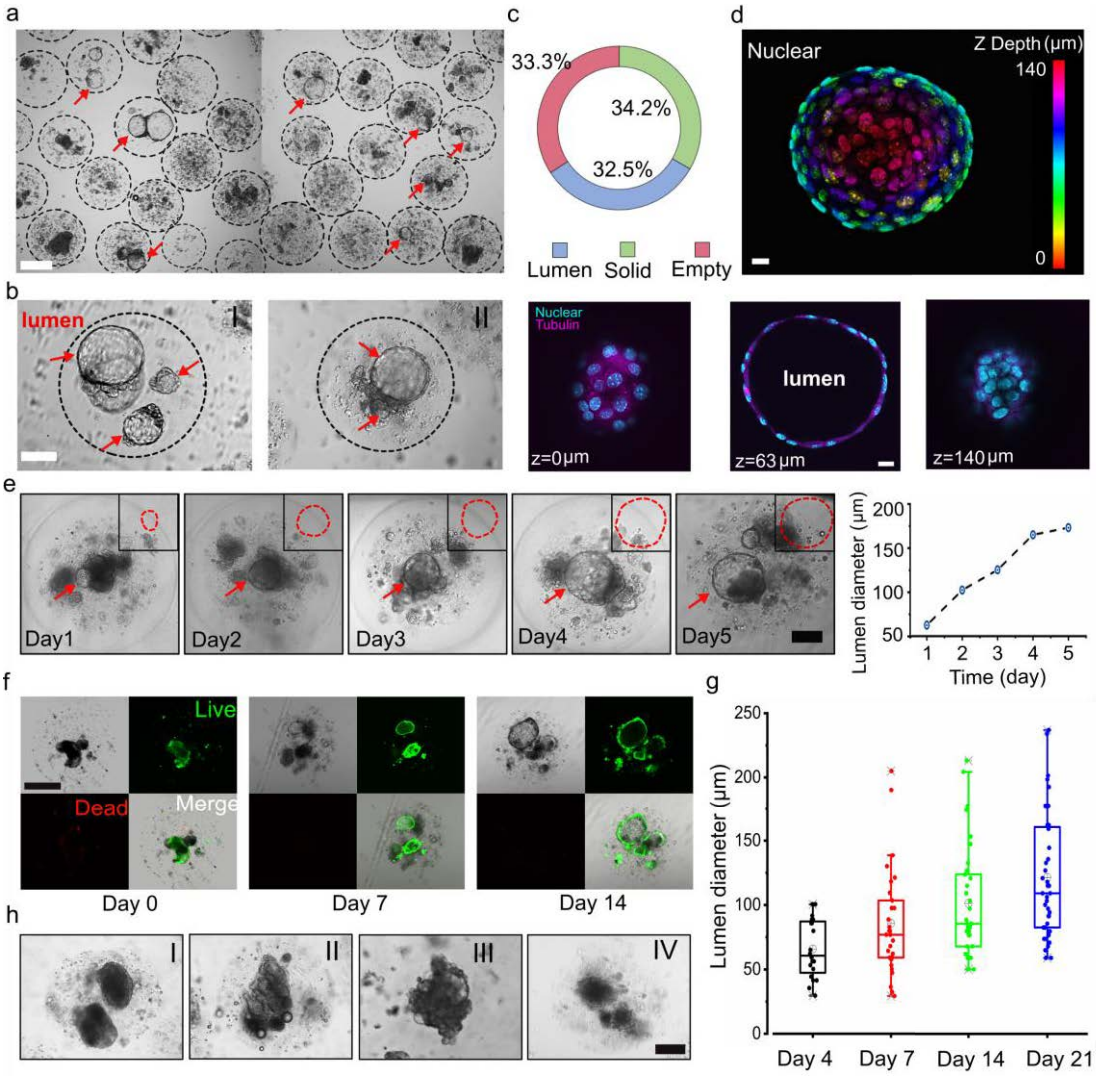

Figure 5–3 | Growth of the mammary tumour organoids in alginate microbeads. (a) High-throughput generation of mammary tumour organoids in the alginate microbeads. Scale bar: 200 μm. (b) Enlarged views of the luminal mammary tumour organoids in the microbeads. Scale bar: 100 μm. (c) Percentage of alginate beads containing lumen, solid organoid, and single cells, respectively. (d) 3D schematic of a 140 μm luminal organoids in the beads: nuclear mapping within the Z range (top) and cross-sectional view of nuclear & tubulin at the z=0, 63 and 140 μm, respectively. Scale bar: 10 μm. (e) Growth of the lumen within 5 days. Scale bar: 100 μm. (f) Viability of the mammary tumour organoids in the solid alginate microbeads at day 0, day 7 and day 14. Scale bar: 200 μm. (g) Lumen size of the organoids in the alginate microbeads. (h) Solid organoids with smooth boundary (I), blocky structures (II),” grape-like” structures (III) and discohesive clusters (IV). Scale bar: 100μm

were formed early, and some were late. These lumen structures were easily noticed under microscopy. **Figure 5-3a** shows the mammary tumour organoids in the microbeads after two-week culture. The enlarged view of the lumen was shown in **Figure 5-3b**. We characterized the organoids in the microbeads and found that around 32.5% of microbeads contained the cystic organoids, 34.2% of microbeads contained the solid organoids, and one-third of the microbeads contained nothing or single cells, as shown in Figure **5-3c**. To confirm the luminal structure, we stained the nuclear and the tubulin of the organoids and checked them under confocal microscopy. As shown in **Figure 5-3d**, the nuclear distribution in depth shows the hollow inside, which is also confirmed by the various-depth image. We tracked the growth of one lumen within 5 days, as shown in **Figure 5-3e**. The lumen diameter grew from around 60 μm to around 180 μm within 5 days, with a speed of about 30 μm/day. Size of the organoids here refers to their projected area.

We tracked the viability of the organoids at day 0, 7 and 14 (**Figure 5-3f**). It shows that the organoids in the microbeads kept high viability. We measured the lumen size statistically for up to three weeks, as shown in **Figure 5-3g**. It shows that the average lumen size can reach around 60 μm at day 4, 75 μm at day 7 and 85μm at day14 and 100 μm at day 21. The maximum size could exceed 200 μm. Some solid-type organoids derived from the chunks could also grow in alginate microbeads. Images under the bright-

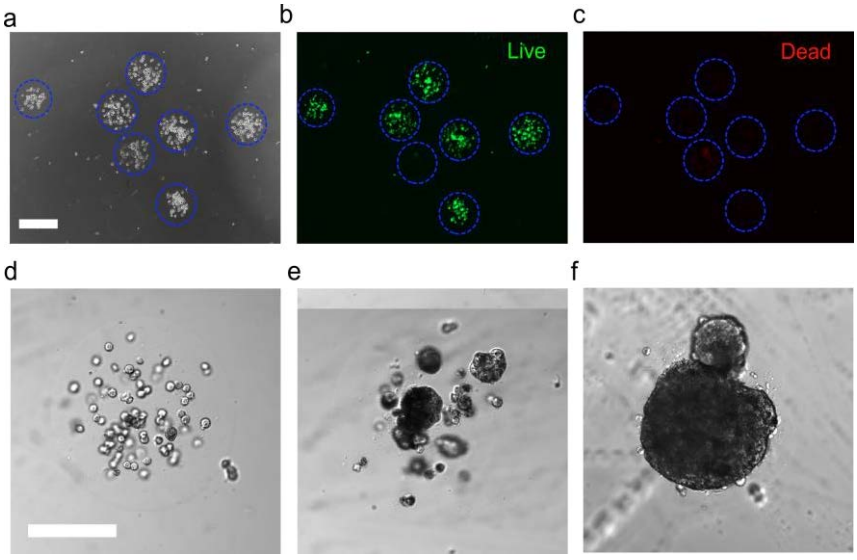

Figure 5–4 | MCF-7 cells in alginate microbeads. (a) Bright-field image of the single MCF-7 cells in the solid alginate beads. (b)&(c) Cell viability in the beads staining by Calcein-AM and propidium iodide. Scale bar: 200 μm. (d) After 2-week culture, most cells remain alive but no proliferation. (e) Small solid tumour formed in around 10% alginate beads. (f) Large solid tumour spheroid formed in around 10% alginate beads. Scale bar: 100 μm.

field microscopy, for instance, indicates the organoids with smooth boundary(I), the blocky structures (II), the 'grape-like' structures (III) and the discohesive clusters (IV), as shown in **Figure 5-3h**. The mammary cancer organoids with these phenotypes were also confirmed in the reference[251], where the organoids were developed in the BME.

As a control, MCF-7 cells were also embedded inside the alginate microbeads and cultured in the same medium, as shown in **Figure 5-4**. However, most of the cells could keep alive inside but showed no proliferation (**Figure 5-4d**). A small number of cells could grow into solid spheroids (**Figure 5-4 e&f**). But no lumen was observed. This indicates that the MCF-7 cell lines don't contain the luminal progenitor cells inside.

5.4.2 **Physiological characterization**

We investigate the Ki67 for proliferation, CD133 (tumour stem cell marker) and the fibronectin. Confocal microscopy was used to characterize the immunostaining results, as shown in **Figure 5-5**. According to the results, the luminal-type and solid-type organoids showed similar Ki67 expression. We measured the number of the $Ki67^+$ cells in the organoids and found around 8~10 $Ki67^+$ cells in each organoid. CD133 is the most commonly used marker of tumour stem cells, expressed in endothelial progenitor cells and mammary glands. As shown in **Figure 5-5b**, both luminal-type and solid-type organoids expressed the CD133. However, the luminal organoids seemed to have a higher expression. Fibronectin serves in cell adhesion, growth and migration, which is the most critical component of the extracellular matrix for organoid culture[256]. Here, fibronectin was also observed in the organoids. In the luminal-type organoids, the fibronectin could mostly be found at the joint of the lumen and solid organoids (**Figure 5-5c**). In the solid-type organoids, they mainly distributed at the edge. The H&E staining of the luminal and solid organoids showed similar structures to that in the fresh PyMT tumour tissues (**Figure 5-5d**), indicating the reconstitution capacity of the organoids developed in the alginate microbeads. This indicated that the organoids cultured in the alginate microbeads could maintain the primary activities.

5.4.3 **Cell compartments of organoids in alginate microbeads**

Mammary gland tissues contain both luminal and basal epithelial lineages. However, only the luminal cells consist of HR^+ and HR^- populations, whereas the basal cells only comprise the HR^- cells[254]. To confirm the luminal compartment in the alginate

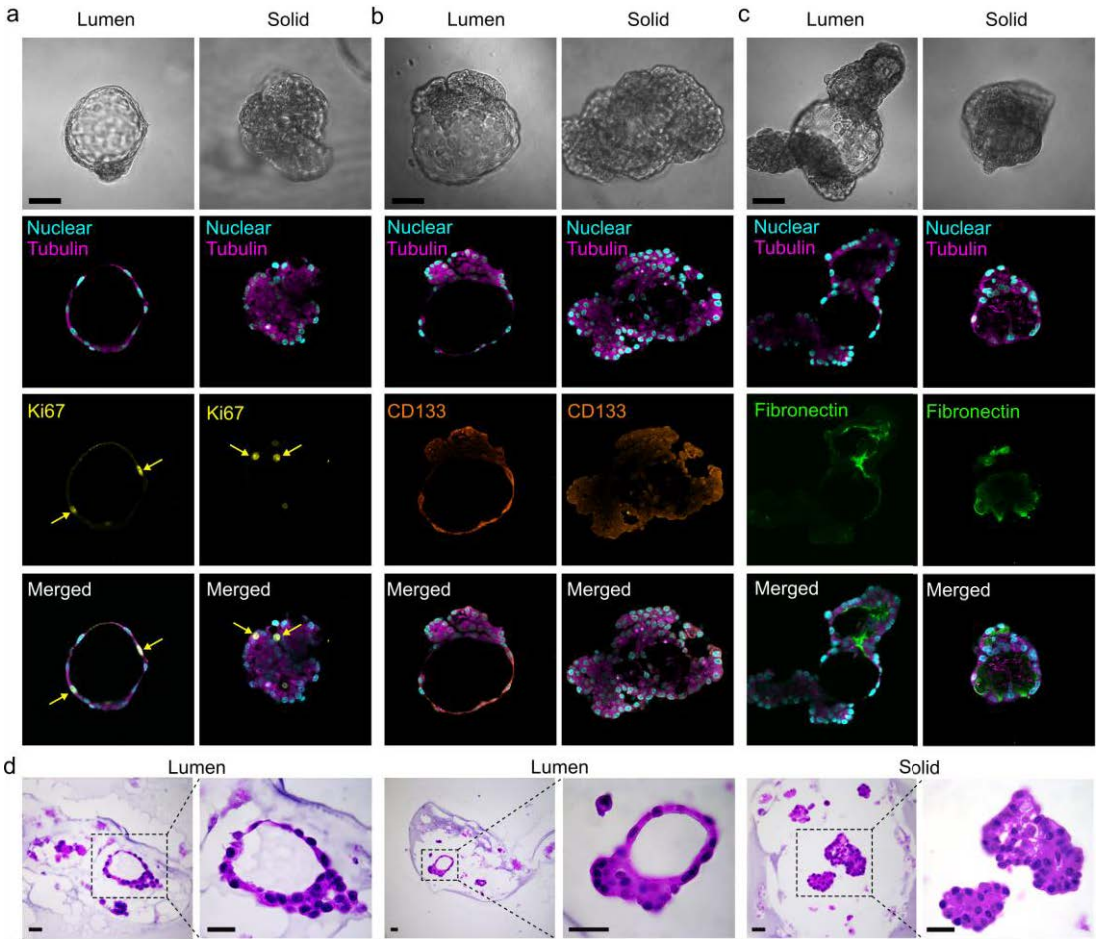

Figure 5–5| Immunostaining of the organoids developed in the alginate microbeads. (a) Ki67 expression in the luminal-type and solid-type organoids. (b) CD133 expression in the luminal-type and solid-type organoids. (c) Fibronectin expression in the luminal-type and solid-type organoids. Scale bar: 100 μm. (d) H&E staining of the organoids developed in the alginate microbeads. Scale bar: 50 μm.

microbeads, both PyMT fresh tumour and organoids collected from the microbeads were stained with the CD45/EpCAM/CD49f/SCA1/CD49b antibodies, then followed by the FACS analysis. As shown in **Figure 5-6 a&b**, the percentage of $CD45^+$ cell reduced from 6.65% in fresh tumour to 1.03% in alginate microbeads after two-week culture. This indicated that it is hard to preserve the immune cells in the alginate microbeads. In fresh tumour, luminal cells ($EpCAM^+$, CD49flo) and basal cells (EpCAMlo, CD49fhi) account for 72.9% and 6.53%, respectively. In alginate microbeads, luminal cells and basal cells account for 59.1% and 3.58%, respectively. Moreover, the HR^+ subpopulation (74.9%) among luminal cells in alginate microbeads is as much as that (77.4%) among luminal cells in the fresh tumour. This indicates that the alginate microbeads could preserve the luminal cells of the organoids, especially supporting the HR^+ cells. Immunostaining

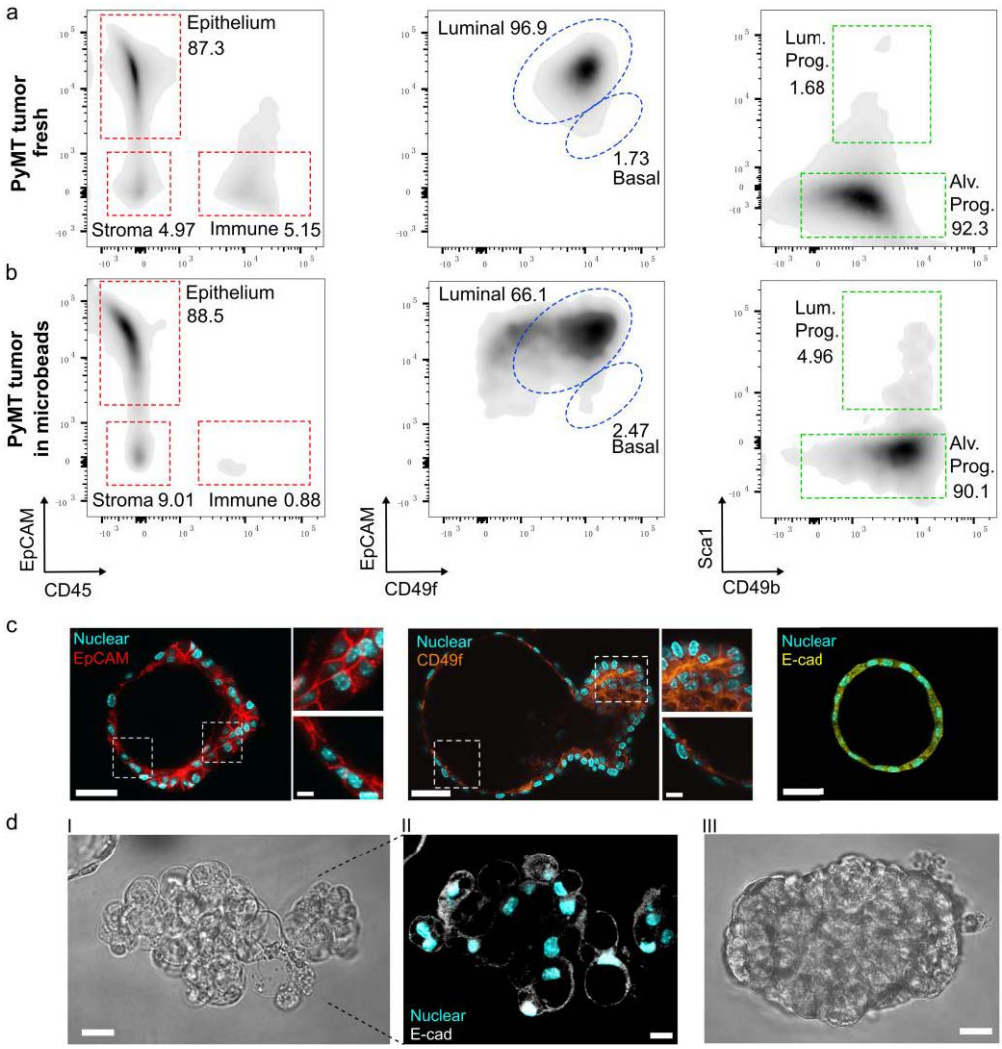

Figure 5–6| Organoid components characterization by FACS. (a) FACS results of the PyMT fresh tumour. (b) FACS results of the PyMT embedded in the alginate microbeads and cultured for 2 weeks. (c) Expression of EpCAM, CD49f and E-cad in the luminal organoids. Scale bar: 50 µm, 10 µm (inset). (d) Image of the structures with the lumen-forming potential (I, II) and without the lumen-forming potential (III). Scale bar: 20 µm.

results for EpCAM, CD49f and E-cad of the luminal organoids in the microbeads also confirmed the results from flow cytometry, as shown in **Figure 5-6c**. This indicates that the organoids developed in the alginate microbeads have the same cell compartments compared to the fresh tumour, except for the immune cells The formation potential of luminal structures can be distinguished from their deteriorated morphology compared to the solid ones (**Figure 5-6d**). FACS results indicate that the organoids developed in the alginate microbeads have a similar epithelial cell composition compared to the fresh tumour. Thus, alginate-encapsulated organoids resemble mammary tumours and could be a good candidate as an *in vitro* tumour model.

Lumen formation arises from the interplay of mechanics and biochemical signalling. Measuring the biomechanics[268], especially the luminal mechanics[269], has been the subject of intense scholarly debate. Various methods have been established to measure the luminal pressure, such as the micro pressure probe, gel deformation assay, pressure sensors, deformable beads, traction microscopy, and atomic force microscopy[57, 270, 271]. It is worth to mentioning that gel deformation assay is a non-invasive and direct method, enabling the relatively wide pressure range. For instance, alginate capsules created by electrospray were developed to measure the pressure loaded by the epithelium lumen[272]. This method could monitor the luminal pressure only when the lumen size grows comparable to that of the capsule size, which also requires the thin wall of the capsule. Here, we established the mechanical analysis of the luminal organoid in alginate microbeads based on the theory of the thick-wall pressure vessel model, which could estimate the mechanics during the whole development of the organoids.

As shown in **Figure 5-7a**, the luminal organoids in the alginate microbeads suffer the radial luminal pressure and the tangential stretching stress. We suppose that the organoid is at the centre of the microbeads. The parameters are set as shown in **Figure 5-7b**: a is the inner radius, b is the outer radius, r is the thickness of the wall, P is the luminal pressure. Considering the alginate as the linear elastic material[58], then we could have the TWPV model (b<10r). In the theory of the TWPV model, the outer radius would not change a lot with the expansion of the lumen, which was proved by our observation.

Figure 5-7c illustrates the bright-field image of the luminal organoid at the centre of the microbeads that could be analysed with the TWPV theory. To confirm the expansion instead of insertion of the luminal organoids in the alginate, fluorescent alginate was synthesized and used. The blank lumen indicated no alginate entered inside. Moreover, with the fluorescent alginate, the deformation of the microbeads was more prominent. According to the TWPV model, the luminal pressure can be given by[273]

$$P = \frac{-4G(b^3-a^3)}{2ma^4+ab^3}\Delta u \tag{5-1}$$

where m=(1-2v)/(1+v), v is the Poisson's ratio, G is the shear modulus of the material, Δu is the expansion displacement. The tangential stress along the radius can be given by[273]

$$\sigma_t = \frac{a^3P}{2(b^3-a^3)}\left(2+\frac{b^3}{x^3}\right) \tag{5-2}$$

where x is radius of interest between a and b.

Here, we assume the initial radius a of the lumen is 20 μm, the initial outer radius b of the microbeads is 230 μm, the shear modulus of the alginate is around 203 Pa[274]. The concentration of the alginate should be 1 wt%. However, when mixing the alginate with the cell centrifuged deposit, a small volume of the medium could be mixed, leading to the final concentration lower than 1 wt%. Thus, we referred to the shear modulus of around 0.7% alginate. According to equation (1), the relationship of luminal pressure and lumen radius is shown in **Figure 5-7 e-I**. We could see that when the luminal diameter reaches 150 μm, the luminal pressure is about 2 kPa. This value is lower than 3 kPa, which is applied by the solid tumour spheroid in the alginate capsule[58], and is close but a little bit higher than that 1.5±0.3 kPa generated by mammalian embryos (100 μm diameter)[275]. It also indicates that the luminal pressure of these organoids is much

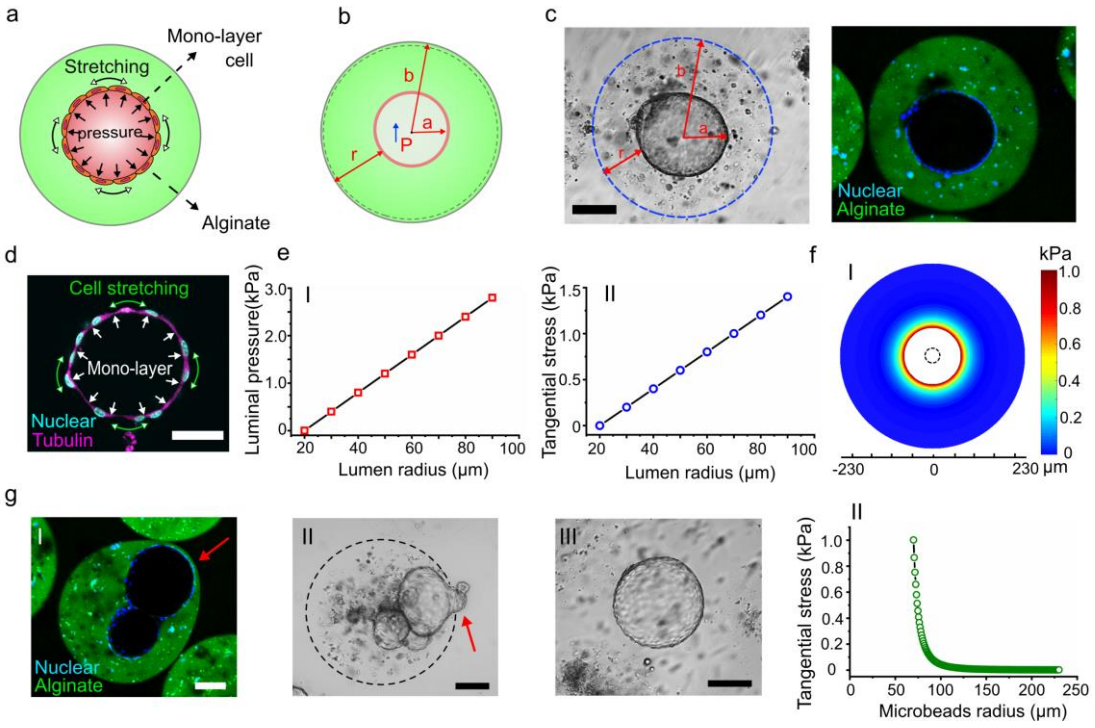

Figure 5–7 | Luminal mechanics analysis based on the microbeads. (a) Luminal pressure and stretching force of the luminal organoids in the alginate microbeads. (b)Luminal expansion model based on theory of the thick-wall pressure vessel and its main parameters. (c) Bright-field image of an organoid at the centra of the alginate microbeads and its expansion in fluorescent alginate microbeads. (d) Fluorescence image of the organoids with mono-layer cell connections. (e) Lumen radius versus the luminal pressure (I) and tangential stress (II). (f) Stress distribution on the microbeads when the luminal pressure is about 2 kPa (I), and its distribution along the radius (II). (g) Large organoids in alginate extrude the microbeads(I); luminal pressure leads to the hump exposed to the outside (II); large organoid released from the alginate microbeads (III). Scale bar: 100 μm.

higher than that 0.12 kPa of the epithelial lumen cultured in a scaffold-free medium[57]. According to equation (2), the tangential stretching stress and lumen radius relationship is shown in **Figure 5-7 e-II**. We could see that when the lumen diameter reaches 150 μm, the tangential stretching stress is around 1.1 kPa. According to the reference, the mono-layer cell can sustain this stress with approximately 20% extension[276]. The fluorescence image of the lumen in **Figure 5-7d** confirmed the mono-layer cell connections and the extended-like performance.

We also characterized the stress distribution on the deformed alginate microbeads along the radius when the luminal pressure is 2kPa, as shown in **Figure 5-7f**. The stress has a significantly decrease along the radius, which means that the whole size of the alginate

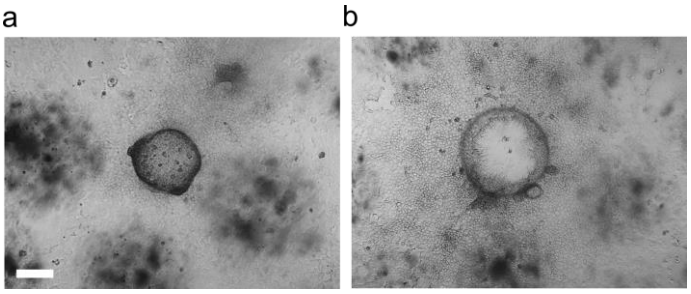

Figure 5–8 | Organoids released from microbeads grew in the dish. (a) Organoid that was released from the alginate microbeads attached on the dish. (b) The released organoid collapsed and grew into the spokewise shape. Scale bar:100μm.

microbeads would not change a lot in radius. Our observation confirmed this. We could also find some organoids with large size that extrudes the alginate microbeads during the culture, as shown in **Figure 5-7 g-I**. Some organoids with the surface exposed to the outside of the alginate can also form the hump caused by the high luminal pressure, as shown in **Figure 5-7 g-II**. Some organoids could be released from the alginate microbeads due to the extra-large size, as shown in **Figure 5-7 g-III**. The released organoids that attach to the cell culture dish could sustain the lumen for around 2 days and then collapse for further spokewise growth, as shown in **Figure 5-8**. In conclusion, the TWPV model combined with the alginate microbeads offers a simple and effective method to analyse the luminal mechanics of organoids.

5.4.4 **Anti-cancer drug screening**

Drug screening requires the high-throughput generation of the organoids. The microbeads definitely meet the demand. Here we focus on response from the luminal organoids. Doxorubicin and Latrunculin A are two typical FDA-approved drugs for mammary tumour. We loaded the microbeads into the agarose microwell array for further analyse. Before the treatment, the microbeads that contained the lumen costed a third of the total. After 24h treatment of the doxorubicin, the lumen collapsed and disappeared in the microbeads. No luminal organoids could be observed, as shown in **Figure 5-9a**. On the contrary, after 24h treatment of Latrunculin A, the lumens in microbeads still existed, as shown in **Figure 5-9b**. The enlarged view was shown in **Figure 5-9c**.

We hypothesized that the different response was caused by the action mechanism of the two drugs. Doxorubicin interacts with DNA by intercalation and inhibition of macromolecular biosynthesis. This inhibits the progression of topoisomerase II, an enzyme which relaxes supercoils in DNA for transcription. It may also increase quinone type free radical production, which may destroy the structure of the lumen structure. On the other, Latrunculin A affect polymerization of actin and the prevention of polymerizing of the actin filaments causes reversible changes in the morphology of mammalian cells. However, the cell-cell connection and ECM was kept intact, where we can still find the lumen structure. We monitored the viability of the organoids after the drug treatment with Calcein-AM and Propidium Iodide. As the fluorescence of doxorubicin overlaps with the Calcein-AM, the doxorubicin-treated organoids were only analysed with Propidium Iodide. **Figure 5-9d** shows the average fluorescent intensity of the dead cells after 2h and 24h. It indicates that after 2h treatment, the average intensity of dead cells was almost the same. After 24h, the intensity of the Latrunculin A group was a little higher than that of the doxorubicin group.

We also compared the drug uptake efficiency of the different-sized organoids. Doxorubicin was used because of its intrinsic fluorescence. After 2h treatment, the fluorescence was examined under confocal microscopy. As shown in **Figure 5-9 e&f**, a noticeable trend was observed: organoids with larger size showed higher uptake of the doxorubicin. Inspired by the research[277-279], we hypothesised that large organoids sustained strong mechanics, leading to more cells' considerable stretching and

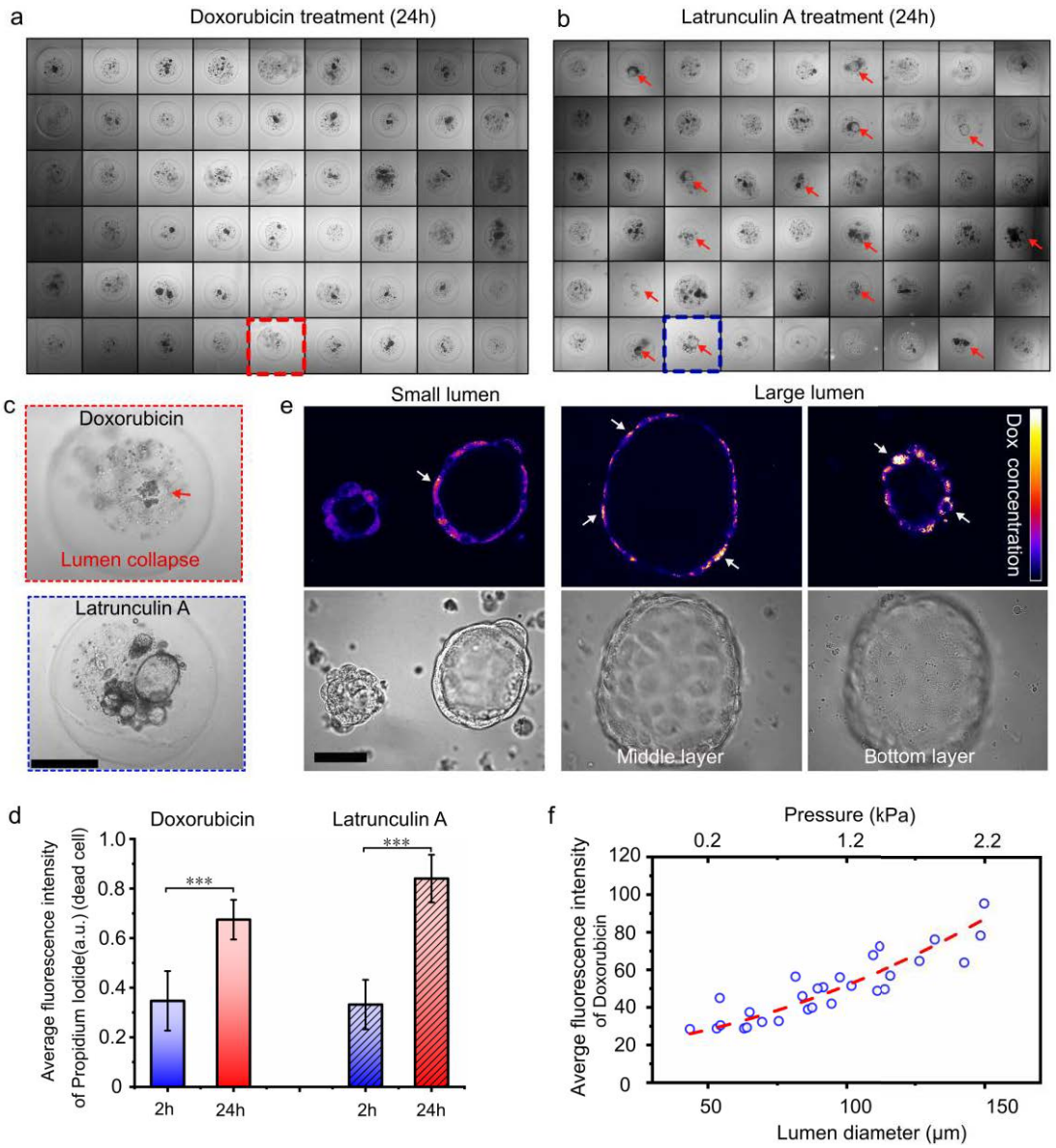

Figure 5–9 | Schematic of the drug screening. (a) Organoids in the agarose array after 24h treatment of doxorubicin: no lumen could be observed. (b) Organoids in the agarose array after 24h treatment of Latrunculin A: lumen could be observed. Red arrows indicate the lumens. (c) Enlarged view of the lumen after the drug treatment. Scale bar: 200μm. (d) Quantification of dead cells after the drug treatment. (mean±sd, n=10, *** p<0.001). (e) Fluorescence images of doxorubicin uptake in different-size organoids. Scale bar: 50 μm. (f) Quantification of the doxorubicin uptake in different-size organoids.

deformation. These mechanics allows higher drug uptake. This indicates that the mammary tumour organoids in the alginate microbeads show a promising application in drug screening.

5.4.5 **Discussion**

Alginate has been widely used as a hydrogel for 3D cell culture and biomedical applications. However, in most cases, the alginate needs to be functionalized with the arginylglycylaspartic acid (RGD) peptide for cell adhesion. Here, we found that the mouse tumour chunks in the alginate without any functionalization can grow into the tumour organoids, especially the luminal type. Thus, pure alginate can maintain the tumour tissues inside and further support the development of the small chunks into organoids. Indeed, we found that some microbeads that only contain the single cells inside can also form the solid-type and luminal type mammary organoids inside. This indicates that even the single progenitor cells in the alginate can grow into organoids within proper activation from growth factors. Thus, this platform can be extended for the establishment of single cell-derived mammary tumour organoids.

We also found that luminal-type organoids in the alginate microbeads did not form the lumen simultaneously. Some lumens occurred after one-day culture. However, some appeared after 3~4-day culture. This indicated that the luminal progenitor cells in the alginate microbeads might under different situations (perhaps different cell cycle) and thus start the luminal formation at different time.

Immunostaining and FACS results indicated that the organoids in the alginate microbeads remain suitable activities and have similar cell compartments compared to the fresh tumour. Unfortunately, the immune cells in the alginate were almost lost during the long-time culture, which may be caused by the lack of relevant growth factors in the medium. It is expected that the platform could also be used to study the interactions between tumour organoids and immune cells by further optimizing the culture mediums for the immune cells.

Herein, the organoids were derived from the mouse PyMT mammary tumour. Due to the limitation of cell source, we did not use the patient/human tumour tissues. Thus, in the future, human mammary tumour tissues could be applied on this platform to test their capacities, which would be more significant for mammary drug screening. Moreover, other kinds of solid tumour can also be tested in the alginate microbeads to explore their potential applications.

Since alginate cannot support the development of single-cell derived tumour organoids, developing the Matrigel/BME2-based droplet technique is highly required. Many works have been tried and prove the feasibility when the situations are fully optimized[79, 80]. However, some issues still exist, such as the complicated system, fragile microbeads and so on. Thus, in this case, developing new hydrogels or enhance the Matrigel compacity is required for high-throughput and low-cost culture, such as exploring the alginate-Matrigel-based hydrogels.

5.5 Conclusions

In this work, mouse mammary tumour organoids, especially the luminal type, were developed in the pure alginate microbeads in a high-throughput way on the microfluidic device. Immunostaining and FACS results indicated that the established organoids can maintain basic activities and showed similar cell compartment compared to the fresh *in vivo* tumour. A TWPV model based on the deformation of the alginate microbeads was established to analyze the mechanics of the luminal organoids. Finally, the organoids on the agarose array were used for the drug screen. Results indicated that the organoids showed an obviously different response to Doxorubicin and Latrunculin A. Size-dependent drug uptake was also observed. This platform offers a versatile and low-cost strategy for luminal-mechanics analysis, high-throughput generation and drug screening of mammary tumour organoids.

Chapter 6 Conclusions and future work

This thesis focuses on combining microfluidics, microfabrication and 3D cell culture to create new tools to investigate the multicellular spheroids and organoids, to optimize the microenvironment for *in vitro* culturing the spheroids and organoids, and to increase the yield of these 3D models for high-throughput analysis. This thesis made several concrete advances in terms of spheroids and organoids on the chip. For studying the size-mediated tumour spheroids, this thesis proposed the generation of gradient-sized spheroids on a single chip. To further investigate the tumour spheroids and their neighbouring cells, the novel unidirectional communication was proposed to avoid the crosstalk and offer continuous effect. To evaluate the mechanical effect on these 3D models, a microfluidic chip was designed for human colon tumour organoids to mimic the peristalsis in a high-throughput manner. To increase the yield and save the cost, alginate microbeads was developed to establish mouse mammary tumour organoids. This thesis opened up some new exciting research in the spheroids and organoids on a chip.

6.1 Conclusions

In this thesis, we first started with the simple tumour spheroids. Conventional generation of tumour spheroids can only allow the uniform-sized or random-sized spheroids. It remains challenging to generate multi-sized tumour spheroids. Here, the strategy of generating gradient-sized spheroids was proposed. Thus, the sized-dependent growth, drug penetration and response could be easily investigated on this chip. It is also proved that co-culturing multi-types of cells to generate more functional spheroids can be achieved. The size-modulation ability can reach 12.8 folds. The method only requires a simple commercial 3D printer for mould fabrication, allowing the investigation of size-mediated spheroids behaviours for biological researchers.

To replicate the *in-vivo* tumour microenvironment, co-culturing the tumour spheroids with other cells, such as stromal cells, is essential. Conventional co-culture methods cannot avoid the cellular crosstalk or cannot offer the continuous effect. In this thesis, we developed unidirectional communication on the chip by controlling the flow direction. Based on this method, we studied the unidirectional communication of breast tumour spheroids with stromal cells. We observed the transformation from normal fibroblasts/ MSCs to cancer-associated fibroblasts under the unidirectional communication with

invasive tumour spheroids. This facilitates the understanding of CAF formation in the tumour microenvironment. TGF-β1 was also proved to be the main factors that induce the transformation. The developed chip offers a new and effective tool for the study of cellular communication.

We further plan to introduce the mechanical cues in the microenvironment for the 3D model culture. Although many works have been developed to apply the mechanical stimulus on tumour spheroids, it is still challenging to apply the mechanical stimuli on the organoids. Here, in this thesis, we designed a chip that enabled the peristalsis of human colon tumour organoids in a high-throughput way. Compared with conventional strategies, the chip allows the contraction of these organoids individually and parallelly. The organoids under peristalsis showed enhanced expression of Lgr5 and Ki67, indicating the critical role of mechanical cues during the development of organoids. Organoids under peristalsis also exhibited different drug response. This proposed strategy can also be applied to other organoids and will ensure more reliable organoids.

Drug screening requires a high-throughput analysis of organoids for more reliable results. However, the conventional culturing organoids in the Matrigel dome hinders the yield and increase the cost due to the expensive Matrigel. Here, we found the culture of mammary tumour organoids can be established in alginate. Thus, alginate-based droplet technology could enhance the yield of mammary tumour organoids, especially luminal-type organoids. The compartment of mammary tumour organoids in alginate microbeads is almost the same as the fresh tumour except for the loss of immune cells. Interestingly, luminal mechanics of the organoids can be measured based on the deformation of the alginate microbeads, which is essential to the epithelial organoids. Size-dependent Dox accumulation was also observed in the luminal organoids, hypothesized to be related to mechanics.

Thus, this thesis bridged several gaps in the spheroids and organoids culture on the chip. All aim to produce more reliable 3D models, and increase the efficiency and reduce the cost for high-throughput analysis with these 3D models.

6.2 Future work

6.2.1 Patient-derived organoids on the chip for more characterization

In this thesis, the human colon tumour organoids were obtained from the ATCC® (American Type Culture Collection), and the mammary tumour organoids were derived from the tumour-bearing mice. We have developed the direct patient-derived organoids on the chip, which may slightly affect the reliability. Thus, we hope to find more collaborations to apply the patient-derived organoids on the proposed chips in the future.

We have not further characterised the chip-developed organoids with gene sequencing to analyze the organoids at the gene level due to the resource limitation. We believe the human colon tumour organoids under peristalsis should have different gene expression compared with that cultured statically. Similarly, the mammary tumour organoids cultured in the alginate microbeads should also correspond with the fresh tumour at the gene level.

Meanwhile, more drugs could be screened on the developed platforms to evaluate their efficiency.

6.2.2 Matrigel droplet for human colon tumour organoids

Matrigel and BME2 gel are suitable for the development of most organoids. The gelation of these hydrogels requires incubation at 37ºC for at least 30 mins, which hinders the high-throughput generation of Matrigel droplets/microbeads. However, in theory, the Matrigel microbeads can be generated by the microfluidic droplet techniques. I tried to generate the Matrigel microbeads on a microfluidic chip. The experiments were operated

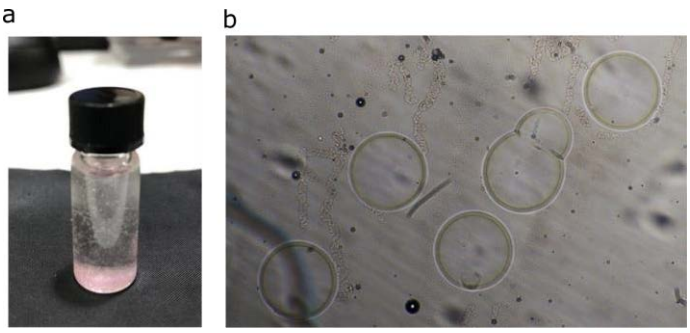

Figure 6–1| Matrigel microbeads generation. (a) Matrigel droplets in mineral oil. (b) Matrigel microbeads in aqueous medium. After gelation, Matrigel microbeads were transferred from mineral oil to PBS.

in a cold room to avoid gelation during dispensing. Matrigel droplets can be easily generated and collected in the mineral oil (**Figure 6-1a**). Then the Matrigel droplets were put in the 37ºC incubator for 30 mins for gelation. However, I found that during the gelation, some microbeads would stick together. In this case, the surfactant Span80 may be optimized or replaced by other surfactants. Furthermore, transferring the Matrigel microbeads from mineral oil to an aqueous medium was difficult. During the transformation, some Matrigel microbeads were broken due to the fragileness. Only a fraction of microbeads can be moved into the culture medium (**Figure 6-1b**). Thus, a mild way to transferring the microbeads is required. In the future, I will continue investigating the Matrigel microbeads by microfluidic droplet techniques. This will benefit the high-throughput analysis for most organoids.

6.2.3 **Heterogeneous uptake of nanoparticles in human colon tumour organoids**

In chapter 4, during the co-culture of human colon tumour organoids with micellar nanoparticles, we found that the uptake of the nanoparticles in the organoids was heterogeneous (**Figure 6-2**). Some cells exhibited higher uptake of the nanoparticles. We

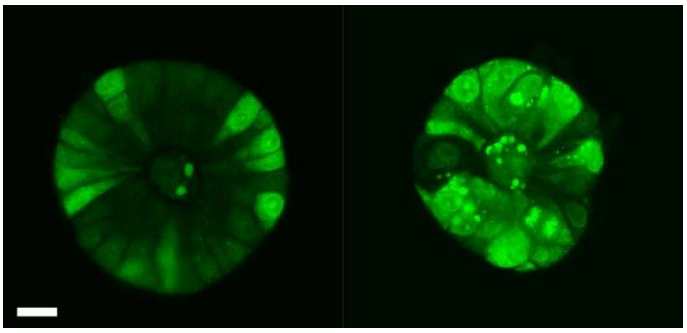

Figure 6-2 | Heterogeneous uptake of the micelle nanoparticle in human colon tumour organoids. Scale bar: 20 µm.

hypothesized that 1) these cells may be under high proliferation or metabolism, thus showed higher uptake; 2) these are the special cells such as the $Lgr5^{+}$ cells, which are responsible for the renewal or differentiation. Thus, exploring the mechanism of heterogeneous uptake may help to open a new way to enhance the efficiency of nanomedicine.

Appendix I

Video 1 Deformation of microwells under periodical pressure

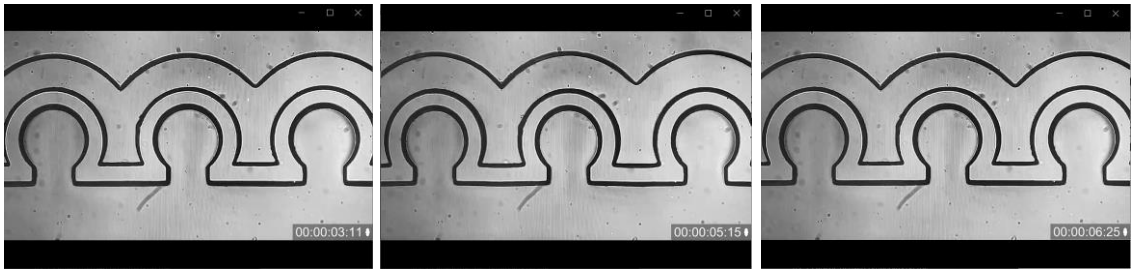

Video 2 Large-lumen organoid under pressure of 50, 150 and 250 kPa

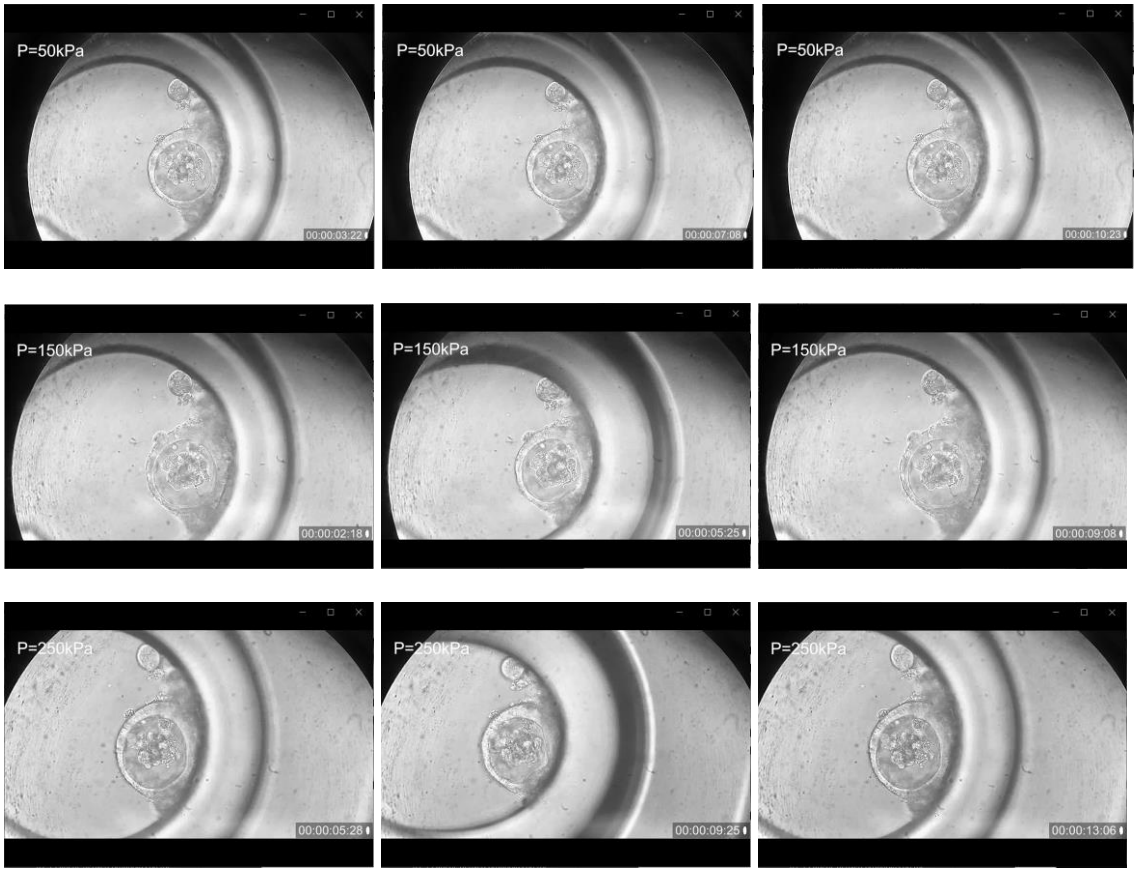

Video 3 Small-lumen organoid under pressure of 50, 150 and 250 kPa

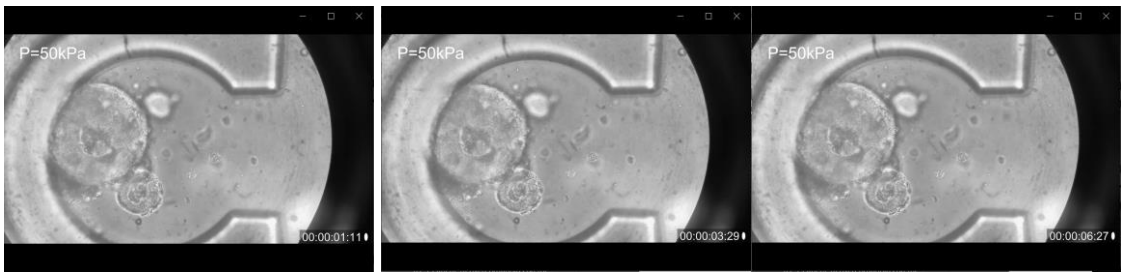

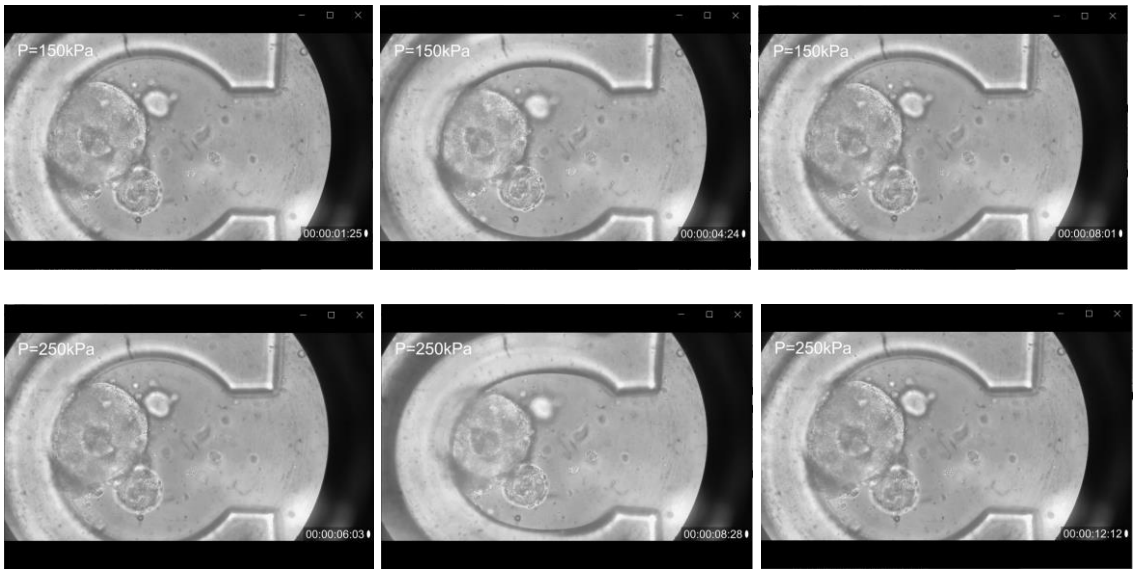

Video 4 Other kinds of organoids in microwells

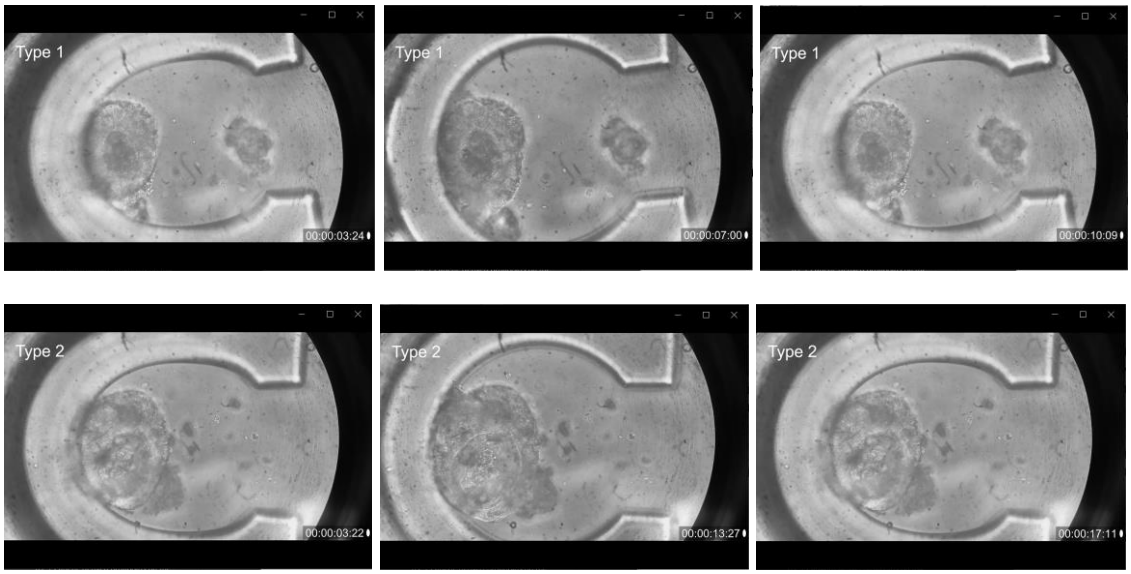

Video 5 Two organoids in one microwell

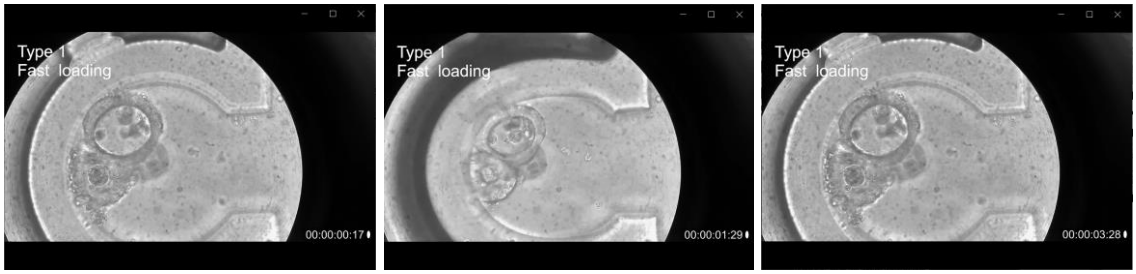

Video 6 Organoids at different positions in microwell

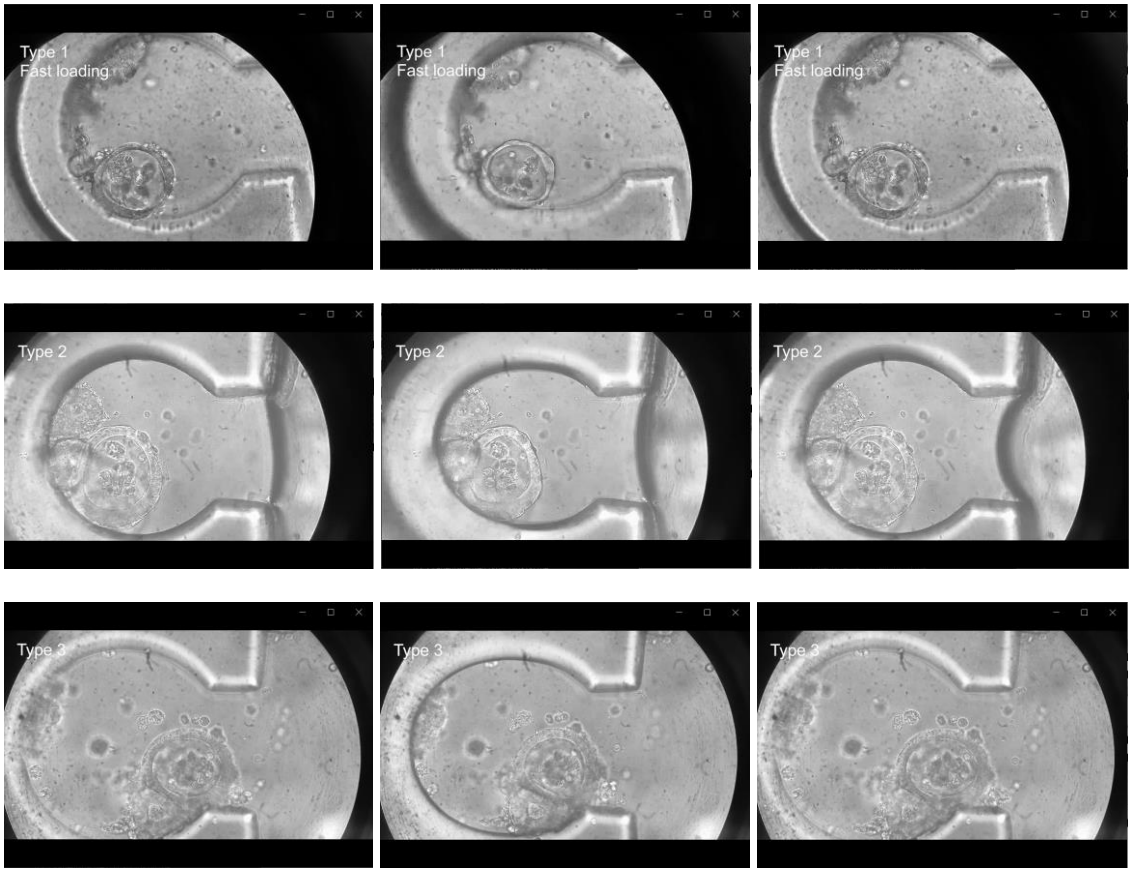

References

[1] B.M. Baker, C.S. Chen, Deconstructing the third dimension: how 3D culture microenvironments alter cellular cues, J Cell Sci 125(Pt 13) (2012) 3015-24.
[2] M. Kapalczynska, T. Kolenda, W. Przybyla, M. Zajaczkowska, A. Teresiak, V. Filas, M. Ibbs, R. Blizniak, L. Luczewski, K. Lamperska, 2D and 3D cell cultures - a comparison of different types of cancer cell cultures, Arch Med Sci 14(4) (2018) 910-919.
[3] Global 3D Cell Culture Market Size & Share Report, 2020-2027, 2021. https://www.grandviewresearch.com/industry-analysis/3d-cell-culture-market.
[4] F. Hirschhaeuser, H. Menne, C. Dittfeld, J. West, W. Mueller-Klieser, L.A. Kunz-Schughart, Multicellular tumour spheroids: an underestimated tool is catching up again, J Biotechnol 148(1) (2010) 3-15.
[5] R.Z. Lin, H.Y. Chang, Recent advances in three-dimensional multicellular spheroid culture for biomedical research, Biotechnol J 3(9-10) (2008) 1172-84.
[6] K. Moshksayan, N. Kashaninejad, M.E. Warkiani, J.G. Lock, H. Moghadas, B. Firoozabadi, M.S. Saidi, N.-T. Nguyen, Spheroids-on-a-chip: Recent advances and design considerations in microfluidic platforms for spheroid formation and culture, Sensors and Actuators B: Chemical 263 (2018) 151-176.
[7] H.-W. Han, S. Asano, S.-h. Hsu, Cellular Spheroids of Mesenchymal Stem Cells and Their Perspectives in Future Healthcare, Applied Sciences 9(4) (2019).
[8] X. Cui, Y. Hartanto, H. Zhang, Advances in multicellular spheroids formation, J R Soc Interface 14(127) (2017).
[9] M. Azharuddin, K. Roberg, A.K. Dhara, M.V. Jain, P. Darcy, J. Hinkula, N.K.H. Slater, H.K. Patra, Dissecting multi drug resistance in head and neck cancer cells using multicellular tumour spheroids, Sci Rep 9(1) (2019) 20066.
[10] R. Barrera-Rodriguez, J.M. Fuentes, Multidrug resistance characterization in multicellular tumour spheroids from two human lung cancer cell lines, Cancer Cell Int 15 (2015) 47.
[11] J.M. Santos, S.P. Camoes, E. Filipe, M. Cipriano, R.N. Barcia, M. Filipe, M. Teixeira, S. Simoes, M. Gaspar, D. Mosqueira, D.S. Nascimento, O.P. Pinto-do, P. Cruz, H. Cruz, M. Castro, J.P. Miranda, Three-dimensional spheroid cell culture of umbilical cord tissue-derived mesenchymal stromal cells leads to enhanced paracrine induction of wound healing, Stem Cell Res Ther 6 (2015) 90.
[12] Y. Li, E. Kumacheva, hydrogel microenvironments for cancer spheroid growth and drug screening Science Advances 4(eaas:8998) (2018).
[13] H. Clevers, Modeling Development and Disease with Organoids, Cell 165(7) (2016) 1586-1597.
[14] M. Simian, M.J. Bissell, Organoids: A historical perspective of thinking in three dimensions, J Cell Biol 216(1) (2017) 31-40.
[15] N. Picollet-D'hahan, M.E. Dolega, D. Freida, D.K. Martin, X. Gidrol, Deciphering Cell Intrinsic Properties: A Key Issue for Robust Organoid Production, Trends Biotechnol 35(11) (2017) 1035-1048.
[16] A. Manfrin, Y. Tabata, E.R. Paquet, A.R. Vuaridel, F.R. Rivest, F. Naef, M.P. Lutolf, Engineered signaling centers for the spatially controlled patterning of human pluripotent stem cells, Nat Methods 16(7) (2019) 640-648.

[17] G.S. Lim, J.H. Hor, N.R.Y. Ho, C.Y. Wong, S.Y. Ng, B.S. Soh, H. Shao, Microhexagon gradient array directs spatial diversification of spinal motor neurons, Theranostics 9(2) (2019) 311-323.
[18] M.R. Carvalho, D. Barata, L.M. Teixeira, S. Giselbrecht, R.L. Reis, J.M. Oliveira, R. Truckenmüller, P. Habibovic, Colorectal tumour-on-a-chip system: A 3D tool for precision onco-nanomedicine, Science Advances 5(eaaw:1317) (2019).
[19] P. Rifes, M. Isaksson, G.S. Rathore, P. Aldrin-Kirk, O.K. Moller, G. Barzaghi, J. Lee, K.L. Egerod, D.M. Rausch, M. Parmar, T.H. Pers, T. Laurell, A. Kirkeby, Modeling neural tube development by differentiation of human embryonic stem cells in a microfluidic WNT gradient, Nat Biotechnol 38(11) (2020) 1265-1273.
[20] W. Lim, S. Park, A Microfluidic Spheroid Culture Device with a Concentration Gradient Generator for High-Throughput Screening of Drug Efficacy, Molecules 23(12) (2018).
[21] T. Mulholland, M. McAllister, S. Patek, D. Flint, M. Underwood, A. Sim, J. Edwards, M. Zagnoni, Drug screening of biopsy-derived spheroids using a self-generated microfluidic concentration gradient, Sci Rep 8(1) (2018) 14672.
[22] O. Frey, P.M. Misun, D.A. Fluri, J.G. Hengstler, A. Hierlemann, Reconfigurable microfluidic hanging drop network for multi-tissue interaction and analysis, Nat Commun 5 (2014) 4250.
[23] Z. Zhang, Y.C. Chen, S. Urs, L. Chen, D.M. Simeone, E. Yoon, Scalable Multiplexed Drug-Combination Screening Platforms Using 3D Microtumour Model for Precision Medicine, Small 14(42) (2018) e1703617.
[24] B. Schuster, M. Junkin, S.S. Kashaf, I. Romero-Calvo, K. Kirby, J. Matthews, C.R. Weber, A. Rzhetsky, K.P. White, S. Tay, Automated microfluidic platform for dynamic and combinatorial drug screening of tumour organoids, Nat Commun 11(1) (2020) 5271.
[25] D. Baptista, L.M. Teixeira, Z.T. Birgani, S. van Riet, T. Pasman, A. Poot, D. Stamatialis, R.J. Rottier, P.S. Hiemstra, P. Habibovic, C. van Blitterswijk, S. Giselbrecht, R. Truckenmuller, 3D alveolar in vitro model based on epithelialized biomimetically curved culture membranes, Biomaterials 266 (2021) 120436.
[26] M. Nikolaev, O. Mitrofanova, N. Broguiere, S. Geraldo, D. Dutta, Y. Tabata, B. Elci, N. Brandenberg, I. Kolotuev, N. Gjorevski, H. Clevers, M.P. Lutolf, Homeostatic mini-intestines through scaffold-guided organoid morphogenesis, Nature 585(7826) (2020) 574-578.
[27] J.A. Brassard, M. Nikolaev, T. Hubscher, M. Hofer, M.P. Lutolf, Recapitulating macro-scale tissue self-organization through organoid bioprinting, Nat Mater 20(1) (2021) 22-29.
[28] T. Sato, H. Clevers, Growing Self-Organizing Mini-Guts from a Single Intestinal Stem Cell: Mechanism and Applications, Science 340 (2013) 1190-1194.
[29] Y. Wang, D.B. Gunasekara, M.I. Reed, M. DiSalvo, S.J. Bultman, C.E. Sims, S.T. Magness, N.L. Allbritton, A microengineered collagen scaffold for generating a polarized crypt-villus architecture of human small intestinal epithelium, Biomaterials 128 (2017) 44-55.
[30] Y. Wang, R. Kim, D.B. Gunasekara, M.I. Reed, M. DiSalvo, D.L. Nguyen, S.J. Bultman, C.E. Sims, S.T. Magness, N.L. Allbritton, Formation of Human Colonic Crypt Array by Application of Chemical Gradients Across a Shaped Epithelial Monolayer, Cell Mol Gastroenterol Hepatol 5(2) (2018) 113-130.

[31] J. Creff, R. Courson, T. Mangeat, J. Foncy, S. Souleille, C. Thibault, A. Besson, L. Malaquin, Fabrication of 3D scaffolds reproducing intestinal epithelium topography by high-resolution 3D stereolithography, Biomaterials 221 (2019) 119404.
[32] Z. Ma, J. Wang, P. Loskill, N. Huebsch, S. Koo, F.L. Svedlund, N.C. Marks, E.W. Hua, C.P. Grigoropoulos, B.R. Conklin, K.E. Healy, Self-organizing human cardiac microchambers mediated by geometric confinement, Nat Commun 6 (2015) 7413.
[33] P. Hoang, J. Wang, B.R. Conklin, K.E. Healy, Z. Ma, Generation of spatial-patterned early-developing cardiac organoids using human pluripotent stem cells, Nat Protoc 13(4) (2018) 723-737.
[34] M. Bosch-Fortea, A.E. Rodriguez-Fraticelli, G. Herranz, M. Hachimi, M.D. Barea, J. Young, B. Ladoux, F. Martin-Belmonte, Micropattern-based platform as a physiologically relevant model to study epithelial morphogenesis and nephrotoxicity, Biomaterials 218 (2019) 119339.
[35] J. Kim, Y. Zheng, A.A. Alobaidi, H. Nan, J. Tian, Y. Jiao, B. Sun, Geometric Dependence of 3D Collective Cancer Invasion, Biophys J 118(5) (2020) 1177-1182.
[36] S. Wei, L. Hongxu, N. Kawazoe, C. Guoping, Gradient patterning and differentiation of mesenchymal stem cells on micropatterned polymer surface, Journal of Bioactive and Compatible Polymers 26(3) (2011) 242-256.
[37] E. Wang, D. Wang, A. Geng, R. Seo, X. Gong, Growth of hollow cell spheroids in microbead templated chambers, Biomaterials 143 (2017) 57-64.
[38] M. Marimuthu, N. Rousset, A. St-Georges-Robillard, M.A. Lateef, M. Ferland, A.M. Mes-Masson, T. Gervais, Multi-size spheroid formation using microfluidic funnels, Lab Chip 18(2) (2018) 304-314.
[39] W. Liu, M. Sun, B. Lu, M. Yan, K. Han, J. Wang, A microfluidic platform for multi-size 3D tumour culture, monitoring and drug resistance testing, Sensors and Actuators B: Chemical 292 (2019) 111-120.
[40] A. Pasturel, P.O. Strale, V. Studer, Tailoring Common Hydrogels into 3D Cell Culture Templates, Adv Healthc Mater 9(18) (2020) e2000519.
[41] Y. Ma, M. Lin, G. Huang, Y. Li, S. Wang, G. Bai, T.J. Lu, F. Xu, 3D Spatiotemporal Mechanical Microenvironment: A Hydrogel-Based Platform for Guiding Stem Cell Fate, Adv Mater 30(49) (2018) e1705911.
[42] P. Romani, L. Valcarcel-Jimenez, C. Frezza, S. Dupont, Crosstalk between mechanotransduction and metabolism, Nat Rev Mol Cell Biol 22(1) (2021) 22-38.
[43] K.H. Vining, D.J. Mooney, Mechanical forces direct stem cell behaviour in development and regeneration, Nat Rev Mol Cell Biol 18(12) (2017) 728-742.
[44] A. Marturano-Kruik, M.M. Nava, K. Yeager, A. Chramiec, L. Hao, S. Robinson, E. Guo, M.T. Raimondi, G. Vunjak-Novakovic, Human bone perivascular niche-on-a-chip for studying metastatic colonization, Proc Natl Acad Sci U S A 115(6) (2018) 1256-1261.
[45] K. Rennert, S. Steinborn, M. Groger, B. Ungerbock, A.M. Jank, J. Ehgartner, S. Nietzsche, J. Dinger, M. Kiehntopf, H. Funke, F.T. Peters, A. Lupp, C. Gartner, T. Mayr, M. Bauer, O. Huber, A.S. Mosig, A microfluidically perfused three dimensional human liver model, Biomaterials 71 (2015) 119-131.
[46] K.A. Homan, N. Gupta, K.T. Kroll, D.B. Kolesky, M. Skylar-Scott, T. Miyoshi, D. Mau, M.T. Valerius, T. Ferrante, J.V. Bonventre, J.A. Lewis, R. Morizane, Flow-enhanced vascularization and maturation of kidney organoids in vitro, Nat Methods 16(3) (2019) 255-262.

[47] Yesl Jun, JaeSeo Lee, Seongkyun Choi, Ji Hun Yang, Maike Sander, Seok Chung, S.-H. Lee, In vivo–mimicking microfluidic perfusion culture of pancreatic islet spheroids, science Advances 5(eaax:4520) (2019).
[48] K.K. Lee, H.A. McCauley, T.R. Broda, M.J. Kofron, J.M. Wells, C.I. Hong, Human stomach-on-a-chip with luminal flow and peristaltic-like motility, Lab Chip 18(20) (2018) 3079-3085.
[49] E. Berger, C. Magliaro, N. Paczia, A.S. Monzel, P. Antony, C.L. Linster, S. Bolognin, A. Ahluwalia, J.C. Schwamborn, Millifluidic culture improves human midbrain organoid vitality and differentiation, Lab Chip 18(20) (2018) 3172-3183.
[50] X. Qian, H.N. Nguyen, M.M. Song, C. Hadiono, S.C. Ogden, C. Hammack, B. Yao, G.R. Hamersky, F. Jacob, C. Zhong, K.J. Yoon, W. Jeang, L. Lin, Y. Li, J. Thakor, D.A. Berg, C. Zhang, E. Kang, M. Chickering, D. Nauen, C.Y. Ho, Z. Wen, K.M. Christian, P.Y. Shi, B.J. Maher, H. Wu, P. Jin, H. Tang, H. Song, G.L. Ming, Brain-Region-Specific Organoids Using Mini-bioreactors for Modeling ZIKV Exposure, Cell 165(5) (2016) 1238-1254.
[51] H.M. Poling, D. Wu, N. Brown, M. Baker, T.A. Hausfeld, N. Huynh, S. Chaffron, J.C.Y. Dunn, S.P. Hogan, J.M. Wells, M.A. Helmrath, M.M. Mahe, Mechanically induced development and maturation of human intestinal organoids in vivo, Nat Biomed Eng 2(6) (2018) 429-442.
[52] M. Elsaadany, M. Harris, E. Yildirim-Ayan, Design and Validation of Equiaxial Mechanical Strain Platform, EQUicycler, for 3D Tissue Engineered Constructs, Biomed Res Int 2017 (2017) 3609703.
[53] H. Lv, J. Dong, Y. Qiu, Y. Yang, Y. Zhu, Microflow in a rhythmically expanding alveolar chip with dynamic similarity, Lab Chip 20(13) (2020) 2394-2402.
[54] Y. Li, M. Chen, J. Hu, R. Sheng, Q. Lin, X. He, M. Guo, Volumetric Compression Induces Intracellular Crowding to Control Intestinal Organoid Growth via Wnt/beta-Catenin Signaling, Cell Stem Cell (2020).
[55] K. Sakthivel, H. Kumar, M.G.A. Mohamed, B. Talebjedi, J. Shim, H. Najjaran, M. Hoorfar, K. Kim, High Throughput Screening of Cell Mechanical Response Using a Stretchable 3D Cellular Microarray Platform, Small 16(30) (2020) e2000941.
[56] A. Desmaison, C. Frongia, K. Grenier, B. Ducommun, V. Lobjois, Mechanical stress impairs mitosis progression in multi-cellular tumour spheroids, PLoS One 8(12) (2013) e80447.
[57] E. Latorre, S. Kale, L. Casares, M. Gomez-Gonzalez, M. Uroz, L. Valon, R.V. Nair, E. Garreta, N. Montserrat, A. Del Campo, B. Ladoux, M. Arroyo, X. Trepat, Active superelasticity in three-dimensional epithelia of controlled shape, Nature 563(7730) (2018) 203-208.
[58] K. Alessandri, B.R. Sarangi, V.V. Gurchenkov, B. Sinha, T.R. Kiessling, L. Fetler, F. Rico, S. Scheuring, C. Lamaze, A. Simon, S. Geraldo, D. Vignjevic, H. Domejean, L. Rolland, A. Funfak, J. Bibette, N. Bremond, P. Nassoy, Cellular capsules as a tool for multicellular spheroid production and for investigating the mechanics of tumour progression in vitro, Proc Natl Acad Sci U S A 110(37) (2013) 14843-8.
[59] D.R. Gossett, H.T. Tse, S.A. Lee, Y. Ying, A.G. Lindgren, O.O. Yang, J. Rao, A.T. Clark, D. Di Carlo, Hydrodynamic stretching of single cells for large population mechanical phenotyping, Proc Natl Acad Sci U S A 109(20) (2012) 7630-5.
[60] P. Memmolo, L. Miccio, F. Merola, M. Mugnano, P. Ferraro, Hydrodynamic Red Blood Cells Deformation by Quantitative Phase Microscopy and Zernike Polynomials, Frontiers in Physics 7 (2019).

[61] M.H. Panhwar, F. Czerwinski, V.A.S. Dabbiru, Y. Komaragiri, B. Fregin, D. Biedenweg, P. Nestler, R.H. Pires, O. Otto, High-throughput cell and spheroid mechanics in virtual fluidic channels, Nat Commun 11(1) (2020) 2190.
[62] G. Fang, H. Lu, A. Law, D. Gallego-Ortega, D. Jin, G. Lin, Gradient-sized control of tumour spheroids on a single chip, Lab Chip 19(24) (2019) 4093-4103.
[63] B.R. Lee, J.W. Hwang, Y.Y. Choi, S.F. Wong, Y.H. Hwang, D.Y. Lee, S.H. Lee, In situ formation and collagen-alginate composite encapsulation of pancreatic islet spheroids, Biomaterials 33(3) (2012) 837-45.
[64] B. Patra, C.C. Peng, W.H. Liao, C.H. Lee, Y.C. Tung, Drug testing and flow cytometry analysis on a large number of uniform sized tumour spheroids using a microfluidic device, Sci Rep 6 (2016) 21061.
[65] S.W. Lee, S. Hong, B. Jung, S.Y. Jeong, J.H. Byeon, G.S. Jeong, J. Choi, C. Hwang, In vitro lung cancer multicellular tumour spheroid formation using a microfluidic device, Biotechnol Bioeng 116(11) (2019) 3041-3052.
[66] D.J. Jung, T.H. Shin, M. Kim, C.O. Sung, S.J. Jang, G.S. Jeong, A one-stop microfluidic-based lung cancer organoid culture platform for testing drug sensitivity, Lab Chip 19(17) (2019) 2854-2865.
[67] N. Brandenberg, S. Hoehnel, F. Kuttler, K. Homicsko, C. Ceroni, T. Ringel, N. Gjorevski, G. Schwank, G. Coukos, G. Turcatti, M.P. Lutolf, High-throughput automated organoid culture via stem-cell aggregation in microcavity arrays, Nat Biomed Eng 4(9) (2020) 863-874.
[68] T. Tao, Y. Wang, W. Chen, Z. Li, W. Su, Y. Guo, P. Deng, J. Qin, Engineering human islet organoids from iPSCs using an organ-on-chip platform, Lab Chip 19(6) (2019) 948-958.
[69] C.X. Zhao, D. Chen, Y. Hui, D.A. Weitz, A.P.J. Middelberg, Controlled Generation of Ultrathin-Shell Double Emulsions and Studies on Their Stability, Chemphyschem 18(10) (2017) 1393-1399.
[70] S. Sart, R.F. Tomasi, G. Amselem, C.N. Baroud, Multiscale cytometry and regulation of 3D cell cultures on a chip, Nat Commun 8(1) (2017) 469.
[71] H.T. Liu, H. Wang, W.B. Wei, H. Liu, L. Jiang, J.H. Qin, A Microfluidic Strategy for Controllable Generation of Water-in-Water Droplets as Biocompatible Microcarriers, Small 14(36) (2018) e1801095.
[72] A.G. Hati, D.C. Bassett, J.M. Ribe, P. Sikorski, D.A. Weitz, B.T. Stokke, Versatile, cell and chip friendly method to gel alginate in microfluidic devices, Lab Chip 16(19) (2016) 3718-27.
[73] S. Utech, R. Prodanovic, A.S. Mao, R. Ostafe, D.J. Mooney, D.A. Weitz, Microfluidic Generation of Monodisperse, Structurally Homogeneous Alginate Microgels for Cell Encapsulation and 3D Cell Culture, Adv Healthc Mater 4(11) (2015) 1628-33.
[74] B. Kwak, Y. Lee, J. Lee, S. Lee, J. Lim, Mass fabrication of uniform sized 3D tumour spheroid using high-throughput microfluidic system, J Control Release 275 (2018) 201-207.
[75] H.F. Chan, Y. Zhang, K.W. Leong, Efficient One-Step Production of Microencapsulated Hepatocyte Spheroids with Enhanced Functions, Small 12(20) (2016) 2720-30.
[76] P. Agarwal, S. Zhao, P. Bielecki, W. Rao, J.K. Choi, Y. Zhao, J. Yu, W. Zhang, X. He, One-step microfluidic generation of pre-hatching embryo-like core-shell

microcapsules for miniaturized 3D culture of pluripotent stem cells, Lab Chip 13(23) (2013) 4525-33.
[77] Y.C. Lu, W. Song, D. An, B.J. Kim, R. Schwartz, M. Wu, M. Ma, Designing compartmentalized hydrogel microparticles for cell encapsulation and scalable 3D cell culture, J Mater Chem B 3(3) (2015) 353-360.
[78] M.E. Dolega, F. Abeille, N. Picollet-D'hahan, X. Gidrol, Controlled 3D culture in Matrigel microbeads to analyze clonal acinar development, Biomaterials 52 (2015) 347-57.
[79] B. Laperrousaz, S. Porte, S. Gerbaud, V. Harma, F. Kermarrec, V. Hourtane, F. Bottausci, X. Gidrol, N. Picollet-D'hahan, Direct transfection of clonal organoids in Matrigel microbeads: a promising approach toward organoid-based genetic screens, Nucleic Acids Res 46(12) (2018) e70.
[80] Y.C. Lu, D.J. Fu, D. An, A. Chiu, R. Schwartz, A.Y. Nikitin, M. Ma, Scalable Production and Cryostorage of Organoids Using Core-Shell Decoupled Hydrogel Capsules, Adv Biosyst 1(12) (2017).
[81] H. Liu, Y. Wang, H. Wang, M. Zhao, T. Tao, X. Zhang, J. Qin, A Droplet Microfluidic System to Fabricate Hybrid Capsules Enabling Stem Cell Organoid Engineering, Adv Sci (Weinh) 7(11) (2020) 1903739.
[82] C. Rinoldi, M. Costantini, E. Kijenska-Gawronska, S. Testa, E. Fornetti, M. Heljak, M. Cwiklinska, R. Buda, J. Baldi, S. Cannata, J. Guzowski, C. Gargioli, A. Khademhosseini, W. Swieszkowski, Tendon Tissue Engineering: Effects of Mechanical and Biochemical Stimulation on Stem Cell Alignment on Cell-Laden Hydrogel Yarns, Adv Healthc Mater 8(7) (2019) e1801218.
[83] K. Iijima, S. Ichikawa, S. Ishikawa, D. Matsukuma, Y. Yataka, H. Otsuka, M. Hashizume, Preparation of Cell-Paved and -Incorporated Polysaccharide Hollow Fibers Using a Microfluidic Device, ACS Biomaterials Science & Engineering 5(11) (2019) 5688-5697.
[84] M.F. Leong, H.F. Lu, T.C. Lim, K. Narayanan, S. Gao, L.Y. Wang, R.P. Toh, H. Funke, M.H. Abdul Samad, A.C. Wan, J.Y. Ying, Alginate Microfiber System for Expansion and Direct Differentiation of Human Embryonic Stem Cells, Tissue Eng Part C Methods 22(9) (2016) 884-94.
[85] A.Y. Hsiao, T. Okitsu, H. Onoe, M. Kiyosawa, H. Teramae, S. Iwanaga, T. Kazama, T. Matsumoto, S. Takeuchi, Smooth muscle-like tissue constructs with circumferentially oriented cells formed by the cell fiber technology, PLoS One 10(3) (2015) e0119010.
[86] S.J. Kim, J. Park, H. Byun, Y.W. Park, L.G. Major, D.Y. Lee, Y.S. Choi, H. Shin, Hydrogels with an embossed surface: An all-in-one platform for mass production and culture of human adipose-derived stem cell spheroids, Biomaterials 188 (2019) 198-212.
[87] Y. Wang, H. Wang, P. Deng, W. Chen, Y. Guo, T. Tao, J. Qin, In situ differentiation and generation of functional liver organoids from human iPSCs in a 3D perfusable chip system, Lab Chip 18(23) (2018) 3606-3616.
[88] Riya Muckom, Xiaoping Bao, Eric Tran, Evelyn Chen, Abirami Murugappan, Jonathan S. Dordick, Douglas S. Clark, D.V. Schaffer, High-throughput 3D screening for differentiation of hPSC-derived cell therapy candidates, Science Advances 5(eaaz:1457) (2020).
[89] B.J. Jin, S. Battula, N. Zachos, O. Kovbasnjuk, J. Fawlke-Abel, J. In, M. Donowitz, A.S. Verkman, Microfluidics platform for measurement of volume changes in immobilized intestinal enteroids, Biomicrofluidics 8(2) (2014) 024106.

[90] R. Weser, A. Winkler, M. Weihnacht, S. Menzel, H. Schmidt, The complexity of surface acoustic wave fields used for microfluidic applications, Ultrasonics 106 (2020) 106160.
[91] C. Richard, A. Fakhfouri, M. Colditz, F. Striggow, R. Kronstein-Wiedemann, T. Tonn, M. Medina-Sanchez, O.G. Schmidt, T. Gemming, A. Winkler, Blood platelet enrichment in mass-producible surface acoustic wave (SAW) driven microfluidic chips, Lab Chip 19(24) (2019) 4043-4051.
[92] S. Jin, X. Wei, J. Ren, Z. Jiang, C. Abell, Z. Yu, Construction of core-shell microcapsules via focused surface acoustic wave microfluidics, Lab Chip 20(17) (2020) 3104-3108.
[93] K. Chen, M. Wu, F. Guo, P. Li, C.Y. Chan, Z. Mao, S. Li, L. Ren, R. Zhang, T.J. Huang, Rapid formation of size-controllable multicellular spheroids via 3D acoustic tweezers, Lab Chip 16(14) (2016) 2636-43.
[94] B. Chen, Y. Wu, Z. Ao, H. Cai, A. Nunez, Y. Liu, J. Foley, K. Nephew, X. Lu, F. Guo, High-throughput acoustofluidic fabrication of tumour spheroids, Lab Chip 19(10) (2019) 1755-1763.
[95] T. Takebe, B. Zhang, M. Radisic, Synergistic Engineering: Organoids Meet Organs-on-a-Chip, Cell Stem Cell 21(3) (2017) 297-300.
[96] S. Kim, H. Lee, M. Chung, N.L. Jeon, Engineering of functional, perfusable 3D microvascular networks on a chip, Lab Chip 13(8) (2013) 1489-500.
[97] S. Kim, M. Chung, J. Ahn, S. Lee, N.L. Jeon, Interstitial flow regulates the angiogenic response and phenotype of endothelial cells in a 3D culture model, Lab Chip 16(21) (2016) 4189-4199.
[98] Y. Nashimoto, R. Okada, S. Hanada, Y. Arima, K. Nishiyama, T. Miura, R. Yokokawa, Vascularized cancer on a chip: The effect of perfusion on growth and drug delivery of tumour spheroid, Biomaterials 229 (2020) 119547.
[99] K. Haase, G.S. Offeddu, M.R. Gillrie, R.D. Kamm, Endothelial Regulation of Drug Transport in a 3D Vascularized Tumour Model, Advanced Functional Materials 30(48) (2020).
[100] S. Oh, H. Ryu, D. Tahk, J. Ko, Y. Chung, H.K. Lee, T.R. Lee, N.L. Jeon, "Open-top" microfluidic device for in vitro three-dimensional capillary beds, Lab Chip 17(20) (2017) 3405-3414.
[101] J. Ko, J. Ahn, S. Kim, Y. Lee, J. Lee, D. Park, N.L. Jeon, Tumour spheroid-on-a-chip: a standardized microfluidic culture platform for investigating tumour angiogenesis, Lab Chip 19(17) (2019) 2822-2833.
[102] S. Rajasekar, D.S.Y. Lin, L. Abdul, A. Liu, A. Sotra, F. Zhang, B. Zhang, IFlowPlate-A Customized 384-Well Plate for the Culture of Perfusable Vascularized Colon Organoids, Adv Mater 32(46) (2020) e2002974.
[103] Y. Jin, J. Kim, J.S. Lee, S. Min, S. Kim, D.-H. Ahn, Y.-G. Kim, S.-W. Cho, Vascularized Liver Organoids Generated Using Induced Hepatic Tissue and Dynamic Liver-Specific Microenvironment as a Drug Testing Platform, Advanced Functional Materials 28(37) (2018).
[104] A.A. Mansour, J.T. Goncalves, C.W. Bloyd, H. Li, S. Fernandes, D. Quang, S. Johnston, S.L. Parylak, X. Jin, F.H. Gage, An in vivo model of functional and vascularized human brain organoids, Nat Biotechnol 36(5) (2018) 432-441.
[105] M.A. Lancaster, Brain organoids get vascularized, Nature Biotechnology 36(5) (2018) 407-408.

[106] B.F.L. Lai, R.X.Z. Lu, Y. Hu, L. Davenport Huyer, W. Dou, E.Y. Wang, N. Radulovich, M.S. Tsao, Y. Sun, M. Radisic, Recapitulating Pancreatic Tumour Microenvironment through Synergistic Use of Patient Organoids and Organ‐on‐a‐Chip Vasculature, Advanced Functional Materials 30(48) (2020).
[107] C. Kim, J. Kasuya, J. Jeon, S. Chung, R.D. Kamm, A quantitative microfluidic angiogenesis screen for studying anti-angiogenic therapeutic drugs, Lab Chip 15(1) (2015) 301-10.
[108] K. Yuki, N. Cheng, M. Nakano, C.J. Kuo, Organoid Models of Tumour Immunology, Trends Immunol 41(8) (2020) 652-664.
[109] C.P. Miller, W. Shin, E.H. Ahn, H.J. Kim, D.H. Kim, Engineering Microphysiological Immune System Responses on Chips, Trends Biotechnol 38(8) (2020) 857-872.
[110] R.W. Jenkins, A.R. Aref, P.H. Lizotte, E. Ivanova, S. Stinson, C.W. Zhou, M. Bowden, J. Deng, H. Liu, D. Miao, M.X. He, W. Walker, G. Zhang, T. Tian, C. Cheng, Z. Wei, S. Palakurthi, M. Bittinger, H. Vitzthum, J.W. Kim, A. Merlino, M. Quinn, C. Venkataramani, J.A. Kaplan, A. Portell, P.C. Gokhale, B. Phillips, A. Smart, A. Rotem, R.E. Jones, L. Keogh, M. Anguiano, L. Stapleton, Z. Jia, M. Barzily-Rokni, I. Canadas, T.C. Thai, M.R. Hammond, R. Vlahos, E.S. Wang, H. Zhang, S. Li, G.J. Hanna, W. Huang, M.P. Hoang, A. Piris, J.P. Eliane, A.O. Stemmer-Rachamimov, L. Cameron, M.J. Su, P. Shah, B. Izar, M. Thakuria, N.R. LeBoeuf, G. Rabinowits, V. Gunda, S. Parangi, J.M. Cleary, B.C. Miller, S. Kitajima, R. Thummalapalli, B. Miao, T.U. Barbie, V. Sivathanu, J. Wong, W.G. Richards, R. Bueno, C.H. Yoon, J. Miret, M. Herlyn, L.A. Garraway, E.M. Van Allen, G.J. Freeman, P.T. Kirschmeier, J.H. Lorch, P.A. Ott, F.S. Hodi, K.T. Flaherty, R.D. Kamm, G.M. Boland, K.K. Wong, D. Dornan, C.P. Paweletz, D.A. Barbie, Ex Vivo Profiling of PD-1 Blockade Using Organotypic Tumour Spheroids, Cancer Discov 8(2) (2018) 196-215.
[111] A.R. Aref, M. Campisi, E. Ivanova, A. Portell, D. Larios, B.P. Piel, N. Mathur, C. Zhou, R.V. Coakley, A. Bartels, M. Bowden, Z. Herbert, S. Hill, S. Gilhooley, J. Carter, I. Canadas, T.C. Thai, S. Kitajima, V. Chiono, C.P. Paweletz, D.A. Barbie, R.D. Kamm, R.W. Jenkins, 3D microfluidic ex vivo culture of organotypic tumour spheroids to model immune checkpoint blockade, Lab Chip 18(20) (2018) 3129-3143.
[112] S.W.L. Lee, G. Adriani, E. Ceccarello, A. Pavesi, A.T. Tan, A. Bertoletti, R.D. Kamm, S.C. Wong, Characterizing the Role of Monocytes in T Cell Cancer Immunotherapy Using a 3D Microfluidic Model, Front Immunol 9 (2018) 416.
[113] J.M. Ayuso, R. Truttschel, M.M. Gong, M. Humayun, M. Virumbrales-Munoz, R. Vitek, M. Felder, S.D. Gillies, P. Sondel, K.B. Wisinski, M. Patankar, D.J. Beebe, M.C. Skala, Evaluating natural killer cell cytotoxicity against solid tumours using a microfluidic model, Oncoimmunology 8(3) (2019) 1553477.
[114] D.D. Truong, A. Kratz, J.G. Park, E.S. Barrientos, H. Saini, T. Nguyen, B. Pockaj, G. Mouneimne, J. LaBaer, M. Nikkhah, A Human Organotypic Microfluidic Tumour Model Permits Investigation of the Interplay between Patient-Derived Fibroblasts and Breast Cancer Cells, Cancer Res 79(12) (2019) 3139-3151.
[115] D. Ohlund, A. Handly-Santana, G. Biffi, E. Elyada, A.S. Almeida, M. Ponz-Sarvise, V. Corbo, T.E. Oni, S.A. Hearn, E.J. Lee, Chio, II, C.I. Hwang, H. Tiriac, L.A. Baker, D.D. Engle, C. Feig, A. Kultti, M. Egeblad, D.T. Fearon, J.M. Crawford, H. Clevers, Y. Park, D.A. Tuveson, Distinct populations of inflammatory fibroblasts and myofibroblasts in pancreatic cancer, J Exp Med 214(3) (2017) 579-596.

[116] M.F. Estrada, S.P. Rebelo, E.J. Davies, M.T. Pinto, H. Pereira, V.E. Santo, M.J. Smalley, S.T. Barry, E.J. Gualda, P.M. Alves, E. Anderson, C. Brito, Modelling the tumour microenvironment in long-term microencapsulated 3D co-cultures recapitulates phenotypic features of disease progression, Biomaterials 78 (2016) 50-61.
[117] Q. Sun, S.H. Tan, Q. Chen, R. Ran, Y. Hui, D. Chen, C.-X. Zhao, Microfluidic Formation of Coculture Tumour Spheroids with Stromal Cells As a Novel 3D Tumour Model for Drug Testing, ACS Biomaterials Science & Engineering 4(12) (2018) 4425-4433.
[118] L. Zhang, K. Chen, H. Zhang, B. Pang, C.H. Choi, A.S. Mao, H. Liao, S. Utech, D.J. Mooney, H. Wang, D.A. Weitz, Microfluidic Templated Multicompartment Microgels for 3D Encapsulation and Pairing of Single Cells, Small 14(9) (2018).
[119] K. Shik Mun, K. Arora, Y. Huang, F. Yang, S. Yarlagadda, Y. Ramananda, M. Abu-El-Haija, J.J. Palermo, B.N. Appakalai, J.D. Nathan, A.P. Naren, Patient-derived pancreas-on-a-chip to model cystic fibrosis-related disorders, Nat Commun 10(1) (2019) 3124.
[120] S. Chen, A. Giannakou, S. Wyman, J. Gruzas, J. Golas, W. Zhong, C. Loreth, L. Sridharan, T.-T. Yamin, M. Damelin, K.G. Geles, Cancer-associated fibroblasts suppress SOX2-induced dysplasia in a lung squamous cancer coculture, Proceedings of the National Academy of Sciences 115(50) (2018) E11671-E11680.
[121] R.F. Tomasi, S. Sart, T. Champetier, C.N. Baroud, Individual Control and Quantification of 3D Spheroids in a High-Density Microfluidic Droplet Array, Cell Rep 31(8) (2020) 107670.
[122] X. Yue, T.D. Nguyen, V. Zellmer, S. Zhang, P. Zorlutuna, Stromal cell-laden 3D hydrogel microwell arrays as tumour microenvironment model for studying stiffness dependent stromal cell-cancer interactions, Biomaterials 170 (2018) 37-48.
[123] M.T. Ghoneim, A. Nguyen, N. Dereje, J. Huang, G.C. Moore, P.J. Murzynowski, C. Dagdeviren, Recent Progress in Electrochemical pH-Sensing Materials and Configurations for Biomedical Applications, Chem Rev 119(8) (2019) 5248-5297.
[124] L. Manjakkal, S. Dervin, R. Dahiya, Flexible potentiometric pH sensors for wearable systems, RSC Advances 10(15) (2020) 8594-8617.
[125] L. Manjakkal, D. Szwagierczak, R. Dahiya, Metal oxides based electrochemical pH sensors: Current progress and future perspectives, Progress in Materials Science 109 (2020).
[126] M.E. Gray, J.R.K. Marland, C. Dunare, E.O. Blair, J. Meehan, A. Tsiamis, I.H. Kunkler, A.F. Murray, D. Argyle, A. Dyson, M. Singer, M.A. Potter, In vivo validation of a miniaturized electrochemical oxygen sensor for measuring intestinal oxygen tension, Am J Physiol Gastrointest Liver Physiol 317(2) (2019) G242-G252.
[127] L. Rivas, S. Dulay, S. Miserere, L. Pla, S.B. Marin, J. Parra, E. Eixarch, E. Gratacos, M. Illa, M. Mir, J. Samitier, Micro-needle implantable electrochemical oxygen sensor: ex-vivo and in-vivo studies, Biosens Bioelectron 153 (2020) 112028.
[128] A. Moya, M. Ortega-Ribera, X. Guimera, E. Sowade, M. Zea, X. Illa, E. Ramon, R. Villa, J. Gracia-Sancho, G. Gabriel, Online oxygen monitoring using integrated inkjet-printed sensors in a liver-on-a-chip system, Lab Chip 18(14) (2018) 2023-2035.
[129] L. Wang, M. Xu, Y. Xie, C. Qian, W. Ma, L. Wang, Y. Song, Ratiometric electrochemical glucose sensor based on electroactive Schiff base polymers, Sensors and Actuators B: Chemical 285 (2019) 264-270.

[130] M.H. Asif, A. Razaq, N. Akbar, B. Danielsson, I. Sultana, Facile synthesis of multisegment Au/Ni/Au nanowire for high performance electrochemical glucose sensor, Materials Research Express 6(9) (2019).
[131] W. Lipińska, K. Siuzdak, J. Karczewski, A. Dołęga, K. Grochowska, Electrochemical glucose sensor based on the glucose oxidase entrapped in chitosan immobilized onto laser-processed Au-Ti electrode, Sensors and Actuators B: Chemical (2020).
[132] P.M. Misun, J. Rothe, Y.R.F. Schmid, A. Hierlemann, O. Frey, Multi-analyte biosensor interface for real-time monitoring of 3D microtissue spheroids in hanging-drop networks, Microsyst Nanoeng 2 (2016) 16022.
[133] G. Cappi, F.M. Spiga, Y. Moncada, A. Ferretti, M. Beyeler, M. Bianchessi, L. Decosterd, T. Buclin, C. Guiducci, Label-free detection of tobramycin in serum by transmission-localized surface plasmon resonance, Anal Chem 87(10) (2015) 5278-85.
[134] F. Real-Fernandez, G. Rossi, F. Lolli, A.M. Papini, P. Rovero, Label-free method for anti-glucopeptide antibody detection in Multiple Sclerosis, MethodsX 2 (2015) 141-4.
[135] S.R. Shin, Y.S. Zhang, D.J. Kim, A. Manbohi, H. Avci, A. Silvestri, J. Aleman, N. Hu, T. Kilic, W. Keung, M. Righi, P. Assawes, H.A. Alhadrami, R.A. Li, M.R. Dokmeci, A. Khademhosseini, Aptamer-Based Microfluidic Electrochemical Biosensor for Monitoring Cell-Secreted Trace Cardiac Biomarkers, Anal Chem 88(20) (2016) 10019-10027.
[136] D.S. Kim, Y.W. Choi, A. Shanmugasundaram, Y.J. Jeong, J. Park, N.E. Oyunbaatar, E.S. Kim, M. Choi, D.W. Lee, Highly durable crack sensor integrated with silicone rubber cantilever for measuring cardiac contractility, Nat Commun 11(1) (2020) 535.
[137] Q. Li, K. Nan, P. Le Floch, Z. Lin, H. Sheng, T.S. Blum, J. Liu, Cyborg Organoids: Implantation of Nanoelectronics via Organogenesis for Tissue-Wide Electrophysiology, Nano Lett 19(8) (2019) 5781-5789.
[138] H. Liu, O.A. Bolonduro, N. Hu, J. Ju, A.A. Rao, B.M. Duffy, Z. Huang, L.D. Black, B.P. Timko, Heart-on-a-Chip Model with Integrated Extra- and Intracellular Bioelectronics for Monitoring Cardiac Electrophysiology under Acute Hypoxia, Nano Lett 20(4) (2020) 2585-2593.
[139] Anna Kalmykov, Changjin Huang, Jacqueline Bliley, Daniel Shiwarski, Joshua Tashman, Arif Abdullah, Sahil K. Rastogi, Shivani Shukla, Elnatan Mataev, Adam W. Feinberg, K. Jimmy Hsia, T. Cohen-Karni, Organ-on-e-chip: Three-dimensional self-rolled biosensor array for electrical interrogations of human electrogenic spheroids, Science Advances 5(eaax0729) (2019).
[140] K.F. Lei, W.W. Ji, A. Goh, C.H. Huang, M.Y. Lee, Investigation of uniform sized multicellular spheroids raised by microwell arrays after the combined treatment of electric field and anti-cancer drug, Biomed Microdevices 21(4) (2019) 94.
[141] Yih Yang Chen, Pamuditha N. Silva, Abdullah Muhammad Syed, Shrey Sindhwani, Jonathan V. Rocheleau, W.C.W. Chana, Clarifying intact 3D tissues on a microfluidic chip for high-throughput structural analysis, Proc Natl Acad Sci U S A 114(6) (2017) E1036.
[142] M. Roy, D. Seo, S. Oh, J.W. Yang, S. Seo, A review of recent progress in lens-free imaging and sensing, Biosens Bioelectron 88 (2017) 130-143.

[143] A. Greenbaum, A. Feizi, N. Akbari, A. Ozcan, Wide-field computational color imaging using pixel super-resolved on-chip microscopy, Opt Express 21(10) (2013) 12469-83.
[144] Yibo Zhang, Yoonjung Shin, Kevin Sung, Sam Yang, Harrison Chen, Hongda Wang, Da Teng, Yair Rivenson, Rajan P. Kulkarni, A. Ozcan, 3D imaging of optically cleared tissue using a simplified CLARITY method and on-chip microscopy, Science Advances 3(e1700553) (2017).
[145] S. Jiang, M. Guan, J. Wu, G. Fang, X. Xu, D. Jin, Z. Liu, K. Shi, F. Bai, S. Wang, P. Xi, Frequency-domain diagonal extension imaging, Advanced Photonics 2(03) (2020).
[146] V. Bianco, B. Mandracchia, V. Marchesano, V. Pagliarulo, F. Olivieri, S. Coppola, M. Paturzo, P. Ferraro, Endowing a plain fluidic chip with micro-optics: a holographic microscope slide, Light Sci Appl 6(9) (2017) e17055.
[147] Z. Luo, A. Yurt, R. Stahl, M.S. Carlon, A.S. Ramalho, F. Vermeulen, A. Lambrechts, D. Braeken, L. Lagae, Fast compressive lens-free tomography for 3D biological cell culture imaging, Opt Express 28(18) (2020) 26935-26952.
[148] R. Diekmann, Ø.I. Helle, C.I. Øie, P. McCourt, T.R. Huser, M. Schüttpelz, B.S. Ahluwalia, Chip-based wide field-of-view nanoscopy, Nature Photonics 11(5) (2017) 322-328.
[149] Y.J. Fan, H.Y. Hsieh, S.F. Tsai, C.H. Wu, C.M. Lee, Y.T. Liu, C.H. Lu, S.W. Chang, B.C. Chen, Microfluidic channel integrated with a lattice lightsheet microscopic system for continuous cell imaging, Lab Chip (2020).
[150] P. Bon, J. Linares-Loyez, M. Feyeux, K. Alessandri, B. Lounis, P. Nassoy, L. Cognet, Self-interference 3D super-resolution microscopy for deep tissue investigations, Nat Methods 15(6) (2018) 449-454.
[151] Y. Liu, F. Wang, H. Lu, G. Fang, S. Wen, C. Chen, X. Shan, X. Xu, L. Zhang, M. Stenzel, D. Jin, Super-Resolution Mapping of Single Nanoparticles inside Tumour Spheroids, Small 16(6) (2020) e1905572.
[152] C. Chen, F. Wang, S. Wen, Q.P. Su, M.C.L. Wu, Y. Liu, B. Wang, D. Li, X. Shan, M. Kianinia, I. Aharonovich, M. Toth, S.P. Jackson, P. Xi, D. Jin, Multi-photon near-infrared emission saturation nanoscopy using upconversion nanoparticles, Nat Commun 9(1) (2018) 3290.
[153] Yongtao Liu, Fan Wang, Hongxu Lu, Shihui Wen, Chaohao Chen, Xuchen Shan, Guocheng Fang, D. Jin, Deep tissue Super-resolution microscopy mapping single nanoparticles inside multicellular spheroids, Enhanced Spectroscopies and Nanoimaging 11468 (2020) 11468G.
[154] John P. Ward, J.R. King, Mathematical modelling of drug transport in tumour multicell spheroids and monolayer cultures, Mathematical Biosciences 181 (2003) 177-207.
[155] R. Glicklis, J.C. Merchuk, S. Cohen, Modeling mass transfer in hepatocyte spheroids via cell viability, spheroid size, and hepatocellular functions, Biotechnol Bioeng 86(6) (2004) 672-80.
[156] T. Ishiguro, H. Ohata, A. Sato, K. Yamawaki, T. Enomoto, K. Okamoto, Tumour-derived spheroids: Relevance to cancer stem cells and clinical applications, Cancer Sci 108(3) (2017) 283-289.
[157] V. Beachley, V. Kasyanov, A. Nagy-Mehesz, R. Norris, I. Ozolanta, M. Kalejs, P. Stradins, L. Baptista, K. da Silva, J. Grainjero, X. Wen, V. Mironov, The fusion of tissue spheroids attached to pre-stretched electrospun polyurethane scaffolds, J Tissue Eng 5 (2014) 2041731414556561.

[158] A.A. Popova, T. Tronser, K. Demir, P. Haitz, K. Kuodyte, V. Starkuviene, P. Wajda, P.A. Levkin, Facile One Step Formation and Screening of Tumour Spheroids Using Droplet-Microarray Platform, Small 15(25) (2019) e1901299.
[159] X. Gong, C. Lin, J. Cheng, J. Su, H. Zhao, T. Liu, X. Wen, P. Zhao, Generation of Multicellular Tumour Spheroids with Microwell-Based Agarose Scaffolds for Drug Testing, PLoS One 10(6) (2015) e0130348.
[160] E.O. Mosaad, K.F. Chambers, K. Futrega, J.A. Clements, M.R. Doran, The Microwell-mesh: A high-throughput 3D prostate cancer spheroid and drug-testing platform, Sci Rep 8(1) (2018) 253.
[161] P. Sabhachandani, V. Motwani, N. Cohen, S. Sarkar, V. Torchilin, T. Konry, Generation and functional assessment of 3D multicellular spheroids in droplet based microfluidics platform, Lab Chip 16(3) (2016) 497-505.
[162] C. Kim, S. Chung, Y.E. Kim, K.S. Lee, S.H. Lee, K.W. Oh, J.Y. Kang, Generation of core-shell microcapsules with three-dimensional focusing device for efficient formation of cell spheroid, Lab Chip 11(2) (2011) 246-52.
[163] H.F. Chan, Y. Zhang, Y.P. Ho, Y.L. Chiu, Y. Jung, K.W. Leong, Rapid formation of multicellular spheroids in double-emulsion droplets with controllable microenvironment, Sci Rep 3 (2013) 3462.
[164] H. Byun, Y. Bin Lee, E.M. Kim, H. Shin, Fabrication of size-controllable human mesenchymal stromal cell spheroids from micro-scaled cell sheets, Biofabrication 11(3) (2019) 035025.
[165] W. Song, D. An, D.I. Kao, Y.C. Lu, G. Dai, S. Chen, M. Ma, Nanofibrous microposts and microwells of controlled shapes and their hybridization with hydrogels for cell encapsulation, ACS Appl Mater Interfaces 6(10) (2014) 7038-44.
[166] A. Laurain, S.W. Walker, Droplet Footprint Control, SIAM Journal on Control and Optimization 53(2) (2015) 771-799.
[167] J. Wang, J.M. Sanger, J.W. Sanger, Differential effects of Latrunculin-A on myofibrils in cultures of skeletal muscle cells: insights into mechanisms of myofibrillogenesis, Cell Motil Cytoskeleton 62(1) (2005) 35-47.
[168] O. Sirenko, T. Mitlo, J. Hesley, S. Luke, W. Owens, E.F. Cromwell, High-content assays for characterizing the viability and morphology of 3D cancer spheroid cultures, Assay Drug Dev Technol 13(7) (2015) 402-14.
[169] R. Baghban, L. Roshangar, R. Jahanban-Esfahlan, K. Seidi, A. Ebrahimi-Kalan, M. Jaymand, S. Kolahian, T. Javaheri, P. Zare, Tumour microenvironment complexity and therapeutic implications at a glance, Cell Commun Signal 18(1) (2020) 59.
[170] S.J. Han, S. Kwon, K.S. Kim, Challenges of applying multicellular tumour spheroids in preclinical phase, Cancer Cell Int 21(1) (2021) 152.
[171] O.I. Hoffmann, C. Ilmberger, S. Magosch, M. Joka, K.W. Jauch, B. Mayer, Impact of the spheroid model complexity on drug response, J Biotechnol 205 (2015) 14-23.
[172] V. Kumar, S. Varghese, Ex Vivo Tumour-on-a-Chip Platforms to Study Intercellular Interactions within the Tumour Microenvironment, Adv Healthc Mater 8(4) (2019) e1801198.
[173] S.Y. Jeong, J.H. Lee, Y. Shin, S. Chung, H.J. Kuh, Co-Culture of Tumour Spheroids and Fibroblasts in a Collagen Matrix-Incorporated Microfluidic Chip Mimics Reciprocal Activation in Solid Tumour Microenvironment, PLoS One 11(7) (2016) e0159013.
[174] S.A. Kim, E.K. Lee, H.J. Kuh, Co-culture of 3D tumour spheroids with fibroblasts as a model for epithelial-mesenchymal transition in vitro, Exp Cell Res 335(2) (2015) 187-96.

[175] W. Song, C.K. Tung, Y.C. Lu, Y. Pardo, M. Wu, M. Das, D.I. Kao, S. Chen, M. Ma, Dynamic self-organization of microwell-aggregated cellular mixtures, Soft Matter 12(26) (2016) 5739-46.
[176] B. Zhao, H. Guan, J.Q. Liu, Z. Zheng, Q. Zhou, J. Zhang, L.L. Su, D.H. Hu, Hypoxia drives the transition of human dermal fibroblasts to a myofibroblast-like phenotype via the TGF-beta1/Smad3 pathway, Int J Mol Med 39(1) (2017) 153-159.
[177] H. Zhang, W. Jiang, R. Liu, J. Zhang, D. Zhang, Z. Li, Y. Luan, Rational Design of Metal Organic Framework Nanocarrier-Based Codelivery System of Doxorubicin Hydrochloride/Verapamil Hydrochloride for Overcoming Multidrug Resistance with Efficient Targeted Cancer Therapy, ACS Appl Mater Interfaces 9(23) (2017) 19687-19697.
[178] B.N. Kholodenko, Cell-signalling dynamics in time and space, Nature Reviews Molecular Cell Biology 7(3) (2006) 165-176.
[179] Steven Telleen, OpenStax, R. Bear，, D. Rintoul, Human Physiology Part 1: Foundation Concepts, OpenStax CNX (2018).
[180] B. Alberts, A. Johnson, J. Lewis, M. Raff, K. Roberts, P. Walter, Molecular biology of the cell, Bruce Alberts...[et al.], Garland Science. New York. US (2002).
[181] James Neitzel, M. Rasband, Cell Communication. https://www.nature.com/scitable/topic/cell-communication-14122659/.
[182] T.J. Moutinho, Jr., J.C. Panagides, M.B. Biggs, G.L. Medlock, G.L. Kolling, J.A. Papin, Novel co-culture plate enables growth dynamic-based assessment of contact-independent microbial interactions, PLoS One 12(8) (2017) e0182163.
[183] Takeo Shimasaki, Satoko Yamamoto, T. Arisawa, Exosome Research and Co-culture Study, Biological and Pharmaceutical Bulletin 41(9) (2018) 1312-1321.
[184] S. Lin, X. Zhi, D. Chen, F. Xia, Y. Shen, J. Niu, S. Huang, J. Song, J. Miao, D. Cui, X. Ding, A flyover style microfluidic chip for highly purified magnetic cell separation, Biosens Bioelectron 129 (2019) 175-181.
[185] K.D.P. Dorayappan, M.L. Gardner, C.L. Hisey, R.A. Zingarelli, B.Q. Smith, M.D.S. Lightfoot, R. Gogna, M.M. Flannery, J. Hays, D.J. Hansford, M.A. Freitas, L. Yu, D.E. Cohn, K. Selvendiran, A Microfluidic Chip Enables Isolation of Exosomes and Establishment of Their Protein Profiles and Associated Signaling Pathways in Ovarian Cancer, Cancer Research 79(13) (2019) 3503-3513.
[186] S. Lin, Z. Yu, D. Chen, Z. Wang, J. Miao, Q. Li, D. Zhang, J. Song, D. Cui, Progress in Microfluidics-Based Exosome Separation and Detection Technologies for Diagnostic Applications, Small 16(9) (2020) e1903916.
[187] S. Shim, M.C. Belanger, A.R. Harris, J.M. Munson, R.R. Pompano, Two-way communication between ex vivo tissues on a microfluidic chip: application to tumour-lymph node interaction, Lab Chip 19(6) (2019) 1013-1026.
[188] T.Q. Vu, R.M. de Castro, L. Qin, Bridging the gap: microfluidic devices for short and long distance cell-cell communication, Lab Chip 17(6) (2017) 1009-1023.
[189] J. Yu, E. Berthier, A. Craig, T.E. de Groot, S. Sparks, P.N. Ingram, D.F. Jarrard, W. Huang, D.J. Beebe, A.B. Theberge, Reconfigurable open microfluidics for studying the spatiotemporal dynamics of paracrine signalling, Nat Biomed Eng 3(10) (2019) 830-841.
[190] I.K. Zervantonakis, S.K. Hughes-Alford, J.L. Charest, J.S. Condeelis, F.B. Gertler, R.D. Kamm, Three-dimensional microfluidic model for tumour cell intravasation and endothelial barrier function, Proc Natl Acad Sci U S A 109(34) (2012) 13515-20.

[191] K. Jeong, Y.J. Yu, J.Y. You, W.J. Rhee, J.A. Kim, Exosome-mediated microRNA-497 delivery for anti-cancer therapy in a microfluidic 3D lung cancer model, Lab Chip 20(3) (2020) 548-557.
[192] H. Jiang, D. Jiang, P. Zhu, F. Pi, J. Ji, C. Sun, J. Sun, X. Sun, A novel mast cell co-culture microfluidic chip for the electrochemical evaluation of food allergen, Biosens Bioelectron 83 (2016) 126-33.
[193] S.W. Lee, H.S. Kwak, M.-H. Kang, Y.-Y. Park, G.S. Jeong, Fibroblast-associated tumour microenvironment induces vascular structure-networked tumouroid, Scientific Reports 8(1) (2018) 2365.
[194] D.R. Bogdanowicz, H.H. Lu, Studying cell-cell communication in co-culture, Biotechnology Journal 8(4) (2013) 395-396.
[195] H. Aboulkheyr Es, S. Zhand, J.P. Thiery, M.E. Warkiani, Pirfenidone reduces immune-suppressive capacity of cancer-associated fibroblasts through targeting CCL17 and TNF-beta, Integrative Biology 12(7) (2020) 188-197.
[196] P. Cirri, P. Chiarugi, Cancer associated fibroblasts: the dark side of the coin, American journal of cancer research 1(4) (2011) 482-97.
[197] R. Kalluri, The biology and function of fibroblasts in cancer, Nature Reviews Cancer 16(9) (2016) 582-598.
[198] R. Kalluri, M. Zeisberg, Fibroblasts in cancer, Nature Reviews Cancer 6(5) (2006) 392-401.
[199] H. Saini, K. Rahmani Eliato, J. Veldhuizen, A. Zare, M. Allam, C. Silva, A. Kratz, D. Truong, G. Mouneimne, J. LaBaer, R. Ros, M. Nikkhah, The role of tumour-stroma interactions on desmoplasia and tumourigenicity within a microengineered 3D platform, Biomaterials 247 (2020) 119975.
[200] A.K. Mitra, M. Zillhardt, Y. Hua, P. Tiwari, A.E. Murmann, M.E. Peter, E. Lengyel, MicroRNAs Reprogram Normal Fibroblasts into Cancer-Associated Fibroblasts in Ovarian Cancer, Cancer Discovery 2(12) (2012) 1100-1108.
[201] M. Shimoda, K.T. Mellody, A. Orimo, Carcinoma-associated fibroblasts are a rate-limiting determinant for tumour progression, Seminars in Cell & Developmental Biology 21(1) (2010) 19-25.
[202] M.F. Pittenger, A.M. Mackay, S.C. Beck, R.K. Jaiswal, R. Douglas, J.D. Mosca, M.A. Moorman, D.W. Simonetti, S. Craig, D.R. Marshak, Multilineage Potential of Adult Human Mesenchymal Stem Cells, Science 284(5411) (1999) 143-147.
[203] W. Cao, B. Liu, F. Xia, M. Duan, Y. Hong, J. Niu, L. Wang, Y. Liu, C. Li, D. Cui, MnO2@Ce6-loaded mesenchymal stem cells as an "oxygen-laden guided-missile" for the enhanced photodynamic therapy on lung cancer, Nanoscale 12(5) (2020) 3090-3102.
[204] S. Kidd, E. Spaeth, J.L. Dembinski, M. Dietrich, K. Watson, A. Klopp, V.L. Battula, M. Weil, M. Andreeff, F.C. Marini, Direct evidence of mesenchymal stem cell tropism for tumour and wounding microenvironments using in vivo bioluminescent imaging, Stem Cells 27(10) (2009) 2614-23.
[205] J.J. Jing Ruan, Hua Song, Qirong Qian, Kan Wang, Can Wang and Daxiang Cui, Fluorescent magnetic nanoparticle-labeled mesenchymal stem cells for targeted imaging and hyperthermia therapy of in vivo gastric cancer, NANO RESEARCH LETTER 7(309) (2012).
[206] K.C. Valkenburg, A.E. de Groot, K.J. Pienta, Targeting the tumour stroma to improve cancer therapy, Nature Reviews Clinical Oncology 15(6) (2018) 366-381.
[207] Y. Shi, L. Du, L. Lin, Y. Wang, Tumour-associated mesenchymal stem/stromal cells: emerging therapeutic targets, Nature Reviews Drug Discovery 16(1) (2017) 35-52.

[208] A. Calon, D.V.F. Tauriello, E. Batlle, TGF-beta in CAF-mediated tumour growth and metastasis, Seminars in Cancer Biology 25 (2014) 15-22.
[209] D. Truong, R. Fiorelli, E.S. Barrientos, E.L. Melendez, N. Sanai, S. Mehta, M. Nikkhah, A three-dimensional (3D) organotypic microfluidic model for glioma stem cells – Vascular interactions, Biomaterials 198 (2019) 63-77.
[210] Z. Xu, Y. Gao, Y. Hao, E. Li, Y. Wang, J. Zhang, W. Wang, Z. Gao, Q. Wang, Application of a microfluidic chip-based 3D co-culture to test drug sensitivity for individualized treatment of lung cancer, Biomaterials 34(16) (2013) 4109-4117.
[211] L.F. Alonzo, M.L. Moya, V.S. Shirure, S.C. George, Microfluidic device to control interstitial flow-mediated homotypic and heterotypic cellular communication, Lab Chip 15(17) (2015) 3521-9.
[212] Y. Zheng, S. Wang, X. Xue, A. Xu, W. Liao, A. Deng, G. Dai, A.P. Liu, J. Fu, Notch signaling in regulating angiogenesis in a 3D biomimetic environment, Lab Chip 17(11) (2017) 1948-1959.
[213] Y.C. Chen, Z. Zhang, S. Fouladdel, Y. Deol, P.N. Ingram, S.P. McDermott, E. Azizi, M.S. Wicha, E. Yoon, Single cell dual adherent-suspension co-culture micro-environment for studying tumour-stromal interactions with functionally selected cancer stem-like cells, Lab Chip 16(15) (2016) 2935-45.
[214] S.M. Rahman, J.M. Campbell, R.N. Coates, K.M. Render, C.E. Byrne, E.C. Martin, A.T. Melvin, Evaluation of intercellular communication between breast cancer cells and adipose-derived stem cells via passive diffusion in a two-layer microfluidic device, Lab on a Chip 20(11) (2020) 2009-2019.
[215] S. Chung, R. Sudo, P.J. Mack, C.R. Wan, V. Vickerman, R.D. Kamm, Cell migration into scaffolds under co-culture conditions in a microfluidic platform, Lab Chip 9(2) (2009) 269-75.
[216] Y.C. Chen, Y.H. Cheng, H.S. Kim, P.N. Ingram, J.E. Nor, E. Yoon, Paired single cell co-culture microenvironments isolated by two-phase flow with continuous nutrient renewal, Lab Chip 14(16) (2014) 2941-7.
[217] X. Du, W. Li, G. Du, H. Cho, M. Yu, Q. Fang, L.P. Lee, J. Fang, Droplet Array-Based 3D Coculture System for High-Throughput Tumour Angiogenesis Assay, Anal Chem 90(5) (2018) 3253-3261.
[218] J. Park, A. Kerner, M.A. Burns, X.N. Lin, Microdroplet-enabled highly parallel co-cultivation of microbial communities, PLoS One 6(2) (2011) e17019.
[219] H.E. Karakas, J. Kim, J. Park, J.M. Oh, Y. Choi, D. Gozuacik, Y.K. Cho, A microfluidic chip for screening individual cancer cells via eavesdropping on autophagy-inducing crosstalk in the stroma niche, Sci Rep 7(1) (2017) 2050.
[220] B.I. Dalal, P.A. Keown, A.H. Greenberg, Immunocytochemical localization of secreted transforming growth factor-beta 1 to the advancing edges of primary tumours and to lymph node metastases of human mammary carcinoma, Am J Pathol 143(2) (1993) 381-9.
[221] J. Guerrero, N. Tobar, M. Cáceres, L. Espinoza, P. Escobar, J. Dotor, P.C. Smith, J. Martínez, Soluble factors derived from tumour mammary cell lines induce a stromal mammary adipose reversion in human and mice adipose cells. Possible role of TGF-β1 and TNF-α, Breast Cancer Research and Treatment 119(2) (2009) 497.
[222] E. Sahai, I. Astsaturov, E. Cukierman, D.G. DeNardo, M. Egeblad, R.M. Evans, D. Fearon, F.R. Greten, S.R. Hingorani, T. Hunter, R.O. Hynes, R.K. Jain, T. Janowitz, C. Jorgensen, A.C. Kimmelman, M.G. Kolonin, R.G. Maki, R.S. Powers, E. Puré, D.C. Ramirez, R. Scherz-Shouval, M.H. Sherman, S. Stewart, T.D. Tlsty, D.A. Tuveson, F.M.

Watt, V. Weaver, A.T. Weeraratna, Z. Werb, A framework for advancing our understanding of cancer-associated fibroblasts, Nature Reviews Cancer 20(3) (2020) 174-186.
[223] C. Ringuette Goulet, G. Bernard, S. Tremblay, S. Chabaud, S. Bolduc, F. Pouliot, Exosomes Induce Fibroblast Differentiation into Cancer-Associated Fibroblasts through TGFβ Signaling, Molecular Cancer Research 16(7) (2018) 1196-1204.
[224] A.E. Karnoub, A.B. Dash, A.P. Vo, A. Sullivan, M.W. Brooks, G.W. Bell, A.L. Richardson, K. Polyak, R. Tubo, R.A. Weinberg, Mesenchymal stem cells within tumour stroma promote breast cancer metastasis, Nature 449(7162) (2007) 557-563.
[225] E. Hergenreider, S. Heydt, K. Treguer, T. Boettger, A.J. Horrevoets, A.M. Zeiher, M.P. Scheffer, A.S. Frangakis, X. Yin, M. Mayr, T. Braun, C. Urbich, R.A. Boon, S. Dimmeler, Atheroprotective communication between endothelial cells and smooth muscle cells through miRNAs, Nat Cell Biol 14(3) (2012) 249-56.
[226] H. Takigawa, Y. Kitadai, K. Shinagawa, R. Yuge, Y. Higashi, S. Tanaka, W. Yasui, K. Chayama, Mesenchymal Stem Cells Induce Epithelial to Mesenchymal Transition in Colon Cancer Cells through Direct Cell-to-Cell Contact, Neoplasia 19(5) (2017) 429-438.
[227] M.R. Dourado, J. Korvala, P. Åström, C.E. De Oliveira, N.K. Cervigne, L.S. Mofatto, D. Campanella Bastos, A.C. Pereira Messetti, E. Graner, A.F. Paes Leme, R.D. Coletta, T. Salo, Extracellular vesicles derived from cancer-associated fibroblasts induce the migration and invasion of oral squamous cell carcinoma, Journal of Extracellular Vesicles 8(1) (2019) 1578525.
[228] G. Huang, G. Lin, Y. Zhu, W. Duan, D. Jin, Emerging technologies for profiling extracellular vesicle heterogeneity, Lab on a Chip 20(14) (2020) 2423-2437.
[229] Y. Yang, V. Bucan, H. Baehre, J. von der Ohe, A. Otte, R. Hass, Acquisition of new tumour cell properties by MSC-derived exosomes, Int J Oncol 47(1) (2015) 244-52.
[230] R. Chowdhury, J.P. Webber, M. Gurney, M.D. Mason, Z. Tabi, A. Clayton, Cancer exosomes trigger mesenchymal stem cell differentiation into pro-angiogenic and pro-invasive myofibroblasts, Oncotarget 6(2) (2015).
[231] P. Zhang, X. Zhou, M. He, Y. Shang, A.L. Tetlow, A.K. Godwin, Y. Zeng, Ultrasensitive detection of circulating exosomes with a 3D-nanopatterned microfluidic chip, Nature Biomedical Engineering 3(6) (2019) 438-451.
[232] J. Kim, B.K. Koo, J.A. Knoblich, Human organoids: model systems for human biology and medicine, Nat Rev Mol Cell Biol 21(10) (2020) 571-584.
[233] S.H. Georgios Vlachogiannis, Alexandra Vatsiou, Yann Jamin, Javier Fernández-Mateos, Khurum Khan, Andrea Lampis, Katherine Eason, Ian Huntingford, Rosemary Burke, Mihaela Rata, Dow-Mu Koh, Nina Tunariu, David Collins, Sanna Hulkki-Wilson, Chanthirika Ragulan, Inmaculada Spiteri, Sing Yu Moorcraft, Ian Chau, Sheela Rao,David Watkins, Nicos Fotiadis, Maria Bali, Mahnaz Darvish-Damavandi, Hazel Lote, Zakaria Eltahir, Elizabeth C. Smyth, Ruwaida Begum, Paul A. Clarke, Jens C. Hahne, Mitchell Dowsett, Johann de Bono, Paul Workman, Anguraj Sadanandam, Matteo Fassan, Owen J. Sansom, Suzanne Eccles, Naureen Starling, Chiara Braconi, Andrea Sottoriva, Simon P. Robinson, David Cunningham, Nicola Valeri, Patient-derived organoids model treatment response of metastatic gastrointestinal cancers, Science 359 (2018) 920-926.
[234] J.B. Mart M. Lamers, Jelte van der Vaart, Kèvin Knoops, Jens Puschhof, Tim I. Breugem, Raimond B. G. Ravelli, J. Paul van Schayck, Anna Z. Mykytyn, Hans Q. Duimel, Elly van Donselaar, Samra Riesebosch, Helma J. H. Kuijpers, Debby Schipper, Willine J. van de Wetering, Miranda de Graaf, Marion Koopmans, Edwin Cuppen, Peter

J. Peters, Bart L. Haagmans, Hans Clevers, SARS-CoV-2 productively infects human gut enterocytes, Science 369 (2020) 50-54.
[235] N. Gjorevski, N. Sachs, A. Manfrin, S. Giger, M.E. Bragina, P. Ordonez-Moran, H. Clevers, M.P. Lutolf, Designer matrices for intestinal stem cell and organoid culture, Nature 539(7630) (2016) 560-564.
[236] N.R. Chevalier, V. Fleury, S. Dufour, V. Proux-Gillardeaux, A. Asnacios, Emergence and development of gut motility in the chicken embryo, PLoS One 12(2) (2017) e0172511.
[237] J. Cremer, I. Segota, C.Y. Yang, M. Arnoldini, J.T. Sauls, Z. Zhang, E. Gutierrez, A. Groisman, T. Hwa, Effect of flow and peristaltic mixing on bacterial growth in a gut-like channel, Proc Natl Acad Sci U S A 113(41) (2016) 11414-11419.
[238] C.P. Gayer, M.D. Basson, The effects of mechanical forces on intestinal physiology and pathology, Cell Signal 21(8) (2009) 1237-44.
[239] L. He, G. Si, J. Huang, A.D.T. Samuel, N. Perrimon, Mechanical regulation of stem-cell differentiation by the stretch-activated Piezo channel, Nature 555(7694) (2018) 103-106.
[240] A.G. Sunghee Estelle Park, Dongeun Huh, Organoids-on-a-chip, Science 364 (2019) 960-965.
[241] H.J. Kim, D. Huh, G. Hamilton, D.E. Ingber, Human gut-on-a-chip inhabited by microbial flora that experiences intestinal peristalsis-like motions and flow, Lab Chip 12(12) (2012) 2165-74.
[242] N. Ashammakhi, R. Nasiri, N.R. Barros, P. Tebon, J. Thakor, M. Goudie, A. Shamloo, M.G. Martin, A. Khademhosseini, Gut-on-a-chip: Current progress and future opportunities, Biomaterials 255 (2020) 120196.
[243] N. Phan, J.J. Hong, B. Tofig, M. Mapua, D. Elashoff, N.A. Moatamed, J. Huang, S. Memarzadeh, R. Damoiseaux, A. Soragni, A simple high-throughput approach identifies actionable drug sensitivities in patient-derived tumour organoids, Commun Biol 2 (2019) 78.
[244] Y. Du, X. Li, Q. Niu, X. Mo, M. Qui, T. Ma, C.J. Kuo, H. Fu, Development of a miniaturized 3D organoid culture platform for ultra-high-throughput screening, J Mol Cell Biol 12(8) (2020) 630-643.
[245] C. Luo, X. Zhu, T. Yu, X. Luo, Q. Ouyang, H. Ji, Y. Chen, A fast cell loading and high-throughput microfluidic system for long-term cell culture in zero-flow environments, Biotechnol Bioeng 101(1) (2008) 190-5.
[246] J. Zhao, H. Lu, Y. Yao, S. Ganda, M.H. Stenzel, Length vs. stiffness: which plays a dominant role in the cellular uptake of fructose-based rod-like micelles by breast cancer cells in 2D and 3D cell culture models?, J Mater Chem B 6(25) (2018) 4223-4231.
[247] M. Lu, F. Chen, C. Cao, C.J. Garvey, N.L. Fletcher, Z.H. Houston, H. Lu, M.S. Lord, K.J. Thurecht, M.H. Stenzel, Importance of Polymer Length in Fructose-Based Polymeric Micelles for an Enhanced Biological Activity, Macromolecules 52(2) (2019) 477-486.
[248] V. Srivastava, T.R. Huycke, K.T. Phong, Z.J. Gartner, Organoid models for mammary gland dynamics and breast cancer, Curr Opin Cell Biol 66 (2020) 51-58.
[249] P.R. Jamieson, J.F. Dekkers, A.C. Rios, N.Y. Fu, G.J. Lindeman, J.E. Visvader, Derivation of a robust mouse mammary organoid system for studying tissue dynamics, Development 144(6) (2017) 1065-1071.
[250] J.M. Rosenbluth, R.C.J. Schackmann, G.K. Gray, L.M. Selfors, C.M. Li, M. Boedicker, H.J. Kuiken, A. Richardson, J. Brock, J. Garber, D. Dillon, N. Sachs, H.

Clevers, J.S. Brugge, Organoid cultures from normal and cancer-prone human breast tissues preserve complex epithelial lineages, Nat Commun 11(1) (2020) 1711.
[251] N. Sachs, J. de Ligt, O. Kopper, E. Gogola, G. Bounova, F. Weeber, A.V. Balgobind, K. Wind, A. Gracanin, H. Begthel, J. Korving, R. van Boxtel, A.A. Duarte, D. Lelieveld, A. van Hoeck, R.F. Ernst, F. Blokzijl, I.J. Nijman, M. Hoogstraat, M. van de Ven, D.A. Egan, V. Zinzalla, J. Moll, S.F. Boj, E.E. Voest, L. Wessels, P.J. van Diest, S. Rottenberg, R.G.J. Vries, E. Cuppen, H. Clevers, A Living Biobank of Breast Cancer Organoids Captures Disease Heterogeneity, Cell 172(1-2) (2018) 373-386 e10.
[252] M.P.H.M. Jansen, J.A. Foekens, I.L. van Staveren, M.M. Dirkzwager-Kiel, K. Ritstier, M.P. Look, M.E. Meijer-van Gelder, A.M. Sieuwerts, H. Portengen, L.C.J. Dorssers, J.G.M. Klijn, E.M.J.J. Berns, Molecular Classification of Tamoxifen-Resistant Breast Carcinomas by Gene Expression Profiling, Journal of Clinical Oncology 23(4) (2005) 732-740.
[253] M. Shehata, H. Kim, R. Vellanki, P.D. Waterhouse, M. Mahendralingam, A.E. Casey, M. Koritzinsky, R. Khokha, Identifying the murine mammary cell target of metformin exposure, Commun Biol 2 (2019) 192.
[254] A.E. Casey, A. Sinha, R. Singhania, J. Livingstone, P. Waterhouse, P. Tharmapalan, J. Cruickshank, M. Shehata, E. Drysdale, H. Fang, H. Kim, R. Isserlin, S. Bailey, T. Medina, G. Deblois, Y.J. Shiah, D. Barsyte-Lovejoy, S. Hofer, G. Bader, M. Lupien, C. Arrowsmith, S. Knapp, D. De Carvalho, H. Berman, P.C. Boutros, T. Kislinger, R. Khokha, Mammary molecular portraits reveal lineage-specific features and progenitor cell vulnerabilities, J Cell Biol 217(8) (2018) 2951-2974.
[255] Z. Zhao, C. Vizetto-Duarte, Z.K. Moay, M.I. Setyawati, M. Rakshit, M.H. Kathawala, K.W. Ng, Composite Hydrogels in Three-Dimensional in vitro Models, Front Bioeng Biotechnol 8 (2020) 611.
[256] N. Broguiere, L. Isenmann, C. Hirt, T. Ringel, S. Placzek, E. Cavalli, F. Ringnalda, L. Villiger, R. Zullig, R. Lehmann, G. Rogler, M.H. Heim, J. Schuler, M. Zenobi-Wong, G. Schwank, Growth of Epithelial Organoids in a Defined Hydrogel, Adv Mater 30(43) (2018) e1801621.
[257] R. Cruz-Acuna, M. Quiros, A.E. Farkas, P.H. Dedhia, S. Huang, D. Siuda, V. Garcia-Hernandez, A.J. Miller, J.R. Spence, A. Nusrat, A.J. Garcia, Synthetic hydrogels for human intestinal organoid generation and colonic wound repair, Nat Cell Biol 19(11) (2017) 1326-1335.
[258] R. Cruz-Acuna, M. Quiros, S. Huang, D. Siuda, J.R. Spence, A. Nusrat, A.J. Garcia, PEG-4MAL hydrogels for human organoid generation, culture, and in vivo delivery, Nat Protoc 13(9) (2018) 2102-2119.
[259] R. Liu, B. Kong, Y. Chen, X. Liu, S. Mi, Formation of helical alginate microfibers using different G/M ratios of sodium alginate based on microfluidics, Sensors and Actuators B: Chemical 304 (2020).
[260] Y. Morimoto, M. Onuki, S. Takeuchi, Mass Production of Cell-Laden Calcium Alginate Particles with Centrifugal Force, Adv Healthc Mater 6(13) (2017).
[261] F. Shao, L. Yu, Y. Zhang, C. An, H. Zhang, Y. Zhang, Y. Xiong, H. Wang, Microfluidic Encapsulation of Single Cells by Alginate Microgels Using a Trigger-Gellified Strategy, Front Bioeng Biotechnol 8 (2020) 583065.
[262] Claudia Fischbacha, Hyun Joon Kong, Susan X. Hsiong, Marta B. Evangelista, Will Yuen, D.J. Mooney, Cancer cell angiogenic capability is regulated by 3D culture and integrin engagement, PNAS 102(2) (2009) 399-404.

[263] Y.C. Lu, T. Chu, M.S. Hall, D.J. Fu, Q. Shi, A. Chiu, D. An, L.H. Wang, Y. Pardo, T. Southard, C.G. Danko, J. Liphardt, A.Y. Nikitin, M. Wu, C. Fischbach, S. Coonrod, M. Ma, Physical confinement induces malignant transformation in mammary epithelial cells, Biomaterials 217 (2019) 119307.
[264] R.A. Perez, H.W. Kim, Core-shell designed scaffolds for drug delivery and tissue engineering, Acta Biomater 21 (2015) 2-19.
[265] P. Agarwal, H. Wang, M. Sun, J. Xu, S. Zhao, Z. Liu, K.J. Gooch, Y. Zhao, X. Lu, X. He, Microfluidics Enabled Bottom-Up Engineering of 3D Vascularized Tumour for Drug Discovery, ACS Nano 11(7) (2017) 6691-6702.
[266] M.M. Capeling, M. Czerwinski, S. Huang, Y.H. Tsai, A. Wu, M.S. Nagy, B. Juliar, N. Sundaram, Y. Song, W.M. Han, S. Takayama, E. Alsberg, A.J. Garcia, M. Helmrath, A.J. Putnam, J.R. Spence, Nonadhesive Alginate Hydrogels Support Growth of Pluripotent Stem Cell-Derived Intestinal Organoids, Stem Cell Reports 12(2) (2019) 381-394.
[267] B.L. Strand, Y.A. Morch, T. Espevik, G. Skjak-Braek, Visualization of alginate-poly-L-lysine-alginate microcapsules by confocal laser scanning microscopy, Biotechnol Bioeng 82(4) (2003) 386-94.
[268] M. Gómez-González, E. Latorre, M. Arroyo, X. Trepat, Measuring mechanical stress in living tissues, Nature Reviews Physics 2(6) (2020) 300-317.
[269] C.J. Chan, T. Hiiragi, Integration of luminal pressure and signalling in tissue self-organization, Development 147(5) (2020).
[270] R. Gomez-Martinez, A.M. Hernandez-Pinto, M. Duch, P. Vazquez, K. Zinoviev, E.J. de la Rosa, J. Esteve, T. Suarez, J.A. Plaza, Silicon chips detect intracellular pressure changes in living cells, Nat Nanotechnol 8(7) (2013) 517-21.
[271] E. Mohagheghian, J. Luo, J. Chen, G. Chaudhary, J. Chen, J. Sun, R.H. Ewoldt, N. Wang, Quantifying compressive forces between living cell layers and within tissues using elastic round microgels, Nat Commun 9(1) (2018) 1878.
[272] A. Trushko, I. Di Meglio, A. Merzouki, C. Blanch-Mercader, S. Abuhattum, J. Guck, K. Alessandri, P. Nassoy, K. Kruse, B. Chopard, A. Roux, Buckling of an Epithelium Growing under Spherical Confinement, Dev Cell 54(5) (2020) 655-668 e6.
[273] P. Schneider, R. Kienzler, Dimensioning of thick-walled spherical and cylindrical pressure vessels, Mathematics and Mechanics of Solids 25(7) (2017) 1405-1415.
[274] E.R. West, M. Xu, T.K. Woodruff, L.D. Shea, Physical properties of alginate hydrogels and their effects on in vitro follicle development, Biomaterials 28(30) (2007) 4439-48.
[275] K. Leonavicius, C. Royer, C. Preece, B. Davies, J.S. Biggins, S. Srinivas, Mechanics of mouse blastocyst hatching revealed by a hydrogel-based microdeformation assay, Proc Natl Acad Sci U S A 115(41) (2018) 10375-10380.
[276] A.R. Harris, L. Peter, J. Bellis, B. Baum, A.J. Kabla, G.T. Charras, Characterizing the mechanics of cultured cell monolayers, Proc Natl Acad Sci U S A 109(41) (2012) 16449-54.
[277] Y. Zhang, J. Yu, H.N. Bomba, Y. Zhu, Z. Gu, Mechanical Force-Triggered Drug Delivery, Chem Rev 116(19) (2016) 12536-12563.
[278] J. Hu, Y. Liu, Cyclic Strain Enhances Cellular Uptake of Nanoparticles, Journal of Nanomaterials 2015 (2015) 1-8.
[279] S. Nandi, N.R. Kale, V. Takale, G.C. Chate, M. Bhave, S.S. Banerjee, J.J. Khandare, Cell deformation and acquired drug resistance: elucidating the major influence of drug-nanocarrier delivery systems, J Mater Chem B 8(9) (2020) 1852-1862.